

**Investigation of Fundamental Processes Governing Secondary
Organic Aerosol Formation in Laboratory Chambers**

Thesis by

Xuan Zhang

In Partial Fulfillment of the Requirements

for the Degree of

Doctor of Philosophy



California Institute of Technology

Pasadena, California

2015

(Defended May 12, 2015)

© 2015

Xuan Zhang

All Rights Reserved

To my parents

Acknowledgements

Pursuing a Ph.D. at Caltech has been the most wonderful journey in my life!

I would like to express my deepest appreciation to my advisor John Seinfeld, for his mentorship, guidance, trust, understanding, unyielding support, and endless opportunities for conducting exciting research throughout my time at Caltech. I started to read John's book « Atmospheric Chemistry and Physics » back when I was in Peking University. I was continuously amazed by how fundamental knowledge in transport and thermodynamics is applied to describe the behavior of little particles in the atmosphere. I would have already felt so lucky to meet such a genius who is mastering in math, physics, and chemistry, and is able to implement the theoretical framework to improve the air quality. Imagine how excited I was when I got to know that Prof. John Seinfeld would serve as my academic and research advisor for my graduate study! I still clearly remember the first day I arrived at Caltech and John himself showed me around the campus and one of the best equipped chamber facilities in the world, the Rooflab chamber! John naturally has the attitude and substance of a genius and it always seems so easy for him to distinguish an exciting research idea from a pedestrian one. I believe that he has shaped the way I look at and approach scientific problems, and I can see my progresses over the course of my Ph.D. study: from getting denied for over 90% of my research proposals in my junior year to receiving more and more approvals and sometimes even compliments on my research projects in my senior year. I know that all of the progresses I have made are attributed to John's willingness and patience to consult with me on a weekly even daily basis and be able to convey real guidance. I also benefit

hugely from John as a successful manager: his ability to effectively manage time and resources so that he can always return emails in minutes, his feedback on my drafts or proposals in days, and be available for all the meetings and discussions. John's support to me is beyond the fact that he can provide unlimited resources and opportunities on scientific research, he also offers generous help in establishing a network of scientific contacts. Last summer the 2nd Sini-U.S. Workshop on Sustainability Issues at the Nexus of Energy, Water, Climate and Air Pollution was held in Pasadena. John was invited to give a keynote speech at this workshop. When he realized that this might be a very good opportunity for me to get some exposure to the leading atmospheric scientists in China, he immediately passed this to me, making me the only graduate student speaker in the whole conference. All in all, I will be always grateful to John for my life and I hope he knows how much I look up to him and appreciate him taking me as his student.

Prof. Rick Flagan has played a central role in my learning experiences of Scanning Mobility Particle Sizer. I am grateful for his patience and willingness to give me step-by-step instructions to put up a Differential Mobility Analyzer and to go over each wire that communicates the hardware with the data acquisition board. When our lab is running short in Condensation Particle Counter (CPC), he spent all day in lab with us, documenting the status of each CPC and possible repair solutions. Rick is a constant source of instrumentation development. Whenever there are instruments breaking down or I have questions related to instrument design, implementation, and maintenance, I can always find a satisfying answer and solution from him. Rick's hands-on research style is also reflected by his cooking skill. I already missed the grilled salmon he made for us in our group barbecue he hosted in the past.

Prof. Paul Wennberg introduced the CalTecher's belief and passion in science by teaching me the first course I had at Caltech. Having Paul's class is always a great challenge but fun. He continuously and convincingly conveys the spirit of exploration and an excitement in regard to teaching and tutoring. Last year, I took atmospheric chemistry II, and I realized that for the first time, I finally got a clear picture of isoprene photochemistry, regardless years of reading in the past. I also find myself always benefiting a lot from discussions or even little conversations with him. His genial nature makes him a good listener, as well as a great advise giver. One of my studies regarding vapor wall losses at humid chamber conditions is originally inspired by our conversations in the coffee room. I am thankful to him for being ever so kind to show interest in my research and for giving his precious advice on my research topic.

I am equally grateful to Prof. Michael Hoffmann's support. His willingness to converse with me like a friend was invaluable to my Ph.D. experience. I remember many impromptu hallway conversations we had, from science to politics in China. I thank him for his valuable and practical suggestions he has given to me for my future career development. I have also witnessed significant improvement of his Mandarin Chinese in the past 5 years and am certainly touched by his interests and friendliness in the culture and custom of my motherland.

Many thanks must also go to Prof. Chris Cappa, for the fruitful collaboration we had last year, leading to a breakthrough that bridges the gap of our understanding of SOA formation between the actual atmosphere and laboratory conditions. Discussions with Chris regarding the reevaluation of SOA yield by vapor wall loss correction inspired my

interests in further studies of the interactions of vapors with the chamber wall, which forms three chapters of my thesis.

Looking back, one person I must thank is Prof. Chen Zhongming, my master advisor in Peking University. I would never be able to study at Caltech without him. I acknowledge him for encouraging me to pursue graduate studies in United States and for continuously supporting me, visiting me and updating me the research progresses in atmospheric science in China.

I have worked with many great scientists at Caltech throughout my PhD. I attribute much of my successful experience in the chamber lab to Christine Loza. She taught me all the skills to work as an atmospheric chemistry experimentalist, from as small as how to screw a Swagelock nut to a union, to as big as how to write up a complicated code to derive the SOA yield under both lower and upper bound corrections. What I treasure most is the countless time we spent together in my second year to build up our brand new Linde & Robinson G16 chamber lab. I was truly impressed by her smart design of the chamber framework and her detailed planning of all the plumbing and drilling works. I want to tell Christine that I am so proud of our work together and up to this moment, our chamber is still running so beautifully! I also benefitted from working with many graduate students and postdocs: I thank Becky Schwantes and Matt Coggon for always being available of running instruments and data analysis for my experiments; I thank Renee McVay for the stimulating discussions on the model framework development. I thank Tran Nguyen for her passionate discussions of isoprene chemistry with me; I thank John Crouse and Jason St. Clair for their brilliant ideas and suggestions related to experimental protocols and instrumentation design; I shifted my interest into

instrumentation and aerosol characterization method development during my last year at Caltech. I would like to thank Scott Hersey to get me started on the PILS and trained me how to use the IC system. I thank Armin Sorooshian and Fred Brechtel for always answering my questions about PILS and helping me troubleshoot when something went wrong. I especially thank Nathan Dalleska to train me on LC/MS and let me bother him countless times for any instrumentation specific questions.

One of the best parts of doing atmospheric aerosol science at Caltech is connecting with Caltech alumni in the aerosol community. I got to know many of them during overlap at Caltech, conference, and their occasional visit to Caltech. I would especially like to thank Arthur Chan, Mannin Chan, Liao Hong, Sally Ng, and Jason Surratt for embracing me to this community, sharing all of your laughter and tears during your Ph.D., and giving me your advise for a academia career path.

I would not have had a joyful life in Caltech without my sincere friends. I thank Zhang Ke, not only for being my lunch/dinner/gym buddy everyday, but also for giving me her valuable thoughts and suggestions on my confusions and concerns. I thank Ci Maolin and Yang Da for acquainting me with a brand new life when I first came to U.S.; for listening to me fussing about all my little problems and comforting me; for puzzling all of my questions in Math and Atmosphere Physics, and for taking me to all the delicious Chinese restaurants in LA. I thank Chu Hao for leading the Caltech Chinese Club 2012 with me, for driving me to Mexico to renew my U.S. visa, and for trying to get me interested in Japanese Cartoon but failed so far. I thank Ma Yiran for being my roommate for four years; for chatting and accompanying with me at home; and for giving me tips on phone plan, car insurance and so on. I thank Jiang Junle for inviting me to his big apartment

having dinner and playing games all the time and for throwing me my surprising birthday party last year. I thank Tan Zhihong for sending me postcards from all over the world, for taking me to have ‘Guoqiao noodles’ before my qualify exam, and for being so generous with his help whenever I need.

Finally, mom and dad: thank you for loving me unconditionally since I was born; for being absolutely proud of me as your only child; for providing me unlimited education opportunities all these years; for supporting me to pursue my Ph.D. in US, although missing me everyday... I would like to dedicate my thesis to you for being my beloved parents!

Abstract

Our understanding of the processes and mechanisms by which secondary organic aerosol (SOA) is formed is derived from laboratory chamber studies. In the atmosphere, SOA formation is primarily driven by progressive photooxidation of SOA precursors, coupled with their gas-particle partitioning. In the chamber environment, SOA-forming vapors undergo multiple chemical and physical processes that involve production and removal via gas-phase reactions; partitioning onto suspended particles vs. particles deposited on the chamber wall; and direct deposition on the chamber wall. The main focus of this dissertation is to characterize the interactions of organic vapors with suspended particles and the chamber wall and explore how these intertwined processes in laboratory chambers govern SOA formation and evolution.

A Functional Group Oxidation Model (FGOM) that represents SOA formation and evolution in terms of the competition between functionalization and fragmentation, the extent of oxygen atom addition, and the change of volatility, is developed. The FGOM contains a set of parameters that are to be determined by fitting of the model to laboratory chamber data. The sensitivity of the model prediction to variation of the adjustable parameters allows one to assess the relative importance of various pathways involved in SOA formation.

A critical aspect of the environmental chamber is the presence of the wall, which can induce deposition of SOA-forming vapors and promote heterogeneous reactions. An experimental protocol and model framework are first developed to constrain the vapor-wall interactions. By optimal fitting the model predictions to the observed wall-induced

decay profiles of 25 oxidized organic compounds, the dominant parameter governing the extent of wall deposition of a compound is identified, i.e., wall accommodation coefficient. By correlating this parameter with the molecular properties of a compound via its volatility, the wall-induced deposition rate of an organic compound can be predicted based on its carbon and oxygen numbers in the molecule.

Heterogeneous transformation of δ -hydroxycarbonyl, a major first-generation product from long-chain alkane photochemistry, is observed on the surface of particles and walls. The uniqueness of this reaction scheme is the production of substituted dihydrofuran, which is highly reactive towards ozone, OH, and NO₃, thereby opening a reaction pathway that is not usually accessible to alkanes. A spectrum of highly-oxygenated products with carboxylic acid, ester, and ether functional groups is produced from the substituted dihydrofuran chemistry, thereby affecting the average oxidation state of the alkane-derived SOA.

The vapor wall loss correction is applied to several chamber-derived SOA systems generated from both anthropogenic and biogenic sources. Experimental and modeling approaches are employed to constrain the partitioning behavior of SOA-forming vapors onto suspended particles vs. chamber walls. It is demonstrated that deposition of SOA-forming vapors to the chamber wall during photooxidation experiments can lead to substantial and systematic underestimation of SOA. Therefore, it is likely that a lack of proper accounting for vapor wall losses that suppress chamber-derived SOA yields contribute substantially to the underprediction of ambient SOA concentrations in atmospheric models.

Contents

Acknowledgements	iv
Abstract.....	x
1. Introduction.....	1-1
1.1 Background and Motivation	1-2
1.2 Organization of Thesis.....	1-3
1.3 Bibliography	1-5
2. A Functional Group Oxidation Model For SOA Formation and Aging	2-1
2.1 Abstract.....	2-2
2.2 Introduction.....	2-2
2.3 Development of a Functional Group Oxidation Model (FGOM).....	2-8
2.3.1 Functionalization	2-9
2.3.2 Fragmentation.....	2-13
2.3.3 Volatility Estimation.....	2-15
2.3.4 Gas-particle partitioning.....	2-18
2.3.5 Particle-phase accretion reactions.....	2-19
2.3.6 Summary of the Functional Group Oxidation Model (FGOM).....	2-20
2.4 Application to SOA Formation for C ₁₂ Alkanes.....	2-22
2.4.1 Organic aerosol growth.....	2-24
2.4.2 Elemental aerosol composition.....	2-26
2.4.3 Role of particle-phase chemistry	2-32
2.5 Comparison of FGOM and SOM.....	2-34

2.6	Acknowledgement	2-39
2.7	Bibliography	2-39
3.	Role of Ozone in SOA Formation from Alkane Photooxidation	3-1
3.1	Abstract	3-2
3.2	Introduction.....	3-3
3.3	Experimental	3-6
3.4	Chemical Mechanism	3-10
3.5	Results and Discussion	3-14
3.5.1	Predicted substituted dihydrofuran formation and reaction with ozone in the dodecane system	3-15
3.5.2	Formation of cyclic hemiacetals and alkyl-substituted dihydrofuran.....	3-16
3.5.3	Products from alkyl-substituted dihydrofuran oxidation	3-19
3.5.4	Ozonolysis vs. OH-oxidation.....	3-21
3.5.5	Experiment and model comparison	3-24
3.6	Atmospheric Implications.....	3-27
3.7	Acknowledgement	3-29
3.8	Bibliography	3-29
4.	Influence of Vapor Wall-loss in Laboratory Chambers on Yields of Secondary Organic Aerosol	4-1
4.1	Abstract.....	4-2
4.2	Introduction.....	4-3
4.3	Materials and Methods.....	4-4

4.3.1	Chamber experiments	4-4
4.3.2	SOA modeling	4-4
4.4	Toluene Photooxidation Experiments.....	4-5
4.5	SOA Modeling and the Influence of Vapor Wall Loss	4-6
4.6	Dependence on Experimental Conditions.....	4-11
4.7	Vapor Losses and Sensitivity to C_w	4-12
4.8	Consideration of Historical Experiments.....	4-13
4.9	Implications	4-14
4.10	Acknowledgement	4-15
4.11	Bibliography	4-15
5.	Vapor Wall Deposition in Teflon Chambers.....	5-1
5.1	Abstract.....	5-2
5.2	Introduction.....	5-3
5.3	Vapor Wall Deposition — Theory.....	5-5
5.3.1	Deposition rate coefficient ($k_{w,depo,i}$).....	5-6
5.3.2	Evaporation rate coefficient ($k_{w,evap,i}$).....	5-8
5.4	Vapor Wall Deposition — Experiment	5-10
5.5	Absorbing Organic Mass on the Chamber Wall (C_w).....	5-13
5.6	Vapor Sorption into FEP Teflon Films.....	5-16
5.7	Accommodation Coefficient on the Chamber Wall ($\alpha_{w,i}$).....	5-18
5.8	Characterizing Chamber Vapor Wall Deposition Rate.....	5-21
5.9	Impact of Vapor Wall Deposition on SOA Yields	5-23

5.10	Conclusions.....	5-25
5.11	Acknowledgements.....	5-27
5.12	Appendix.....	5-27
5.13	Bibliography	5-28

6. Conclusions and Future Work..... 6-1

Appendix A. Application of the Statistical Oxidation Model (SOM) to secondary organic aerosol formation from photooxidation of C₁₂ alkanes.

Appendix B. Organic aerosol formation from the reactive uptake of isoprene epoxydiols (IEPOX) onto non-acidified inorganic seeds.

Appendix C. Secondary organic aerosol yields of 12-carbon alkanes.

List of Tables

2.1. Secondary organic aerosol yields and initial experimental conditions for OH oxidation of C ₁₂ alkanes.....	2-50
2.2. Best-fit parameters for OH-initiated oxidation of C ₁₂ alkanes.....	2-51
2.3. Comparison of the treatment of gas-phase chemistry, including functionalization and fragmentation, particle-phase chemistry, including oxidation and accretion reactions, and gas-particle partitioning between SOM and FGOM.....	2-53
3.1. Experimental conditions for the photooxidation of dodecane.....	3-40
3.2. Proposed structures unique to the alkyl-substituted dihydrofuran chemistry.....	3-41
4.1. Average biases in SOA yields due to vapor wall-losses for various VOCs under low- and high-NO _x conditions.	4-20
5.1. Experimental conditions for production of oxidized organic vapors.....	5-33
5.2. Best-fit values of $\alpha_{w,i}$ and C_w on chamber walls for vapors.....	5-34

List of Figures

- 2.1. Scheme for SOA formation and evolution, showing multi-generational gas- and particle- phase reactions, in the Functional Group Oxidation Model..... 2-54
- 2.2. Chemical mechanisms of alkane photooxidation. 2-55
- 2.3. Carbon number range for products of OH oxidation of dodecane under low-NO_x conditions. For illustration, the shaded region ($C^\circ \leq 1000 \mu\text{g}/\text{m}^3$) is taken to represent the combination of carbon number and volatility for which a molecule can appreciably partition to the particle phase. 2-56
- 2.4. Simulated (colors) and observed (black) time-dependent organic aerosol growth from the photooxidation of four C₁₂ alkanes under high- (red) and low- (green) NO_x conditions. Note that “sim.1” represents the full fitting of the six empirical parameters and “sim.2” refers to fitting by only two parameters, r_p and f_v , to the organic mass concentration..... 2-57
- 2.5. Time evolution of predicted gas- and particle- phase multi-generational products from OH oxidation of C₁₂ alkanes under high- and low-NO_x conditions..... 2-58
- 2.6. Simulated (colors) and observed (black) temporal profiles of particulate O:C ratio from the photooxidation of C₁₂ alkanes under high- (red) and low- (green) NO_x conditions. Dark colors denote “sim.1” and light colors denote “sim.2”..... 2-59
- 2.7. Simulated (colors) and observed (black) temporal profiles of particulate H:C ratio from the photooxidation of C₁₂ alkanes under high- (red) and low- (green) NO_x conditions. Dark colors denote “sim.1” and light colors denote “sim.2”..... 2-60

- 2.8. Simulated (colors) and observed (black) temporal profiles of particulate oxidation state (OS_C) from the photooxidation of C_{12} alkanes under high- (red) and low- (green) NO_x conditions. 2-61
- 2.9. Effect of particle-phase oxidative reactions on the SOA growth from the low- NO_x photooxidation of dodecane. 2-62
- 2.10. Comparison of FGOM with SOM for low- NO_x dodecane SOA formation. 2-63
- 2.11. van Krevelen diagram. FGOM and SOM simulated H:C vs. O:C temporal profile, together with chamber measured data for low- NO_x dodecane system. 2-64
- 3.1. Schematic mechanism for the photooxidation of dodecane under (a) high- and (b) low- NO_x conditions. Note only the first three generations of products are shown here. The boxes indicate compounds and associated reaction pathways incorporated in the model simulation. 3-42
- 3.2. Proposed mechanism for the OH-initiated oxidation of alkyl-substituted dihydrofuran under (a) high- and (b) low- NO_x conditions. The boxes indicate compounds or reaction pathways incorporated in the model simulation. CIMS monitored species have m/z noted in red. Estimated vapor pressure (atm) of each compound is indicated in blue. 3-44
- 3.3. Model-predicted relative abundance of δ -hydroxycarbonyl and alkyl-substituted dihydrofuran, together with other 1st generation products under high- NO_x (H) and other 3rd generation products under low- NO_x (L) conditions in gas (g) and particle (p) phases. All the organic masses are normalized by the initial organic mass. 3-46

3.4. Temporal profiles of ion $C_{12}H_{22}O \cdot H^+$ ($m/z = 183$) and $C_{12}H_{24}O_2 \cdot CF_3O^-$ ($m/z = 285$) measured by CIMS and ion $C_{12}H_{23}O^+$ ($m/z = 183$) measured by AMS under high- and low- NO_x conditions.	3-47
3.5. Time-dependent evolution of ion $C_{12}H_{22}O \cdot H^+$ ($m/z = 183$) measured by CIMS and ion $C_{12}H_{23}O^+$ ($m/z = 183$) measured by AMS at 3%, 10%, 20%, and 50% RH.	3-48
3.6. Time-dependent evolution of CIMS measured signals at m/z 299, and m/z 249 and 315, as a function of O_3 levels under high- and low- NO_x conditions over the course of 20 h photooxidation.	3-49
3.7. Time-dependent evolution of AMS measured ion intensities of $C_2H_4O_2^+$ and $C_3H_5O_2^+$ as a function of decay of the $C_{12}H_{23}O^+$ signal.	3-50
3.8. SOA evolution as a function of OH exposure vs. O_3 exposure from dodecane photochemistry under high- NO_x conditions in the f_{44} vs. f_{43} space.	3-51
3.9. (A) SOA average carbon oxidation state as a function of OH exposure from dodecane photochemistry under high- NO_x conditions. Exp.1 corresponds to a regime in which OH-oxidation of dihydrofuran is dominant. Exp. 3, 4, and 5 correspond to a regime in which ozonolysis of dihydrofuran is dominant, at 10%, 20%, and 50% RH, respectively. (B) van Krevelen diagram. AMS measured O:C vs. H:C ratios for the four experiments under the OH total exposure ranging from 1.0×10^7 to 2.0×10^7 molecules cm^{-3} h. Gray dash lines denote the average carbon oxidation state.	3-52
3.10. Comparison of CIMS measured ions in positive and negative mode, with chemical structures proposed in Table 2, with model simulations using experimental conditions of Exp. #2.	3-53

- 3.11. (A) Comparison of the predicted dodecane decay and SOA growth with observations (Exp.#2). (B) The contribution of dihydrofuran chemistry (DHF+OH/O₃) vs. dodecane photochemistry (DOD+OH) to the total organic mass. (C) Molar fractions of major functional groups after 3 h of photochemical reaction (when alkyl-substituted dihydrofuran peaks and organic loading is $\sim 50 \mu\text{g m}^{-3}$) as predicted by SIM1. Note that “other” includes dihydrofuran, tetrahydrofuran, and ether moieties. (D) Comparison of the predicted average carbon oxidation state with observations (Exp.#2). 3-55
- 3.12. Regimes of dominance of ozonolysis vs. OH-oxidation of substituted dihydrofuran. Daily maximum OH concentrations vary by regions in the troposphere, i.e., $10^5 - 10^6$ molecules cm^{-3} for background air, $10^6 - 10^7$ molecules cm^{-3} for rural air, and $> 10^7$ molecules cm^{-3} for urban air, with a global average concentration of 1×10^6 molecules cm^{-3} . Daily average surface ozone mixing ratios in rural areas are between 10 and 50 ppb, while these can exceed 100 ppb in polluted urban areas. 3-56
- 4.1. Hourly averaged lower bound SOA yields over the course of a toluene photooxidation experiment as a function of initial AS seed surface area for (A) high-NO_x and (B) low-NO_x conditions. 4-21
- 4.2. Observed (points) and simulated (lines) SOA concentrations for each photochemical oxidation experiment performed for different initial inorganic seed surface area for (A) low-NO_x and (B) high-NO_x conditions. The dashed lines indicate the experiment to which the SOM was explicitly fit, and the solid lines indicate simulation results based on those fits. (C) The wall-loss bias factor, R_{wall} , as a function of seed surface

area. Filled symbols use the optimal k_w/α pair and the corresponding best-fit SOM parameters determined from (A) and (B).	4-22
4.3. Calculated SOA yield bias as a function of initial toluene concentration and OH concentration when $k_w = 2.5 \times 10^{-4} \text{ s}^{-1}$ and $C_w = 10 \text{ mg m}^{-3}$. The R_{wall} values for a given [toluene] and [OH] are indicated by colors and contours and are averaged over the period when $C_{\text{SOA}} > 0.5 \text{ } \mu\text{g m}^{-3}$ to the end of an experiment at 18 h. Results are based on the optimal fit of the SOM to the low-NO _x experiments.....	4-23
4.4. Calculated vapor wall-loss bias, R_{wall} , as a function of the effective wall mass concentration, C_w , for the low-NO _x toluene photooxidation experiments at varying initial seed surface area.....	4-24
5.1. Theoretical framework representing the vapor-wall interactions. Concentrations of organic vapor i in the well-mixed core, in the boundary layer, over the surface of chamber walls, and in the chamber walls are denoted by $\bar{C}_{v,i}$, $C_{v,i}$, $C_{0,i}$, and $\bar{C}_{w,i}$, respectively.....	5-38
5.2. Example of the experimental procedure to assess vapor wall deposition using 3-nitrooxy-6-dodecanol ($m/z = (-) 332$): Period (1) organic oxidation product generation; Period (2) vapor wall deposition at 298 K in the dark; Period (3) chamber temperature ramp from 298 K to 318 K; and Period (4) temperature held at 318 K in the dark.	5-39
5.3. CIMS traces of oxidized organic vapors generated from the photooxidation of isoprene, toluene, α -pinene and dodecane under high/low-NO conditions over the four chamber periods in Figure 2.....	5-40

- 5.4. Comparison of vapor-wall interactions for α -pinene + OH products under controlled experimental conditions in used (circle) vs. unused (triangle) Teflon chambers. 30-min averaged data are shown here for clarity. 5-43
- 5.5. Inferred total amount of (a) equivalent absorbing organic mass on chamber walls, C_w (g m^{-3}), and (b) dimensionless Henry's law constants, H_i , as a function of saturation concentration, C_i^* ($\mu\text{g m}^{-3}$). 5-44
- 5.6. Inferred accommodation coefficients of organic oxidation products on chamber walls ($\log_{10}(\alpha_{w,i})$) as a function of saturation concentrations ($\log_{10}(C_i^*)$) and average carbon oxidation state (OS_C). 5-45
- 5.7. Predicted vapor wall deposition rate ($k_{w,i} / \text{s}^{-1}$) of organic compounds in a Teflon chamber as a function of carbon number (n_C) and oxygen number (n_O). 5-46
- 5.8. Comparison of estimated gas-particle equilibration timescale ($\tau_{g/p,i}$) as a function of the gas-particle mass accommodation coefficient ($\alpha_{p,i}$, lower x-axis) and the ratio of total particle surface area to the chamber wall area (R_a , colour bar), and vapor wall deposition timescale ($\tau_{g/w,i}$) as a function of gas-wall mass accommodation coefficient ($\alpha_{w,i}$, upper x-axis). 5-47

Chapter 1

Introduction

1.1 Background and motivation

Secondary organic aerosol (SOA) constitutes a major fraction of sub-micrometer particulate matter in the atmosphere (Jimenez et al., 2009) and consequently has important impacts on regional and global climate and human health (IPCC, 2001). The chemical and physical processes associated with SOA formation are complex and varied. In general, volatile organic compounds (VOC) from anthropogenic and biogenic emissions undergo multiple generations of photooxidation in the gas phase, to yield products that are generally oxidized, functionalized, and have sufficiently low volatilities to partition into the particle phase, as SOA.

Laboratory chambers are ubiquitous in studies of atmospheric chemistry. A primary goal of chamber-based atmospheric aerosol research is to understand the fundamental mechanisms by which gas-phase photochemistry coupled with gas-particle partitioning leads to SOA formation and evolution. Chamber-measured SOA yields (mass of SOA formed per mass of VOC reacted) have been widely parameterized into regional/global atmospheric models, and chemical mechanisms leading to SOA formation and aging have been derived based on the gas/particle-phase identification of intermediate/semi/low-volatility compounds generated in controlled chamber experiments. Despite important advances that were made during the last decade, world-wide data have been accumulating that point to the fact that model predictions of SOA levels based on the chamber experiments derived parameterization are substantially lower than ambient observations (Heald et al., 2005; Volkamer et al., 2006; Ensberg et al., 2013).

An unavoidable consequence of the use of a laboratory chamber is interaction of vapors and particles with the chamber wall. Losses of particles to the chamber wall are routinely accounted for, but there has been little evaluation of the effects on SOA yields of losses of the oxidized vapors that are precursors to SOA to chamber walls. This thesis focuses on understanding 1) the nature of Teflon chamber wall as an absorbing medium; 2) the wall-induced deposition behaviours of a variety of oxidized organic vapors; 3) Possible chemical reactions occurring at the chamber wall surface; 4) incorporation of mathematical expressions of vapor-wall interactions into SOA predictive models; and 5) the influence of vapor wall deposition on the chamber measured SOA yields.

1.2 Organization of Thesis

In chapter 2, a new variation of the SOA model is developed based on explicit chemical information in terms of the types of functional groups that result from the oxidation of a parent VOC. We term this the Functional Group Oxidation Model (FGOM). We first describe the development of the FGOM, and then apply it to SOA formation from the low- and high- NO_x photooxidation of four C_{12} alkanes.

In Chapter 3, we identified a heterogeneous chemical reaction scheme that is occurring on the chamber wall, i.e., the heterogeneous formation of substituted dihydrofurans and their subsequent gas-phase reaction with ozone. We present the results of a series of chamber dodecane photooxidation experiments under two reaction regimes, i.e., “OH-dominant”, in which over 70% of substituted dihydrofurans are oxidized by OH, vs. “ O_3 -dominant”, in which 80% – 90% of substituted dihydrofurans react with O_3 . Gas-phase products that are unique to the substituted dihydrofuran chemistry are identified. The

impact of ozonolysis of substituted dihydrofurans on the particle-phase product distribution from the photooxidation of dodecane is investigated by comparing intensities of certain ions that are indicative of ozonolysis chemistry.

In Chapter 4, we demonstrated that vapor losses on the chamber wall can lead to substantially underestimated SOA formation, by factors as much as 4. Accounting for such losses has the clear potential to bring model predictions and observations of organic aerosol levels into much closer agreement.

In Chapter 5, we developed an experimental protocol and a model framework to constrain the vapor-wall interactions in Teflon chambers. We measured the wall deposition rates of 25 oxidized organic compounds generated from the photooxidation of isoprene, toluene, α -pinene, and dodecane in two chambers that had been extensively used and in two new unused chambers. We found that the extent of prior use of the chamber did not significantly affect the sorption behavior of the Teflon films. By optimizing the model output to the observed vapor decay profiles, we identified that the dominant parameter governing the extent of wall deposition of a compound is its wall accommodation coefficient ($\alpha_{w,i}$), which can be correlated through its volatility with the number of carbons and oxygens in the molecule. Among the 25 compounds studied, the maximum wall deposition rate is exhibited by the most highly oxygenated and least volatile compounds.

1.3 Bibliography

Cappa, C. and Wilson, K. R.: Multi-generation gas-phase oxidation, equilibrium partitioning, and the formation and evolution of secondary organic aerosol, *Atmos. Chem. Phys.*, 12, 9505-9528, 2012.

Cappa, C., Zhang, X., Loza, C. L., Craven, J. S., Yee, L. D., and Seinfeld, J. H.: Application of the Statistical Oxidation Model (SOM) to secondary organic aerosol formation from photooxidation of C₁₂ Alkanes, *Atmos. Chem. Phys. Discuss.*, 12, 27077-27109, 2012.

Ensberg, J. J., Hayes, P. L., Jimenez, J. L., Gilman, J. B., Kuster, W. C., deGouw, J. A., Holloway, J. S., Gordon, T. D., Jathar, S., Robinson, A. L., and Seinfeld, J. H.: Emission factor ratios, SOA mass yields, and the impact of vehicular emissions on SOA formation, *Atmos. Chem. Phys.*, 13(10), 27779-27810, 2013.

Heald, C. L., Jacob, D. J., Park, R. J., Russell, L. M., Huebert, B. J., Seinfeld, J. H., Liao, H., and Weber, R. J.: A large organic aerosol source in the free troposphere missing from current models, *Geophys. Res. Lett.*, 32, L18809, 2005.

Jimenez, J. L., Canagaratna, M. R., Donahue, N. M., Prevot, A. S. H., Zhang, Q., Kroll, J. H., DeCarlo, P. F., Allan, J. D., Coe, H., Ng, N. L., Aiken, A. C., Docherty, K. S., Ulbrich, I. M., Grieshop, A. P., Robinson, A. L., Duplissy, J., Smith, J. D., Wilson, K. R., Lanz, V. A., Hueglin, C., Sun, Y. L., Tian, J., Laaksonen, A., Raatikainen, T., Rautiainen, J., Vaattovaara, P., Ehn, M., Kulmala, M., Tomlinson, J. M., Collins, D. R., Cubison, M. J., Dunlea, E. J., Huffman, J. A., Onasch, T. B., Alfarra, M. R., Williams, P. I., Bower,

K., Kondo, Y., Schneider, J., Drewnick, F., Borrmann, S., Weimer, S., Demerjian, K., Salcedo, D., Cottrell, L., Griffin, R., Takami, A., Miyoshi, T., Hatakeyama, S., Shiono, A., Sun, J. Y., Zhang Y. M., Dzepina, K., Kimmel, J. R., Sueper, D., Jayne, J. T., Herndon, S. C., Trimborn, A. M., Williams, L. R., Wood, E. C., Middlebrook, A. M., Kolb, C. E., Baltensperger, U., and Worsnop, D. R.: Evolution of organic aerosols in the atmosphere, *Science*, 326, 1525-1529, 2009.

Intergovernmental Panel on Climate Change (IPCC): *Climate Change: The Scientific Basis*, Cambridge University Press, UK, 2001.

Volkamer, R., Jimenez, J. L., Martini, F. S., Dzepina, K., Zhang, Q., Salcedo, D., Molina, L. T., Worsnop, D. R., and Molina, M. J.: Secondary organic aerosol formation from anthropogenic air pollution: Rapid and higher than expected, *Geophys. Res. Lett.*, 33, L17811, 2006.

Chapter 2

A Functional Group Oxidation Model (FGOM) for SOA Formation and Aging

* Reproduced with permission from “A Functional Group Oxidation Model (FGOM) for SOA formation and aging” by X. Zhang and J. H. Seinfeld, *Atmospheric Chemistry and Physics*, 13, 5907-5926, 2013. Copyright 2013 by Authors.

2.1 Abstract

Secondary organic aerosol (SOA) formation from a volatile organic compound (VOC) involves multiple generations of oxidation that include functionalization and fragmentation of the parent carbon backbone and, likely, particle-phase oxidation and/or accretion reactions. Despite the typical complexity of the detailed molecular mechanism of SOA formation and aging, a relatively small number of functional groups characterize the oxidized molecules that constitute SOA. Given the carbon number and set of functional groups, the volatility of the molecule can be estimated. We present here a Functional Group Oxidation Model (FGOM) that represents the process of SOA formation and aging. The FGOM contains a set of parameters that are to be determined by fitting of the model to laboratory chamber data: total organic aerosol concentration, and O:C and H:C atomic ratios. The sensitivity of the model prediction to variation of the adjustable parameters allows one to assess the relative importance of various pathways involved in SOA formation. An analysis of SOA formation from the high- and low-NO_x photooxidation of four C₁₂ alkanes (n-dodecane, 2-methylundecane, hexylcyclohexane, and cyclododecane) using the FGOM is presented, and comparison with the Statistical Oxidation Model (SOM) of Cappa et al. (2012) is discussed.

2.2 Introduction

Development of a predictive model for secondary organic aerosol (SOA) formation and evolution represents one of the most challenging problems in atmospheric chemistry. In principle, the benchmark for describing SOA formation is a fully explicit chemical model, based on a complete multi-generation gas-phase oxidation mechanism for the

parent VOC. A quintessential example is GECKO-A, in which an exhaustive gas-phase VOC oxidation mechanism is generated automatically based on chemical kinetic and mechanistic specifications (Aumont et al., 2005; Camredon et al., 2007; Lee-Taylor et al., 2011; Aumont et al., 2012). Vapor pressures are estimated (based on group-contribution methods) for each of the thousands of products generated in the mechanism, from which gas-particle partitioning equilibrium constants are computed. The overall yield of SOA for the system as well as its complete chemical make-up are predicted. In such an explicit model, the predictions depend critically on the chemical rules and reaction rate constants imbedded in the mechanism. For the types of highly functionalized compounds involved in SOA formation, experimentally verified rate constants and mechanisms are generally available for only the first few steps of oxidation. Nonetheless, an explicit model like GECKO-A or MCM 3.1 (Jenkin et al., 1997; Saunders et al., 2003; Bloss et al., 2005) embodies the current state of understanding of atmospheric reaction mechanisms. The molecular vapor pressure prediction method used also plays an important role in the overall SOA yield predicted (Valorso et al., 2011), although this is the case for any SOA model incorporating specific or lumped gas-phase photochemical mechanisms. Whereas it is desirable to embody within a model as much basic understanding of the SOA formation and evolution process as possible, it is necessary to keep in mind that an important goal of SOA model development is a computational module that can be included in 3-dimensional atmospheric chemical transport models. Consequently, the challenge is to balance the desire for chemical fidelity with the need for computational feasibility.

Aerosol Mass Spectrometer (AMS) measurements of organic aerosols, now a routine component of atmospheric measurements and chamber experiments, enable derivation of the atomic O:C and H:C ratios of SOA, from which one can infer its overall oxidation state (Kroll, et al., 2011). The volatility of SOA is not generally measured routinely, although the volatility of the organic mixture is an essential property of SOA formation. Any SOA model requires a prediction of aerosol volatility, which is related to the molecular properties of the components comprising the SOA, as embodied, for example, in carbon number and oxidation state. The relationship between oxidation state and volatility is not unique; that is, molecular mixtures with the same overall oxidation state do not necessarily exhibit the same overall volatility.

The traditional approach to representing SOA formation, as embodied in the 2-product model (Odum et al., 1996), is based on fitting an empirical gas-particle partitioning model to chamber SOA yield data as a function of the mass concentration of absorbing aerosol. The Volatility Basis Set (VBS) (Donahue et al., 2006) is an extension of the 2-product concept, in which VOC oxidation products are assigned to volatility “bins” spanning the range of ambient organic effective saturation mass concentrations (C^*). As the oxidation products undergo multi-generation reaction (often referred to as “aging”), each generation of reaction products is assigned to a volatility class (Robinson et al., 2007). The extent of gas-particle partitioning associated with each volatility bin depends on both the C^* of that class and the total mass concentration of the absorbing medium (M_0). The stoichiometric assignments of oxidation products to volatility classes are determined through fitting the model to chamber data.

Compelling evidence exists from field observations that current SOA models consistently underpredict ambient organic aerosol concentration (Tsigaridis and Kanakidou, 2003; Heald et al., 2005, 2006; Volkamer et al., 2006; Jimenez et al., 2009). Such underprediction is almost certainly a result of a number of factors. First, the traditional SOA models on which these earlier modeling studies are based generally do not account explicitly for degree of oxidation and aging, aspects that are key to prediction of SOA formation. Second, the laboratory chamber data on which current models are based generally do not exhibit the degree of oxidation observed in atmospheric organic aerosol. Finally, the VOC and POA emission inventories that drive atmospheric models in all likelihood understate the fluxes of key SOA-forming species.

Three recent studies have been directed at a next generation of SOA models. Pankow and Barsanti (2009) introduced the “carbon number - polarity grid” (CNPG) framework. They expanded the “2-product” concept to the “ $np+mP$ ” approach (n products with m possible types of very low volatility compounds) to represent the lumped oxidation and accretion products (Barsanti et al., 2011). Three levels of reactions (the oxidation of parent hydrocarbon and n products, and the formation of m particle-phase compounds) are included to represent the complexity of the mix of condensable primary and secondary compounds as a function of time. Donahue et al. (2011, 2012 a, b) developed the two-dimensional Volatility Basis Set (2D-VBS) employing saturation mass concentration and the degree of oxidation (The average oxidation state of aerosol, OS_C ($2 \times O:C - H:C$), can be used interchangeably with the O:C ratio.) to describe the coupled aging and phase partitioning of organic aerosol. A point in the 2-D space represents an ensemble of molecules with the same C^* and OS_C . In the 2-D VBS space, if the number

of carbon atoms, n_C , in the carbon backbone does not change during oxidation, products will form along lines of constant n_C , i.e., lines extending from the lower right (high C^* vs. low OS_C) to the upper left (low C^* vs. high OS_C). When chamber data are available, the volatility distribution of the products is obtained by SOA mass yield fitting. The products are spread over the OS_C coordinate to produce a distribution that matches bulk AMS data and any known products. Cappa and Wilson (2012) formulated the Statistical Oxidation Model (SOM) that describes SOA formation as a statistical evolution in the space of numbers of carbon and oxygen atoms, n_C and n_O , with fitting parameters that govern the probability of fragmentation vs. functionalization, the number of oxygen atoms added per functionalization reaction, and the decrease in vapor pressure accompanying addition of an oxygen atom.

The new generation of models, as exemplified by the 2D-VBS and the SOM, represents SOA formation and evolution in terms of the competition between functionalization and fragmentation, the extent of oxygen atom addition, and the change of volatility. As in the earlier generation of SOA models, predictions can be adjusted to fit laboratory chamber data by determination of the optimal values of a number of parameters in the model. (This is in contrast to the fully explicit chemical model, for which rate constants and branching ratios are generally specified a priori based on structure-activity relationships, for example.) We present here a new variation of the SOA model that is based on explicit chemical information in terms of the types of functional groups that result from the oxidation of a parent VOC. We term this the Functional Group Oxidation Model (FGOM). As in the 2D-VBS and the SOM, the FGOM is characterized by a set of parameters that are determined by analysis of chamber

data. Key issues that must be addressed in SOA model development include: (1) In fragmentation, does C-C bond scission occur at any of the C-C bonds in the molecule or does the model specify, for example, that fragmentation always produces C_1 and C_{n-1} ? (2) How important are particle-phase reactions to the evolution of SOA, and how is such chemistry represented? (3) To what extent does particle phase chemistry increase the oxidation state of the aerosol and what is its effect on particle volatility? Such issues have important implications for simulations of the overall mass concentration of SOA and its oxidation state.

We first describe the development of the FGOM, and then apply it to SOA formation from the low- and high- NO_x photooxidation of four C_{12} alkanes. An important aspect of the present work is a comparison of the FGOM to the SOM, both of which are built on a similar foundation. It turns out that, even with the number of adjustable parameters, complete matching to organic aerosol mass concentration and O:C and H:C ratios over the course of an oxidation is challenging. Assessing the sensitivity of predictions to assumptions made in the model development is crucial in interpreting results of its application.

2.3 Development of a Functional Group Oxidation Model (FGOM)

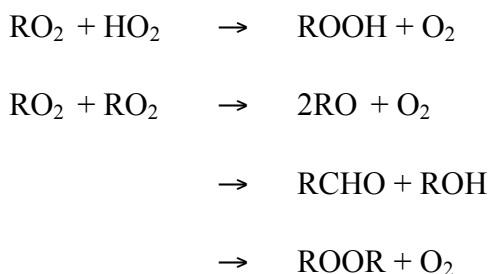
SOA formation from a parent VOC involves multiple generations of oxidation coupled to gas-particle partitioning. Note that a “generation” is simply the number of times that a molecule has reacted with oxidants (OH, O_3 or NO_3), starting from the parent VOC. In the general process depicted in Fig. 1, S_i^g represents the spectrum of gas-phase products at the i^{th} generation, each product having its own chemical identity and volatility. The multi-

generation progression of the chemistry is characterized by a competition between functionalization and fragmentation. Each S_i^g may, in principle, partition to the aerosol phase, S_i^p . Once in the aerosol phase, S_i^p may itself undergo chemical reaction. In Fig. 1, these reactions are assumed to parallel mechanistically those in the gas-phase, although that assumption need not be invoked. The particle-phase species may be converted to essentially non-volatile compounds, denoted N^p by reactions that can be either non-oxidative or oxidative in nature (Kroll and Seinfeld, 2008). The non-oxidative reactions are typified by the association of two condensed-phase organic molecules.

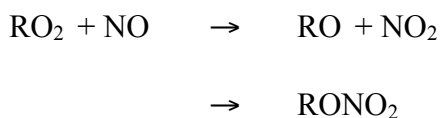
The schematic in Fig. 1 defines the overall structure of the Functional Group Oxidation Model (FGOM). We term the model FGOM, in that a comprehensive chemical mechanism, such as MCM 3.1 or GECKO-A, is used to predict the types of functional groups that characterize the oxidation of the parent organic molecule, yet the detailed mechanism is not employed in the model itself. With the carbon number and the spectrum of functional groups specified, the vapor pressure of the compound defines the relationship between S_i^g and S_i^p . Because the full chemical mechanism of SOA formation is not generally known, predictive SOA models built upon chamber data are characterized by a set of parameters, the values of which are determined by optimal fitting to experimental data. Gas-phase oxidant (e.g. OH, O₃, and NO₃) concentrations need to be specified based on chamber conditions. The quantitative behavior of the FGOM is expressed by a set of kinetic equations for S_i^g , S_i^p , and N^p .

2.3.1 Functionalization

The essential nature of functionalization is the addition, for a particular parent VOC, of a certain number and type of functional groups at each generation of reaction. The mechanism underlying the addition of different functional groups is guided by the specific chemistry. More than one functional group can be added per generation, and the types of functional groups added vary by generation. Reaction rate constants for different functionalization steps are lumped according to the structure of the parent VOC molecule and the chemical transformation of different functional groups based on structure-activity relationships (Kwok and Atkinson, 1995). For purpose of discussion, one can consider OH reaction as the oxidative process in SOA formation, although, if appropriate, other oxidants, such as O₃ and NO₃ can be considered as well. Consideration of the general mechanism of OH oxidation allows one to identify the types of functional groups involved. OH-initiated oxidation leads to a peroxy radical (RO₂), the fate of which controls the SOA-forming mechanism (Kroll and Seinfeld, 2008). At sufficiently low NO_x concentrations, RO₂ self-reactions will dominate the fate of RO₂:



In the presence of sufficient NO_x, RO₂ reacts preferentially with NO and NO₂, e.g.



Alkoxy radicals (RO) formed either isomerize through a 1,5 H-atom shift to a δ -hydroxyalkyl radical, which introduces an extra OH group, react with O₂ to form carbonyls, or undergo fragmentation. Thus, functional groups introduced from peroxy radical reactions include hydroperoxide (–OOH), nitrate (–ONO₂), hydroxyl (–OH), and carbonyl (–C=O). If the parent hydrocarbon contains a non-aromatic ring, decomposition of the RO will not lead to a decrease of carbon number. The addition of OH introduces an extra hydroxyl group to the parent hydrocarbon. Addition of OH to an aromatic ring is mechanistically different from that to a C=C bond. The progressive photochemical reactions of oxidation products proceeds by: (1) H-atom abstraction from C–H bonds and, to a lesser extent, from the O–H bond of alcohols; (2) H-atom abstraction from C–H bonds of carbonyls; (3) oxidation of –OOH and –ONO₂ groups; and (4) Photolysis of –OOH and –ONO₂ groups.

The addition of various combinations of these four groups via photochemical oxidation accounts for a majority of the gas-phase reactions involving semi-volatile product aging. This assumption is based on observations pertinent to the photooxidation of VOCs and IVOCs (alkanes, alkenes, terpenes, and aromatics). Progressive gas-phase oxidation of VOC leads to the formation of oxygenated products that include alcohol, ketone, aldehyde, carboxylic acid, alkyl nitrate, hydroperoxide and/or peroxyacyl nitrate functional groups (Atkinson, 2000). Additional functionalities, such as ether and ester groups, are also found in smaller amounts. Most of these moieties are assumed to be represented by a combination of the four surrogate functional groups with comparable chemical identities (volatility and oxidation state): 1) Carbonyl and aldehyde share similar chemical and physical properties. The decreases of the logarithm of vapor

pressure upon the addition of $-\text{CHO}$ and $-\text{C}=\text{O}$ are predicted by SIMPOL.1 to be 1.3196 and 0.9364, respectively. In EVAPORATION, these two functional groups have the same contribution ($\Delta\text{LVP} = 1.1951$) to the vapor pressure decrease; 2) Carboxylic acid can be represented by the sum of $-\text{C}=\text{O}$ and OH . Based on the prediction of SIMPOL.1, the decrease of the logarithm of vapor pressure upon the addition of one $-\text{C}(\text{O})\text{OH}$ group is 3.5121, which is roughly similar to the sum of ΔLVP values, 3.3114, upon the addition of one $-\text{OH}$ ($\Delta\text{LVP} = 2.1834$) and one $-\text{C}=\text{O}$ ($\Delta\text{LVP} = 1.1280$) group. The increase of oxidation state resulting from the addition of $-\text{C}(\text{O})\text{OH}$ or the sum of $-\text{OH}$ and $-\text{C}=\text{O}$ is the same, i.e. $6/n_{\text{C}}$. In view of this, the formation of a carboxylic group, which results from the H-atom abstraction from aldehyde, can be considered as the addition of a $-\text{OH}$ group onto a carbonyl group; and 3) The contribution of an ether group to vapor pressure is close to that from carbonyl. Epoxides have been observed from the photooxidation of isoprene under low- NO_x conditions (Paulot et al., 2009). The contribution of the formation of an epoxide group to ΔLVP and $\Delta\text{OS}_{\text{C}}$ are ~ 0.7948 and $4/n_{\text{C}}$, respectively, compared with 1.1280 and $4/n_{\text{C}}$ by the addition of one $-\text{C}=\text{O}$ group. Note that the structure-property relationships used in vapor pressure prediction models are more complicated (Camredon and Aumont, 2006) and the vapor pressures of a large subset of organics in the atmosphere can not be simply represented by the four functional groups identified in this study. The functionalization channel in FGOM is a generalized predictive technique that is intended to capture key processes. The set of functional groups in FGOM that characterize the progressive oxidation reactions can, in principle, be expanded and updated for different hydrocarbon systems.

Particle-phase oxidative reactions can occur via heterogeneous OH uptake to particles and OH-initiated oxidation in the bulk (e.g., Ravishankara, 1997; Knopf et al., 2005; Zahardis and Petrucci, 2007; Shiraiwa et al., 2011). As noted, we will assume that particle-phase oxidation reactions proceed in parallel with and via the same chemical mechanisms as in the gas phase. The reaction rate of OH oxidation of compound ‘X’ in the particle phase can be expressed as:

$$\frac{d[X]_p}{dt} = k'_p[X]_p \quad (2.1)$$

where k'_p , the pseudo first-order particle-phase reaction rate constant, is related to the corresponding gas-phase reaction by $k'_p = r_p k_g [\text{OH}]_g$, and where k_g is the corresponding gas-phase bimolecular reaction rate constant, $[\text{OH}]_g$ is the gas-phase OH radical concentration, and r_p is the ratio of the OH reaction rate constant in the particle phase to that in the gas phase. r_p is one of the free parameters of the model. Since particle size dependence of the kinetic parameters is not considered in the model, size dependence of r_p is not accounted for.

2.3.2 Fragmentation

More heavily oxidized molecules can fragment more easily (Kroll et al., 2009). Fragmentation thus tends to lead to a reduction in the ability to form organic aerosol. The probability of fragmentation f for a stable molecule has been proposed to be represented as a function of the O:C ratio of the molecule (Jimenez et al., 2009; Murphy et al., 2011, 2012; Cappa and Wilson, 2012; Chacon-Madrid et al., 2012; Donahue et al., 2012 b): $f = (\text{O:C})^{f_v}$, where f_v is a parameter to be determined by fitting of data. Fragmentation does not necessarily substantially change the average O:C ratio of SOA; fragmentation leads to

products with fewer carbon and, generally, more oxygen atoms, although the ultimate contribution of these products to the SOA mass depends on their volatilities. Species with a higher O:C ratio have a greater probability of fragmentation. In this way, f_v is a key factor that influences the total organic aerosol mass concentration.

In the SOA model structure, it is necessary to make an assumption concerning the mechanism of fragmentation. In the SOM, the distribution of fragments is computed in two alternative ways: (1) A random probability for the location of the C-C bond scission, thus affecting the resulting size of the scission product; and (2) Fragmentation leads to production of only C_1 species, along with the appropriate co-product. Cappa and Wilson (2012) found that the “random fragmentation” and the “one carbon loss fragmentation” yield a very similar set of optimal parameters for chamber-generated α -pinene SOA. The 2-D VBS assumes that the C-C bond scission from the precursor is randomly distributed along the carbon backbone. The distribution of products over the OS_C - n_C space is computed in such a way that the less volatile bins to the left of the midpoint bin (nominally $C_{n/2}$) have the same O:C as the precursor, while the more volatile bins to the right of the midpoint bin progress diagonally towards the bin with highest O:C (i.e., $C^* = 10^9 \mu\text{g}/\text{m}^3$, O:C = 1.0). Half of the products formed from the first-step fragmentation are assumed to be intermediates that can undergo further functionalization. As a result, a number of heavy fragments with similar C^* and O:C as their precursors are produced. We invoke here the assumption that fragmentation leads to the formation of a one-carbon compound (C_1), which is formaldehyde, together with a co-product (C_{n-1}) that has the same collection of functional groups but one fewer carbon atom than the parent compound. The “random fragmentation” assumption in SOM acts to rapidly distribute

mass over the entire n_C vs. n_O space. The initial products upon the first-step fragmentation in the 2-D VBS form a “hockey stick” shape, and the further oxidation of half of the initial products fills a wide area in the O:C vs. C^* space (Jimenez et al., 2009; Donahue et al., 2012). The “one carbon loss fragmentation” assumption leads to a somewhat slower progression of prediction of smaller fragments. These three different assumptions concerning the mechanism of fragmentation lead eventually to a similar final state characterized by a distribution of intermediates of a more volatile and oxygenated nature.

The role of fragmentation is evident in the chemical mechanisms shown in Fig. 2. It is assumed that any of the hydrogen atoms on a secondary carbon is more or less equally vulnerable to OH attack, so instead of the exact structure of a specific molecule, we focus on the type and number of functional groups associated with a carbon backbone. Under low- NO_x conditions, photolysis of $-OOH$ groups and peroxy-peroxy reactions are the primary pathways leading to scission of the carbon skeleton. In the domain of low- NO_x $RO_2 + HO_2$ dominated chemistry, the photolysis of an $-OOH$ group generates an alkoxy radical, which decomposes to a carbonyl group (formaldehyde in the C_1+C_{n-1} case) and an alkyl radical (R). Reaction of R with O_2 followed by reaction with HO_2 regenerates the $-OOH$ group; In $RO_2 + RO_2$ dominated chemistry, the self-reaction of RO_2 produces $-C=O$, $-OH$, and RO. The decomposition of RO leads to $-C=O$ and R' . R' reacts solely with O_2 to form $R'O_2$, which can initiate another $RO_2 + RO_2$ or $RO_2 + HO_2$ cycle. Under high- NO_x conditions, RO is produced primarily from the photolysis of $-ONO_2$ and $RO_2 + NO$ reactions. RO decomposes to a carbonyl and an alkyl radical, which reacts with O_2 to reform RO_2 . In the presence of a sufficiently high concentration of NO_x , RO_2 will

preferentially react with NO to form an alkoxy radical or a $-\text{ONO}_2$ group again. We shall take $-\text{ONO}_2$ as the only functional group formed upon the photolysis of $-\text{ONO}_2$ because of its larger contribution to the decrease of vapor pressure than the fragments from the decomposition of an alkoxy radical. We also assume that the OH oxidation of an alcohol produces solely a carbonyl, so the presence of $-\text{OH}$ will not affect the type of functional groups added upon fragmentation.

2.3.3 Volatility Estimation

In fragmentation, if sufficient addition of functional groups takes place, each of the products may still have a sufficiently low vapor pressure to be considered as semi-volatile. A critical feature of the model is a relationship between saturation mass concentration, C° , and the carbon number of a compound.

From the point of view of predicting physical properties, description in terms of functional groups tends to be more useful than in terms of elemental composition. But, by the same token, the experimentally measureable quantities tend to be best related to elemental composition. In order to reconcile these two approaches to molecular characterization in terms of SOA, it is useful to develop a correlation that relates vapor pressure of a pure component (or C°) to both functional groups and elemental amounts. The theory underlying this approach will be developed generally and subsequently applied in analysis of SOA formation from C_{12} alkanes.

Frequently used vapor pressure estimation methods are based on expressing the logarithm of vapor pressure as a linear combination of contributions from individual functional groups (Capouet and Müller, 2006; Pankow and Asher, 2008; Compernelle et

al., 2011). On the other hand, an approximate linear relationship between C° and elemental composition, as developed by Donahue et al. (2011), proves to be advantageous. Here we merge the “group contribution” and “element contribution” methods in order to relate the carbon number to a given saturation concentration of a compound i . The resulting expression is

$$\log_{10} \frac{10^6 p_{L,i}^0 (12n_C^i + hn_C^i + 16n_O^i + 14n_N^i)}{RT} = (n_C^0 - n_C^i)b_C - n_O^i b_O - 2 \frac{n_C^i n_O^i}{n_C^i + n_O^i} b_{CO} - \sum n_{func}^i b_{func} \quad (2.2)$$

where 10^6 is a unit conversion (g/m^3 to $\mu\text{g/m}^3$), b_C is the carbon-carbon interaction term, b_O is the oxygen-oxygen interaction term, b_{CO} is the carbon-oxygen interaction term, b_{func} is the interaction term for different functional groups, n_C^0 is the reference carbon number, n_C^i is the carbon number of compound i , n_O^i is the oxygen number of compound i , n_N^i is the nitrogen number of compound i , n_{func}^i is the number of different functional groups in compound i , and h is the ratio of hydrogen number to carbon number of compound i . For the application to the alkane system to be presented, we have determined n_C^0 , b_C , b_O , b_{CO} , and b_{func} by fitting the above equation to the estimated vapor pressures of 1080 standard aliphatic compounds. After optimal fitting of equation (2) to the standard compound vapor pressures, the predicted carbon number of a compound lies within the range of 10% uncertainty of its actual value.

To illustrate the application of the volatility-composition correlation, consider the mechanism of the OH-oxidation of dodecane ($\text{C}_{12}\text{H}_{26}$). For a typical ambient organic aerosol loading of several $\mu\text{g/m}^3$, let us assume for purpose of illustration that any

compound with the saturation concentration less than $10^3 \mu\text{g m}^{-3}$ can partition appreciably to the particle phase. The grey shaded region in Fig. 3 defines the particle phase “boundary” for compounds having carbon numbers 12 and fewer. The lines define the carbon number range and types of functional groups for oxidation products of dodecane under low- NO_x conditions. The magenta line in the lower left hand corner of the grey shaded region, for example, indicates that a product with two $-\text{OOH}$ groups and 12 to 7 carbon atoms has sufficiently low volatility to lie in the semi-volatile region defined by $C^\circ < 10^3 \mu\text{g m}^{-3}$. However, the cyan line in the upper right hand corner of the “condensable region” indicates that a molecule with only one $-\text{C}=\text{O}$ group would need at least 17 carbon atoms to fall into the semi-volatile region. This would necessitate some types of accretion reaction to occur given the C_{12} parent molecule. The trade-off between functionalization and fragmentation in the volatility of the products becomes evident in such a graphic representation.

2.3.4 Gas-particle Partitioning

Gas-particle equilibrium partitioning of semi-volatile products is assumed. From Raoult’s law, $p_i = p_{L,i}^0 \gamma_i \chi_i$, where $p_{L,i}^0$ (atm) is the vapor pressure of compound i as a liquid, γ_i is its activity coefficient on the mole fraction basis, and χ_i is the mole fraction of compound i in the particle phase. When multiple condensed-phase compounds exists, the gas-particle partition coefficient $K_{p,i}$ ($\text{m}^3/\mu\text{mol}$) of compound i is expressed as:

$$K_{p,i} = \frac{S_i^p/S_T^p}{S_i^g} = \frac{RT}{10^6 p_{L,i}^0 \gamma_i} \quad (2.3)$$

where S_i^g is the molar concentration ($\mu\text{mol}/\text{m}^3$) of i in the gas phase; S_i^p is the equilibrium molar concentration ($\mu\text{mol}/\text{m}^3$) of i in the particle phase; S_T^p is the molar concentration per unit volume of air ($\mu\text{mol}/\text{m}^3$) of all the species in the absorbing organic particle phase. R ($\text{m}^3 \text{ atm mol}^{-1} \text{ K}^{-1}$) is the gas constant, and T (K) is temperature. The effective saturation concentration C_i^* ($\mu\text{g}/\text{m}^3$) is expressed as:

$$C_i^* = \frac{C_i^g C_T^p}{C_i^p} = \frac{10^6 p_{L,i}^0 \gamma_i \overline{M}_w}{RT} \quad (2.4)$$

where C_i^g is the mass concentration ($\mu\text{g}/\text{m}^3$) of i in the gas phase; C_i^p is the equilibrium mass concentration ($\mu\text{g}/\text{m}^3$) of i in the particle phase; C_T^p is the mass concentration per unit volume of air ($\mu\text{g}/\text{m}^3$) of all the species in the absorbing organic particle phase. \overline{M}_w is the average molecular weight of the absorbing organic particle phase (g/mol). Thus the fraction of i in the particle phase, ϕ_i^p is:

$$\phi_i^p = \frac{1}{1 + 1 / (K_{p,i} S_T^p)} = \frac{1}{1 + C_i^* / C_T^p} \quad (2.5)$$

Note that the mole fraction based activity coefficient is assumed to be unity here. Non-ideal interactions between organic and inorganic species in the aerosol phase influence the gas/particle partitioning of semi-volatiles. Thermodynamic models show that the saturation concentration of species i is usually overpredicted by assuming ideal condensed phase behavior, and the extent of overprediction differs by functional groups and is affected by aerosol water content, as well as temperature and SOA loading (Zuend et al., 2010, 2012). Inclusion of particle-phase nonideality and phase separation is beyond the scope of the current study.

2.3.5 Particle-phase accretion reactions

Recent modeling studies have suggested that dehydration reactions in the particle phase can play an important role in determining the characteristics of the oxidation state (Chen et al., 2011; Cappa and Wilson, 2012), although the detailed mechanisms are uncertain. In the present FGOM framework, particle-phase accretion reactions (non-oxidative) are allowed to occur and assumed to generate essentially non-volatile products. These reactions are treated as bimolecular, with a reaction rate constant k_a ($\text{m}^3 \text{mol}^{-1} \text{s}^{-1}$), which is a fitting parameter of the model. We assume that all of these non-volatile compounds can be represented as a single generalized species, which is characterized by its time-dependent molar amount and the set $[C_x, H_y, O_z]$, where the parameters x , y , and z represent the numbers of carbon, hydrogen, and oxygen atoms characterizing the non-volatile particle-phase composition. The parameters x , y , z are tunable parameters of the model. Note that certain limits are set for mathematically optimizing the x value in order to conserve the carbon mass: the upper limit of the x value is the sum of carbon numbers of two molecules with the parent carbon skeleton and the x value can not be lower than the sum of carbon numbers of two molecules that have the lowest carbon numbers in the category of semi-volatile compounds defined by equation (2). The oxygen and hydrogen masses are not conserved in the specification of y and z , in view of the formation of water molecules during the oligomerization processes.

2.3.6 Summary of the Functional Group Oxidation Model (FGOM)

The structure of the FGOM is summarized as follows. The type and number of functional groups added to the parent molecule over multi-generation oxidation are specified from

consideration of an explicit chemical mechanism, such as GECKO-A or MCM (MCM is employed in the current FGOM model structure). As functionalization proceeds, a spectrum of products that are characterized by various combinations of functional groups together with the parent carbon backbone is generated. The accompanying fragmentation leads to products with the same functional groups as the parent product but with fewer C atoms. The automatically generated fragments are subject to the same oxidation mechanisms as the parent products. Vapor pressures of oxidation products are estimated by the vapor pressure prediction model “EVAPORATION” (Compernelle et al. 2011). Products formed partition to the particle phase, where they may either be oxidized following the same gas-phase mechanism, or undergo accretion reactions. The model contains six tunable parameters: r_p , the ratio of the particle-phase oxidative reaction rate constant to that in the gas phase; f_v , the parameter characterizing the probability of fragmentation; k_a , the accretion reaction rate constant in the particle phase; and a matrix $[C_x, H_y, O_z]$ of the carbon, hydrogen, and oxygen numbers of the non-volatile products. These six parameters are incorporated in a set of differential equations governing the kinetics of all the species in the mechanism. The differential equations are solved numerically, with instantaneous equilibrium partitioning calculated at each time step. The number of differential equations for a certain VOC system depends on the chemical nature of the parent hydrocarbon (e.g., structure, volatility, etc.) and the complexity of the functionalization mechanism. Evolution of these six parameters describes the gas- and particle-phase chemistry, together with the instantaneous equilibrium partitioning process. Their values are determined by optimal fitting of the model simulations of organic mass growth and elemental compositions with laboratory chamber data (organic

aerosol mass, O:C, and H:C). These three properties are equally weighted to constitute the overall optimization objective function. The Levenberg-Marquardt method implemented in MATLAB's "System Identification Toolbox" (MathWorks, 2002) is used for the nonlinear minimization. The essential feature of the FGOM model that distinguishes it from explicit chemical models is the simplified treatment of fragmentation processes: the fragmentation operator (in the form of f_v) is applied to determine the probability that a given stable molecule will fragment, instead of accounting for the detailed free radical chemistry. Owing to the consideration of carbon-number conserved oxidation reactions based on the explicit chemistry, the FGOM model differs from the 2-D VBS or SOM models in terms of the treatment of particle-phase oxidative and non-oxidative reactions through the parameters r_p , k_a , and $[C_x, H_y, O_z]$.

2.4 Application to SOA Formation for C₁₂ Alkanes

The Functional Group Oxidation Model is applied to predict SOA formation from the OH-initiated oxidation of four C₁₂ alkanes (dodecane, methylundecane, hexylcyclohexane, and cyclododecane) under both high- and low- NO_x conditions. Experiments were carried out in the dual 28 m³ Teflon reactors in the Caltech Environmental Chamber. Detailed descriptions of experimental protocols can be found elsewhere (Yee et al., 2012; Craven et al., 2012). Experimental conditions are summarized in Table 1. Different OH radical sources were employed to achieve high- and low- NO_x levels. For low-NO_x conditions, experiments were designed to capture 36 h of total photooxidation during which the OH concentration produced from the photolysis of H₂O₂ remains essentially constant. Under high-NO_x conditions, the OH source is

HONO. The photolysis rate of HONO is about an order of magnitude higher than that of H_2O_2 , leading to a depletion of OH within ~ 3 h. For both cases, the time-dependent OH concentration can be obtained by optimal fitting of the predicted parent hydrocarbon decay with its measured temporal profile. Three measured SOA properties, i.e., organic mass growth, O:C ratio, and H:C ratio, are employed to constrain the performance of FGOM. Two simulations were run for each C_{12} alkane system: sim.1, the full fitting of the six empirical parameters in the FGOM to the chamber data, and sim.2, fitting two parameters “ f_v ” and “ r_p ” to the organic mass concentration. The best-fit parameters obtained for the four C_{12} alkanes for both high- NO_x and low- NO_x conditions are given in Table 2.

Questions associated with the application of FGOM are: 1) How well does the model reproduce the measured SOA properties? 2) Are all six parameters equally influential in terms of representing SOA formation and evolution? and 3) How well do these mathematically best-fit parameters express the actual chemistry thought to be occurring in the system? Some general findings include: f_v values are generally lower under high- NO_x conditions, indicating more intense fragmentation. The abundance of RO is the most important determinant of the degree of fragmentation. In the presence of NO_x , the primary fate of RO_2 is reaction with NO, producing RO. All of the low- NO_x experiments fall into the $\text{HO}_2 + \text{RO}_2$ dominant regimes, as $> 95\%$ RO_2 will react with HO_2 . Although the photolysis of the $-\text{OOH}$ group formed from $\text{HO}_2 + \text{RO}_2$ reaction leads to the formation of RO, the yield of RO via this path is still an order of magnitude lower than under high- NO_x conditions. In addition, f_v values for cycloalkanes are higher than those for straight-chain alkanes, which is consistent with the mechanism of the decomposition

of RO in a non-aromatic ring. Optimal r_p values for the eight alkane systems range from 10^{-3} to 10^{-1} , that is, the particle-phase oxidation reaction rates are predicted to be at least one order of magnitude slower than those in the gas phase. The role of particle-phase oxidative reactions in the SOA formation from C_{12} alkanes is, therefore, not strongly influential during the initial period of time. However, for species with very low vapor pressure (e.g., 1×10^{-11} atm), 99.8 % of which will end up being in the particle phase at a moderate organic aerosol loading, e.g., $40 \mu\text{g}/\text{m}^3$, particle-phase oxidative reactions are as influential as those in the gas phase even if r_p is of the order of 10^{-3} . Most semi-volatile products generated from the functionalization channel of the FGOM have vapor pressure higher than 10^{-10} atm, and as a result, their particle-phase oxidative reactions are predicted to be a minor path when r_p is less than 10^{-1} , a prediction that is consistent with field and experimental evidence (Murphy, et al., 2007; DeCarlo et al., 2008; George et al., 2008; Lambe et al., 2009). Optimal k_a values for the eight alkane systems range from 10^3 to $10^4 \text{ m}^3 \text{ mol}^{-1} \text{ s}^{-1}$, indicating that accretion reactions occurring in the particle phase are predicted to play an important role in SOA properties, given the high local concentrations of the species in the condensed phase. Take the low- NO_x photooxidation of dodecane as an example; the predicted non-volatile species eventually account for $\sim 30\%$ of the total organic aerosol, see Fig. 9. Optimal values of the matrix $[C_x, H_y, O_z]$ for the eight systems indicate a highly dehydrated nature of the non-volatile species. Since the explicit particle-phase reaction mechanisms in these systems are not yet clear, one cannot assess unambiguously the effect of particle-phase reactions on the SOA aging. We will return to the importance of the five particle-phase parameters in Section 3.3.

2.4.1 Organic Aerosol Growth

The predicted (FGOM) temporal profiles of organic aerosol mass (C_{OA}), together with the wall-loss-corrected chamber data, for the four C_{12} alkane systems based on the optimal fit parameters in Table 2 are shown in Fig. 4. SOA yields under high- NO_x conditions are lower than those under low- NO_x conditions because of both the shorter OH radical exposure time and the more intense fragmentation in the presence of NO_x . The SOA growth curves under various NO_x levels show different patterns. Particles start to grow immediately after the initiation of photochemistry under high- NO_x conditions, whereas a short lag occurs before organic aerosol mass accumulates under low- NO_x . The initial OH concentration under high- NO_x conditions is an order of magnitude higher than that in low- NO_x , which substantially accelerates the progression of multi-generation oxidation and consequently the early stage formation of low-volatility compounds. In addition, the RO chemistry occurring under high- NO_x conditions leads to products spanning a wider range of volatilities after only one generation of oxidation.

The level off of C_{OA} at the end of the experiments is generally not captured for all the eight alkane systems. The level off could have resulted from re-evaporation of particles under low- NO_x conditions and the cessation of OH production under high- NO_x conditions. Reproduction of C_{OA} requires accurate representation of the trade-off between the fragmentation of semi-volatile products and the formation of particle-phase non-volatile products, which results in an accumulation of total particle organic mass. The C_{OA} growth curves for cyclododecane under high- NO_x conditions are not as closely simulated as for the other alkanes. For cyclododecane, particles are observed to grow fairly rapidly after the inception of photooxidation.

An essential feature of the FGOM is the prediction of the emergence of a spectrum of functional groups as the oxidation proceeds. For the alkanes investigated here, the C₁₂ backbone is not predicted to break until 3 – 5 functional groups have been added to the parent chain. As a result, 7 – 8 generations of oxidation are predicted to occur until the last remaining C₁₂ backbone is fragmented. In the FGOM model, every possible oxidation step leading to functionalization is implicitly considered in the generalized mechanism. The extent to which aging proceeds then depends on the availability of oxidants. Figure 5 shows the predicted contribution of different generations of products to the total organic aerosol mass for the eight alkane systems. The OH exposure time under low-NO_x conditions is, on average, ~ 3 times higher than that under high-NO_x conditions. As a result, the 2nd and 3rd generation products are dominant components at high-NO_x, whereas 4th and later generation products account for over 50% of the total aerosol mass at the end of the low-NO_x experiments. The temporal distribution of multi-generational products reflects different chemical mechanisms governing the photochemistry under high- vs. low- NO_x conditions. Due to the importance of RO chemistry in the presence of NO_x, a spectrum of products spanning a large range of volatility and oxidation states are formed upon the OH initiated photooxidation. Under low-NO_x conditions, products containing the –OOH group dominate the particle phase due to their low volatilities, although most of these are consumed rapidly in the gas phase. In general, the extent of agreement between predicted and observed chamber data for the initial SOA growth depends on the matrix of functional groups generated as oxidation proceeds. For example, GECKO-A generates 2% trifunctional species in the first-generation products from C₁₆ alkanes (Aumont et al., 2012), products that are not

included in MCM 3.1. Because of their low volatility, a small amount of trifunctional species could contribute substantially to the particle mass.

2.4.2 Elemental aerosol composition

Wall-loss corrected chamber SOA yield data (i.e. yields computed accounting for particle deposition on chamber walls) have been used as a standard for the fitting of empirical models, such as the 2-product model and the 1-D VBS. The subtleties of using AMS derived atomic ratios (O:C and H:C) as well lie in the uncertainties in the AMS elemental analysis, which arise from variations in the ionization and fragmentation of compounds in the AMS and uncertainties in analysis of high-resolution mass spectra (Chhabra et al., 2011). The ionization efficiency for different molecules varies, depending on the identity and structure of molecules being ionized. Uncorrected O:C and H:C tend to be biased low due to the neutral losses of oxygen- and hydrogen-containing fragments, such as H₂O, CO₂, H, and H₂. As a result, the raw measurement of elemental composition requires calibration factors derived from the standard analysis. In this study, the calibration factors applied to AMS measured O:C and H:C are 0.75 and 0.91, respectively (Aiken et al., 2007, 2008). The uncertainties in O:C and H:C ratios, defined as the average absolute value of the relative error of each data point from any standard analyzed with respect to the regression line, were measured to be 31% and 10%, respectively (Aiken et al., 2008). In this study, we use these two values as the upper boundaries, marked as gray error bars in Figures 6 and 7, considering the fact that organic aerosol is a mixture of thousands of pure compounds. A transient set of data points for a particular experiment serves as the basis for carrying out the fitting processes (Here these comprise the AMS derived O:C

and H:C). When comparing the optimal model fit with experimentally measured O:C and H:C, the model output can be considered to reasonably match the experimental ratios as long as the prediction falls within the gray region.

Figure 6 shows the measured and simulated particle average O:C ratios for the OH oxidation of dodecane, methylundecane, hexylcyclohexane, and cyclododecane. The experiments simulated here result in moderate levels of oxidation, i.e. O:C \sim 0.3 in the semi-volatile oxygenated organic aerosol (SV-OOA) range (Ng et al., 2010, 2011). Note that for a typical experiment, we first sample the purified chamber air with a filter in line to measure the organic loadings by AMS for three replicates and obtain the average organic loading value as the AMS detection limit. If the organic aerosol mass growth in the chamber is below the detection limit, that AMS measurement is deemed unreliable. For low-NO_x experiments, particle growth usually starts after about 4 hours of reaction. During this initial period, the noise to signal ratio is high and data are deemed not reliable. The measured O:C ratio begins at zero and then rapidly increases as the early low volatility compounds condense. As C_{OA} increases, species with higher volatilities are capable of partitioning to the particle phase, causing O:C to decrease. The O:C trend thus represents a competition between the decrease due to the partitioning of higher volatility compounds with fewer O-atoms and the increase that results from partitioning of more oxygenated compounds as multiple generations unfold. Owing to less reliable data at the onset of AMS sampling, we consider the data points in the middle of the span, i.e. O:C \sim 0.2 – 0.3, as the “standard” for the comparison with simulations from “sim.1”. Predictions under high-NO_x conditions are generally consistent with the measured values. No increase in O:C ratio is observed because of the experimental depletion of OH

radicals after ~ 3 h reaction. In general, the O:C ratios under high-NO_x conditions are predicted to be higher than under low-NO_x conditions because the formation of –ONO₂ groups introduces more oxygen to the particles than the –OOH group. The agreement between predicted and measured O:C ratios under low-NO_x conditions is less satisfactory. Simulations with solely gas-phase chemistry can reproduce the O:C trend, which is in agreement with our current understanding of SOA formation and aging driven by gas-phase photooxidation of semivolatiles, but fail to match the measured O:C values. When an oligomer formation channel is incorporated, the model output is capable of matching the measured O:C ratio eventually, but exhibits a different temporal profile pattern: while the observed O:C is rising, the modeled O:C is falling within ~ 20 h reaction. This results from the difference between the theoretical alkane SOA makeup and the chemical properties of actual alkane SOA measured by AMS in the chamber. Consider the dodecane low-NO_x case (Figure 6) as an example: the starting point of the O:C ratio measured by the AMS is ~ 0.2 , which means that a typical compound that is present in the particle phase with a C₁₂ carbon backbone has, on average, 2.4 oxygen atoms. However, based on the vapor pressure prediction models (SIMPOL.1 or EVAPORATION), such a “compound” cannot have sufficiently low vapor pressure to be dominant in the particle phase at the beginning of the photochemistry. Overall, the inconsistency between modeled and measured O:C ratios reflects a discrepancy between the fitting of a semi-explicit model to a presumed elemental composition standard, and the current understanding of gas-phase photochemistry leading to the SOA formation.

For each of the four alkane systems studied here, gas-phase chemistry alone is not able to match the chamber measured O:C ratio, assuming it is perfectly correct. Oligomer

formation, on the other hand, provides a pathway that could possibly shift the modeled O:C ratio close to the observations. As noted, the FGOM does not reproduce the observed O:C data for the cyclododecane case. The initial organic mass growth observed from the OH oxidation of cyclododecane is consistent with rapid functionalization. Based on gas-phase chemical mechanisms, cycloalkanes should become more oxygenated as the breakage of the carbon ring introduces more than one extra O atom, compared with straight-chain alkanes. However, the measured O:C for the cyclododecane low-NO_x case is the lowest among the four alkanes. The model can replicate the measured ratio only if the average oxygen number of non-volatile compounds is decreased to 3. The model prediction suggests a more effective dehydration process occurring in cyclododecane than other systems, as long as the AMS measurements are comparable for the 8 experiments and the matrix of functional groups is applicable for the four C₁₂ alkanes.

Measured and predicted H:C ratios of the SOA are shown in Fig.7. The simulated H:C ratios match those observed after several hours of reaction for each experiment. The reason that it still takes several hours of photooxidation to reach the gray region (uncertainties of O:C and H:C) is that the oligomer formation takes time to be competitive with the oxidation reactions in both gas and particle phases, which are dominant at the beginning of the oxidation. The starting points, however, varied by 15%: the predicted H:C ratio starts from 2, decreasing to ~ 1.7, whereas AMS measurements show that the H:C ratio is roughly constant, with an average ranging from 1.6 to 1.7, over the course of each experiment. The functional group contributing the highest decrease in H:C ratio is -C=O. On the basis of the gas-phase chemistry, at least 3 -C=O additions to the parent hydrocarbon are needed to reach the observed H:C ratio. One generation of

oxidation can introduce at most one -C=O to the SOA, as the functional groups that are most likely to induce partitioning into the particle phase are -OOH and -ONO_2 , resulting in a higher contribution to the decrease of vapor pressure than -C=O . This means that > 3 generations of oxidation are needed to produce the “right” molecule. Note that certain combinations of functional groups, like -OOH and -OH , that have sufficiently low vapor pressure to be incorporated in the particles, do not change the H:C ratio. Therefore, products with H:C ratio even lower than 1.7 generated via either gas- or particle- phase chemistry could exist. While we have not explicitly considered the -C(O)OH group, this group can be represented by the sum of -C=O and -OH . In addition, -COOH groups can be produced only via fragmentation, which might be accompanied by an increase of vapor pressure. Thus, the contribution of -COOH to the chemical composition of alkane SOA is deemed less important as those of other functional groups. Gas-phase photochemistry alone can not produce such a low H:C ratio measured by AMS. Dehydration processes in the particle phase, on the other hand, are necessary to obtain the desired H:C ratio, although this process is likely not sufficiently fast to drive the H:C ratio immediately to ~ 1.7 at the onset of photochemistry.

Particle-phase accretion reactions (dehydration) play an important role in order to fit the model output to the chamber generated SOA data. However, this conclusion can be biased significantly by the variations in the AMS elemental analysis. AMS signals of water in both gas and particle phase occur at H_2O^+ ($m/z = 18$), OH^+ ($m/z = 17$), and O^+ ($m/z = 16$), which are also produced from organic aerosols. All of the eight alkanes experiments were carried out under dry conditions so that the interference of gas-phase water vapor is considered to be insignificant. Water present in particles or produced from

dehydration reactions, however, can still bias the contribution of organic aerosols to signals of H_2O^+ , OH^+ , and O^+ . The oxidation state, on the other hand, is insensitive to the parameters in the fragmentation table, which assign contributions of water to the three ion signals. Using the best-fit values constrained by C_{OA} , O:C and H:C, the modeled temporal profiles of oxidation state tend to match the observations better, see Fig. 8. Model output with only gas-phase chemistry incorporated tends to underpredict the oxidation state. This is because the intense loss of hydrogen atoms can not be reproduced, indicating that the dehydration pathway is still somehow necessary.

2.4.3 Role of particle-phase chemistry

Ample experimental evidence indicates the potential importance of oligomerization processes in the SOA formation. The esterification from carboxylic acids or inorganic acids and alcohols or amines is considered to be a potentially important dehydration reaction channel in the particle phase. Esters, acid anhydride, and organosulfates have been widely observed in chamber studies (Gao et al., 2004 a, b; Surratt et al., 2006, 2007 a, b; Szmigielski et al., 2007; Iinuma et al., 2007 a, b). Other dehydration reactions, such as acetal formation from the reaction of alcohols and hemiacetals and peroxyhemiacetal formation from the reaction of peroxyhemiacetals and peroxides, have also been proposed to potentially occur within the lifetime of ambient aerosols (Ziemann and Atkinson, 2012). Acetals have been identified in SOA formed from methylglyoxal uptake recently (Yasmeen et al., 2010). To assess the role of non-oxidative particle-phase reactions on SOA formation from C_{12} alkanes, one may shut off the accretion reaction channel ($k_a = 0$) and fit only f_v and r_p to the SOA data. Although under this condition the

model is capable of reproducing the observed organic aerosol growth curves, O:C and H:C ratios are overpredicted by 35% and 30%, respectively. Progressive oxidation chemistry is not capable of explaining the measured O:C and H:C ratios. Thus, gas-phase oxidation alone, coupled to gas-particle partitioning, does not lead to condensed phase OA with sufficiently low volatility and high oxidation state. One concludes that the non-oxidative chemistry afforded by the accretion reaction channel is required to simulate the observed oxidation state of the alkane SOA by producing essentially non-volatile dehydrated compounds.

Particle-phase oxidative reactions constitute an additional channel in the “VOC to SOA pump”. As noted, it is assumed that these reactions parallel those in the gas phase in terms of the functionalization and fragmentation pathways available, but at a rate that is a factor of r_p (<1) of the gas-phase rate. Fragmentation at each generation both in the gas and particle phases leads to a systematic cleavage of the original carbon backbone. If this cleavage is not compensated for by additional functionalization, the molecules produced will have higher volatility than their precursors, and a decrease in overall organic aerosol mass occurs regardless of whether the pathway occurs in the gas or particle phase. The existence of the particle-phase oxidation channel acts to accelerate the overall SOA evolution and therefore can lead to a more rapid aging than in its absence.

Figure 9 shows the simulated organic aerosol growth from the photooxidation of dodecane under low- NO_x conditions when $r_p = 0$ or 1, with other parameters held at their best-fit values. When $r_p = 0$, the predicted organic aerosol growth is able to match the measured C_{OA} because the r_p value for low- NO_x dodecane obtained from the optimization is 10^{-3} , implying a negligible particle-phase oxidation pathway. When $r_p = 1$, the

predicted C_{OA} is less than 20% of that measured in the chamber after 35 h of reaction. Although the incorporation of the accretion channel increases the predicted C_{OA} , this increase is insignificant in the presence of highly effective particle-phase oxidation reactions ($r_p = 1$). Obviously, the “ $r_p = 1$ ” simulation is an unrealistic case such that two parallel oxidation pathways with the same set of reaction rate constants exist in the gas and particle phases during SOA aging. The overall gas- and particle- phase rates of functionalization and fragmentation processes are accelerated in such a way that the decrease of volatility from the addition of functional groups cannot compensate for the increase of volatility due to the cleavage of the carbon backbone. As a result, the semi-volatile products are mostly consumed during the rapid aging process to produce intermediates with a higher volatility circumventing the accumulation of the organic aerosol.

2.5 Comparison of FGOM and SOM

The two semi-explicit SOA models, FGOM and SOM, employ distinct, but related, frameworks to characterize SOA properties. Both models represent functionalization and fragmentation, and each treats the fragmentation process with a tunable parameter “ P_f ”, that represents the probability of fragmentation. The molar yields of smaller molecules from fragmentation processes are assumed to be randomly assigned or with only one carbon atom loss in SOM, and with only one carbon atom loss in FGOM. The functionalization channel in SOM is represented in a statistical manner. The addition of average O-atoms per generation of oxidation and the decrease of volatility per addition of O-atoms are tunable parameters, as shown in Table 3. FGOM automatically generates all

possible compounds with the combination of four different functional groups and certain carbon numbers, as suggested by the generalized gas-phase chemistry. The one major difference between these two models is the treatment of particle-phase non-oxidative reactions: SOA formation and aging are driven solely by gas-phase photochemistry in SOM whereas the extent of accretion reaction channel is adjusted by four tunable parameters in FGOM. Both FGOM and SOM attempt to reproduce the observed chamber generated SOA properties (organic aerosol mass, O:C and H:C ratio) through optimal fitting of the empirical parameters in each model, e.g. Fig. 4, 6, 7, and 8 in this study and Fig. 1 and 3 in Cappa et al. (2012), to the same set of alkane SOA data generated from the Caltech Environmental Chamber. Comparison between these two sheds light on understanding the sensitivity of SOA growth to different reaction pathways in gas and particle phases.

One can map the simulation results of these two models onto the OS_C - $\log C^*$ space (Fig. 10). Atmospheric aging leads to increased functionality on the C_{12} skeleton and thus higher average oxidation state, which is reflected by both models. The SOM predicts OS_C (-1.1 ~ -0.6) vs. FGOM (-1.8 ~ -1.0). The AMS measured OS_C ($= 2 \times O:C - H:C$) of dodecane SOA is bounded by these two predictions, ranging from -1.2 to -1. The underestimation of OS_C by FGOM at the early stage is largely due to the starting point of the H:C ratio, as discussed in Section 3.2. The SOM-generated OS_C is shaped primarily by the simulated O:C ratio, since the adjustable parameter “H-atom loss per O-atom added” is determined as a constant. The overprediction of OS_C by SOM thus results from the overprediction of the O:C ratio at the end of the simulation.

The SOM simulated composition exhibits effective saturation concentrations ($\log C^*$) of monomers that are, on average, one order of magnitude lower than those in FGOM. Values of the best-fit parameters in SOM for the low- NO_x dodecane case can be found in Table 2 in Cappa et al. (2012). The decrease of vapor pressure upon the addition of one oxygen on a log scale (ΔLVP), 2.20, corresponds to the addition of an $-\text{OH}$ group, which leads to the largest decrease of vapor pressure per oxygen atom according to the vapor pressure prediction models “SIMPOL.1” and “EVAPORATION”. This ΔLVP value suggests that in order to reproduce the observed concentration of chamber-generated organic aerosol, the gas-phase chemistry should proceed such that the addition of any functional group on the carbon chain results in a decrease of the logarithm of vapor pressure by 2.20 per oxygen atom. The vapor pressure estimation module developed for use in FGOM for the alkanes constrains the ΔLVP values per O-atom addition to range from 0.79 to 1.97 upon the addition of the array of functional groups (The predicted decreases of the logarithm of vapor pressure (atm) upon the addition of $-\text{OOH}$, $-\text{ONO}_2$, $-\text{OH}$, and $-\text{C}=\text{O}$ are 2.83, 2.36, 1.97, and 1.20, respectively). This is confirmed as the probability of fragmentation in SOM ($m_{\text{frag}} = 0.077$) is higher than that in FGOM ($f_v = 0.61$ with accretion channel and $f_v = 0.77$ without accretion channel).

The simulated SOA chemical compositions are also shown in the $\text{OS}_C\text{-n}_C$ space in Fig 10. The average carbon numbers predicted by these two models cover distinctly different ranges. The temporal profile of aerosol n_C predicted by FGOM decreases initially to ~ 10.6 and then increases to ~ 15.2 at the end of the experiment. In the FGOM, two principal pathways govern the dynamics of carbon number: C-C bond cleavage and particle-phase accretion reactions. The degree of C-C bond cleavage determines the lower

limit of the average SOA carbon number, whereas the extent of accretion reactions sets the carbon number upper limit. The optimal FGOM fitting results suggest that oligomerization in the particle phase is required to predict the observed oxidative aging of dodecane SOA, in particular the evolution of the O:C and H:C.

Why do these two approaches that more or less equally capture the chamber-generated SOA properties exhibit such different oxidation trajectories in OS_C-n_C space? While FGOM exhibits the pull of oligomers, the oxidation trajectory generated by SOM progressively evolves in a direction that involves significant formation of highly oxidized small fragments. In the SOM, the individual species are characterized by the average carbon and oxygen number (n_O/n_C pairs), pairs that do not necessarily correspond to actual compounds, since functional group information is not explicitly simulated. Again, for the dodecane low- NO_x case, the ΔLVP and [1O, 2O, 3O, 4O] values are 2.2 and [0.79, 0.17, 0.03, 0.0], respectively, meaning that upon one generation of oxidation, the average number of oxygens added is 1.22 and the total decrease of vapor pressure on a log scale is 2.7, which equals the addition of approximately 1.3 $-OH$, 1.2 $-OOH$, 1.2 $-ONO_2$ or 2.4 $-C=O$ groups. This intense decrease of volatility upon only one generation allows the formation of small highly oxygenated fragments but with sufficiently low volatilities to contribute appreciably to the particle phase. As noted, these small fragments, as represented by n_O/n_C pairs, are not actual products reflected in current gas-phase photochemical mechanisms. However, their presence in the particle phase in a significant amount shifts the oxidation trajectory to the upper right corner in OS_C-n_C space.

Neither FGOM nor SOM can exactly describe the actual oxidation trajectory of alkane SOA because the chamber generated constraints are limited. However, information of the role of particle-phase chemistry can be extracted by comparing these two model outputs. In SOM, the measured van Krevelen slope is used to determine the H-atom loss per O-atom added with other six parameters held at their best-fit values adjusted by C_{OA} and O:C, as opposed to fitting all of the free parameters together to C_{OA} , O:C, and H:C. As shown in Fig. 11, the best-fit value of H-atom loss per O-atom added is 1.77 in SOM in the dodecane low- NO_x case, indicating the formation of an unsaturated carbon bond upon one step of oxidation. The ΔLVP value per O-atom added, however, indicates that the functional group likely to be added is $-OH$, with a van Krevelen slope of 1. This discrepancy reflects the fact that the best-fit parameters in the SOM can not reproduce the observed O:C or H:C ratios without a dehydration reaction channel. This returns us to the fundamental question: to what extent can gas-phase chemistry alone account for the SOA formation? Several products generated by the gas-phase mechanism in FGOM, detected in the chamber dodecane low- NO_x experiments (Yee et al., 2012), have sufficiently low volatility to form a substantial amount of organic aerosol mass. Nonetheless, the inescapable conclusion is that the presence of accretion reactions is necessary to reconcile both the disagreement between the indications of the best-fit parameters in SOM and the inability of the FGOM to reproduce the measured elemental composition based solely on gas-phase chemistry. Evaluating the extent to which particle-phase chemistry is important for virtually all SOA parent VOCs awaits a more complete understanding of gas-phase chemistry and measured SOA chemical properties.

2.6 Acknowledgement

This work was supported by U.S. Department of Energy grant DE-SC0006626. Helpful discussions with Chris Cappa are appreciated.

2.7 Bibliography

Aiken, A. C., DeCarlo, P. F., Jimenez, J. L.: Elemental analysis of organic species with electron ionization high-resolution mass spectrometry, *Anal. Chem.*, 79, 8350-8358, 2007.

Aiken, A. C., DeCarlo, P. F., Kroll, J. H., Worsnop, D. R., Huffman, J. A., Docherty, K. S., Ulbrich, I. M., Mohr, C., Kimmel, J. R., Sueper, D., Sun, Y., Zhang, Q., Trimborn, A., Northway, M., Ziemann, P. J., Canagaratna, M. R., Onasch, T. B., Alfarra, M. R., Prevot, A. S. H., Dommen, J., Duplissy, J., Metzger, A., Baltensperger, U., and Jimenez, J. L.: O/C and OM/OC ratios of primary, secondary, and ambient organic aerosols with high-resolution time-of-flight aerosol mass spectrometry, *Environ. Sci. Technol.*, 42, 4478-4485, 2008.

Atkinson, R.: Atmospheric chemistry of VOCs and NO_x, *Atmos. Environ.*, 36, 1483-1498, 2000.

Aumont, B., Szopa, S., and Madronich, S.: Modeling the evolution of organic carbon during its gas-phase tropospheric oxidation: development of an explicit model based on a self generating approach, *Atmos. Chem. Phys.*, 5, 2497-2517, 2005.

Aumont, B., Valorso, R., Mouchel-Vallon, C., Camredon, M., Lee-Taylor, J., and Madronich, S.: Modeling SOA formation from the oxidation of intermediate volatility n-alkanes, *Atmos. Chem. Phys.*, 12, 7577-7589, 2012.

- Barsanti, K. C., Smith, J. N., and Pankow, J. F.: Application of the np+mP modeling approach for simulating secondary organic particulate matter formation from α -pinene oxidation, *Atmos. Environ.*, 45, 6812-6819, 2011.
- Bloss, C., Wagner, V., Jenkin, M. E., Volkamer, R., Bloss, W. J., Lee, J. D., Heard, D. E., Wirtz, K., Martin-Reviejo, M., Rea, G., Wenger, J. C., and Pilling, M. J.: Development of a detailed chemical mechanism (MCMv3.1) for the atmospheric oxidation of aromatic hydrocarbons, *Atmos. Chem. Phys.*, 5, 641-664, 2005.
- Camredon, M. and Aumont, B.: Assessment of vapor pressure estimation methods for secondary organic aerosol modeling, *Atmos. Environ.*, 40, 2105-2116, 2006.
- Camredon, M., Aumont, B., Lee-Taylor, J., and Madronich, S.: The SOA/VOC/NO_x system: an explicit model of secondary organic aerosol formation, *Atmos. Chem. Phys.*, 7, 5599-5610, 2007.
- Capouet, M. and Müller, J. -F.: A group contribution method for estimating the vapor pressures of α -pinene oxidation products, *Atmos. Chem. Phys.*, 6, 1455-1467, 2006.
- Cappa, C. and Wilson, K. R.: Multi-generation gas-phase oxidation, equilibrium partitioning, and the formation and evolution of secondary organic aerosol, *Atmos. Chem. Phys.*, 12, 9505-9528, 2012.
- Cappa, C., Zhang, X., Loza, C. L., Craven, J. S., Yee, L. D., and Seinfeld, J. H.: Application of the Statistical Oxidation Model (SOM) to secondary organic aerosol formation from photooxidation of C₁₂ Alkanes, *Atmos. Chem. Phys. Discuss.*, 12, 27077-27109, 2012.

Chacon-Madrid, H. J., Murphy, B. N., Pandis, S. N., and Donahue, N. M.: Simulations of smog-chamber experiments using the two-dimensional volatility basis set: linear oxygenated precursors, *Environ. Sci. Technol.*, 46, 11179-11186, 2012.

Chen, Q., Liu, Y. J., Donahue, N. M., Shilling, J. E., and Martin, S. T.: Particle-phase chemistry of secondary organic material: modeled compared to measured O:C and H:C elemental ratios provide constraints, *Environ. Sci. Technol.*, 45, 4763-4770, 2011.

Chhabra, P. S., Flagan, R. C., and Seinfeld, J. H.: Elemental analysis of chamber organic aerosol using an aerodyne high-resolution aerosol mass spectrometer, *Atmos. Chem. Phys.*, 10, 4111-4131, 2010.

Craven, J. S., Yee, L. D., Ng, N. L., Canagaratna, M. R., Loza, C. L., Schilling, K. A., Yatavelli, R. L. N., Thornton, J. A., Ziemann, P. J., Flagan, R. C., and Seinfeld, J. H.: Analysis of secondary organic aerosol formation and aging using positive matrix factorization of high-resolution aerosol mass spectra: application to the dodecane low-NO_x system, *Atmos. Chem. Phys. Discuss.*, 12, 16647-16699, 2012.

Compernelle, S., Ceulemans, K., and Müller, J. -F.: EVAPORATION: a new vapor pressure estimation method for organic molecules including non-additivity and introamolecular interactions, *Atmos. Chem. Phys.*, 11, 9431-9450, 2011.

DeCarlo, P. F., Dunlea, E. J., Kimmel, J. R., Aiken, A. C., Sueper, D. Crouse, J., Wennberg, P. O., Emmons, L. Shinozuka, Y., Clarke, A., Zhou, J., Tomlinson, J., Collins, D. R., Knapp, D., Weinheimer, A. J., Montzka, D. D., Campos, T., and Jimenez, J. L.: Fast airborne aerosol size and chemistry measurements above Mexico city and Central Mexico during the MILAGRO campaign, *Atmos. Chem. Phys.*, 8, 4027-4048, 2008.

Donahue, N. M., Robinson, C. O., and Pandis, S. N.: Coupled partitioning, dilution, and chemical aging of semivolatile organics, *Environ. Sci. Technol.*, 40, 2635-2643, 2006.

Donahue, N. M., Epstein, S. A., Pandis, S. N., and Robinson, A. L.: A two-dimensional volatility basis set: 1. organic-aerosol mixing thermodynamics, *Atmos. Chem. Phys.*, 11, 3303-3318, 2011.

Donahue, N. M., Kroll, J. H., Pandis, S. N., and Robinson, A. L.: A two-dimensional volatility basis set – Part 2: Diagnostics of organic-aerosol evolution, *Atmos. Chem. Phys.*, 12, 615-634, 2012.

Donahue, N. M., Henry, K. M., Mentel, T. F., Kiendler-Scharr, A., Spindler, C., Bohn, B., Brauers, T., Dorn, H. P., Fuchs, H., Tillmann, R., Wahner, A., Saathoff, H., Naumann, K.-H., Möhler, O., Leisner, T., Müller, L., Reinning, M.-C., Hoffman, T., Salo, K., Hallquist, M., Frosch, M., Bilde, M., Tritscher, T., Barmet, P., Praplan, A. P., DeCarlo, P. F., Domenn, J., Prévôt, A. S. H., and Baltensperger, U.: Aging of biogenic secondary organic aerosol via gas-phase OH radical reactions, *Proc. Natl. Acad. Sci.*, 109, 13503-13508, 2012.

Gao, S., Keywood, M., Ng, N. L., Surratt, J., Varutbangkul, B., Bahreini, R., Flagan, R. C., Seinfeld, J. H.: Low-molecular-weight and oligomeric components in secondary organic aerosol form the ozonolysis of cycloalkenes and α -pinene, *J. Phys. Chem. A.*, 108, 10147-10164, 2004a.

Gao, S., Ng, N. L., Keywood, M., Varutbangkul, V., Bahreini, R., Nenes, A., He, J. W., Yoo, K. Y., Beauchamp, J. L., Hodyss, R. P.: Particle phase acidity and oligomer formation from secondary organic aerosol, *Environ. Sci. Technol.*, 38, 6582-6589, 2004b.

George, I. J., Slowik, J. and Abbatt, J. P. D.: Chemical aging of ambient organic aerosol from heterogeneous reaction with hydroxyl radicals, *Geophys. Res. Lett.*, 35 (13), L13811, doi: 10.1029/2008GL033884, 2008.

Heald, C. L., Jacob, D. J., Park, R. J., Russell, L. M., Huebert, B. J., Seinfeld, J. H., Lia, H., and Weber, R. J.: A large organic aerosol source in the free troposphere missing from current models, *Geophys. Res. Lett.*, 32, L18809, doi: 10.1029/2005GL023831, 2005.

Heald, C. L., Jacob, D. J., Turquety, S., Hudman, R. C., Weber, R. J., Sullivan, A. P., Peltier, R. E., Atlas, E. L., deGouw, J. A., Warneke, C., Holloway, J. S., Newman, J. A., Flocke, F. M., and Seinfeld, J. H.: Concentrations and sources of organic carbon aerosols in the free troposphere over North American, *J. Geophys. Res.*, 111, D23S47, doi: 10.1029/2006JD007705, 2006.

Iinuma, Y., Müller, C., Berndt, T., Böge, O., Claeys, M., Herrmann, H.: Evidence for the existence of organosulfates from β -pinene ozonolysis in ambient secondary organic aerosol., *Environ. Sci. Technol.*, 41, 6678-6683, 2007a.

Iinuma, Y., Müller, C., Böge, O., Gnauk, T., Herrmann, H.: The formation of organic sulfate esters in the limonene ozonolysis secondary organic aerosol (SOA) under acidic conditions, *Atmos. Environ.*, 41, 5571-5583, 2007b.

Jimenez, J. L., Canagaratna, M. R., Donahue, N. M., Prevot, A. S. H., Zhang, Q., Kroll, J. H., DeCarlo, P. F., Allan, J. D., Coe, H., Ng, N. L., Aiken, A. C., Docherty, K. S., Ulbrich, I. M., Grieshop, A. P., Robinson, A. L., Duplissy, J., Smith, J. D., Wilson, K. R., Lanz, V. A., Hueglin, C., Sun, Y. L., Tian, J., Laaksonen, A., Raatikainen, T., Rautiainen, J., Vaattovaara, P., Ehn, M., Kulmala, M., Tomlinson, J. M., Collins, D. R., Cubison, M. J., Dunlea, E. J., Huffman, J. A., Onasch, T. B., Alfarra, M. R., Williams, P. I., Bower,

K., Kondo, Y., Schneider, J., Drewnick, F., Borrmann, S., Weimer, S., Demerjian, K., Salcedo, D., Cottrell, L., Griffin, R., Takami, A., Miyoshi, T., Hatakeyama, S., Shiono, A., Sun, J. Y., Zhang Y. M., Dzepina, K., Kimmel, J. R., Sueper, D., Jayne, J. T., Herndon, S. C., Trimborn, A. M., Williams, L. R., Wood, E. C., Middlebrook, A. M., Kolb, C. E., Baltensperger, U., and Worsnop, D. R.: Evolution of organic aerosols in the atmosphere, *Science*, 326, 1525-1529, 2009.

Jenkin, M. E., Saunders, S. M., and Pilling, M. J.: The tropospheric degradation of volatile organic compounds: a protocol for mechanism development, *Atmos. Environ.*, 31, 81-104, 1997.

Knopf, D. A., Anthony, L. M., and Bertram, A. K.: Reactive uptake of O₃ by multicomponent and multiphase mixtures containing oleic acid, *J. Phys. Chem. A*, 109, 5579-5589, 2005.

Kroll, J. H. and Seinfeld, J. H.: Chemistry of secondary organic aerosol: Formation and evolution of low-volatility organics in the atmosphere, *Atmos. Environ.*, 42, 3593-3624, 2008.

Kroll, J. H., Smith, J. D., Che, D. L., Kessler, S. H., Worsnop, D. R., and Wilson, K. R.: Measurement of fragmentation and functionalization pathways in the heterogeneous oxidation of oxidized organic aerosol, *Phys. Chem. Chem. Phys.*, 11, 8005-8014, 2009.

Kroll, J. H., Donahue, N. M., Jimenez, J. L., Kessler, S. H., Canagaratna, M. R., Wilson, K. R., Altieri, K. E., Mazzoleni, L. R., Wozniak, A. S., Bluhm, H., Mysak, E. R., Smith, J. D., Charles, E. K., and Worsnop, D. R.: Carbon oxidation state as a metric for describing the chemistry of atmospheric organic aerosol, *Nature Chem.*, 3, 133-139, 2011.

Kwok, E. S. C. and Atkinson, R.: Estimation of hydroxyl radical reaction rate constants for gas-phase organic compounds using a structure-reactivity relationship: An update, *Atmos. Environ.*, 29, 1685-1695, 1995.

Lambe, A. T., Miracolo, M. A., Hennigan, C. J., Robinson, A. L., and Donahue, N. M.: Effective rate constants and uptake coefficients for the reactions of organic molecular markers (n-alkanes, hopanes, and steranes) in motor oil and diesel primary organic aerosols with hydroxyl radicals, *Environ. Sci. Technol.*, 43, 8794-8800, 2009.

Lee-Taylor, J., Madronich, S., Aumont, B., Baker, A., Camredon, M., Hodzic, A., Tyndall, G. S., Apel, E., and Zaveri, R. A.: Explicit modeling of organic chemistry and secondary organic aerosol partitioning for Mexico City and its outflow plume, *Atmos. Chem. Phys.*, 11, 13219-13241, 2011.

MathWorks, 2002. MATLAB.

Murphy, D. M., Cziczo, D. J., Hudson, P. K., and Thomson, D. S.: Carbonaceous material in aerosol particles in the lower stratosphere and tropopause region, *J. Geophys. Res.*, 112, D04203, doi: 10.1029/2006JD007297, 2007.

Murphy, B. N., Donahue, N. M., Fountoukis, C., and Pandis, S. N.: Simulating the oxygen content of ambient organic aerosol with the 2D volatility basis set, *Atmos. Chem. Phys.*, 11, 7859-7873, 2011.

Murphy, B. N., Donahue, N. M., Fountoukis, C., Dall'Osto, M., O'Dowd, C., Kiendler-Scharr, A., and Pandis, S. N.: Functionalization and fragmentation during ambient organic aerosol aging: application of the 2-D volatility basis set to field studies, *Atmos. Chem. Phys. Discuss.*, 12, 9857-9901, 2012.

Ng, N. L., Canagaratna, M. R., Zhang, Q., Jimenez, J. L., Tian, J., Ulbrich, I. M., Kroll, J. H., Docherty, K. S., Chhabra, P. S., Bahreini, R., Murphy, S. M., Seinfeld, J. H., Hildebrandt, L., Donahue, N. M., DeCarlo, P. F., Lanz, V. A., Prévôt, A. S. H., Dinar, E., Rudich, Y., and Worsnop, D. R.: Organic aerosol components observed in Northern Hemispheric datasets from Aerosol Mass Spectrometry, *Atmos. Chem. Phys.*, 10, 4625-4641, 2010.

Ng, N. L., Canagaratna, M. R., Jimenez, J. L., Chhabra, P. S., Seinfeld, J. H., and Worsnop, D. R.: Changes in organic aerosol composition with aging inferred from aerosol mass spectra, *Atmos. Chem. Phys.*, 11, 6465-6474, 2011.

Odum, J. R., Hoffmann, T., Bowman, F., Collins, D., Flagan, R. C., and Seinfeld, J. H.: Gas/particle partitioning and secondary organic aerosol yields, *Environ. Sci. Technol.*, 30, 2580-2585, 1996.

Pankow, J. F. and Asher, W. E.: SIMPOL.1: a simple group contribution method for predicting vapor pressures and enthalpies of vaporization of multifunctional organic compounds, *Atmos. Chem. Phys.*, 8, 2773-2796, 2008.

Pankow, J. F. and Barsanti, K. C.: The carbon number-polarity grid: A means to manage the complexity of the mix of organic compounds when modeling atmospheric organic particulate matter, *Atmos. Environ.*, 43, 2829-2835, 2009.

Paulot, F., Crouse, J. D., Kjaergaard, G., Andreas, K. Clair, J. M. S., Seinfeld, J. H., and Wennberg, P. O.: Unexpected epoxide formation in the gas-phase photooxidation of isoprene, *Nature*, 325, 730-733, 2009.

Ravishankara, A. R.: Heterogeneous and multiphase chemistry in the troposphere, *Science*, 276, 1058-1065, 1997.

Robinson, A. L., Donahue, N. M., Shrivastava, M. K., Weitkamp, E. A., Sage, A. M., Grieshop, A. P., Lane, T. E., Pierce, J. R., and Pandis, S. N.: Rethinking organic aerosols: Semivolatile emissions and photochemical aging, *Science*, 315, 1259-1262, 2007.

Saunders, S. M., Jenkin, M. E., Derwent, R. G., and Pilling, M. J.: Protocol for the development of the Master Chemical Mechanism, MCM v3 (Part A): tropospheric degradation of non-aromatic volatile organic compounds, *Atmos. Chem. Phys.*, 3, 161-180, 2003.

Shiraiwa, M., Ammann, M., Koop, T., and Pöschl, U.: Gas uptake and chemical aging of semisolid organic aerosol particles, *Proc. Natl. Acad. Sci.*, 108, 11003-11008, 2011.

Surratt, J. D., Murphy, S. M., Kroll, J. H., Ng, N. L., Hilderbrandt, L., Sorooshian, A., Szmigielski, R., Vermeylen, R., Maenhaut, W., Claeys, M., Flagan, R. C., and Seinfeld, J. H.: Chemical composition of secondary organic aerosol formed from the photooxidation of isoprene, *J. Phys. Chem., A*, 110, 9665-9690, 2006.

Surratt, J. D., Kroll, J. H., Kleindienst, T. E., Edney, E. O., Claeys, M., Sorooshian, A., Ng, N. L., Offenberg, J. H., Lewandowski, M., Jaoui, M., Flagan, R. C., and Seinfeld, J. H.: Evidence for organosulfates in secondary organic aerosol, *Environ. Sci. Technol.*, 41, 517-527, 2007a.

Surratt, J. D., Lewandowski, M., Offenberg, J. H., Jaoui, M., Kleindienst, T. E., Edney, E. O., and Seinfeld, J. H.: Effect of acidity on secondary organic aerosol formation from isoprene, *Environ. Sci. Technol.*, 41, 5363-5369, 2007b.

Szmigielski, R., Surratt, J. D., Vermeylen, R., Szmigielska, K., Kroll, J. H., Ng, N. L., Murphy, S. M., Sorooshian, A., Seinfeld, J. H., and Claeys, M.: Characterization of 2-methylglyceric acid oligomers in secondary organic aerosol formed from the

photooxidation of isoprene using trimethylsilylation and gas chromatography/ion trap mass spectrometry, *J. Mass Spectrom.*, 42, 101–116, 2007.

Tsigaridis, K. and Kanakidou, M.: Global modeling of secondary organic aerosol in the troposphere: a sensitivity analysis, *Atmos. Chem. Phys.*, 3, 1839-1869, 2003.

Valorso, R., Aumont, B., Camredon, M., Raventos-Duran, T., Mouchel-Vallon, C., Ng, N. L., Seinfeld, J. H., Lee-Taylor, J., and Madronich, S.: Explicit modeling of SOA formation from α -pinene photooxidation: sensitivity to vapor pressure estimation, *Atmos. Chem. Phys.*, 11, 6895-6910, 2011.

Volkamer, R., Jimenez, J. L., sanMartini, F., Dzepina, K., Zhang, Q., Salcedo, D., Molina, L. T., Worsnop, D. R., and Molina, M. J.: Secondary organic aerosol formation from anthropogenic air pollution: Rapid and higher than expected, *Geophys. Res. Lett.*, 33, L17811, doi: 10.1029/2006GL026899, 2006.

Yee, L. D., Craven, J. S., Loza, C. L., Schilling, K. A., Ng, N. L., Canagaratna, M. R., Ziemann, P. J., Flagan, R. C., and Seinfeld, J. H.: Secondary organic aerosol formation from low-NO_x photooxidation of dodecane: evolution of multigeneration gas-phase chemistry and aerosol formation, *J. Phys. Chem. A*, 116, 6211-6230, 2012.

Yasmeen, F. Sauret, N., Gal, J. –F., Maria, P. –C., Massi, L., Maenhaut, W., and Claeys, M.: Characterization of oligomers from methylglyoxal under dark conditions: a pathway to produce secondary organic aerosol through cloud processing during nighttime, *Atmos. Chem. Phys.*, 10, 3803-3812, 2010.

Zahardis, J. and Petrucci, G. A.: The oleic acid-ozone heterogeneous reaction system: products, kinetics, secondary chemistry, and atmospheric implications of a model system – a review, *Atmos. Chem. Phys.*, 7, 1237–1274, 2007.

Ziemann, P. J. and Atkinson, R.: Kinetics, products, and mechanisms of secondary organic aerosol formation, *Chem. Soc. Rev.*, 41, 6582-6605, 2012.

Zuend, A., Marcolli, C., Peter, T., and Seinfeld, J. H.: Computation of liquid-liquid equilibria and phase stabilities: implications for RH-dependent gas/particle partitioning of organic-inorganic aerosols, *Atmos. Chem. Phys.*, 10, 7795-7820, 2010.

Zuend, A. and Seinfeld, J. H.: Modeling the gas-particle partitioning of secondary organic aerosol: the importance of liquid-liquid phase separation, *Atmos. Chem. Phys.*, 12, 3857-3882, 2012.

Table 2.1. Secondary organic aerosol yields and initial experimental conditions for OH oxidation of C₁₂ alkanes.

	Compound	OH source	Seed Conc. (NH ₄) ₂ SO ₄ μm ³ /cm ³	HC ₀ (ppb)	NO ₀ (ppb)	NO ₂₀ (ppb)	OH ₀ (mole/cm ³)	Yield ^a (%)
High NO _x	dodecane	H ₂ O ₂	8.6	32.2	343	429	4.20×10 ⁷	5.8
	methylundecane	H ₂ O ₂	15.4	72.4	366	424	3.90×10 ⁷	5.6
	hexylcyclohexane	H ₂ O ₂	12.1	22.1	320	399	3.19×10 ⁷	17.7
	cyclododecane	H ₂ O ₂	7.5	13.8	289	444	2.40×10 ⁷	41.3
Low NO _x	dodecane	HONO	10.8	34.0	< 2	< 4	2.59×10 ⁶	16.0
	methylundecane	HONO	15.2	28.0	< 2	< 4	2.29×10 ⁶	15.1
	hexylcyclohexane	HONO	10.5	15.6	< 2	< 4	2.81×10 ⁶	34.8
	cyclododecane	HONO	13.8	10.4	< 2	< 4	3.04×10 ⁶	47.3

^a The values determined here are final yields, i.e., the mass of aerosol formed per mass of alkane reacted after 3 h and 35 h, respectively, in high- vs. low-NO_x experiments.

Table 2.2. Best-fit parameters for OH-initiated oxidation of C₁₂ alkanes. r_p is the ratio of the particle-phase oxidative reaction rate constant to that in the gas phase. f_v is the parameter characterizing the probability of fragmentation. k_a is the accretion reaction rate constant in the particle phase. The matrix [C_x, H_y, O_z] represents the carbon, hydrogen, and oxygen numbers of the non-volatile products. For each alkane, the first entry is the full set nonlinear minimization (sim.1) and the second entry is the fit of only f_v and r_p to the total organic mass concentration (sim.2).

		f_v ^a	r_p ^b	k_a ^c (m ³ mol ⁻¹)	[C _x H _y O _z] ^d
High NO _x	dodecane	0.57	1.12×10 ⁻²	9.99×10 ³	[21.21 21.83 3.23]
		0.65	9.90×10 ⁻³	—	—
	methylundecane	0.66	1.07×10 ⁻²	1.02×10 ⁴	[24.00 30.21 1.16]
		0.81	1.00×10 ⁻²	—	—
	hexylcyclohexane	0.76	1.35×10 ⁻¹	5.28×10 ⁴	[22.12 31.23 5.84]
		1.10	1.00×10 ⁻³	—	—
	cyclododecane	0.89	1.00×10 ⁻³	1.05×10 ⁴	[23.49 27.42 3.30]
		1.42	1.00×10 ⁻³	—	—
Low NO _x	dodecane	0.61	1.00×10 ⁻³	5.95×10 ³	[24.00 39.38 5.59]
		0.77	1.00×10 ⁻³	—	—
	methylundecane	0.67	1.00×10 ⁻³	5.70×10 ³	[24.00 37.78 5.32]
		0.91	1.00×10 ⁻³	—	—
	hexylcyclohexane	0.82	8.99×10 ⁻²	6.01×10 ³	[18.03 26.44 6.00]
		1.00	1.00×10 ⁻³	—	—
	cyclododecane	0.89	1.00×10 ⁻³	1.86×10 ³	[23.36 31.42 3.29]
		2.00	1.00×10 ⁻³	—	—

^a The probability of fragmentation (P_f) should be within the range of 0 to 1.

^b The upper and lower limits for r_p are set to be 1 and 10⁻³, respectively.

^c No upper limit is applied to k_a .

^d The upper limit of x value should be 24 for C_{12} alkanes studied here and the x value can not be lower than the sum of two molecules with the lowest carbon numbers in the category of semi-volatile compounds defined by equation (2); the upper limit of y value should be the hydrogen number of the C_{24} alkane; and z value ranges from 0 to the sum of two molecules that have the largest oxygen number generated from the functionalization channel.

Table 2.3. Comparison of the treatment of gas-phase chemistry, including functionalization and fragmentation, particle-phase chemistry, including oxidation and accretion reactions, and gas-particle partitioning between two models: 1) Statistical Oxidation Model (SOM) and 2) Functional Group Oxidation Model (FGOM).

	2D-VBS ^a	SOM ^b	FGOM
	-- Probability of fragmentation $P = (\text{O:C})^f$	-- Probability of fragmentation $P = c_{frag} \text{O}$ or $P = (\text{O:C})^{m_{frag}}$	-- Probability of fragmentation $P = (\text{O:C})^{f_v}$
	-- Decrease in saturation concentration per generation	-- Decrease in vapor pressure per O-atom added	-- Particle phase oxidation rates
	-- Number of O-atoms added per generation	-- Number of O-atoms added per generation -- Number of H-atoms lost per O-atom added	-- Particle phase accretion reaction rates -- Chemical properties of the non-volatile species
Func.	-- Change in the O:C ratio -- Decrease in C*	-- Addition of oxygen -- Decrease in vapor pressure	-- Addition of functional groups -- Decrease in vapor pressure
Frag.	-- A function of O:C ratio	-- A function of oxygen number or O:C ratio	-- A function of O:C ratio
Oxidation	-- OH radical uptake coefficient is unity -- Follows gas-phase oxidation mechanisms	-- OH radical uptake coefficient is unity -- One extra oxygen is added per generation of oxidation -- Fragmentation is treated the same as gas-phase	-- Reaction rates are best-fit parameters -- Follows gas-phase oxidation mechanisms -- Fragmentation is treated the same as gas-phase -- Bimolecular reaction with an adjustable reaction rate constant
Accretion	—	—	-- The elemental composition of non-volatile species is defined by empirical parameters

^a Assumed that C-C bond scission is randomly distributed along the carbon backbone, resulting in an even molar distribution for all carbon numbers between C_{n-1} and C_1 .

^b The distribution of fragments upon fragmentation is computed in two ways: (1) A random probability for the location of C-C bond scission, and (2) Fragmentation leads to C_{n-1} and C_1 and species.

Figure 2.1. Scheme for SOA formation and evolution, showing multi-generational gas- and particle- phase reactions, in the Functional Group Oxidation Model. “S” and “N” denote semi-volatile and non-volatile compounds, respectively. Note that the single product for each generation shown here represents a spectrum of products spanning a range of volatilities and oxidation states. The oxidation of semi-volatile compounds comprises two processes: functionalization (red arrows) and fragmentation (yellow arrows). Instantaneous equilibrium partitioning is assumed (green arrows). Non-oxidative (accretion) reactions are considered as bimolecular irreversible reactions (blue arrows).

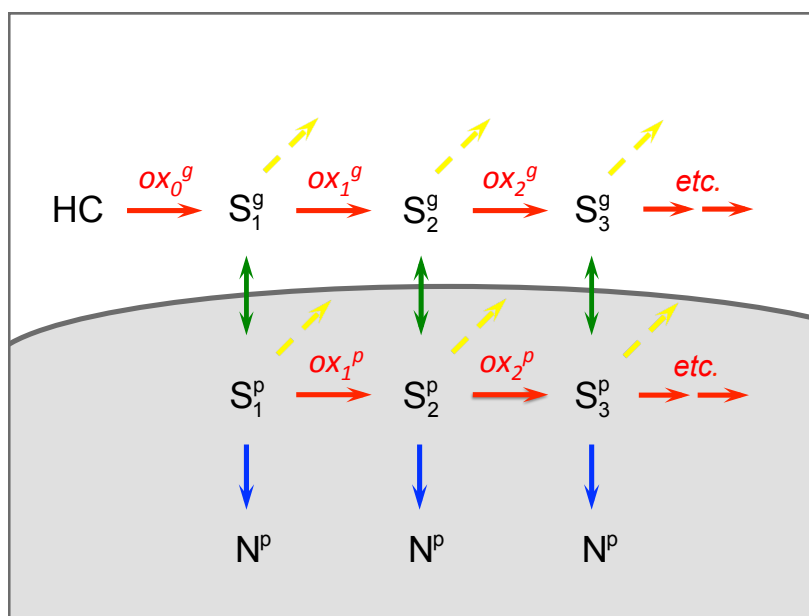


Figure 2.2. Chemical mechanisms of alkane photooxidation underlying fragmentation processes.

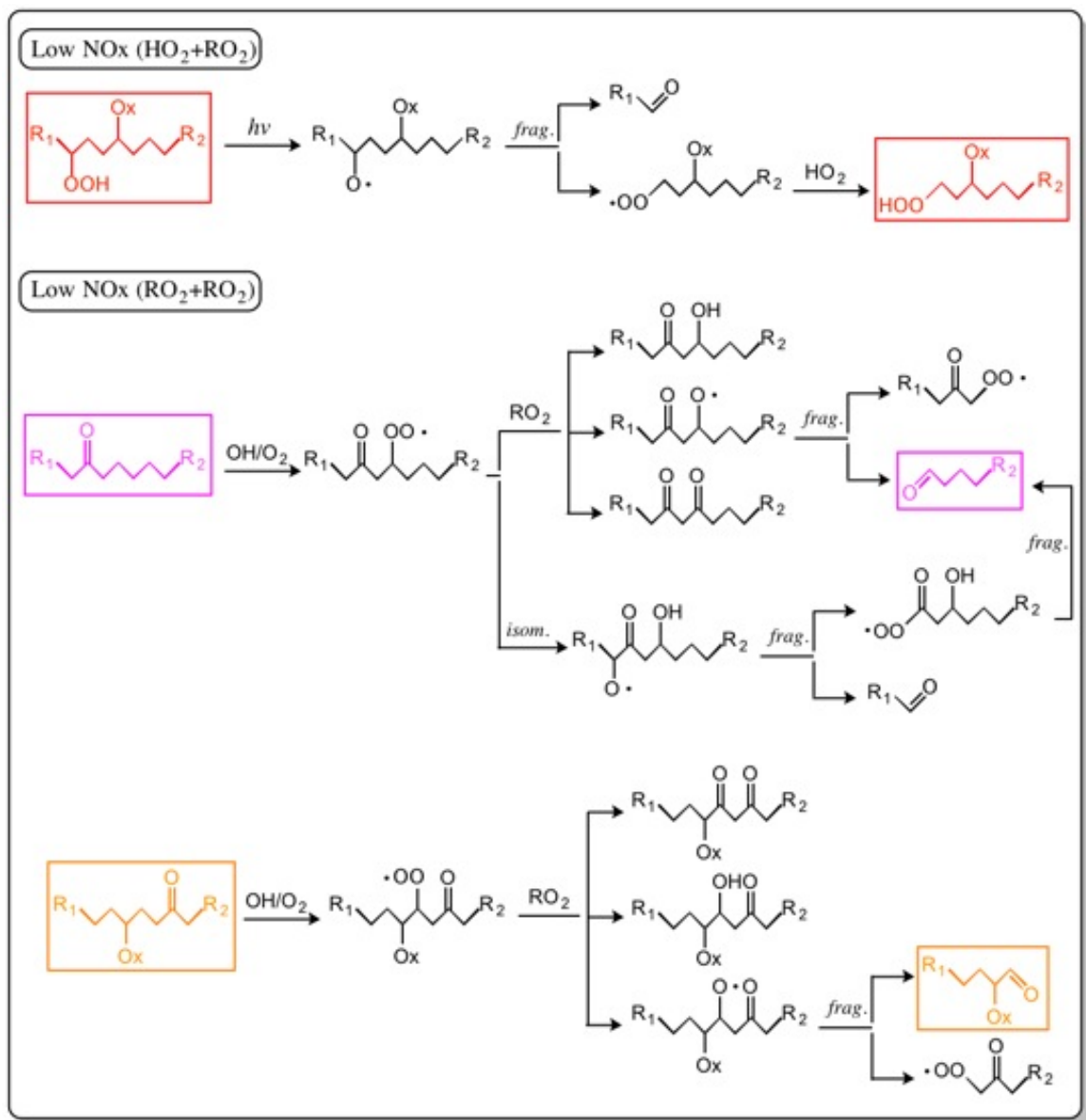


Figure 2.3. Carbon number range for products of OH oxidation of dodecane under low- NO_x conditions. For illustration, the shaded region ($C^\circ \leq 1000 \mu\text{g}/\text{m}^3$) is taken to represent the combination of carbon number and volatility for which a molecule can appreciably partition to the particle phase.

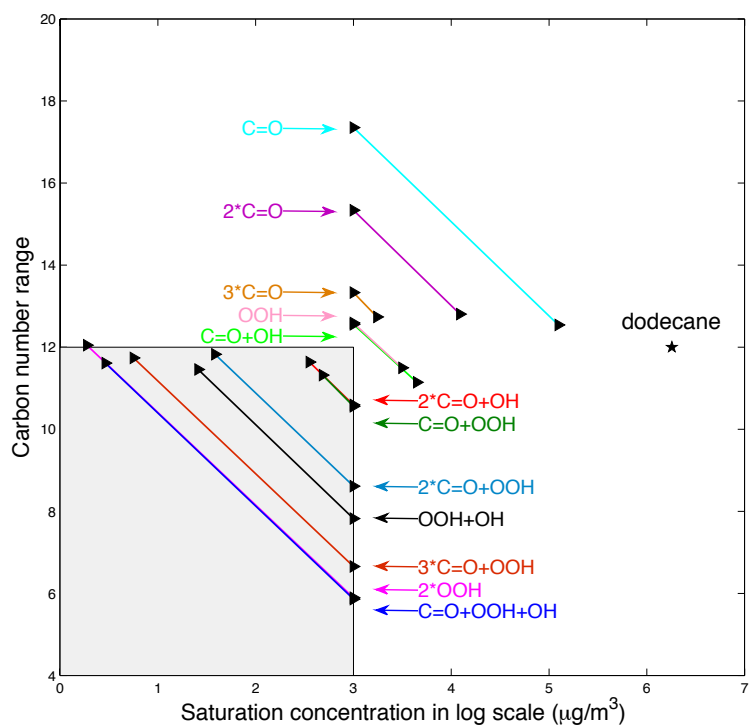


Figure 2.4. Simulated (colors) and observed (black) time-dependent organic aerosol growth from the photooxidation of four C₁₂ alkanes under high- (red) and low- (green) NO_x conditions. Note that “sim.1” represents the full fitting of the six empirical parameters and “sim.2” refers to fitting by only two parameters, r_p and f_v , to the organic mass concentration.

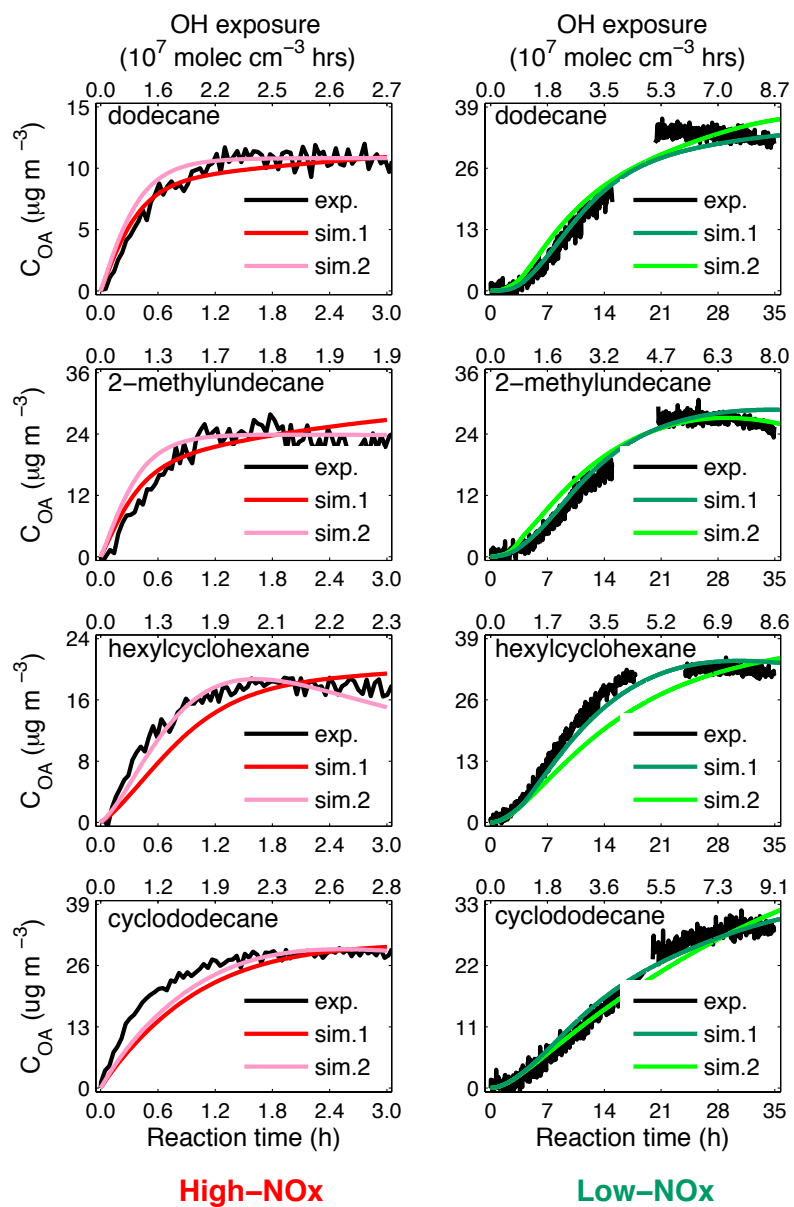


Figure 2.5. Time evolution of predicted gas- and particle- phase multi-generational products from OH oxidation of C₁₂ alkanes under high- and low-NO_x conditions (upper and lower panel, respectively).

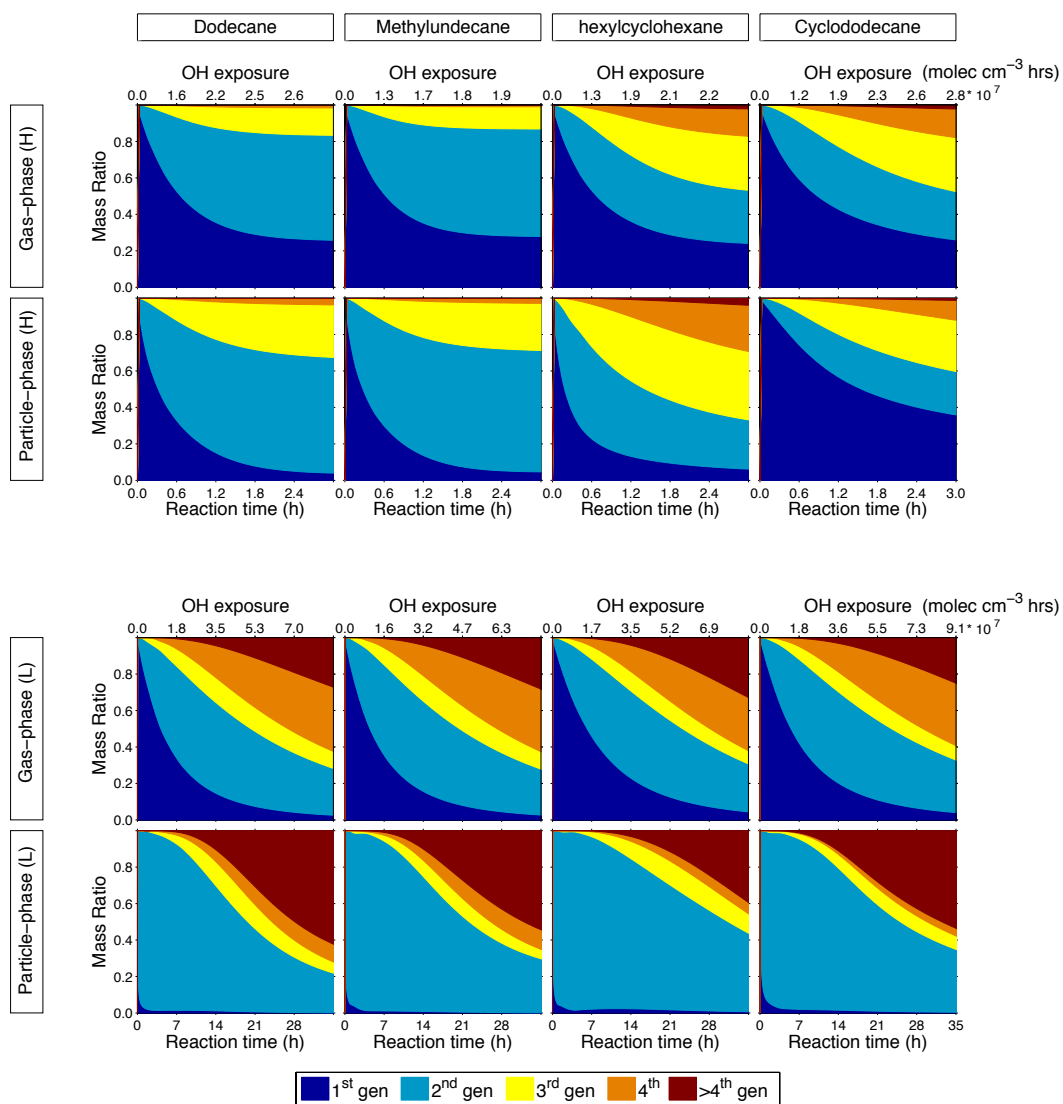


Figure 2.6. Simulated (colors) and observed (black) temporal profiles of particulate O:C ratio from the photooxidation of C₁₂ alkanes under high- (red) and low- (green) NO_x conditions. Dark colors denote “sim.1” and light colors denote “sim.2”.

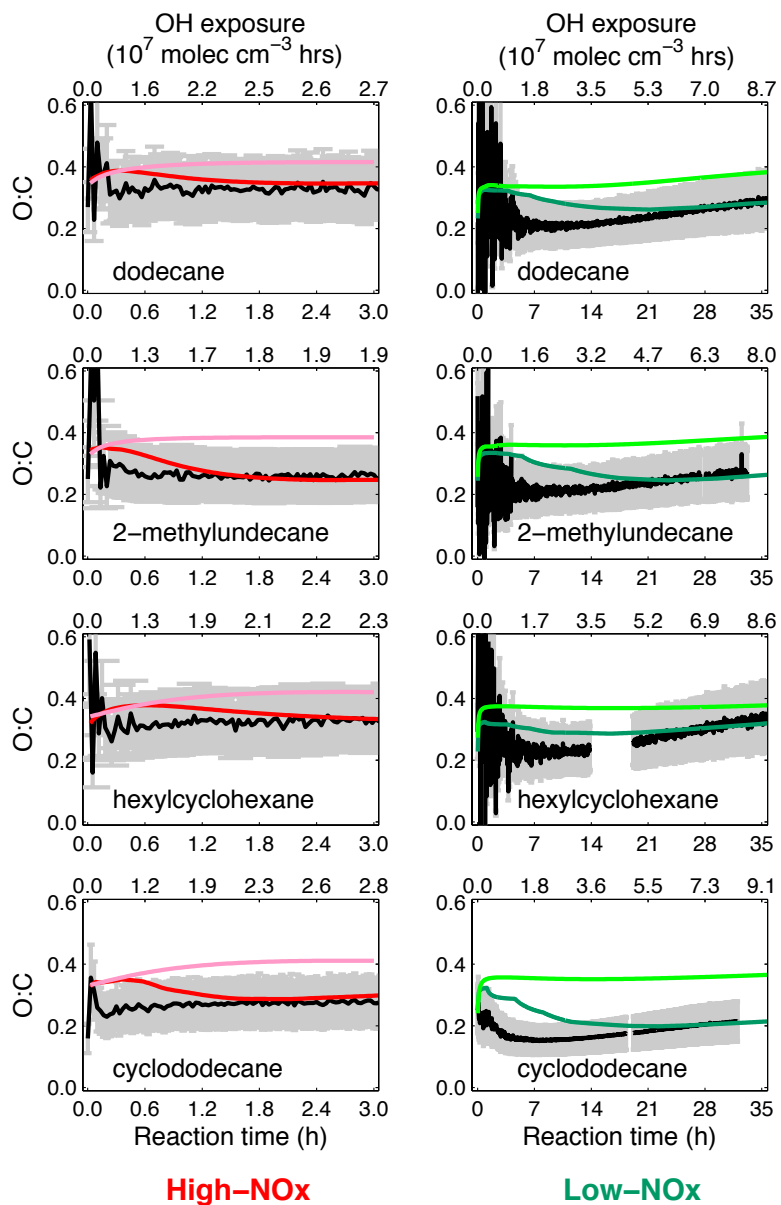


Figure 2.7. Simulated (colors) and observed (black) temporal profiles of particulate H:C ratio from the photooxidation of C₁₂ alkanes under high- (red) and low- (green) NO_x conditions. Dark colors denote “sim.1” and light colors denote “sim.2”.

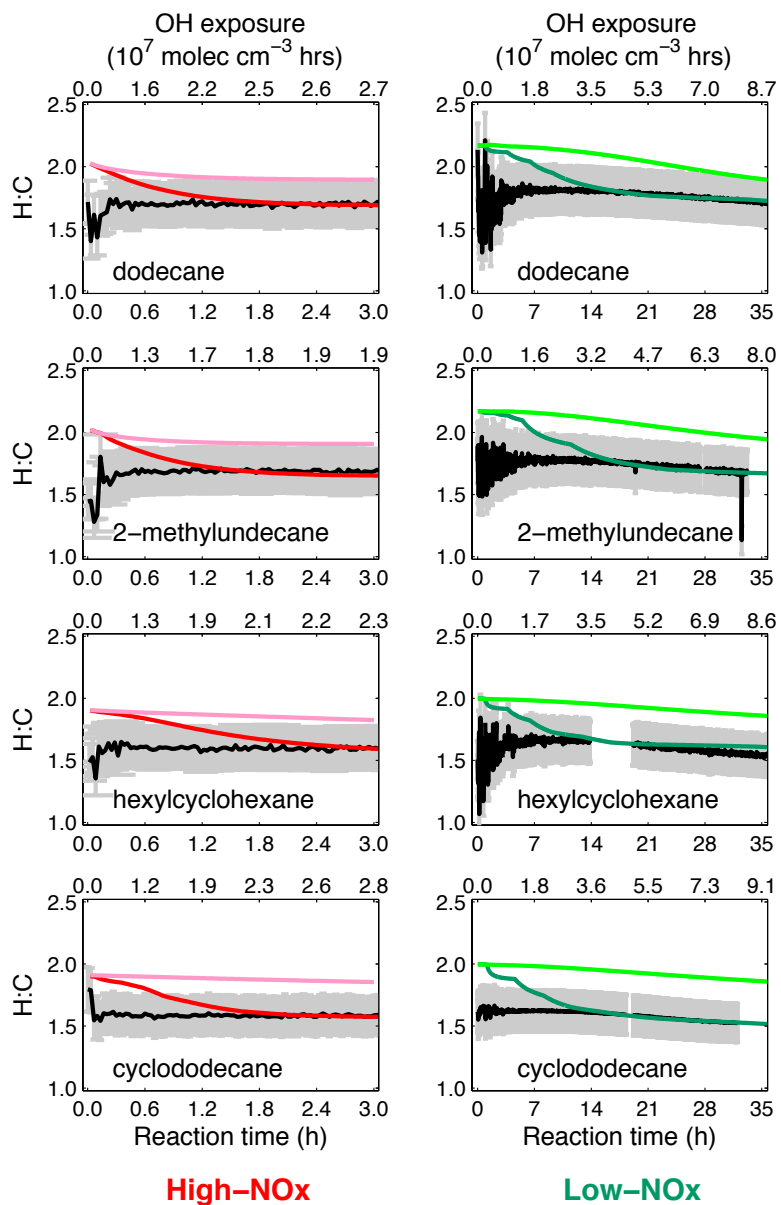


Figure 2.8. Simulated (colors) and observed (black) temporal profiles of particulate oxidation state (OS_C) from the photooxidation of C_{12} alkanes under high- (red) and low- (green) NO_x conditions. Dark colors denote “sim.1” and light colors denote “sim.2”.

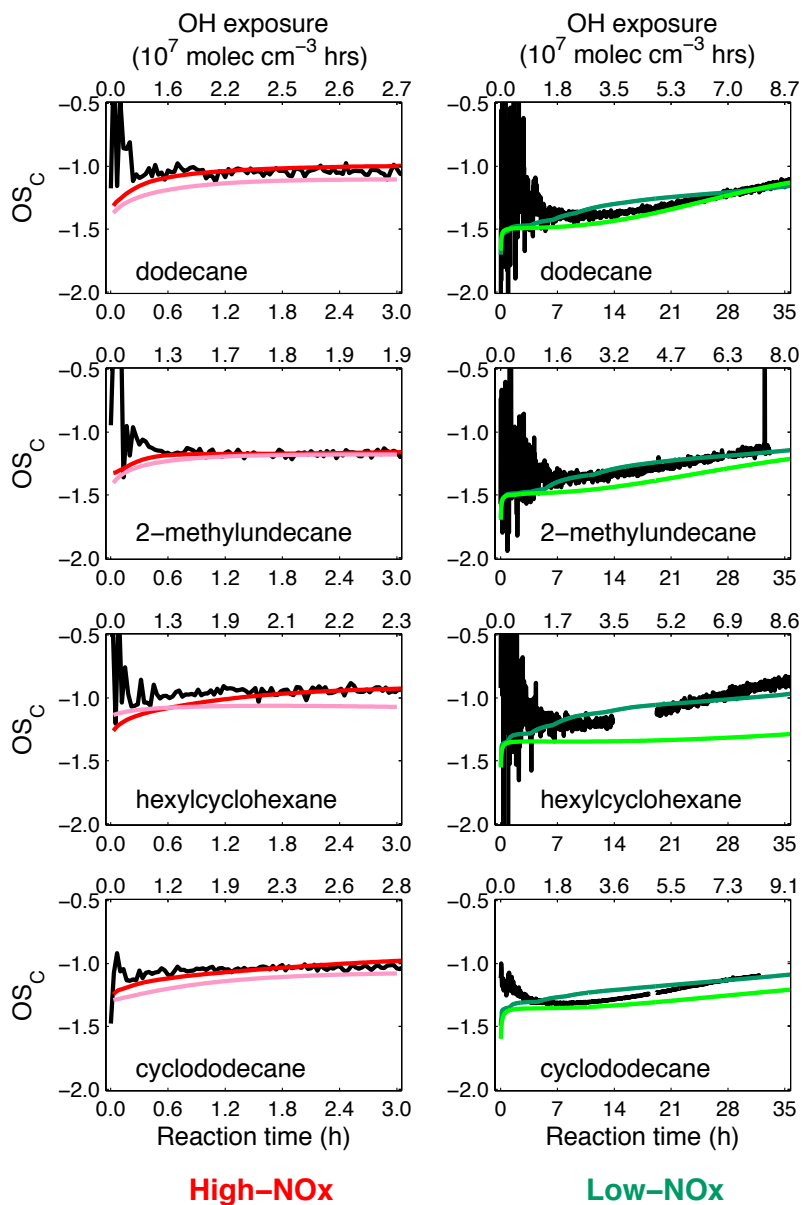


Figure 2.9. Effect of particle-phase oxidative reactions on the SOA growth from the low- NO_x photooxidation of dodecane. Four simulations are run here: (1) No particle-phase oxidative chemistry, as shown in red curve ($r_p = 0$ with other parameters held at their best-fit values); (2) Particle-phase oxidation reaction kinetics is same as gas phase, as shown in magenta curve ($r_p = 1$ with other parameters held at their best-fit values); (3) No particle-phase chemistry, as shown in blue curve ($r_p = 0$ and $k_a = 0$, with other parameters held at their best-fit values); (4) Particle-phase oxidation reaction kinetics is same as gas phase but no accretion reaction channel, as shown in cyan curve ($r_p = 1$ and $k_a = 0$, with other parameters held at their best-fit values).

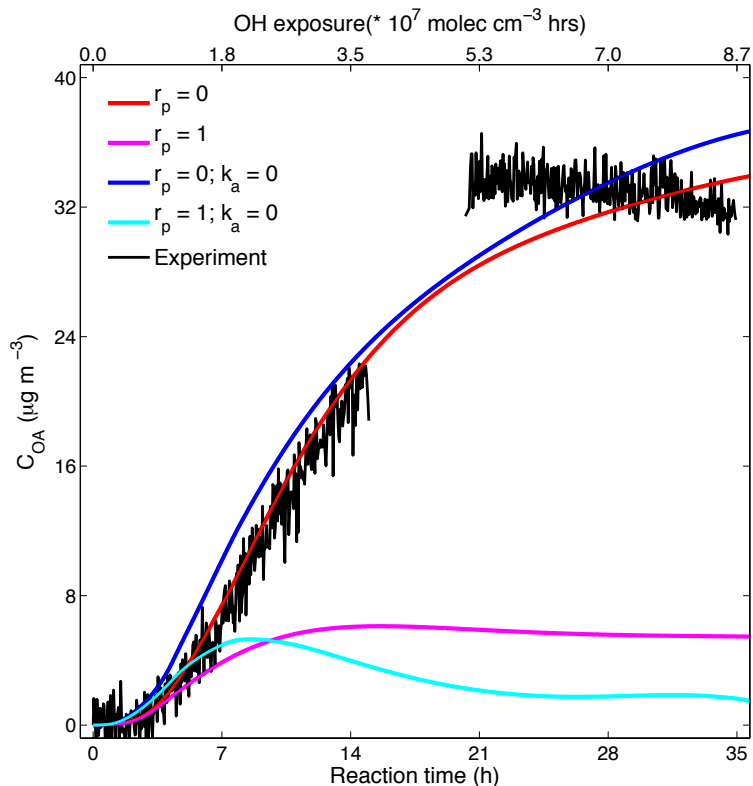


Figure 2.10. Comparison of FGOM with SOM for low- NO_x dodecane SOA formation. The upper panel is the FGOM predicted SOA composition represented by saturation concentration and average oxidation state after 7 (A), 14 (B), 21 (C), and 28 (D) hours of reaction, respectively. The middle panel is the SOM predicted SOA composition at same time points as FGOM. The lower panel is the simulated results of these two models in n_C vs. OS_C space.

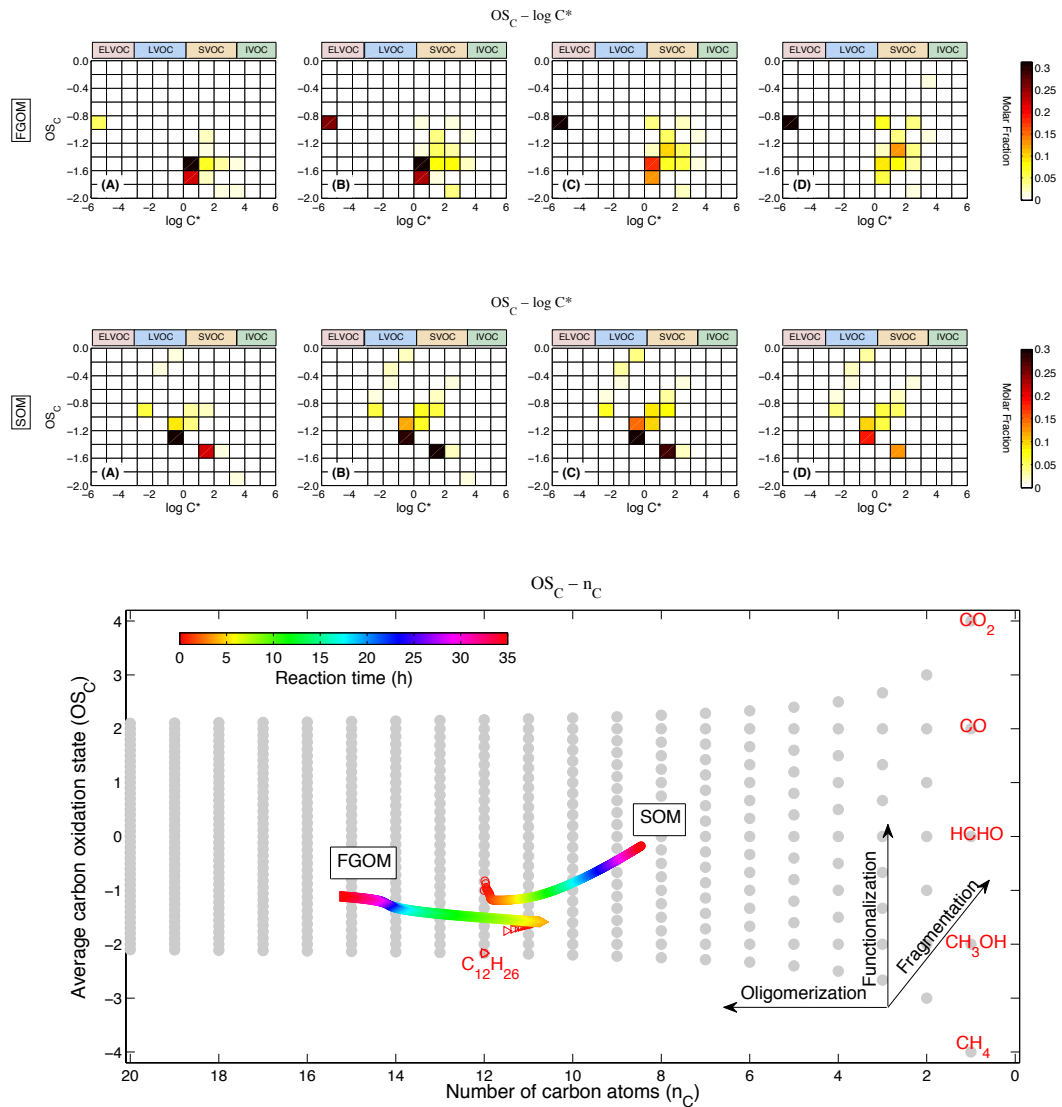
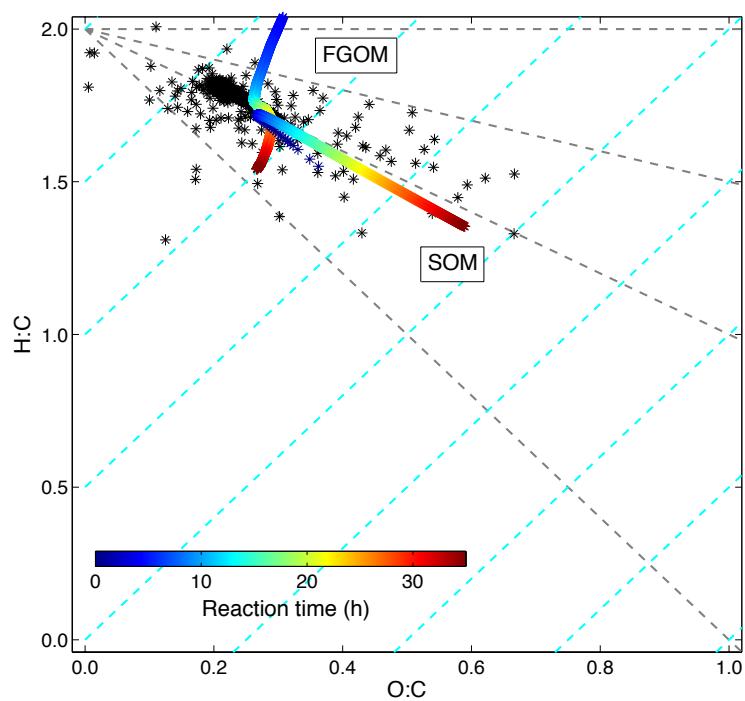


Figure 2.11. van Krevelen diagram. FGOM and SOM simulated H:C vs. O:C temporal profile, together with chamber measured data (black asterisks) for low- NO_x dodecane system. Black dash lines represent changes in slopes upon the addition of different functional groups (from top to bottom: $-\text{OH}$, NA, $-\text{COOH}$ or $-\text{C}=\text{O}$ plus $-\text{OH}$, and $-\text{C}=\text{O}$). Canyon dash lines map the oxidation state along the van Krevelen diagram.



Chapter 3

Role of ozone in SOA formation from alkane photooxidation

* Reproduced with permission from “Role of ozone in SOA formation from alkane photooxidation” by X. Zhang, R. H. Schwantes, M. M. Coggon, C. L. Loza, K. A. Schilling, R. C. Flagan, and J. H. Seinfeld, *Atmospheric Chemistry and Physics*, 14, 1733-1753, 2014. Copyright 2014 by Authors.

3.1 Abstract

Long-chain alkanes, which can be categorized as intermediate volatility organic compounds (IVOCs), are an important source of secondary organic aerosol (SOA). Mechanisms for the gas-phase OH-initiated oxidation of long-chain alkanes have been well documented; particle-phase chemistry, however, has received less attention. The δ -hydroxycarbonyl, which is generated from the isomerization of alkoxy radicals, can undergo heterogeneous cyclization and dehydration to form substituted dihydrofuran. Due to the presence of C=C bonds, the substituted dihydrofuran is predicted to be highly reactive with OH, and even more so with O₃ and NO₃, thereby opening a reaction pathway that is not usually accessible to alkanes. This work focuses on the role of substituted dihydrofuran formation and its subsequent reaction with OH, and more importantly ozone, in SOA formation from the photooxidation of long-chain alkanes. Experiments were carried out in the Caltech Environmental Chamber using dodecane as a representative alkane to investigate the difference in aerosol composition generated from “OH-oxidation dominating” vs. “ozonolysis dominating” environments. A detailed mechanism incorporating the specific gas-phase photochemistry, together with the heterogeneous formation of substituted dihydrofuran and its subsequent gas-phase OH/O₃ oxidation, is used to evaluate the importance of this reaction channel in dodecane SOA formation. We conclude that: 1) the formation of δ -hydroxycarbonyl and its subsequent heterogeneous conversion to substituted dihydrofuran is significant in the presence of NO_x; 2) the ozonolysis of substituted dihydrofuran dominates over the OH-initiated oxidation under conditions prevalent in urban and rural air; and 3) a spectrum of highly-oxygenated products with carboxylic acid, ester, and ether functional groups are

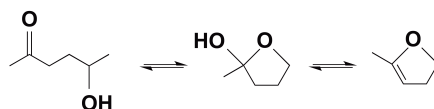
produced from the substituted dihydrofuran chemistry, thereby affecting the average oxidation state of the SOA.

3.2 Introduction

Alkanes are important constituents of gasoline and vehicle emissions (Hoekman, 1992; Zielinska et al., 1996; Kirchstetter et al., 1999; Gentner et al. 2012; Jathar et al., 2013), accounting for ~50% of volatile organic compounds (VOCs) in the urban atmosphere (Fraser et al., 1997; Schauer et al., 1999 and 2002). The unresolved complex mixture (UCM) of organics, which is potentially a significant source of secondary organic aerosol (SOA) formation in the atmosphere, has recently been shown to comprise many long-chain alkanes (Isaacman et al., 2012), which are expected to contribute SOA formation (Robinson et al., 2007).

Laboratory chamber investigations of SOA formation from long-chain alkanes (Lim and Ziemann, 2005, 2009 a, b, c; Presto et al., 2009, 2010; Miracolo et al., 2010, 2011; Craven et al., 2012; Lambe et al., 2012; Tkacik et al., 2012; Yee et al., 2012; Loza et al., 2013) provide a framework for understanding chemical mechanisms and determination of SOA yields (Jordan et al., 2008; Aumont et al., 2012 and 2013; Cappa et al., 2012; Zhang and Seinfeld, 2013). Particle-phase products from OH oxidation of alkanes contain a number of functional groups: organonitrate ($-\text{ONO}_2$), hydroxyl ($-\text{OH}$), carbonyl ($-\text{C}=\text{O}$), ester ($-\text{C}(\text{O})\text{O}-$), and hydroperoxide ($-\text{OOH}$). Ambient measurements of organic aerosol composition have shown, in addition, that the carboxylic acid functional group ($-\text{C}(\text{O})\text{OH}$) is closely associated with products from fossil fuel combustion sources (Liu et al., 2011; Russell et al., 2011), of which alkanes are a principal component.

Atmospheric alkanes react in daytime exclusively with OH, producing an array of peroxy radicals (RO₂). In the presence of sufficient NO, the alkoxy radical (RO) is the key product of the subsequent RO₂ reaction with NO. RONO₂ is also produced, with a branching ratio of 0.1 – 0.3 (Arey et al., 2001). For alkanes with carbon number ≥ 5, the 1, 5-H shift isomerization is the dominant reaction pathway for RO, producing a δ-hydroxycarbonyl, the primary fate of which is reaction with OH (Jenkin et al., 2003; Saunders et al., 2003; Bloss et al., 2005), with a lifetime of ~ 11.5 h at room temperature and a typical ambient OH concentration of 1 × 10⁶ molecules cm⁻³. One particular δ-hydroxycarbonyl, 5-hydroxy-2-pentanone, was found to cyclize to form the cyclic hemiacetal. The cyclic hemiacetal can subsequently lose water to form 4, 5-dihydro-2-methylfuran, with an overall lifetime as short as ~ 1.1 h at 298 K (Cavalli et al., 2000; Martin et al., 2002). The presence of water vapor can, in principle, serve to convert the 4, 5-dihydro-2-methylfuran back to 5-hydroxy-2-pentanone, leading to an equilibrium between these two species within several hours (Martin et al., 2002; Baker et al., 2005; Holt et al., 2005; Reisen et al., 2005):



This conversion to 4, 5-dihydro-2-methylfuran is not unique to 5-hydroxy-2-pentanone but also occurs for other C₅-C₁₇ δ-hydroxycarbonyls (Lim and Ziemann, 2005, 2009 a, b, c), at a rate that increases with the length of the carbon chain (Holt et al., 2005; Ziemann and Atkinson, 2012). The substituted dihydrofuran is highly reactive towards OH, O₃, and NO₃ in the gas phase, owing to the presence of a C=C double bond. For typical

ambient concentrations of OH, O₃, and NO₃, i.e., 2×10^6 molecules cm⁻³ (12 h average), 30 ppb (24 h average), and 5×10^8 molecules cm⁻³ (12 h average), respectively, the lifetimes of the substituted dihydrofuran with respect to reactions with these oxidants in the gas phase are 1.3 h, 7 min, and 24 s, respectively (Martin et al., 2002; Ziemann and Atkinson, 2012). Based on these estimates, ozonolysis of substituted dihydrofurans may dominate OH oxidation during daytime in the urban atmosphere.

SOA formation from long-chain alkanes involves multiple generations of OH oxidation that include functionalization (O-atom addition in forms of a variety of moieties) and fragmentation of the parent carbon backbone. These two routes can eventually lead to highly oxygenated fragments that partition into the particle phase. Two recent modeling studies of C₁₂ alkanes suggest that particle-phase chemistry might play a potentially important role in the chemical composition of alkane SOA; this is inferred from the fact that simulations driven solely by gas-phase chemistry can successfully reproduce the chamber measured SOA yield, but these fail to replicate the observed particulate O:C and H:C ratios in the absence of a particle-phase chemistry channel (Cappa et al., 2012; Zhang and Seinfeld, 2013). The extent to which particle-phase chemistry is important in alkane SOA formation has not been clearly established.

We address here the heterogeneous formation of substituted dihydrofurans and their subsequent gas-phase reaction with ozone in SOA formation from alkanes. We present the results of a series of chamber dodecane photooxidation experiments under two reaction regimes, i.e., “OH-dominant”, in which over 70% of substituted dihydrofurans are oxidized by OH, vs. “O₃-dominant”, in which 80% – 90% of substituted dihydrofurans react with O₃. Gas-phase products that are unique to the substituted

dihydrofuran chemistry are identified. The impact of ozonolysis of substituted dihydrofurans on the particle-phase product distribution from the photooxidation of dodecane is investigated by comparing intensities of certain ions that are indicative of ozonolysis chemistry. We also develop a detailed mechanism with the incorporation of substituted dihydrofuran chemistry and simulate the effect of this reaction channel on SOA yield from the photooxidation of dodecane.

3.3 Experimental

Experiments were conducted in the new Caltech dual 24-m³ Environmental Chamber, in which the temperature (T) and relative humidity (RH) are automatically controlled. Prior to each experiment, the Teflon chambers were flushed with clean, dry air for 24 h until the particle number concentration $< 10 \text{ cm}^{-3}$ and volume concentration $< 0.01 \mu\text{m}^3 \text{ cm}^{-3}$. Seed aerosol was injected into the chamber by atomizing 0.015 M aqueous ammonium sulfate solution to provide sufficient surface area for the partition of semi-volatile products. Hydrogen peroxide (H₂O₂) was used for the OH source by evaporating 85 and 226 μL of 50% wt aqueous solution into the chamber with 5 L min^{-1} of purified air for ~ 110 min, resulting in an approximate starting H₂O₂ concentration of 1.5 and 4 ppm, respectively, under high- and low-NO_x conditions. The 4 ppm H₂O₂ concentration employed in low-NO_x experiments creates a RO₂+HO₂ dominant reaction regime. We replaced H₂O₂ with nitrous acid (HONO) as the OH source for one experiment in order to minimize the formation of ozone. HONO was prepared by dropwise addition of 15 mL of 1 wt% NaNO₂ into 30 mL of 10 wt% H₂SO₄ in a glass bulb and introduced into the chambers with 5 L min^{-1} of purified air for ~ 40 min. To minimize the vapor phase wall

loss along the injection line, 60 μL of dodecane (Sigma-Aldrich, 98% purity) was injected into a glass bulb, which was connected directly into the Teflon chamber via a 1/4" I.D. Swagelock to NPT fitting located on a Teflon plate. Heated 5 L min^{-1} of purified air flowed through the glass bulb into the chamber for 30 min, introducing ~ 200 ppb dodecane into the chamber. After ~ 1 h mixing, photooxidation was initiated by irradiating the chamber with black lights with output wavelength ranging from 300 to 400 nm.

Experiments were carried out under conditions in which the peroxy radicals formed from the initial OH reaction with dodecane react either essentially exclusively with NO (so-called high- NO_x) (Exp. #1, #2, #3, #4, and #5) or essentially exclusively with HO_2 (so-called low- NO_x) (Exp. #6, #7, and #8). For each condition, "O₃-dominant" vs. "OH-dominant" environments were generated by varying the OH source, initial NO, NO₂, and O₃ concentrations, and the additional NO injection rate during the irradiation period (Table 1). The ozonolysis vs. OH oxidation of substituted dihydrofuran is calculated to be equally competitive when the ratio of O₃ to OH concentration is $6.3 \times 10^4 : 1$ (approximately 2.6 ppb O₃ vs. 1.0×10^6 molecules cm^{-3} OH). Under low- NO_x conditions, NO, NO₂, NO_x, and O₃ were below detection limits, and no ozone formation was observed over the course of 20 h experiments. OH-oxidation of dihydrofuran is dominant with average OH concentrations of 1.8×10^6 and 1.5×10^6 molecules cm^{-3} , respectively, in Exp. #6 and #8. OH concentration is calculated by optimal fitting of the exponential decay of the GC-FID measured dodecane temporal profile. In order to evaluate the effect of the ozonolysis of dihydrofuran chemistry on the dodecane SOA formation under low- NO_x conditions, additional ~ 30 ppb of ozone was injected into the chamber before the

onset of irradiation (Exp. #7). Under high-NO_x conditions, HONO was used as the OH source for the “OH-dominant” environment (Exp. #1). Double HONO injection was carried out in order to fully consume dodecane (before the onset and after ~ 3 h of irradiation). The average OH concentration is ~ 5.0 × 10⁶ molecules cm⁻³, whereas O₃ peaks at 8 ppb after 60 min of photooxidation and rapidly decays to ~ 0 ppb within 2 h. In this case, > 73% of dihydrofuran is oxidized by OH over the course of Exp. #1. An “O₃-dominant” environment was generated by injecting NO (38 – 287 ppb) and NO₂ (12 – 156 ppb) before the onset of irradiation. Continuous NO injection with a certain flow rate (20 – 100 ppb h⁻¹) was conducted over the course of experiments to reach a sufficient amount of O₃ and to maintain high-NO_x levels. Under experimental conditions in Exp. #2, #3, #4, and #5, the average OH concentrations are calculated to be 1.7 × 10⁶, 2.0 × 10⁶, 1.4 × 10⁶, and 1.3 × 10⁶ molecules cm⁻³, respectively, and the maximum O₃ mixing ratios are 20, 380, 150, and 250 ppb, respectively. As a result, ~ 82%, ~ 96%, ~ 97%, and ~ 98% of dihydrofuran reacts with O₃ when dihydrofuran peaks after ~ 3 h of photooxidation. High humidity experiments were also carried out as a set of control experiments (Exp. #4, #5, and #8) addressing the role of water vapor in the heterogeneous interconversion between δ-hydroxycarbonyls and substituted dihydrofurans.

A suite of instruments was used to investigate gas- and particle-phase chemistry. T, RH, NO, NO_x, and O₃ were continuously monitored. Dodecane concentration was monitored by taking hourly samples at ~ 0.13 L min⁻¹ of chamber air for 3 min onto a Tenax adsorbent, which was loaded into the inlet of a gas chromatograph with flame ionization detection (GC/FID, Agilent 6890N), desorbed at 275 °C for 13 min, and then

injected onto an HP-5 column (15 m × 0.53 mm ID × 1.5 μm thickness, Hewlett-Packard) held at 30 °C. The oven was ramped from 30 to 275°C at 10 °C min⁻¹ and held at 275 °C for 5 min. The retention time for dodecane is ~ 27.5 min. The gas-phase species were monitored using a custom-modified Varian 1200 triple-quadrupole chemical ionization mass spectrometer (CIMS) (Crouse et al., 2006; Paulot et al., 2009). In negative mode operation, CF₃O⁻ was used as the reagent ion to cluster with an analyte such as hydroperoxide or acid [R], producing [R·CF₃O]⁻ or *m/z* [M+85]⁻, where M is the molecular weight of the analyte. For more strongly acidic species [H·X], the transfer product, [H·X·F]⁻ or *m/z* [M+19]⁻, is formed during ionization. Carboxylic acids tend to have contributions to both the transfer and cluster product, in which case the overall signal of a compound is considered as the sum of the two product signals. In positive mode operation, an analyte [R] can undergo proton transfer reaction, producing an ion in the form of [R·H]⁺, and/or react with *n* positively charged water clusters to form a cluster in the form of [(H₂O)_n·R·H]⁺. Positive mode is employed in this study for tracking less polar compounds, such as the substituted dihydrofuran.

Particle size distribution and number concentration were measured by a cylindrical differential mobility analyzer (DMA; TSI Model 3081) coupled to a condensation particle counter (TSI Model 3010). Real-time particle mass spectra were collected continuously by an Aerodyne High Resolution Time-of-Flight Aerosol Mass Spectrometer (DeCarlo et al., 2006; Canagaratna et al., 2007). The AMS switched once every minute between the high resolution “W-mode” and the lower resolution, higher sensitivity “V-mode”. The V-mode was utilized for quantification, as the higher *m/z*

values exhibit a more favorable signal-to-noise ratio. The W-mode was used for ion identification and clarification.

3.4 Chemical Mechanism

A photochemical mechanism was used to simulate the gas-phase photochemistry of NO_x , HO_x , and O_3 corresponding to the experimental conditions. Photolysis rate constants are calculated using the irradiance spectrum measured for the chamber UV lights, and absorption cross sections and quantum yields from Sander et al. (2011).

The kinetic scheme for the gas-phase OH-initiated oxidation of dodecane and the further OH oxidation of multi-generational products was developed primarily based on the MCMv3.2 (<http://mcm.leeds.ac.uk/MCM/>). Products identified in Lim and Ziemann (2005; 2009 a, b, c) that are not in MCM are also included here. The kinetic scheme was incorporated in the photochemical model to estimate yields of particle-phase products generated in the chamber. A simplified flow chart illustrating the mechanism for the multi-generation gas-phase chemistry is shown in Fig. 1 (a) & (b). In general, the OH-initiated oxidation of dodecane leads to RO_2 , the fate of which controls the distribution of further generation products. When sufficient NO_x is present (the concentration of NO , i.e., > 5 ppb, is at least four orders of magnitude higher than RO_2 , i.e., $< 5 \times 10^7$ molecules cm^{-3}), over 99% of RO_2 reacts with NO , leading to RO or alkyl nitrate (RONO_2). The branching ratios for the production of RO and RONO_2 are obtained from Jordan et al. (2008). RO can isomerize through a 1,5 H-atom shift to a δ -hydroxyalkyl radical, react with O_2 , or undergo fragmentation. The alkyl nitrate formed either undergoes photolysis or reacts with OH via H-atom abstraction from a C-atom or reacts

with OH via H-atom abstraction from a C-atom with a $-\text{ONO}_2$ group attached to produce a $-\text{C}=\text{O}$ group. The δ -hydroxyalkyl radical reacts with O_2 and then NO and undergoes another isomerization to produce a δ -hydroxycarbonyl. At sufficiently low NO_x concentrations, the simulated HO_2 concentration ($\sim 1 \times 10^{10}$ molecules cm^{-3}) is ~ 20 times higher than RO_2 ($\sim 5 \times 10^8$ molecules cm^{-3}). $\text{RO}_2 + \text{HO}_2$ dominates the fate of RO_2 , producing a hydroperoxide (ROOH). Further oxidation of ROOH involves the photolysis of the $-\text{OOH}$ group, H-atom abstraction, and the OH oxidation of a C-atom with a $-\text{OOH}$ group attached to produce a $-\text{C}=\text{O}$ group. Products through eight generations of oxidation are included in the mechanism, although only the formation of the first three generations of products is illustrated in Fig. 1. The reaction rate constants are obtained from MCM v3.2. In the absence of specific data, the photolysis rate constants of the $-\text{OOH}$, $-\text{C}=\text{O}$, and $-\text{ONO}_2$ groups on the carbon backbone are assumed to be the same as those for methyl peroxide (CH_3OOH), 2-butanol ($\text{C}_3\text{H}_7\text{CHO}$), and *n*-propyl nitrate (*n*- CH_3ONO_2).

Cyclization and subsequent dehydration of δ -hydroxycarbonyl to substituted dihydrofuran is a heterogeneous process, including 1) gas-phase diffusion and reactive uptake of δ -hydroxycarbonyl to particles, 2) cyclization of δ -hydroxycarbonyl to cyclic hemiacetal, and 3) dehydration of cyclic hemiacetal to substituted dihydrofuran. (Atkinson et al., 2008; Lim and Ziemann, 2009 c). The extent of this heterogeneous process occurring on/in particles has been predicted to predominate over chamber walls (Lim and Ziemann, 2009 c). In this study, we represent the individual steps of the conversion of δ -hydroxycarbonyl to substituted dihydrofuran by an overall first-order decay rate of $3 \times 10^{-3} \text{ s}^{-1}$. This value is estimated by monitoring the decay of 5-hydroxy-

2-pentanone using CIMS in the presence of $20 \mu\text{m}^3 \text{cm}^{-3}$ $(\text{NH}_4)\text{SO}_4/\text{H}_2\text{SO}_4$ seeds at 3% RH. This assumed decay rate is consistent with those measured in previous studies (Cavalli et al., 2000; Martin et al., 2002, Holt et al., 2005; Lim and Ziemann, 2009 c). The equilibrium constant K ($K = [4, 5\text{-dihydro-2-methylfuran}]/[5\text{-hydroxy-2-pentanone}]$) is estimated to be ~ 7 at 3% RH from the CIMS measured 5-hydroxy-2-pentanone decay curve, based on the assumption that the decrease in the 5-hydroxy-2-pentanone concentration is accompanied by stoichiometric formation of the corresponding 4, 5-dihydro-2-methylfuran. Note that although the proportion of the heterogeneous conversion occurring on the chamber walls is unknown, the potential contribution of chamber walls to the particle-phase production of substituted dihydrofuran has been accounted for by employing the measured overall conversion rate in the mechanism.

The substituted dihydrofuran formed evaporates rapidly due to its high volatility and undergoes reactions with OH, O₃, and NO₃ in the gas phase (Ziemann and Atkinson, 2012), with reaction rate constants of 2.18×10^{-10} , $3.49 \times 10^{-15} \text{ cm}^3 \text{ molecule}^{-1} \text{ s}^{-1}$, and $1.68 \times 10^{-10} \text{ cm}^3 \text{ molecule}^{-1} \text{ s}^{-1}$, respectively (Martin et al., 2002; Atkinson et al., 2008). Reaction with NO₃ is not important under the conditions of this study. In general, the OH addition to an alkyl-substituted dihydrofuran produces either an alkyl-substituted tetrahydrofuran or a carbonyl ester, see Fig. 2 (a) (Martin et al., 2002, Lim and Ziemann, 2005, 2009 a, b, c, Jordan et al., 2008). The mechanism for the O₃ reaction with an alkyl-substituted dihydrofuran, as shown in Fig. 2 (b), was developed following the ozonolysis of 4,5-dihydro-2-methylfuran (Martin et al., 2002), alkyl vinyl ethers (Thiault et al., 2002; Klotz et al., 2004; Sadezky et al., 2006) and monoterpenes (Jenkin et al., 2000; Jenkin, 2004). The reaction of alkyl-substituted dihydrofuran with O₃ involves the

addition of O₃ to the C=C double bond to produce an energy-rich primary ozonide, which rapidly decomposes into two excited Criegee intermediates. The energy-rich Criegee intermediates are either collisionally stabilized, or decompose to yield OH (or OH+CO) and an additional α -carbonyl peroxy radical (or peroxy radical). The resulting α -carbonyl peroxy radical (or peroxy radical) can undergo the well-established reactions available for peroxy radicals, see Fig. 2 (b). The stabilized Criegee intermediates are predicted to react primarily with water (Martin et al., 2002), leading to 3-propoxy-nonanal (C₁₂H₂₂O₃) and 3-propoxy-nonanoic acid (C₁₂H₂₂O₃), with molar yields of 90% and 10%, respectively. The total yield of 3-propoxy-nonanal is predicted to be 18%, which is close to the yield of succinaldehydic acid methyl ester (23%) from the ozonolysis of 4,5-dihydro-2-methylfuran (Martin et al., 2002).

We consider SOA formation by dodecane photooxidation, including heterogeneous formation of substituted dihydrofuran and its subsequent reaction with OH/O₃. Gas-particle equilibrium partitioning of semi-volatile products is assumed. The branching ratio and vapor pressure ($P_{L,i}^0$ /atm) at 300 K (predicted by SIMPOL.1 (Pankow and Asher, 2008)) of each product from the OH/O₃ initiated oxidation of alkyl-substituted dihydrofuran are labeled in Fig. 2. The corresponding effective saturation concentrations ($C^* = 10^6 P_{L,i}^0 \gamma_i \overline{M}_w / RT$) range from $7.0 \times 10^1 \mu\text{g m}^{-3}$ to $4.7 \times 10^4 \mu\text{g m}^{-3}$, for which approximately 0.1% ~ 41.7%, respectively, of these products are in the particle phase at an organic loading of $\sim 50 \mu\text{g/m}^3$. Compounds with the lowest volatility ($\sim 10^{-9}$ atm) are produced mostly from the RO₂ + NO \rightarrow RONO₂ reaction, the branching ratio of which ranges from 0.11 to 0.28. As a result, the total amount of organic nitrates in the particle-phase is relatively high, see Fig. 9 (C). Compounds generated from the RO₂ + NO \rightarrow RO

+ NO₂ reaction have higher molar yields (0.72 – 0.89). But they are too volatile ($\sim 10^{-6}$ – 10^{-7} atm) to partition significantly into the particle phase. The stabilized Criegee intermediate reaction with water is predicted to predominate over reaction with NO/NO₂ at RH > 3%. The ester containing carboxylic acid (C₁₂H₂₂O₄) is predicted to be present in the particle phase due to its sufficiently low volatility ($\sim 10^{-8}$ atm), see Fig. 9 (C).

3.5 Results and Discussion

In this section, we seek to evaluate the impact of substituted dihydrofuran chemistry on dodecane SOA formation as follows: 1) Predict the yield of alkyl-substituted dihydrofuran from the photooxidation of dodecane under both high- and low-NO_x conditions, and the fraction of alkyl-substituted dihydrofuran that reacts with O₃ in the “O₃-dominant” regime (Section 4.1); 2) Measure the time-dependent evolution of cyclic hemiacetal and alkyl-substituted dihydrofuran at 3%, 10%, 20% and 50% RH (Section 4.2); 3) Propose gas-phase products that are unique to dihydrofuran chemistry based on the CIMS speciation (Section 4.3); 4) Compare particle-phase chemical composition under “OH-dominant” vs. “O₃-dominant” environments via identifying AMS measured ions representative of dihydrofuran oxidation products (Section 4.4); and 5) Estimate the change in SOA yield and elemental composition by incorporating the complete substituted-dihydrofuran formation and removal pathways into the dodecane SOA prediction model (Section 4.5).

3.5.1 Predicted substituted dihydrofuran formation and reaction with ozone in the dodecane system

To what extent is the formation of substituted dihydrofuran and its subsequent chemistry important in the formation of dodecane SOA? A mechanism simulation was conducted, with initial conditions similar to those employed in the chamber (Table 1), i.e., 200 ppb dodecane, 1.5 ppm H₂O₂, 100 ppb O₃, and 100 ppb + 30 ppb h⁻¹ NO for high-NO_x conditions and 200 ppb dodecane, 4 ppm H₂O₂, 100 ppb O₃, and 0 ppb NO_x for low-NO_x conditions, respectively. Figure 3 shows the predicted mass distribution of δ -hydroxycarbonyl, alkyl-substituted dihydrofuran, together with other products of the same generation. δ -hydroxycarbonyl is predicted to account for > 90% total organic mass of first-generation products under high-NO_x conditions, see Fig. 3 A (H), but < 5% to the total organic mass of the third-generation products under low-NO_x conditions, see Fig. 3 A (L). Inclusion of the heterogeneous conversion pathway from δ -hydroxycarbonyl to alkyl-substituted dihydrofuran is predicted to result in a rapid consumption of δ -hydroxycarbonyl under dry conditions, as opposed to a slow decay from OH oxidation. Alkyl-substituted dihydrofuran accounts for up to 70% of the decay of δ -hydroxycarbonyl, as shown in Fig. 3 B (H). As discussed earlier, an ozonolysis dominant environment occurs for O₃ > 3 ppb at a typical OH concentration of 1.0×10^6 molecules cm⁻³. In the high-NO_x simulation case, ozone is predicted to lead to 82% - 98% of the total alkyl-substituted dihydrofuran loss over the course of photooxidation, see Fig. 3 D (H).

The alkyl-substituted dihydrofuran is not the only product that contains a dihydrofuran structure in the dodecane photooxidation system. The first generation product, 3-dodecyl nitrate under high-NO_x conditions is an example. Three pathways exist that could produce semi-volatile compounds containing a dihydrofuran structure from the further photochemical reaction of 3-dodecyl nitrate: 1) photolysis of the –ONO₂ group leads to an alkyl-substituted dihydrofuran; 2) abstraction of an H-atom by OH potentially leads to an organonitrate-substituted dihydrofuran; and 3) H-atom abstraction from a C-atom with the –ONO₂ functional group attached and further H-atom abstraction from a C-atom potentially leads to a carbonyl-substituted dihydrofuran. It is worth noting that the gas-phase ozonolysis of alkyl-substituted dihydrofuran under high-NO_x conditions contributes to most of the ozonolysis reactions because the alkyl-substituted dihydrofuran is a major first-generation product, as shown in Fig. 3 B (H).

3.5.2 Formation of cyclic hemiacetals and alkyl-substituted dihydrofuran

CIMS measurement at (+) m/z 183 in positive mode represents the ion C₁₂H₂₂O·H⁺ generated from the proton transfer reaction with alkyl-substituted dihydrofuran ($M_w = 182$). An additional source of (+) m/z 183 is the proton transfer reaction followed by dehydration of hydroxyl dodecanone ($M_w = 200$), which is also detected as a fluoride cluster product at (–) m/z 285 (C₁₂H₂₄O₂·CF₃O[–]) in negative mode. Figure 4 shows temporal profiles of (+) m/z 183 and (–) m/z 285 monitored under both high- and low-NO_x conditions (Exp. 2 vs. Exp. 6). The (+) m/z 183 ion was detected in each of the two experiments, but with distinct time-dependent patterns. Under high NO_x-conditions, (+) m/z 183 peaks during first 3 h of irradiation, indicating fast formation of alkyl-substituted dihydrofuran, and decays during the next 15 h photooxidation. Under low-NO_x

conditions, however, the (+) m/z 183 signal eventually reaches a plateau, which is more consistent with the pattern of (-) m/z 285. This behavior is consistent with the mechanism prediction that the alkyl-substituted dihydrofuran is formed in significant amounts only under high-NO_x conditions (Fig. 3 B (H)). An alternative explanation for the temporal profiles of (+) m/z 183 under low-NO_x conditions is that this ion is formed by dehydration of the cyclic hemiacetal following protonation in CIMS. The occurrence of a plateau could be indicative of an absence of dehydration in the particle phase due to the lack of an acid catalyst (no HNO₃ formation from NO₂+OH reaction as in the high NO_x cases). However, based on the model prediction, cyclic hemiacetal is not likely to accumulate since the formation of its precursor, δ -hydroxycarbonyl, is a minor pathway when the RO₂+HO₂ reaction is dominant and the photolysis of the resulting peroxide is not important.

The AMS measured m/z 183 (C₁₂H₂₃O⁺) is the major characteristic ion for cyclic hemiacetal. This ion is produced by the neutral loss of OH ($M_w = 17$) from the 2-position in the cyclic hemiacetal ($M_w = 200$) during electron ionization (Gong et al., 2005; Lim and Ziemann, 2009 c). In addition, the C₁₂H₂₃O⁺ ion is suggested to be the characteristic fragment of carbonyl-hydroperoxide-derived peroxyhemiacetal (Yee et al., 2012). The temporal profiles of the C₁₂H₂₃O⁺ ion under both high- and low-NO_x conditions (Exp. 2 vs. Exp. 6) exhibit distinct growth patterns (Fig. 4). Under high-NO_x conditions, the C₁₂H₂₃O⁺ ion signal increases rapidly to a maximum during the first 2 h and decays over the next ~ 14 h. The temporal behavior of the C₁₂H₂₃O⁺ ion is a result of its rapid formation, i.e., uptake of δ -hydroxycarbonyl onto particles and subsequent cyclization, and relatively slower removal, i.e., dehydration. Under low-NO_x conditions, the C₁₂H₂₃O⁺

ion increases over the course of a 20 h experiment because of the accumulative formation of peroxyhemiacetal. During the first 3 h of irradiation under low-NO_x conditions, the organic loading is below the AMS detection limit so that the C₁₂H₂₃O⁺ ion signal does not appear in Fig. 4 during this period. The C₁₂H₂₃O⁺ ion signal under low-NO_x conditions therefore potentially represents peroxyhemiacetal, since the formation of peroxides is the major reaction pathway in the RO₂+HO₂ dominant regime. This is again consistent with the mechanism prediction that the formation of alkyl-substituted dihydrofuran is unimportant under low-NO_x conditions (Fig. 3 B (L)).

Figure 5 shows temporal profiles of the ion C₁₂H₂₂O·H⁺ detected by CIMS and the ion C₁₂H₂₃O⁺ detected by AMS in the presence of NO_x under varying RH. In general, the AMS ion C₁₂H₂₃O⁺ peaks ~ 3 h earlier than the CIMS ion C₁₂H₂₂O·H⁺. The decay rates of AMS ion C₁₂H₂₃O⁺, which is calculated by assuming first-order kinetics, are 4.02 × 10⁻³, 3.06 × 10⁻³, 1.71 × 10⁻³, and 1.37 × 10⁻³ s⁻¹, respectively, at RH of 3%, 10%, 20%, and 50%. Aerosol water content could slow down the formation and removal rate of AMS ion C₁₂H₂₃O⁺, mainly because: 1) water could accelerate the hydration rate, thus changing the equilibrium coefficient of the interconversion between cyclic hemiacetal and dihydrofuran; and 2) the addition of water might neutralize the particle-phase acid (e.g., HNO₃) which is thought to catalyze the cyclization of δ-hydroxycarbonyl to cyclic hemiacetal (Lim and Ziemann, 2009 c). The decay rates of AMS ion C₁₂H₂₃O⁺ are within the same order of magnitude of that measured for 5-hydroxy-2-pentanone at 3% RH, indicating that the dehydration of cyclic hemiacetal is the rate-limiting step in the overall heterogeneous conversion process. Water vapor influences CIMS sensitivity to certain compounds in negative mode by clustering with the reagent ion CF₃O⁻ to form

$[\text{H}_2\text{O}\cdot\text{CF}_3\text{O}]^-$. The decreasing intensity of the ion $\text{C}_{12}\text{H}_{22}\text{O}\cdot\text{H}^+$ as RH increases is likely indicative of this effect.

3.5.3 Products from alkyl-substituted dihydrofuran oxidation

Products unique to the alkyl-substituted dihydrofuran oxidation chemistry have been proposed based on CIMS measured m/z signals, see Table 2 for chemical structures. Authentic standards are not commercially available for these products. Compounds from the dodecane photooxidation route that share the same m/z signal with alkyl-substituted dihydrofuran oxidation products are also presented in Table 2. The CIMS signal ($-$) m/z 346 is composed of 2-nitroso-2-alkyl-3-hydroxyl-5-heptyl-tetrahydrofuran and 2-carbonyl-5-hydroxyl-2-dodecyl-nitrate. The latter is a 3rd generation product resulting from the further oxidation of dodecyl nitrate. The branching ratio for the addition of an $-\text{ONO}_2$ group is much lower than that for the formation of the RO radical, so that the interference of 2-carbonyl-5-hydroxyl-2-dodecyl-nitrate in the ($-$) m/z 346 signal can be neglected. The CIMS signal ($-$) m/z 299 represents 3-propoxy-nonanal, which is a primary product from both OH-oxidation and ozonolysis of alkyl-substituted dihydrofuran, and 8-hydroxy-3,5-dodecanedione, which is produced from the further oxidation of dodecyl nitrate. As discussed earlier, the formation and transformation of dodecyl nitrate is predicted to be a minor pathway so that the ($-$) m/z 299 is dominated by 3-propoxy-nonanal.

A distinct feature of proposed products from the dihydrofuran oxidation by either OH or O_3 is the formation of an ester group ($-\text{C}(\text{O})\text{O}-$) or an ether group ($-\text{O}-$), both of which can not be accessed from photochemical reaction pathways initiated by the OH

attack on the aliphatic hydrocarbon. The OH oxidation channel leads solely to the formation of tetrahydrofuran and carbonyl ester. In the ozonolysis pathway, on the other hand, the reaction of stabilized Criegee intermediates with water produces one ester group containing aldehyde (3-propoxy-nonanal) and carboxylic acid (3-propoxy-nonanoic acid); see proposed structures in Table 2. From the intact C₁₂ skeleton and highly oxygenated nature, these two products are consistent with CIMS signals in (-) *m/z* 299 and (-) *m/z* 249 and 315 in negative mode with little interference from other products.

Figure 6 shows the temporal profiles of (-) *m/z* 299, as well as (-) *m/z* 249 and 315, under “O₃-limiting” (Exp. #2) and “O₃-rich” (Exp. #3) conditions. The decay rates of their precursor (+) *m/z* 183, as calculated by assuming first-order kinetics, are $1.19 \times 10^{-5} \text{ s}^{-1}$ and $1.44 \times 10^{-5} \text{ s}^{-1}$, respectively. Under “O₃-rich” conditions, both species increase and eventually level off. When O₃ reaction is less competitive, the CIMS signals start to decrease after 10 h photooxidation. Note that these three ions were also detected under low-NO_x conditions. No significant increase in their signals was observed in the “O₃-rich” environment (Exp. #7), compared with the “O₃-limiting” case (Exp. #6). If they were assigned the same chemical structures as those proposed under high-NO_x conditions, their growth pattern would suggest a minor formation of their precursor alkyl-substituted dihydrofuran. This can be attributed to the slowdown or even termination of the dehydration of cyclic hemiacetal in the absence of strong acid catalysis (Atkinson et al., 2008; Lim and Ziemann, 2009 c).

3.5.4 Ozonolysis vs. OH-oxidation

Carboxylic acids produce significant signals at m/z 60 and 73, specifically $C_2H_4O_2^+$ and $C_3H_5O_2^+$, in the AMS measurement (Aiken et al., 2008). The formation of these two ions, as a function of the time-dependent decay of the ion $C_{12}H_{23}O^+$, is shown under different RH conditions in Fig. 7. The largest slope of either $\Delta C_2H_4O_2^+ / \Delta C_{12}H_{23}O^+$ or $\Delta C_3H_5O_2^+ / \Delta C_{12}H_{23}O^+$ is associated with the highest RH, i.e., 50%. On the contrary, the production of $C_2H_4O_2^+$ and $C_3H_5O_2^+$ is not significant under dry conditions. Also, the changes in slopes along with changes in RH values are consistent for both ions. This indicates that the formation of the carboxylic acid functional group detected in particles is associated with the water vapor concentration in the gas phase, consistent with the reaction of the stabilized Criegee intermediates with water in the substituted dihydrofuran oxidation system.

Two dominant oxygen-containing ions, m/z 44 (mostly CO_2^+) and m/z 43 ($C_3H_7^+$ and $C_2H_3O^+$), have been widely used to characterize organic aerosol evolution in chamber and field observations. Previous studies have shown that CO_2^+ results mostly from the thermal decarboxylation of an organic acid group (Alfarra, 2004). The f_{44} (ratio of m/z 44, mostly CO_2^+ , to total signal in the component mass spectrum) axis is also considered to be an indicator of photochemical aging (Alfarra et al., 2004; Aiken et al., 2008; Kleinman et al., 2008). It has been found that increasing OH exposure increases f_{44} and decreases f_{43} (ratio of m/z 43, mostly $C_2H_3O^+$, to total signal in the component mass spectrum) for SOA generated from gas-phase alkanes (Lambe et al., 2011). The $C_2H_3O^+$ ion at m/z 43 is assumed predominantly due to non-acid oxygenates, such as saturated carbonyl groups (Ng et al., 2011). The evolution of dodecane SOA from four experiments

(Table 1), characterized by different OH and O₃ exposure, and different RH levels, is shown in $f_{\text{CO}_2^+} - f_{\text{C}_2\text{H}_3\text{O}^+}$ space in Fig. 8. Overall, high-NO_x dodecane SOA lies to the lower left of the triangular region derived for ambient SOA. The relatively high organic loading (~ 200 ppb dodecane) employed in this study favors partitioning of less oxidized species, which would remain in the gas phase under atmospheric conditions. For each experiment, $f_{\text{CO}_2^+}$ decreases and $f_{\text{C}_2\text{H}_3\text{O}^+}$ increases with increasing SOA at the beginning of irradiation. After several hours photooxidation, the trends reverse, resulting in increasing $f_{\text{CO}_2^+}$ and decreasing $f_{\text{C}_2\text{H}_3\text{O}^+}$. Curvature in $f_{\text{CO}_2^+} - f_{\text{C}_2\text{H}_3\text{O}^+}$ space has been also observed in other chamber/flow reactor studies (Kroll et al., 2009; Ng et al., 2010; Chhabra et al., 2011; Lee et al., 2011; Lambe et al., 2011). When the organic loading is small, only the highly oxygenated and least volatile species partition to the particle phase. As particles grow, more volatile and less oxidized species are able to participate in equilibrium partitioning, leading to a decrease in $f_{\text{CO}_2^+}$. Progressive oxidation of semi-volatile products in the gas phase eventually leads to multi-functionalized species contributing to the increase of $f_{\text{CO}_2^+}$.

Both O₃- and OH- initiated oxidation of substituted dihydrofuran lead to the formation of $f_{\text{CO}_2^+}$, via the thermal decarboxylation of an organic acid group and photochemical aging, respectively. The contribution of each reaction pathway to the intensity of $f_{\text{CO}_2^+}$ can be evaluated based on the $f_{\text{CO}_2^+} - f_{\text{C}_2\text{H}_3\text{O}^+}$ plot. As discussed in Section 2.1, Exp. #1 is designed as an “OH-dominant” case, in which it is estimated that > 73% of the dihydrofuran reacts with OH over the course of the experiment. Exp. #3, #4, and #5 were designed to be “O₃-dominant” at 10%, 20%, and 50% RH, respectively.

Approximately 96 %, 97 %, and 98 % of substituted dihydrofuran is predicted to react with O₃ when it peaks after ~ 3 h of photooxidation in Exp. #3, #4, and #5, respectively. As shown in Fig. 8, the intensities of $f_{CO_2^+}$ in Exp #1, #3, #4, and #5 are 0.019, 0.020, 0.028, and 0.030, respectively, at the same OH exposure, i.e., 2×10^7 molecules cm⁻³ h. The increase in $f_{CO_2^+}$ intensities results from the increasing O₃ and RH levels in these four experiments. Overall, Exp. #1 exhibits the least intensity of $f_{CO_2^+}$ at the end of the experiment, i.e., 0.017, although the total OH exposure is the highest, i.e., 3.8×10^7 molecules cm⁻³ h. The total OH exposures for Exp. #3, 4, and 5 are 3.5×10^7 , 2.2×10^7 , and 2.1×10^7 molecules cm⁻³ h, respectively, which are less than that in Exp. #1. However, the intensities of $f_{CO_2^+}$ for these three experiments are 35% – 82% higher than that in Exp. #1 at the end of experiments. In addition, the intensity of $f_{CO_2^+}$ increases along with increasing RH and O₃ exposure for these three experiments, varying from 0.023 to 0.031. The highest $f_{CO_2^+}$ intensity shown in Exp. #5 corresponds to the highest O₃ exposure and RH level, but lowest OH exposure.

The difference in elemental composition of organic particles produced from “O₃-dominant” vs. “OH-dominant” environments is also examined via the AMS measured O:C and H:C ratios in the van Krevelen plot and the time-dependent evolution of the average carbon oxidation state ($OS_C = 2 \times O:C - H:C$), see Fig.9. In general, the OS_C values calculated fall into a region characterized by oxidized primary organic aerosol and semivolatile oxidized organic aerosol (Kroll et al., 2011). The measured O:C (~ 0.2) and H:C (~ 1.7) ratios at an OH exposure in the order of ~ 10^7 molecules cm⁻³ h agree with those measured for organic aerosols generated from C₁₀-C₁₇ alkanes (Lambe et al., 2011,

2012). As mentioned earlier, the four experiments (Exp. #1, #3, #4, and #5) were conducted in such a way that the total OH exposure is decreasing, whereas the total O₃ and RH exposure is increasing along with increasing experimental numbers (e.g., Exp. 5 has the least OH exposure but the largest O₃ and RH exposure). A clear trend observed from the van Krevelen plot is that O:C increases whereas H:C decreases under elevated O₃ and RH levels. The effect of ozonolysis of substituted dihydrofuran chemistry on the aerosol chemical composition can be evaluated by comparing OS_C (O:C vs. H:C) for these four experiments under the same OH exposure. Consistent with our findings in $f_{\text{CO}_2^+} - f_{\text{C}_2\text{H}_3\text{O}^+}$ space, the highest OS_C is observed under the highest O₃ exposure and RH level, but lowest OH exposure (98% substituted dihydrofuran reacts with O₃ at 55% RH). With the same OH exposure, e.g., 1.5×10^7 molecules cm⁻³ h, the average carbon oxidation state increases from -1.36 in “O₃-limiting” environments (Exp. #1) to -1.25 in “O₃-dominant” environments (Exp. #5). One concludes that ozonolysis of substituted dihydrofuran plays an important role in the formation of highly oxidized aerosol in alkane SOA.

3.5.5 Experiment and model comparison

Figure 10 shows the temporal profiles of CIMS measured ions in (+/-) mode, with structures proposed in Table 2, together with the corresponding model predictions under conditions of Exp. #2. In general, four time-dependent growth patterns are observed in experiments, which are also captured by model predictions. “Pattern #1” denotes species with rapid removal pathways, e.g., m/z 301 (-), with a proposed structure of δ -hydroxycarbonyl. In the current mechanism, the overall heterogeneous conversion rate of

δ -hydroxycarbonyl to substituted dihydrofuran is taken as $3 \times 10^{-3} \text{ s}^{-1}$. The model output is consistent with the observed time-dependent trend when this rate is used. Up to $\sim 90\%$ of m/z 301 (-) is consumed due to this rapid heterogeneous reaction pathway at 3% RH after 18 h of photooxidation. “Pattern #2” is indicative of a species that also reacts rapidly, but with a much slower consumption rate than species of “Pattern #1”. A typical example here is m/z 183 (+), which represents the alkyl-substituted dihydrofuran. The reaction rate constants of alkyl-substituted dihydrofuran with either OH or O_3 are at least an order of magnitude higher than the generic reaction rate constant for the OH abstraction reaction, which is the dominant gas-phase pathway in the dodecane photooxidation mechanism. The simulated peak occurs ~ 2 h earlier than observations, indicating that the formation rate of alkyl-substituted dihydrofuran might be slower than the decay rate of its precursor, δ -hydroxycarbonyl, considering that fact that the acid-catalyzed dehydration process in the particle phase is the rate-limiting step. The extent to which the formation rate is slower than the decay rate, however, is unknown since the measurement of rate constants for individual steps is infeasible in this study. “Pattern #3” reflects the temporal profiles for a majority of ions here, e.g., m/z 328 (-), 299 (-), 249 (-), 315 (-), and 332 (-). Compounds proposed for the above m/z can be categorized as semi-volatile products. In the gas phase, they undergo functionalization or fragmentation, or partition into the particle phase as the precursors of SOA. Overall, the temporal profiles of species in “Pattern #3” are governed by the progressive photochemistry in the gas phase and gas-particle equilibrium partitioning. “Pattern #4”, including m/z 346 (-) and 328 (-) here, represent “nonvolatile” species. Owing to their low volatilities, they will immediately partition to the particle phase once formed and the gas-phase

photooxidation becomes negligible, although it might still occur via the OH attack on C-atoms.

Figure 11 (A) shows the simulated SOA growth (SIM.1) using the initial conditions in Exp. #2, together with the observed total organic aerosol mass as a function of reaction time and OH exposure. The model reproduces the chamber measured SOA yield at 3% RH when the conversion rate of $3 \times 10^{-3} \text{ s}^{-1}$ is employed to represent the heterogeneous conversion of δ -hydroxycarbonyl to dihydrofuran. A second simulation (SIM.2) was run with the complete dihydrofuran chemistry removed while other parameters were held constant. The total organic mass is $\sim 42\%$ higher as a result after 18 h photooxidation. The formation of alkyl-substituted dihydrofuran from δ -hydroxycarbonyl is accompanied by an increase of vapor pressure from 5.36×10^{-7} to 1.08×10^{-4} atm at 300 K, as predicted by SIMPOL.1, and the total organic mass formed decreases. Although the addition of OH to the C=C double bond in the substituted dihydrofuran introduces an extra OH group, the decrease of vapor pressure owing to the addition of one OH group does not compensate for the heterogeneous conversion of both -C=O and -OH groups in δ -hydroxycarbonyl to an -O- group in a non-aromatic ring in dihydrofuran. The predicted the average carbon oxidation state is $\sim 7 - 15\%$ higher than observations. The overprediction is within the uncertainties in the O:C (31%) and H:C (10%) measurement by AMS (Aiken et al., 2008). Incorporation of the substituted dihydrofuran formation and removal pathways in the model leads to an increase in the simulated OS_C . Compared with compounds produced from dodecane photooxidation under high- NO_x conditions, products from dihydrofuran chemistry tend to have a higher O:C but lower H:C due to the formation of ether, ester, and carboxylic acid functional groups. As a result, the

calculated average carbon oxidation state is higher in the presence of chemical reactions that accelerate the aerosol aging process.

3.6 Atmospheric Implications

The importance of ozone in the SOA formation from the photooxidation of long-chain alkanes under atmospherically relevant conditions depends on two factors: 1) the relative concentration of O_3 vs. OH; and 2) the heterogeneous conversion rate of δ -hydroxycarbonyls to substituted dihydrofurans. Figure 12 shows regimes of ozonolysis vs. OH-oxidation of substituted dihydrofuran corresponding to ranges of OH and O_3 concentrations. The OH-initiated oxidation of substituted dihydrofuran is predicted to dominate only under remote atmospheric conditions. Most alkane emissions occur in areas where ozone levels exceed 10 ppb, where the ozonolysis of dihydrofuran should be dominant.

Under conditions of the current study, the substituted dihydrofuran chemistry is predicted to account for > 95% of the removal pathways of δ -hydroxycarbonyl (Fig. 1 D (H)) and up to ~ 80% of the total organic mass formed from dodecane photooxidation (Fig. 11 (B)). This estimate sets the upper limit in terms of the contribution of substituted dihydrofuran chemistry to alkane SOA production in the actual atmosphere, where the RH is higher (50% vs. 3%), the ambient aerosols are less acidic, and the organic aerosol masses are lower ($\sim 10 \mu\text{g m}^{-3}$) than in the chamber experiments ($\sim 50 \mu\text{g m}^{-3}$ after 3 h of irradiation). Experimental evidence in this study shows that the heterogeneous conversion still occurs at 50% RH but with less efficiency (Fig. 3). The water vapor abundance at 50% RH, however, compensates for the production of the less substituted dihydrofuran,

leading to an eventually higher yield of carboxylic acids (Section 4.4). If the conversion of δ -hydroxycarbonyl to substituted dihydrofuran occurs efficiently in the atmosphere, this could be a source of carboxylic acid in the ambient aerosols. It has been suggested that the heterogeneous formation of substituted dihydrofuran is acid-catalyzed (Atkinson et al. 2008; Lim and Ziemann, 2009 a, b, c). Aerosols generated in the chamber environment in the presence of NO_x are expected to be highly acidic due to the formation of HNO_3 . In the atmosphere, where ambient particles are less acidic or even neutralized, the heterogeneous conversion of δ -hydroxycarbonyl to substituted dihydrofuran might be a minor process.

In summary, two impacts of substituted dihydrofuran chemistry on alkane SOA formation are expected. First, the SOA yield from the photooxidation of long-chain alkanes can be overpredicted without accounting for substituted dihydrofuran formation and removal pathways. Second, a substantial amount of carboxylic acid, ester, and tetrahydrofuran moieties can be produced, leading to higher O:C but much lower H:C ratios, and thus a higher oxidation state of alkane SOA in general. In this manner, the dihydrofuran chemistry can be considered as a “dehydration” channel in alkane SOA formation.

3.7 Acknowledgement

This work was supported by National Science Foundation grant AGS-1057183.

3.8 Bibliography

Aiken, A. C., DeCarlo, P. F., and Jimenez, J. L.: Elemental analysis of organic species with electron ionization high-resolution mass spectrometry, *Anal. Chem.*, 79, 8350-8358, doi:8310.1021/ac071150w, 2007.

Aiken, A. C., Decarlo, P. F., Kroll, J. H., Worsnop, D. R., Huffman, J. A., Docherty, K. S., Ulbrich, I. M., Mohr, C., Kimmel, J. R., Sueper, D., Sun, Y., Zhang, Q., Trimborn, A., Northway, M., Ziemann, P. J., Canagaratna, M. R., Onasch, T. B., Alfarra, M. R., Prevot, A. S. H., Dommen, J., Duplissy, J., Metzger, A., Baltensperger, U., and Jimenez, J. L.: O/C and OM/OC ratios of primary, secondary, and ambient organic aerosols with high-resolution time-of-flight aerosol mass spectrometry, *Environ. Sci. Technol.*, 42, 4478-4485, 2008.

Alfarra, M. R., Coe, H., Allan, J. D., Bower, K. N., Boudries, H., Canagaratna, M. R., Jimenez, J. L., Jayne, J. T., Garforth, A. A., Li, S. M., and Worsnop, D. R.: Characterization of urban and rural organic particulate in the lower Fraser valley using two Aerodyne aerosol mass spectrometers, *Atmos. Environ.*, 38, 5745-5758, 2004.

Arey, J., Aschmann, S. M., Kwok, E. S. C., Atkinson, R.: Alkyl nitrate, hydroxyalkyl nitrate, and hydroxycarbonyl formation from the NO_x-air photooxidations of C₅-C₈ n-alkanes, *J. Phys. Chem. A.*, 105, 1020-1027, 2001

Atkinson, R., Arey, J., and Aschmann, S. M.: Atmospheric chemistry of alkanes: Review and recent developments, *Atmos. Environ.*, 42, 5859-5871, 2008.

Aumont, B., Valorso, R., Mouchel-Vallon, C., Camredon, M., Lee-Taylor, J., and Madronich, S.: Modeling SOA formation from the oxidation of intermediate volatility n-alkanes, *Atmos. Chem. Phys.*, 12, 7577-7589, 2012.

Aumont, B., Camredon, M., Mouchel-Vallon, C., La, S., Ouzebidour, F., Valorso, R., Lee-Taylor, J., and Madronich, S.: Modeling the influence of alkane molecular structure on secondary organic aerosol formation, *Faraday Discuss.*, 165, 1-16, 2013.

Bloss, C., Wagner, V., Jenkin, M. E., Volkamer, R., Bloss, W. J., Lee, J. D., Heard, D. E., Wirtz, K., Martin-Reviejo, M., Rea, G., Wenger, J. C., and Pilling, M. J.: Development of a detailed chemical mechanism (MCMv3.1) for the atmospheric oxidation of aromatic hydrocarbons, *Atmos. Chem. Phys.*, 5, 641-664, 2005.

Canagaratna, M. R., Jayne, J. T., Jimenez, J. L., Allan, J. D., Alfarra, M. R., Zhang, Q., Onasch, T. B., Drewnick, F., Coe, H., Middlebrook, A., Delia, A., Williams, L. R., Trimborn, A. M., Northway, M. J., DeCarlo, P. F., Kolb, C. E., Davidovits, P., and Worsnop, D. R.: Chemical and microphysical characterization of ambient aerosols with the Aerodyne aerosol mass spectrometer, *Mass Spectrom. Rev.*, 26, 185-222, 2007.

Cappa, C. D., Zhang, X., Loza, C. L., Craven, J. S., Yee, L. D., and Seinfeld, J. H.: Application of the Statistical Oxidation Model (SOM) to secondary organic aerosol formation from photooxidation of C₁₂ Alkanes, *Atmos. Chem. Phys. Discuss.*, 12, 27077-27109, 2012.

Cavalli, F., Barnes, I., and Becker, K. H.: FTIR kinetic, product, and modeling study of the OH-initiated oxidation of 1-butanol in air, *Environ. Sci. Technol.*, 36, 1263-1270, 2000.

Chhabra, P. S., Ng, N. L., Canagaratna, M. R., Corrigan, A. L., Russell, L. M., Worsnop, D. R., Flagan, R. C., and Seinfeld, J. H.: Elemental composition and oxidation of chamber organic aerosol, *Atmos. Chem. Phys.*, 11, 8827-8845, 2011.

Craven, J. S., Yee, L. D., Ng, N. L., Canagaratna, M. R., Loza, C. L., Schilling, K. A., Yatavelli, R. L. N., Thornton, J. A., Ziemann, P. J., Flagan, R. C., and Seinfeld, J. H.: Analysis of secondary organic aerosol formation and aging using positive matrix factorization of high-resolution aerosol mass spectra: application to the dodecane low-NO_x system, *Atmos. Chem. Phys.*, 12, 11795-11817, 2012.

Crouse, J. D., McKinney, K. A., Kwan, A. J., and Wennberg, P. O.: Measurement of gas-phase hydroperoxides by chemical ionization mass spectrometry, *Anal. Chem.*, 78, 6726-6732, 2006.

DeCarlo, P. F., Kimmel, J. R., Trimborn, A., Northway, M. J., Jayne, J. T., Aiken, A. C., Gonin, M., Fuhrer, K., Horvath, T., Docherty, K. S., Worsnop, D. R., and Jimenez, J. L.: Field-deployable, high-resolution, time-of-flight aerosol mass spectrometer, *Anal. Chem.*, 78, 8281-8289, 2006.

Fraser, M. P., Cass, G. R., Simoneit, B. R. T., Rasmussen, R. A.: Air quality model evaluation data for organics. 4. C₂-C₃₆ non-aromatic hydrocarbons, *Environ. Sci. Technol.*, 31, 2356-2367, 1997.

Gentner, D. R., Isaacman, G., Worton, D. R., Chan, A. W. H., Dallmann, T. R., Davis, L., Liu, S., Day, D. A., Russell, L. M., Wilson, K. R., Weber, R., Guha, A., Harley, R. A., and Goldstein, A. H.: Elucidating secondary organic aerosol from diesel and gasoline

vehicles through detailed characterization of organic carbon emissions, P. Natl. Acad. Sci. USA, 109, 18318-18323, 2012.

Gong, H. M., Matsunaga, A., and Ziemann, P. J.: Products and mechanism of secondary organic aerosol formation from reactions of linear alkenes with NO₃ radicals, J. Phys. Chem. A., 109, 4312-4324, 2005.

Hoekman, S. K.: Speciated measurements and calculated reactivities of vehicle exhaust emissions from conventional and reformulated gasolines, Environ. Sci. Technol., 26, 1206-1216, 1992.

Holt, T., Atkinson, R., and Arey, J.: Effect of water vapor concentration on the conversion of a series of 1,4-dihydroxycarbonyls to dihydrofurans, J. Photochem. Photobiol. A: Chem., 176, 231-237, 2005.

Jathar, S. H., Miracolo, M. A., Tkacik, D. S., Donahue, N. M., Adams, P. J., and Robinson, A. L.: Secondary Organic Aerosol Formation from Photo-Oxidation of Unburned Fuel: Experimental Results and Implications for Aerosol Formation from Combustion Emissions, Environ. Sci. Technol., 47 (22), 12886-12893, 2013.

Jenkin, M. E., Shallcross, D. E., Harvey, J. H.: Development and application of a possible mechanism for the generation of *cis*-pinic acid from the ozonolysis of α - and β -pinene, Atmos. Environ., 34, 2837-2850, 2000.

Jenkin, M. E., Saunders, S. M., Wagner, V., and Pilling, M. J.: Protocol for the development of the Master Chemical Mechanism, MCM v3 (Part B): tropospheric

degradation of aromatic volatile organic compounds, *Atmos. Chem. Phys.*, 3, 181–193, 2003.

Jenkin, M. E.: Modeling the formation and composition of secondary organic aerosol from α - and β -pinene ozonolysis using MCM v3, *Atmos. Chem. Phys.*, 4, 1741-1757, 2004.

Jordan, C. E., Ziemann, P. J., Griffin, R. J., Lim, Y. B., Atkinson, R., and Arey, J.: Modeling SOA formation from OH reactions with C₈-C₁₇ n-alkanes, *Atmos. Environ.*, 42, 8015-8026, 2008.

Isaacman, G., Chan, A. W. H., Nah, T., Worton, D. R., Ruehl, C. R., Wilson, K. R., and Goldstein, A. H.: Heterogeneous OH oxidation of motor oil particles causes selective depletion of branched and less cyclic hydrocarbons, *Environ. Sci. Technol.*, 46, 10632-10640, 2012.

Kirchstetter, T. W., Singer, B. C., Harley, R. A., Kendall, G. R., and Traverse, M.: Impact of California reformulated gasoline on motor vehicle emissions. 1. Mass emission rates, *Environ. Sci. Technol.*, 33, 318-328, 1999.

Kleinman, L. I., Springston, S. R., Daum, P. H., Lee, Y. N., Nunnermacker, L. J., Senum, G. I., Wang, J., Weinstein-Lloyd, J., Alexander, M. L., Hubbe, J., Ortega, J., Canagaratna, M. R., and Jayne, J.: The time evolution of aerosol composition over the Mexico City plateau, *Atmos. Chem. Phys.*, 8, 1559-1575, 2008. Klotz, B., Barnes, I., and Imamura, T.: Product study of the gas-phase reactions of O₃, OH and NO₃ radicals with methyl vinyl ether, *Phys. Chem. Chem. Phys.*, 6, 1725-1734, 2004.

Kroll, J. H., Smith, J. D., Che, D. L., Kessler, S. H., Worsnop, D. R., and Wilson, K. R.: Measurement of fragmentation and functionalization pathways in the heterogeneous oxidation of oxidized organic aerosol, *Phys. Chem. Chem. Phys.*, 11, 8005-8014, 2009.

Kroll, J. H., Donahue, N. M., Jimenez, J. L., Kessler, S. H., Canagaratna, M. R., Wilson, K. R., Altieri, K. E., Mazzoleni, L. R., Wozniak, A. S., Bluhm, H., Mysak, E. R., Smith, J. D., Charles, E. K., and Worsnop, D. R.: Carbon oxidation state as a metric for describing the chemistry of atmospheric organic aerosol, *Nature Chem.*, 3, 133-139, 2011.

Lambe, A. T., Onasch, T. B., Croasdale, D. R., Wright, J. P., Martin, A. T., Franklin, J. P., Massoli, P., Kroll, J. H., Canagaratna, M. R., Brune, W. H., Worsnop, D. R., and Davidovits, P.: Transitions from functionalization to fragmentation reactions of laboratory secondary organic aerosol (SOA) generated from the OH oxidation of alkanes precursors, *Environ. Sci. Technol.*, 46, 5430-5437, 2012.

Lee, A. K. Y., Herckes, P., Leaitch, W. R., Macdonald, A. M., and Abbatt, J. P. D.: Aqueous OH oxidation of ambient organic aerosol and cloud water organics: Formation of highly oxidized products, *Geophys. Res. Lett.*, 38, L11805, 2011.

Lim, Y. B. and Ziemann, P. J.: Products and mechanism of secondary organic aerosol formation from reactions of n-alkanes with OH radicals in the presence of NO_x, *Environ. Sci. Technol.*, 39, 9229-9236, 2005.

Lim, Y. B. and Ziemann, P. J.: Effects of molecular structure on aerosol yields from OH radical-initiated reactions of linear, branched, and cyclic alkanes in the presence of NO_x, *Environ. Sci. Technol.*, 43, 2328-2334, 2009 a.

Lim, Y. B. and Ziemann, P. J.: Chemistry of secondary organic aerosol formation from OH radical-initiated reactions of linear, branched, and cyclic alkanes in the presence of NO_x, *Aero. Sci. Technol.*, 43, 604-619, 2009 b.

Lim, Y. B. and Ziemann, P. J.: Kinetics of the heterogeneous conversion of 1,4-hydroxycarbonyls to cyclic hemiacetals and dihydrofurans on organic aerosol particles, *Phys. Chem. Chem. Phys.*, 11, 8029-8039, 2009c.

Liu, S., Day, D. A., Shields, J. E., and Russell, L. M.: Ozone-driven day time formation of secondary organic aerosol containing carboxylic acid groups and alkane groups, *Atmos. Chem. Phys.*, 11, 8321-8341, 2011.

Loza, C. L., Craven, J. S., Yee, L. D., Coggon, M. M., Schwantes, R. H., Shiraiwa, M., Zhang, X., Schilling, K. A., Ng, N. L., Canagaratna, M. R., Ziemann, P. J., Flagan, R. C., and Seinfeld, J. H.: Secondary organic aerosol yields of 12-carbon alkanes, *Atmos. Chem. Phys. Discuss.*, 13, 20677-20727, 2013.

MathWorks, 2002. MATLAB.

Martin, P., Tuazon, E. C., Aschmann, S. M., Arey, J., and Atkinson, R.: Formation and atmospheric reaction of 4,5-dihydro-2-methylfuran, *J. Phys. Chem. A*, 106, 11492-11501, 2002.

Miracolo, M. A., Presto, A. A., Lambe, A. T., Hennigan, C. J., Donahue, N. M., Kroll, J. H., Worsnop, D. R., and Robinson, A. L.: Photooxidation of low-volatility organics found in motor vehicle emissions: production and chemical evolution of organic aerosol mass, *Environ. Sci. Technol.*, 44, 1638-1643, 2010.

Miracolo, M. A., Hennigan, C. J., Ranjan, M., Nguyen, N. T., Gordon, T. D., Lipsky, E. M., Presto, A. A., Donahue, N. M., Robinson, A. L.: Secondary aerosol formation from photochemical aging of aircraft exhaust in a smog chamber. *Atmos. Chem. Phys.*, 11, 4135-4147, 2011.

Ng, N. L., Canagaratna, M. R., Zhang, Q., Jimenez, J. L., Tian, J., Ulbrich, I. M., Kroll, J. H., Docherty, K. S., Chhabra, P. S., Bahreini, R., Murphy, S. M., Seinfeld, J. H., Hildebrandt, L., Donahue, N. M., DeCarlo, P. F., Lanz, V. A., Prévôt, A. S. H., Dinar, E., Rudich, Y., and Worsnop, D. R.: Organic aerosol components observed in Northern Hemispheric datasets from Aerosol Mass Spectrometry, *Atmos. Chem. Phys.*, 10, 4625-4641, 2010.

Ng, N. L., Canagaratna, M. R., Jimenez, J. L., Chhabra, P. S., Seinfeld, J. H., and Worsnop, D. R.: Changes in organic aerosol composition with aging inferred from aerosol mass spectra, *Atmos. Chem. Phys.*, 11, 6465-6474, 2011.

Odum, J. R., Hoffmann, T., Bowman, F., Collins, D., Flagan, R. C., and Seinfeld, J. H.: Gas/particle partitioning and secondary organic aerosol yields, *Environ. Sci. Technol.*, 30, 2580-2585, 1996.

Pankow, J. F. and Asher, W. E.: SIMPOL.1: a simple group contribution method for predicting vapor pressures and enthalpies of vaporization of multifunctional organic compounds, *Atmos. Chem. Phys.*, 8, 2773-2796, 2008.

Paulot, F., Crouse, J. D., Kjaergaard, H. G., Kurten, A., St. Clair, J. M., Seinfeld, J. H., and Wennberg, P. O.: Unexpected epoxide formation in the gas-phase photooxidation of isoprene, *Science*, 325, 730-733, 2009.

Presto, A. A., Miracolo, M. A., Kroll, J. H.; Worsnop, D. R., Robinson, A. L., and Donahue, N. M.: Intermediate-volatility organic compounds: a potential source of ambient oxidized organic aerosol, *Environ. Sci. Technol.* 43, 4744-4749, 2009.

Presto, A. A., Miracolo, M. A., Donahue, N. M., Robinson, A. L.: Secondary organic aerosol formation from high-NO_x photo-oxidation of low volatility precursors: n-alkanes, *Environ. Sci. Technol.* 44, 2029-2034, 2010.

Reisen, F., Aschmann, S. M., Atkinson, R., Arey, J.: 1, 4-Hydroxycarbonyl products of the OH radical initiated reactions of C₅-C₈ n-alkanes in the presence of NO, *Environ. Sci. Technol.*, 39, 4447-4453, 2005.

Robinson, A. L., Donahue, N. M., Shrivastava, M. K., Weitkamp, E. A., Sage, A. M., Grieshop, A. P., Lane, T. E., Pierce, J. R., and Pandis, S. N.: Rethinking organic aerosols: semivolatile emissions and photochemical aging, *Science*, 315, 1259-1262, 2007.

Russell, L. M., Bahadur, R., and Ziemann, P. J.: Identifying organic aerosol sources by comparing functional group composition in chamber and atmospheric particles, *Proc. Natl. Acad. Sci.*, 108, 3516-3521, 2011.

Sadezky, A., Chaimbault, P., Mellouki, A., Römpf, A., Winterhalter, R., Moortgat, G. K., and Le Bras, G.: Formation of secondary organic aerosol and oligomers from the ozonolysis of enol ethers, *Atmos. Chem. Phys.*, 6, 5009-5024, 2006.

Sander, S. P., Abbatt, J., Barker, J. R., Burkholder, J. B., Friedl, R. R., Golden, D. M., Huie, R. E., Kolb, C. E., J., K. M., Moortgat, G. K., Orkin, V. L., and Wine, P. H.: Chemical kinetics and photochemical data for use in atmospheric studies, Evaluation No.

17. JPL Publication 10-6, Jet Propulsion Laboratory, Pasadena, <http://jpldataeval.jpl.nasa.gov>, 2011.

Saunders, S. M., Jenkin, M. E., Derwent, R. G., and Pilling, M. J.: Protocol for the development of the Master Chemical Mechanism, MCM v3 (Part A): tropospheric degradation of non-aromatic volatile organic compounds, *Atmos. Chem. Phys.*, 3, 161-180, 2003.

Schauer, J. J., Kleeman, M. J., Gass, G. R., Simoneit, B. R. T.: Measurement of emissions from air pollution sources. 2. C₁ through C₃₀ organic compounds from medium duty diesel trucks, *Environ. Sci. Technol.*, 33, 1578-1587, 1999.

Schauer, J. J., Kleeman, M. J., Gass, G. R., Simoneit, B. R. T.: Measurement of emissions from air pollution sources. 5. C₁ - C₃₂ organic compounds from gasoline-powered motor vehicles, *Environ. Sci. Technol.*, 33, 1578-1587, 1999.

St. Clair, J. M., McCabe, D. C., Crouse, J. D., Steiner, U., and Wennberg, P. O.: Chemical ionization tandem mass spectrometer for the in situ measurement of methyl hydrogen peroxide, *Rev. Sci. Instrum.*, 81, 094102, doi:10.1063/1.3480552, 2010.

Thiault, G., Thévenet, R., Mellouki, A., and Le Bras, G.: OH and O₃ initiated oxidation of ethyl vinyl ether, *Phys. Chem. Chem. Phys.*, 4, 613-619, 2002.

Tkacik, D. S., Presto, A. A., Donahue, N. M., Robinson, A. M.: Secondary organic aerosol formation from intermediate-volatility organic compounds: cyclic, linear, and branched alkanes, *Environ. Sci. Technol.*, 46, 8773-8781, 2012.

Yee, L. D., Craven, J. S., Loza, C. L., Schilling, K. A., Ng, N. L., Canagaratna, M. R., Ziemann, P. J., Flagan, R. C., and Seinfeld, J. H.: Secondary organic aerosol formation from Low-NO_x photooxidation of dodecane: evolution of multi-generation gas-phase chemistry and aerosol composition, *J. Phys. Chem. A*, 116, 6211-6230, 2012.

Zhang, X. and Seinfeld, J. H.: A Functional Group Oxidation Model (FGOM) for SOA formation and aging, *Atmos. Chem. Phys.*, 13, 5907-5926, 2013.

Zielinska, B., Sagebiel, J. C., Harshfield, G., Gertler, A. W., Pierson, W. R.: Volatile organic compounds up to C₂₀ emitted from motor vehicles, measurement methods, *Atmos. Environ.*, 30, 2269-2286, 1996.

Ziemann, P. J. and Atkinson, R.: Kinetics, products, and mechanisms of secondary organic aerosol formation, *Chem. Soc. Rev.*, 41, 6582-6605, 2012.

Table 3.1. Experimental conditions for the photooxidation of dodecane.

	Exp.	T ₀ (K)	RH ₀ (%)	HC ₀ (ppb)	(NO) ₀ (ppb)	(NO ₂) ₀ (ppb)	(O ₃) ₀ (ppb)	Initial Seed vol. (μm ³ m ⁻³)	Additional NO inj. (ppb/h)×(h)
High-NO _x ^a	1	~ 300	~ 3	208	430	576	< DL ^g	18	—
	2	~ 300	~ 3	208	287	12	~ 2	24	Y ^c
	3	~ 300	~ 11	206	45	33	~ 2	30	Y ^d
	4	~ 300	~ 20	178	38	156	~ 2	28	Y ^e
	5	~ 300	~ 55	214	69	30	~ 2	43	Y ^f
Low-NO _x ^b	6	~ 300	~ 3	208	< DL	< DL	< DL	19	—
	7	~ 300	~ 3	214	< DL	< DL	32.6	25	—
	8	~ 300	~ 55	216	< DL	< DL	< DL	58	—

^a Under high-NO_x conditions, the simulated NO concentration (> 5 ppb) is at least four orders of magnitude higher than RO₂ (< 5 × 10⁷ molecules cm⁻³). Over 99% of RO₂ is predicted to react with NO.

^b Under low-NO_x conditions, the simulated HO₂ concentration (~ 1 × 10¹⁰ molecules cm⁻³) is ~ 20 times higher than RO₂ (~ 5 × 10⁸ molecules cm⁻³). RO₂ + HO₂ dominates the fate of RO₂.

^c NO source was controlled at 100 ppb/h for the first 7 h reaction and then 25 ppb/h for the remainder of the reaction.

^d NO source was controlled at 25 ppb/h over the course of the experiment.

^e NO source was controlled at 30 ppb/h for the first 3 h reaction and then 100 ppb/h for the next 1 h of reaction and then back to 30 ppb/h for the remainder of the reaction.

^f NO source was controlled at 50 ppb/h over the course of the experiment.

^g Detection limits (DL) for O₃, NO, and NO₂ are 0.5 ppb, 0.4 ppb, and 0.4 ppb, respectively. H₂O₂ has an interference on the O₃ detection, increasing the O₃ monitor readout by ~ 2-3 ppb in the current study.

Table 3.2. Proposed structures for CIMS ions unique to the alkyl-substituted dihydrofuran chemistry. C and T indicate the cluster and transfer product, respectively.

Commercial standards are not available.

Observed m/z	Chemical formula	Proposed structure	Chemical pathway	Interference
183 (+)	C ₁₂ H ₂₂ O		Heterogeneous conversion	
328 (-)	C ₁₂ H ₂₁ NO ₄		Heterogeneous conversion	—
346 (-)	C ₁₂ H ₂₃ NO ₅		OH-oxidation	
299 (-)	C ₁₂ H ₂₂ O ₃		OH-oxidation Ozonolysis	
249 (-)	C ₁₂ H ₂₂ O ₄		Ozonolysis	—
315(-)	C ₁₂ H ₂₂ O ₄		Ozonolysis	—
332 (-)	C ₁₁ H ₂₁ O ₅ N		Ozonolysis	—
348 (-)	C ₁₁ H ₂₁ O ₆ N		Ozonolysis	—
301(-)	C ₁₁ H ₂₀ O ₄		Ozonolysis	—

Figure 3.1 (a). Schematic mechanism for the photooxidation of dodecane under high- NO_x conditions. Note only first-generation products are shown here. The boxes indicate compounds and associated reaction pathways incorporated in the model simulation.

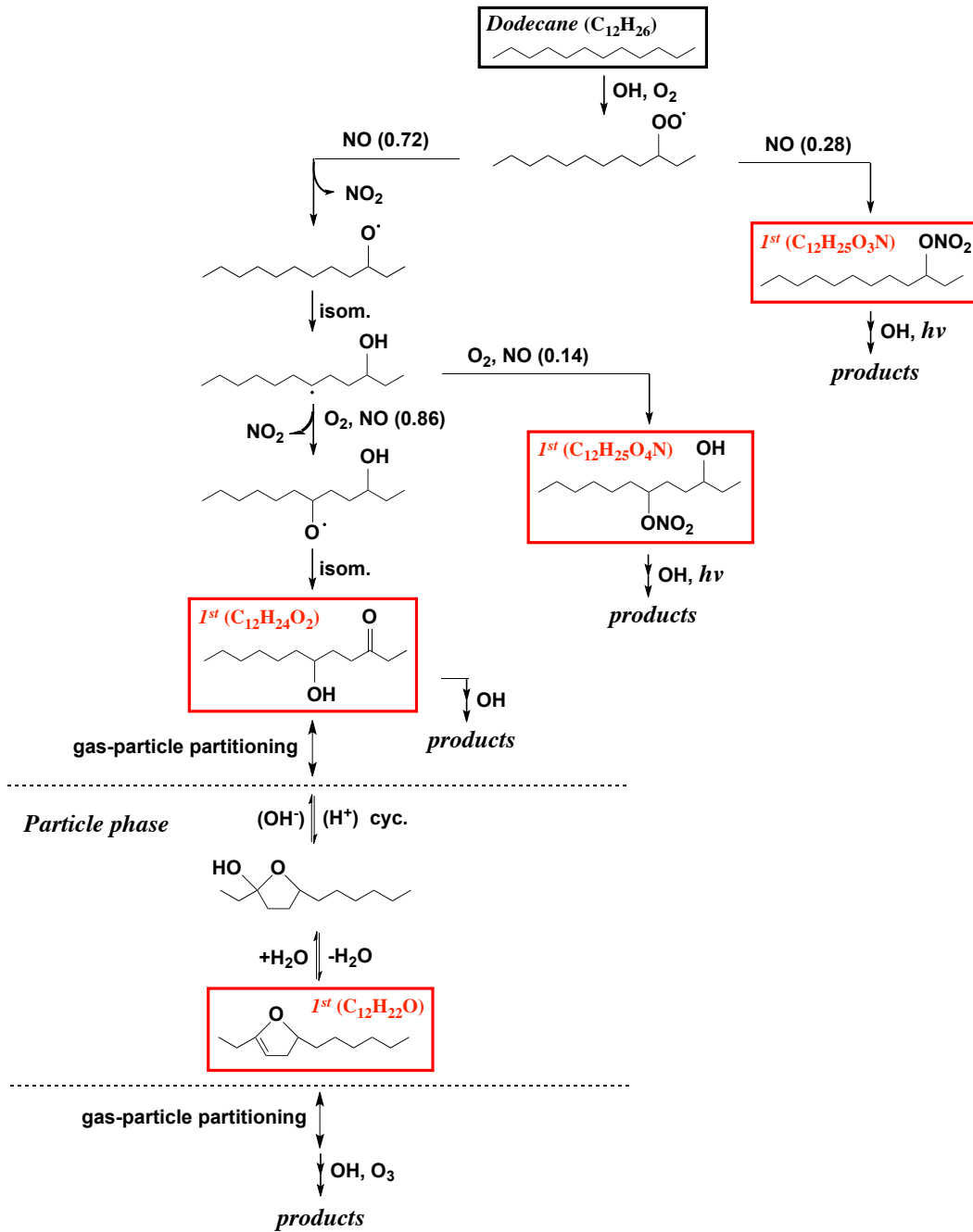


Figure 3.1 (b). Schematic mechanism for the photooxidation of dodecane under low- NO_x conditions. Note only the first three generations of products are shown here. The boxes indicate compounds and associated reaction pathways incorporated in the model simulation.

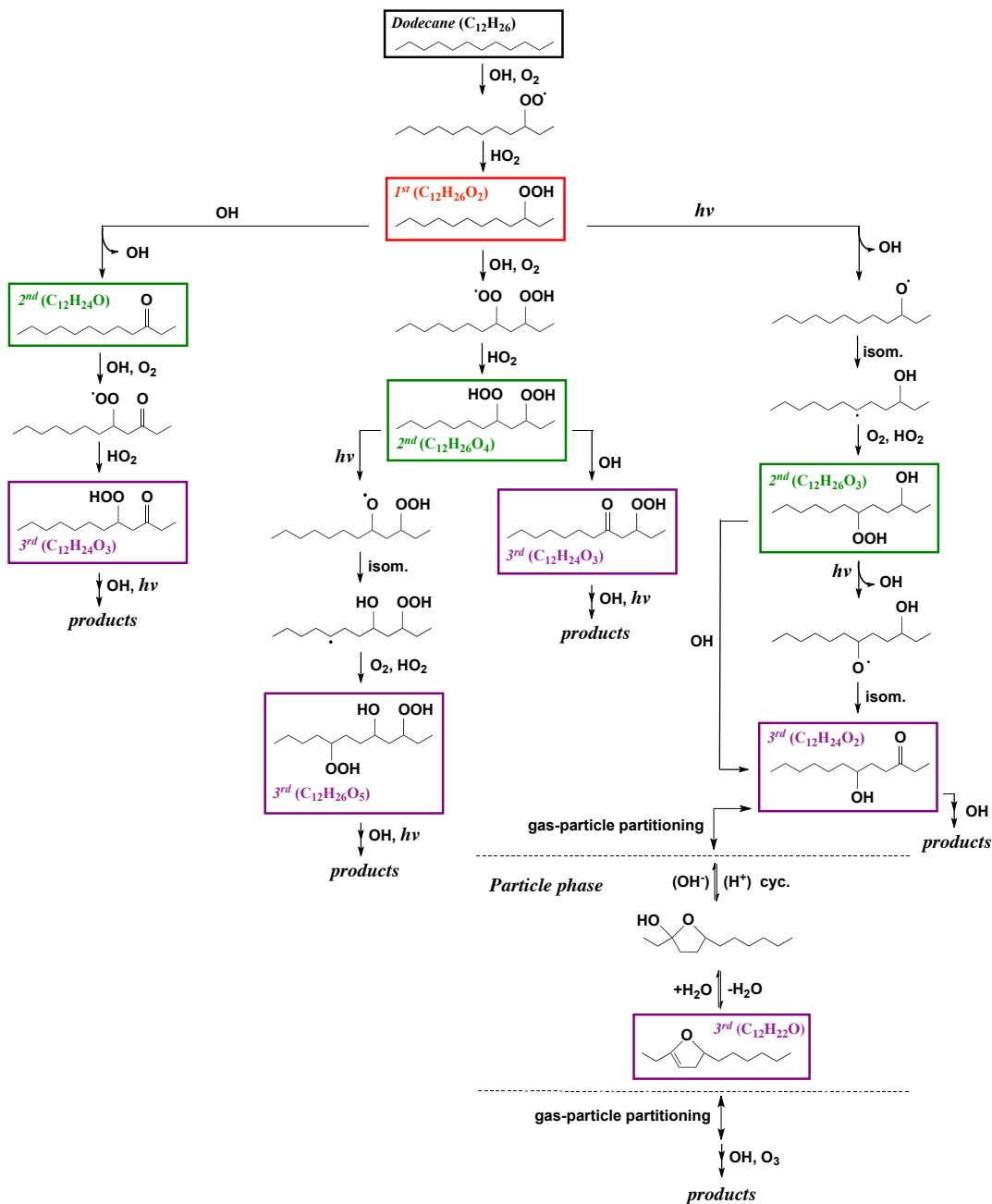


Figure 3.2 (a). Proposed mechanism for the OH-initiated oxidation of alkyl-substituted dihydrofuran under high- NO_x conditions. The boxes indicate compounds or reaction pathways incorporated in the model simulation. CIMS monitored species have m/z noted in red. Estimated vapor pressure (atm) of each compound is indicated in blue.

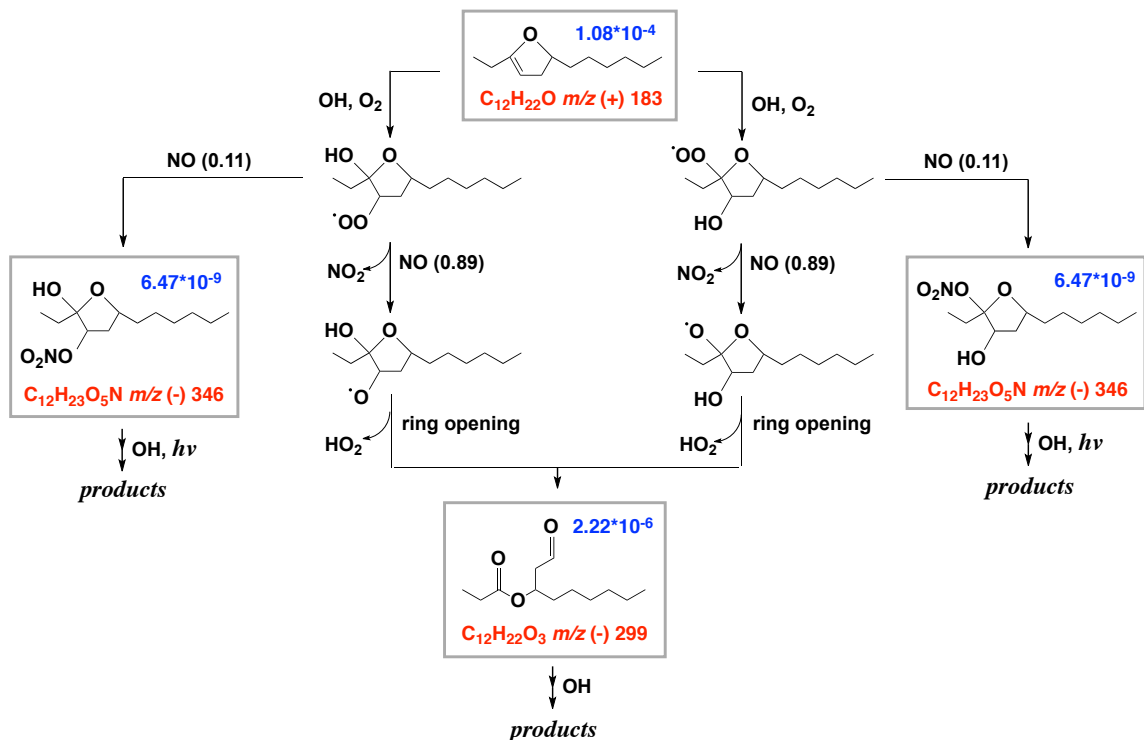


Figure 3.2 (b). Proposed mechanism for the ozonolysis of alkyl-substituted dihydrofuran under high- NO_x conditions. The boxes indicate compounds or reaction pathways incorporated in the model simulation. CIMS monitored species have m/z noted in red. Estimated vapor pressure (atm) of each compound is indicated in blue.

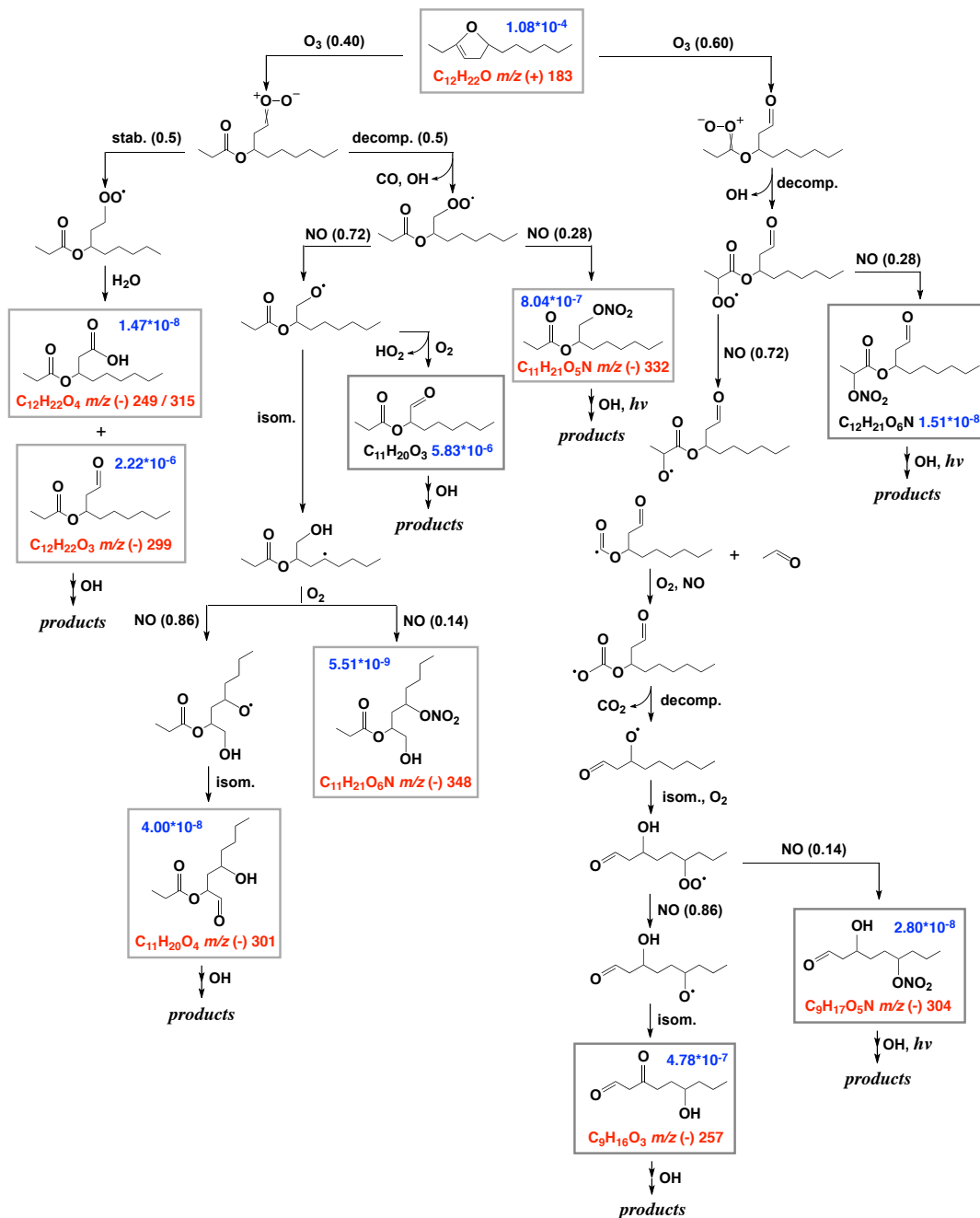


Figure 3.3. Model-predicted relative abundance of δ -hydroxycarbonyl and alkyl-substituted dihydrofuran, together with other 1st generation products under high-NO_x (H) and other 3rd generation products under low-NO_x (L) conditions in gas (g) and particle (p) phases. All the organic masses are normalized by the initial organic mass (~ 200 ppb dodecane). (A) represents the relative abundance of products without a heterogeneous alkyl-substituted dihydrofuran formation channel; (B) represents the relative abundance of products when the heterogeneous channel is incorporated into the scheme but in the absence of any sink of alkyl-substituted dihydrofuran; (C) represents the relative abundance of products when the OH oxidation is the only sink of alkyl-substituted dihydrofuran; (D) represents the relative abundance of products using the complete gas- and particle- phase mechanism.

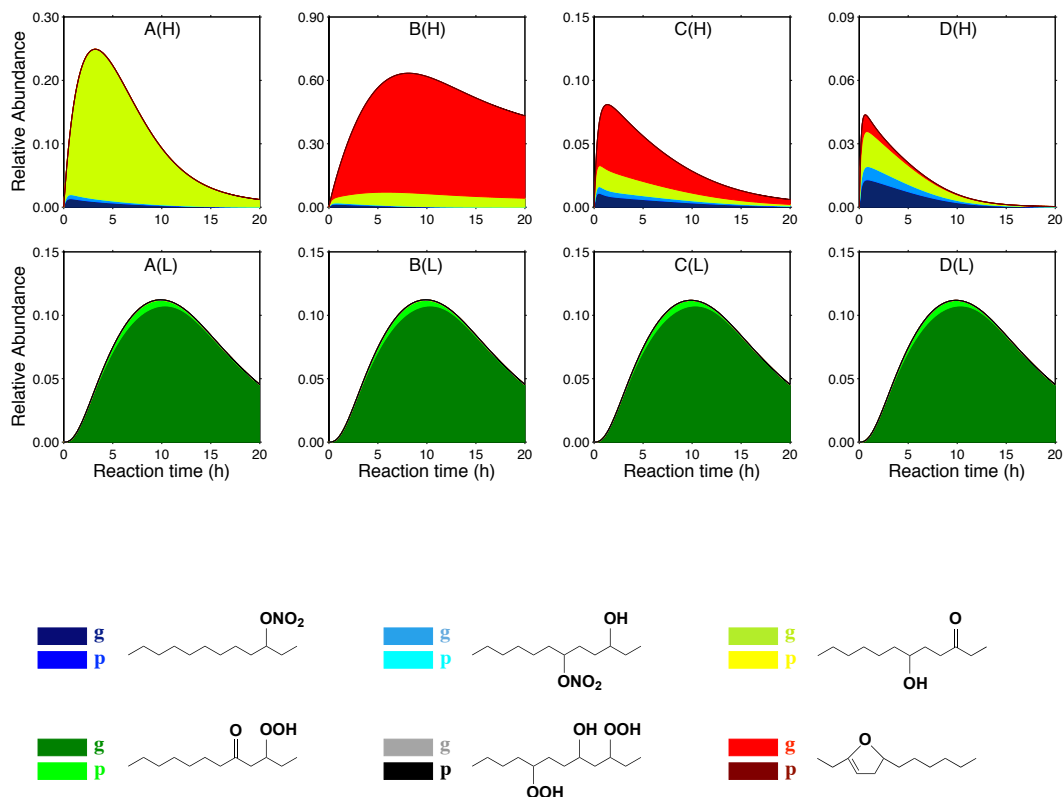


Figure 3.4. Temporal profiles of ion $C_{12}H_{22}O \cdot H^+$ ($m/z = 183$) and $C_{12}H_{24}O_2 \cdot CF_3O^-$ ($m/z = 285$) measured by CIMS and ion $C_{12}H_{23}O^+$ ($m/z = 183$) measured by AMS under high- and low- NO_x conditions. Details of experimental conditions are given in Table 1.

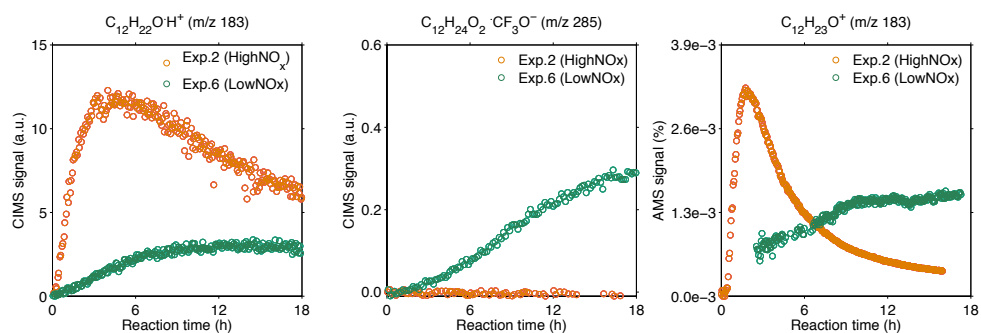


Figure 3.5. Time-dependent evolution of ion $C_{12}H_{22}O \cdot H^+$ ($m/z = 183$) measured by CIMS and ion $C_{12}H_{23}O^+$ ($m/z = 183$) measured by AMS at 3%, 10%, 20%, and 50% RH.

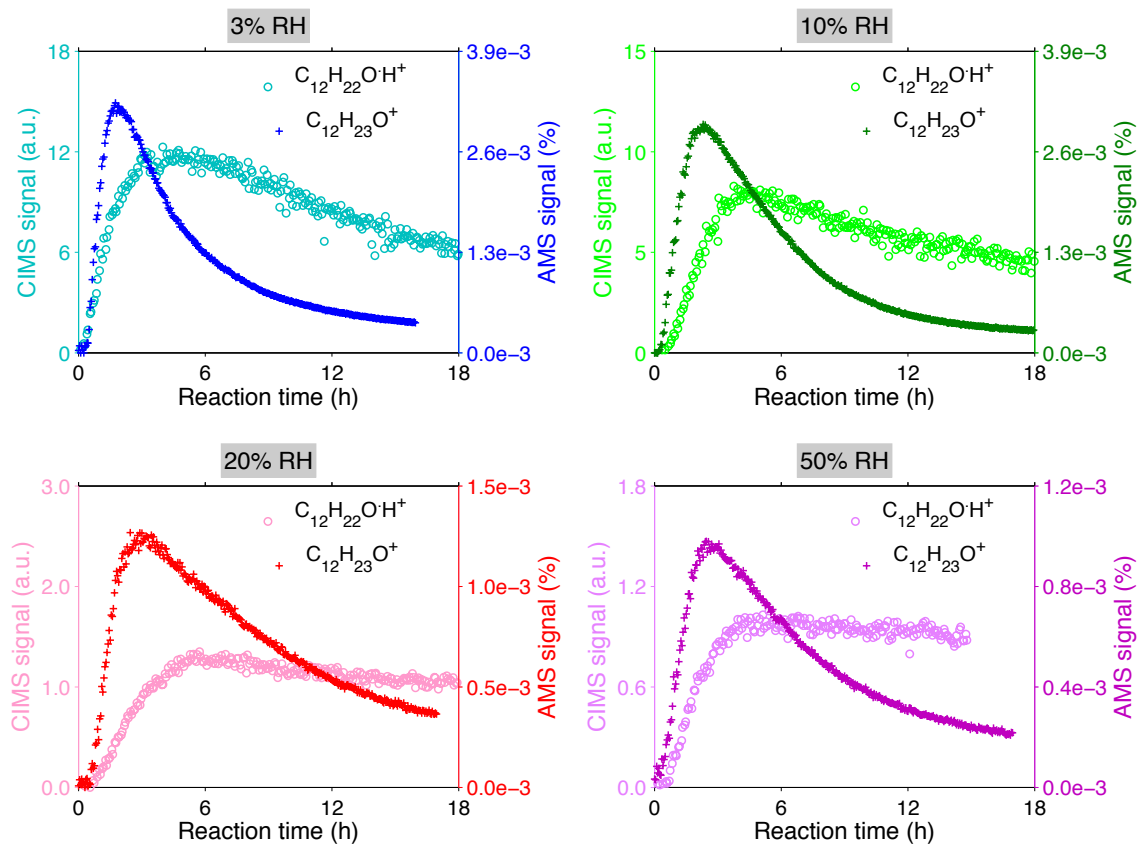


Figure 3.6. Time-dependent evolution of CIMS measured signals at m/z 299, and m/z 249 and 315, as a function of O_3 levels under high- and low- NO_x conditions over the course of 20 h photooxidation.

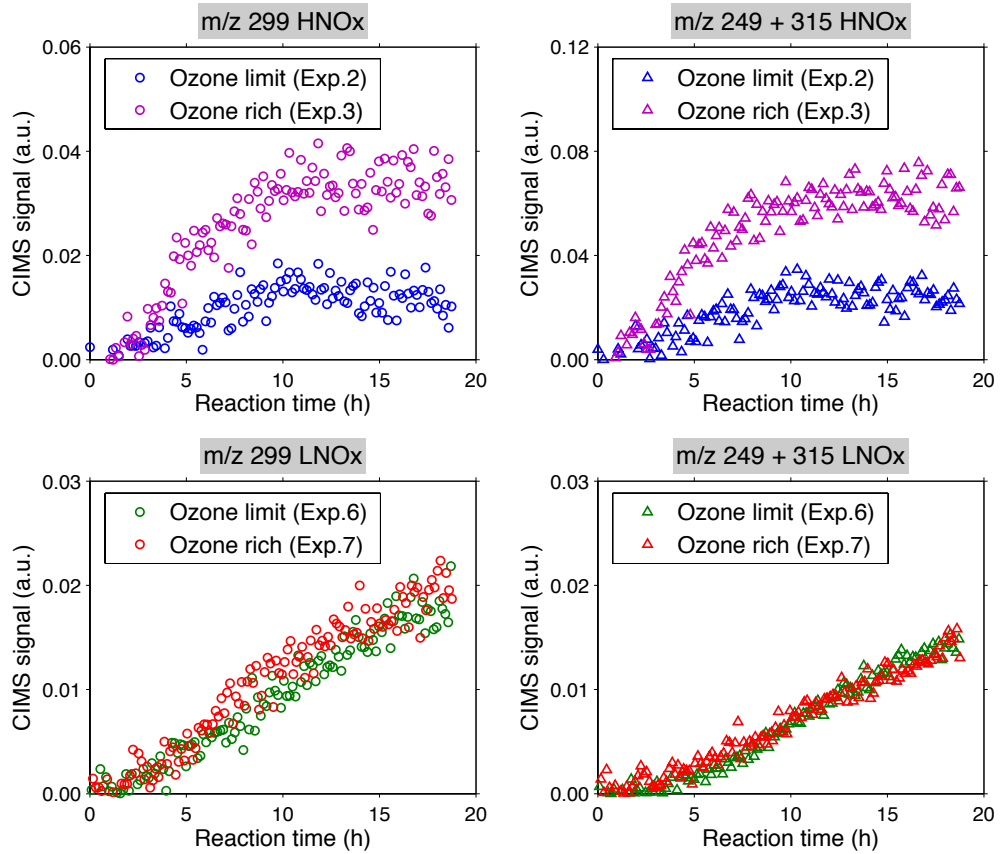


Figure 3.7. Time-dependent evolution of AMS measured ion intensities of $C_2H_4O_2^+$ and $C_3H_5O_2^+$ as a function of decay of the $C_{12}H_{23}O^+$ signal.

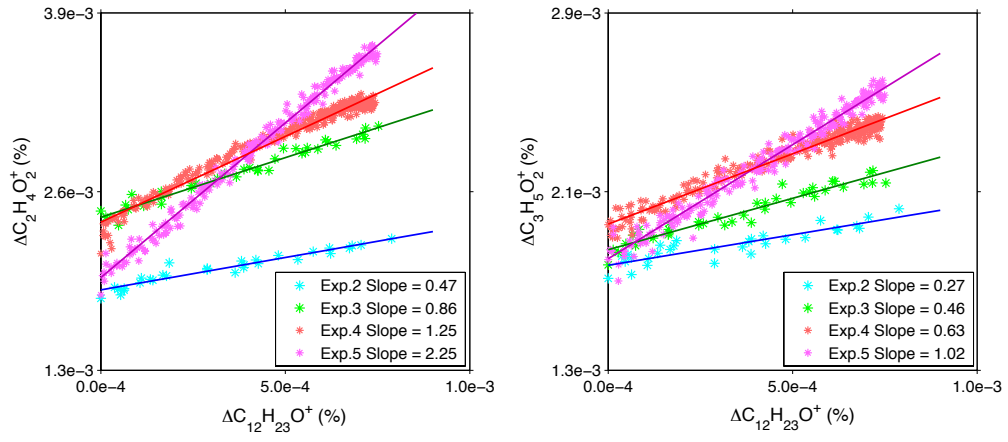


Figure 3.8. SOA evolution as a function of OH exposure vs. O_3 exposure from dodecane photochemistry under high- NO_x conditions in the f_{44} vs. f_{43} space. The top-left graph shows the combination of all the data and the bottom-left graph shows an expanded version. The other graphs show the specific behavior of each experiment: Exp.1 corresponds to a regime in which OH-oxidation of dihydrofuran is dominant. Exp. 3, 4, and 5 correspond to a regime in which ozonolysis of dihydrofuran is dominant, at 10%, 20%, and 50% RH, respectively.

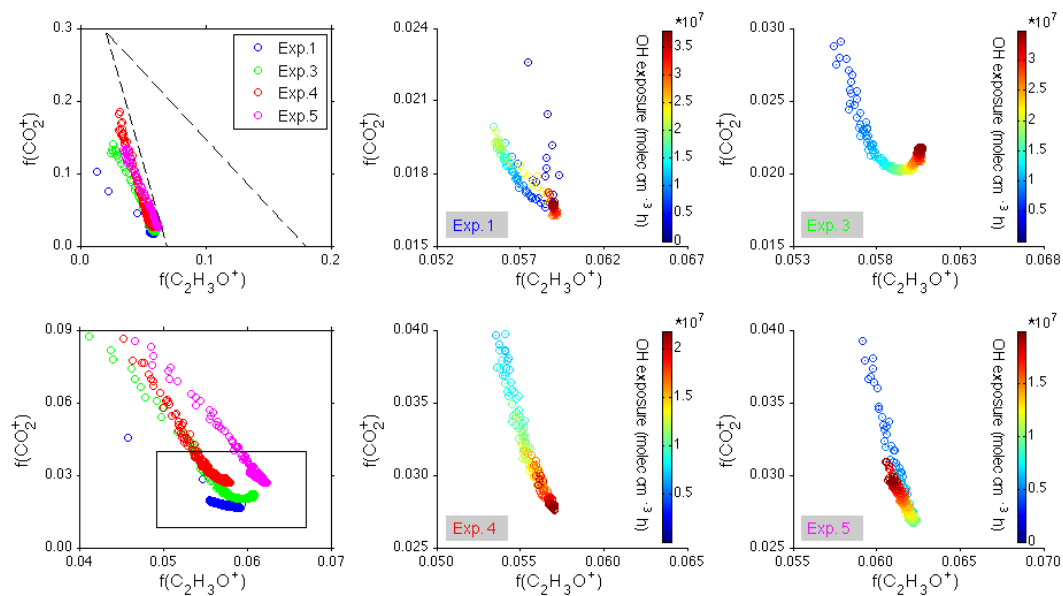


Figure 3.9. (A) SOA average carbon oxidation state as a function of OH exposure from dodecane photochemistry under high- NO_x conditions. Exp.1 corresponds to a regime in which OH-oxidation of dihydrofuran is dominant. Exp. 3, 4, and 5 correspond to a regime in which ozonolysis of dihydrofuran is dominant, at 10%, 20%, and 50% RH, respectively. (B) van Krevelen diagram. AMS measured O:C vs. H:C ratios for the four experiments under the OH total exposure ranging from 1.0×10^7 to 2.0×10^7 molecules cm^{-3} h. Gray dash lines denote the average carbon oxidation state.

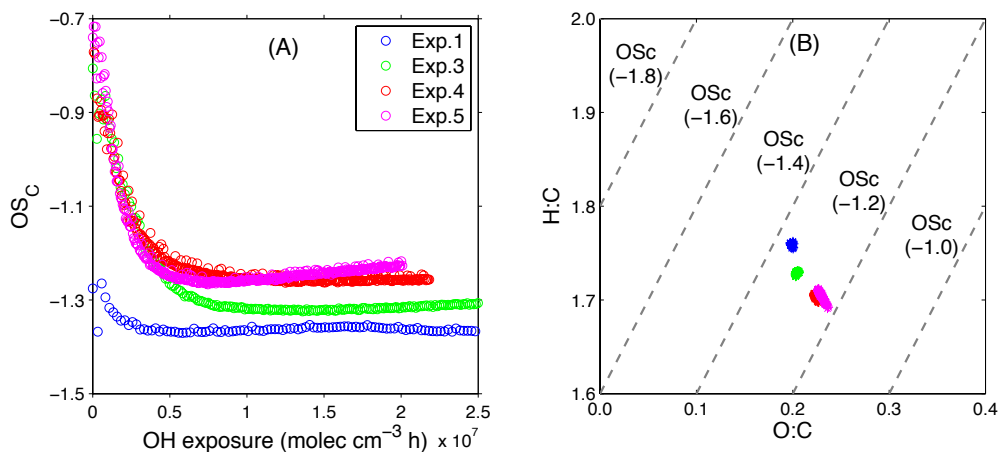
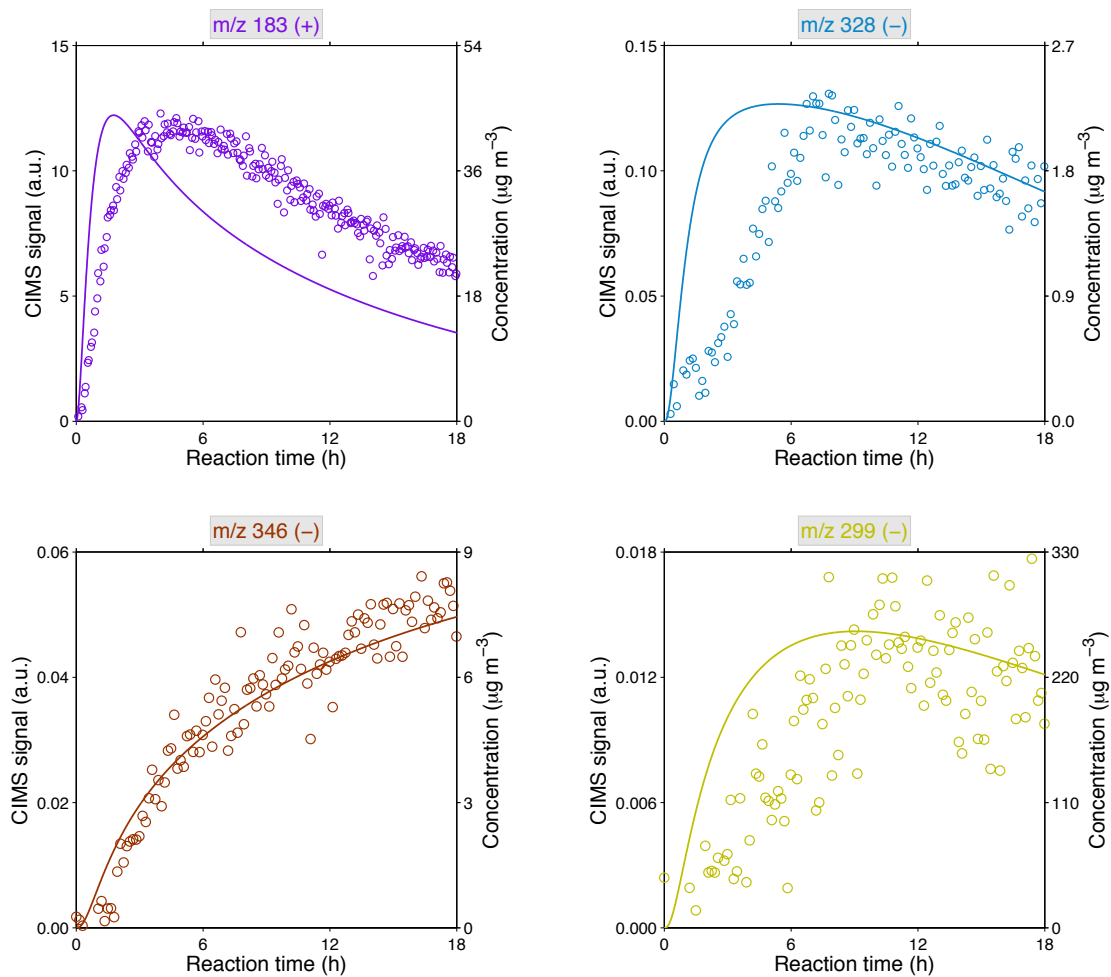


Figure 3.10. Comparison of CIMS measured ions in positive and negative mode, with chemical structures proposed in Table 2, with model simulations using experimental conditions of Exp. #2.



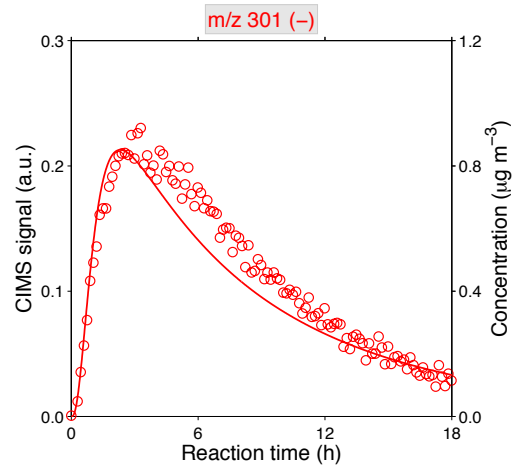
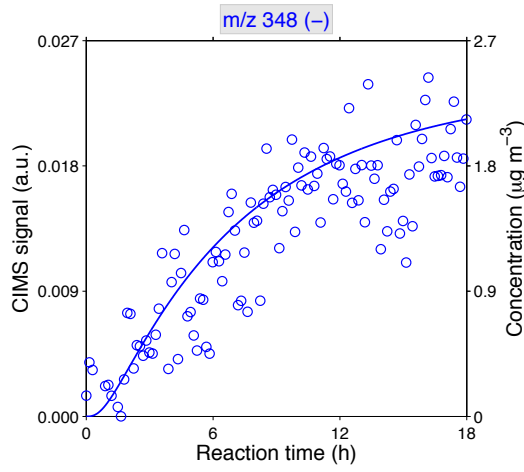
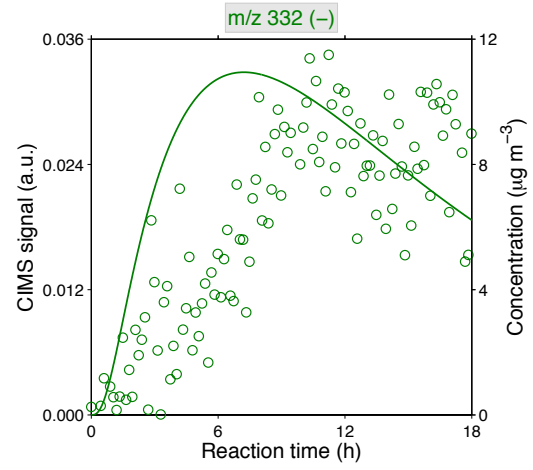
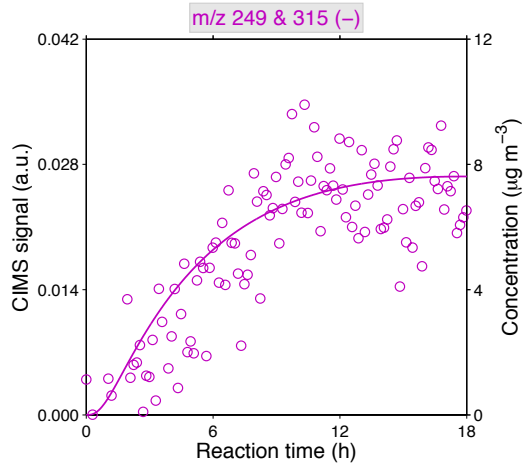


Figure 3.11. (A) Comparison of the predicted dodecane decay and SOA growth with observations (Exp.#2). SIM1 represents the full mechanism simulations under initial conditions of Exp.#2. SIM2 is the simulations in the absence of the substituted dihydrofuran formation channel. (B) The contribution of dihydrofuran chemistry (DHF+OH/O₃) vs. dodecane photochemistry (DOD+OH) to the total organic mass. (C) Molar fractions of major functional groups after 3 h of photochemical reaction (when alkyl-substituted dihydrofuran peaks and organic loading is $\sim 50 \mu\text{g m}^{-3}$) as predicted by SIM1. Note that “other” includes dihydrofuran, tetrahydrofuran, and ether moieties. (D) Comparison of the predicted average carbon oxidation state with observations (Exp.#2).

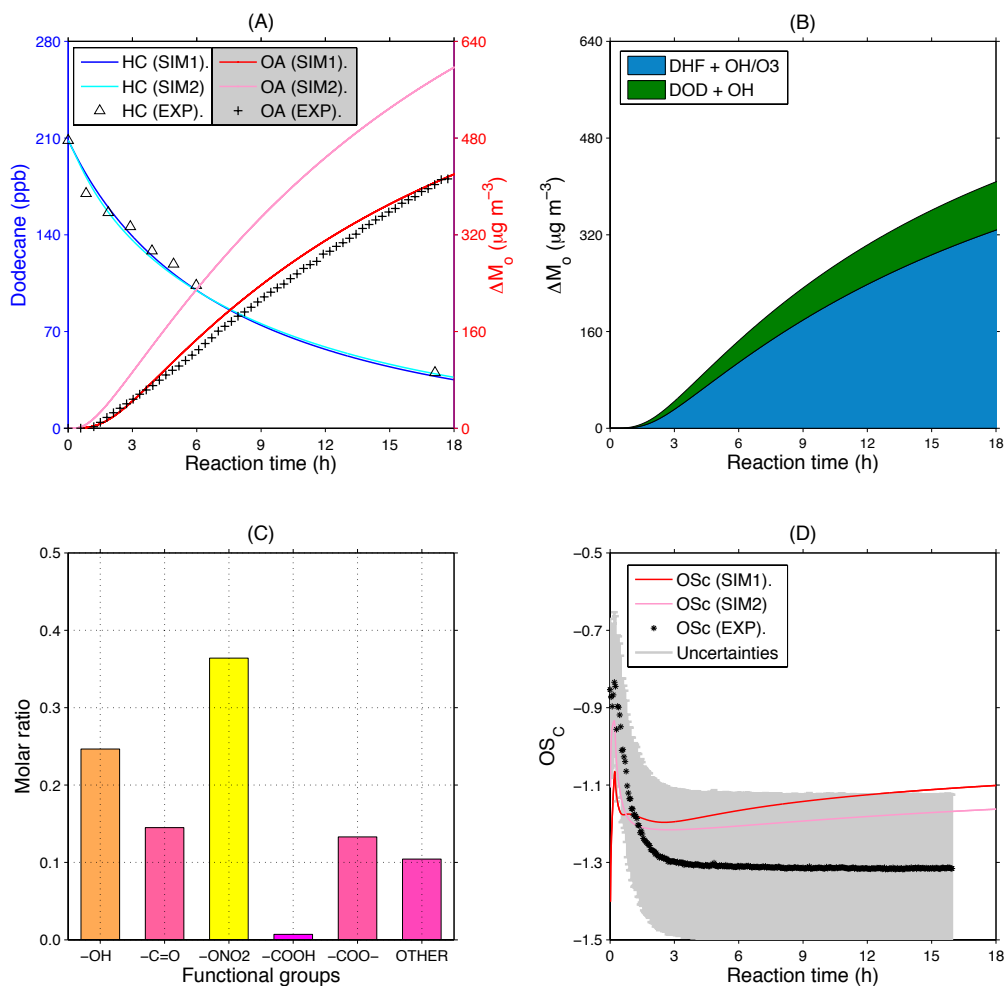
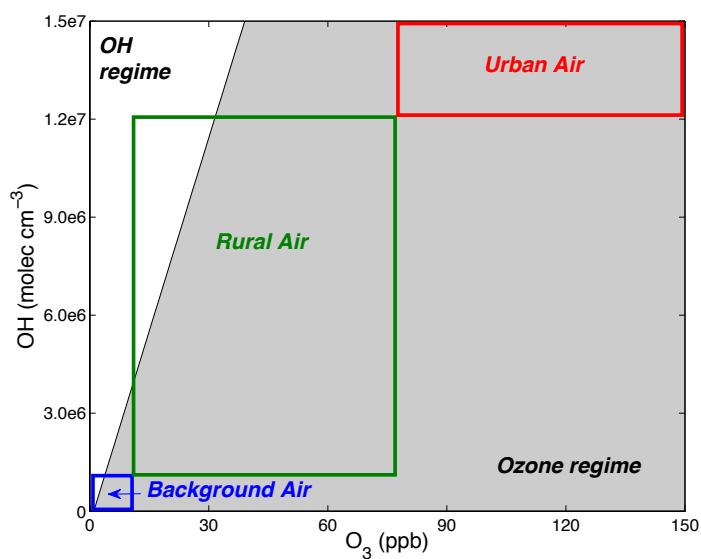


Figure 3.12. Regimes of dominance of ozonolysis vs. OH-oxidation of substituted dihydrofuran. Daily maximum OH concentrations vary by regions in the troposphere, i.e., $10^5 - 10^6$ molecules cm^{-3} for background air, $10^6 - 10^7$ molecules cm^{-3} for rural air, and $> 10^7$ molecules cm^{-3} for urban air, with a global average concentration of 1×10^6 molecules cm^{-3} . Daily average surface ozone mixing ratios in rural areas are between 10 and 50 ppb, while these can exceed 100 ppb in polluted urban areas.



Chapter 4

Influence of vapor wall-loss in laboratory chambers on yields of secondary organic aerosol

* Reproduced with permission from “Influence of vapor wall loss in laboratory chambers on yields of secondary organic aerosol” by X.Zhang[‡], C. D. Cappa[‡], S. Jathar, R. C. McVay, J. J. Ensberg, M. J. Kleeman, and J. H. Seinfeld, *Proceedings of the National Academy of Sciences of the United State of America*, 111(16), 5802-5807, 2014. Copyright 2014 by the National Academy of Sciences of the United States of America.

4.1 Abstract

Secondary organic aerosol (SOA) constitutes a major fraction of sub-micrometer atmospheric particulate matter. Quantitative simulation of SOA within air quality and climate models—and its resulting impacts—depends on the translation of SOA formation observed in laboratory chambers into robust parameterizations. Worldwide data have been accumulating indicating that model predictions of SOA are substantially lower than ambient observations. While possible explanations for this mismatch have been advanced, none has addressed the laboratory chamber data themselves. Losses of particles to the walls of chambers are routinely accounted for, but there has been little evaluation of the effects on SOA formation of losses of semi-volatile vapors to chamber walls. Here, we experimentally demonstrate that such vapor losses can lead to substantially underestimated SOA formation, by factors as much as 4. Accounting for such losses has the clear potential to bring model predictions and observations of organic aerosol levels into much closer agreement.

4.2 Introduction

Most of the understanding concerning the formation of secondary organic aerosol (SOA) from atmospheric oxidation of volatile organic compounds (VOCs) over the past 30 years has been developed from data obtained in laboratory chambers (Odum et al., 1997). SOA is a major component of particulate matter smaller than 1 μm (Jimenez et al., 2009) and consequently has important impacts on regional and global climate and human health and welfare. Accurate simulation of SOA formation and abundance within 3D models is critical to quantifying its atmospheric impacts. Measurements of SOA formation in

laboratory chambers provide the basis for the parameterizations of SOA formation (Odum et al., 1996) in regional air quality models and global climate models (Carlton et al., 2010). A number of studies indicate that ambient SOA concentrations are underpredicted within models, often substantially so, when these traditional parameterizations are used (Heald et al., 2005; Volkamer et al., 2006). Some of this bias has been attributed to missing SOA precursors in emissions inventories, such as so-called intermediate volatility organic compounds (IVOCs), to ambient photochemical aging of semi-volatile compounds occurring beyond that in chamber experiments (Robinson et al., 2007) or to aerosol water/cloud processing (Ervens et al., 2011). The addition of a more complete spectrum of SOA precursors into models has not, however, closed the measurement/prediction gap robustly. For example, recent analysis of organic aerosol (OA) concentrations in Los Angeles revealed that observed OA levels, which are dominated by SOA, exceed substantially those predicted by current atmospheric models (Ensberg et al., 2013), in accord with earlier findings in Mexico City (Dzepina et al., 2011).

Here, we demonstrate that losses of SOA-forming vapors to chamber walls during photooxidation experiments can lead to substantial and systematic underestimation of SOA. Recent experiments have demonstrated that losses of organic vapors to the typically Teflon walls of a laboratory chamber can be substantial (Matsunaga and Ziemann, 2010), but the effects on SOA formation have not yet been quantitatively established. In essence, the walls serve as a large reservoir of equivalent OA mass that compete with the particulate SOA for SOA-forming compounds.

4.3 Materials and methods

4.3.1 Chamber experiments

Toluene photooxidation experiments were carried out in the new 24 m³ Teflon environmental reaction chambers at Caltech. Liquid toluene was evaporated into the chamber to achieve a concentration of ~38 ppb gas-phase mixing ratio (= 143 mg m⁻³). Hydroxyl radicals were generated from photolysis of H₂O₂ either with (high-NO_x) or without (low-NO_x) addition of NO to the chamber. Dried ammonium sulfate seed particles were added via atomization of an aqueous solution of ammonium sulfate solution until the desired seed concentration was obtained. The toluene, seed particles, H₂O₂ and NO_x were allowed to mix in the chamber for 1 hour, after which time the black lights were turned on to initiate H₂O₂ photolysis. Particle number size distributions were measured using a cylindrical differential mobility analyzer coupled to a condensation particle counter. More details are available in *Supplementary Materials*.

4.3.2 SOA modeling

The statistical oxidation model (SOM) (Cappa and Wilson, 2012) was used to analyze the experimental observations. The SOM simulates the multi-generational gas-phase oxidation of a precursor VOC that has N_C carbon atoms and N_O oxygen atoms as reactions cause the precursor and product species to functionalize, increasing N_O , and/or fragment, decreasing N_C . Addition of oxygen atoms leads to a decrease in vapor pressure, which drives condensation of the gas-phase species. Mass-transfer between the gas and particle phases is treated dynamically. The parameters that describe functionalization, fragmentation and the decrease in vapor pressure upon oxygen addition are adjusted by

fitting to the experimental observations of time-dependent SOA formation. More details are provided in *Supplementary Materials*.

4.4 Toluene photooxidation experiments

The effect of vapor wall loss on SOA formation has been comprehensively assessed based on results from a series of 18-h toluene photooxidation experiments conducted in the Caltech environmental chamber under both high- and low-NO_x conditions (*Supplementary Materials, Toluene photooxidation experiments, Table S1*). Toluene is a component of motor vehicle emissions and an important SOA precursor (Odum et al., 1997). Initial [VOC]/[NO_x] ratios were 5.4 ± 0.3 ppbC/ppb, similar to current conditions in Los Angeles, CA. In these experiments, the ratio of initial seed particle surface area (*SA*) to chamber wall *SA* was systematically varied by changing the concentration and diameter of (NH₄)₂SO₄ seed aerosol while keeping all other conditions the same (i.e. hydroxyl radical (OH) and toluene concentration). In this manner, the influence of seed *SA* on SOA formation can be isolated.

Figure 1 shows the observed time-dependent SOA yields, defined as the mass of SOA formed per mass of VOC reacted, determined from the evolution of the particle size distributions (Fig. S1) as a function of initial seed *SA* for the high- and low-NO_x experiments. The SOA concentrations have been corrected for physical deposition of particles to the walls (*Supplementary Materials, Particle wall-loss correction*), which is the appropriate correction to use here as our analysis explicitly accounts for loss of vapors to the walls, discussed further below. Except for the unseeded experiment, the SOA yield for each low-NO_x experiment is reasonably constant with time (from 4 to 18 h) and *C*_{OA} at any given *SA*. For each high-NO_x experiment there is a clear increase in the

yield with C_{OA} and time. The toluene SOA yield at a given C_{OA} is generally lower for high- NO_x than for low- NO_x conditions at a comparable initial seed SA . These differences in the time-dependent yields indicate differences in the chemical pathways leading to SOA formation between low and high- NO_x conditions. Most importantly, the absolute amount of SOA formed for the same initial conditions increases with seed SA , with an indication of a plateau being reached at the highest seed SA . The SOA formed in the unseeded experiments is particularly small. Typical laboratory chamber experiments use initial seed $SA < 10^3 \text{ m}^2 \text{ cm}^{-3}$, which corresponds to seed-to-wall ratios of $< 1 \times 10^{-3}$ in most chambers. These experiments definitively demonstrate that SOA yields vary with seed SA . This variability may partially explain some of the differences in SOA yields reported in the literature.

4.5 SOA modeling and the influence of vapor wall loss

The increase in yield with seed SA is consistent with loss of vapors to the chamber walls and likely results from an increase in the rate of mass transfer of vapor species to the particles relative to the walls. Quantitative understanding of the role of vapor wall-loss is necessary to characterize the extent to which SOA yields in chamber experiments are underestimated relative to the atmosphere. The loss of “extremely low volatility” organic compounds (EVLOCs) to chamber walls has recently been implicated as important for understanding SOA formation for a different chemical system, α -pinene + O_3 (Ehn et al., 2014; Kokkola et al., 2014). The competition between vapor condensation to particles versus to chamber walls is quantitatively examined here using a time-dependent, parameterizable model of SOA formation, the statistical oxidation model (SOM) (Cappa and Wilson, 2012; Cappa et al., 2013) (*Supplementary Materials, The Statistical*

Oxidation Model). The SOM accounts for vapor wall-losses based on observations showing that wall-losses of semi-volatile species in Teflon chambers are reversible (Matsunaga and Ziemann, 2010). Such wall-loss is modelled dynamically and depends on the equivalent OA mass of the chamber walls (C_w , mg m^{-3}), the first-order vapor wall-loss rate coefficient (k_w , s^{-1}), and the vapor saturation concentration of compounds i (C_i^* , $\mu\text{g m}^{-3}$). k_w reflects the combined effects of turbulent mixing in the chamber, molecular diffusion of vapor molecules through the near-wall boundary layer, and any penetration into chamber walls. k_w is likely to be chamber-specific, as the extent of turbulent mixing depends on specific chamber operating conditions, but is reasonably independent of compound identity (Matsunaga and Ziemann, 2010). Values of k_w for a range of gases were estimated in one study (McMurry and Grosjean, 1985) to range from $\sim 2 \times 10^{-5}$ - 10^{-3} s^{-1} , corresponding to timescales of many hours to 10 minutes. The largest k_w values are appropriate only for chambers with active mixing, which the Caltech chamber does not have (*Supplementary Materials, Vapor wall-loss*). Observations (Matsunaga and Ziemann, 2010) suggest that C_w varies somewhat with compound identity, ranging from ~ 2 - 24 mg m^{-3} , compared to chamber OA concentrations that are usually 1-3 orders of magnitude smaller; a value of 10 mg m^{-3} is used here as the base-case. Gas-particle partitioning is modelled dynamically assuming absorptive partitioning, including correction for non-continuum effects and imperfect accommodation, the latter of which is characterized by the mass accommodation coefficient, α . The accommodation coefficient reflects the overall transfer of vapor molecules into the particle bulk, and is likely dependent on the chemical make-up of both the vapor and particle phases and processes that occur at the particle surface. This formulation is more general than most previous

analyses of SOA formation in environmental chambers, which typically assume instantaneous gas-particle equilibrium.

Optimal values for k_w and α have been determined for the sets of low- and high- NO_x experiments by comparing observed and simulated best-fit time-dependent C_{OA} profiles for a wide range of k_w and α . The k_w/α pair that provides for the best overall agreement with the time-dependent SOA formation observed across all experiments at a given NO_x condition, excluding the nucleation experiments, is considered the optimal solution (Fig. 2a-b) (*Supplementary Materials, Optimizing k_w and α* , Fig. S3). For low- NO_x experiments, the optimal $k_w = 2.5 \times 10^{-4} \text{ s}^{-1}$ and $\alpha = 2 \times 10^{-3}$. The independently determined values for high- NO_x experiments are similar: $k_w = 2.5 \times 10^{-4} \text{ s}^{-1}$ and $\alpha = 1 \times 10^{-3}$. The simulations provide good overall agreement with the observed seed SA dependence only for a combination of a small α and $k_w \sim O(10^{-4}) \text{ s}^{-1}$, indicating that both parameters are important to describing chamber SOA formation. (It should be noted that a reasonable fit for an individual experiment can be obtained for many k_w/α pairs, including when instantaneous gas-particle equilibrium is assumed, i.e., when $\alpha = 1$. This is not meant to imply that the absolute values of these parameters are not important, but that only in analyzing the combined data sets at multiple seed SA can optimal k_w and α be determined.) The determined optimal k_w values are consistent with theoretical estimates (*Supplementary Materials, Vapor wall-loss*, Fig. S4) and some observations (Matsunaga and Ziemann, 2010), but larger than some previous observations in the Caltech chamber (Loza et al., 2013), most likely reflecting the limited time resolution of those observations, which might not have allowed for separation of

filling and mixing of the chamber from wall-loss, but potentially also reflecting differences between chemical systems.

The small optimal α values required to reproduce the observed seed SA dependence likely reflect mass-transfer limitations within the particle phase, which can occur for highly viscous SOA particles (Shiraiwa et al., 2013). When $\alpha \sim 10^{-3}$, mass accommodation is relatively slow and the vapors and particles cannot be assumed to be in instantaneous equilibrium. The timescale associated with reaching gas-particle equilibrium ($t_{g-p,eqm}$) varies with seed SA and size (*Supplementary Materials, Gas-particle partitioning timescales*, Fig. S5). Given $\alpha = 10^{-3}$, $t_{g-p,eqm}$ ranges from ~ 230 min for the smallest seed SA to only ~ 30 min for the largest seed SA. Thus, at the smallest seed SA $t_{g-p,eqm}$ is similar to the timescale determined for gas wall-loss ($1/k_w = 67$ min) and the influence of gas wall-loss is more pronounced.

Importantly, loss of condensable vapors to the chamber walls leads to a low-bias in the observed SOA formed even for the experiments with the highest seed SA. To quantitatively assess this bias, simulations have been performed using the best-fit SOM parameters determined for the optimal k_w/α pair above, but with $k_w = 0$ (no wall-loss). The ratio $R_{wall} = C_{SOA}(k_w=0)/C_{SOA}(k_w,optimal)$ has been calculated for each experiment and quantifies the bias in the SOA yield due to traditionally unaccounted for vapor wall-losses. The magnitude of R_{wall} depends on the experiment considered, decreasing with increasing seed SA and reaching a plateau at large seed SA (Fig. 2c). For the seeded experiments, R_{wall} averaged over the period when $C_{OA} > 0.5 \mu\text{g m}^{-3}$ varied from 3.6 (± 0.6) to 2.1 (± 0.2) for low- NO_x and from 4.2 (± 0.9) to 2.1 (± 0.2) for high- NO_x in going from lowest to highest seed SA, and where the uncertainties are one standard deviation over the

averaging period. These ratios correspond to end-of-experiment corrected mass yields of 1.6 (low-NO_x) and 0.93 (high-NO_x), substantially exceeding the values currently used in chemical transport models for toluene (~0.47 for low-NO_x and ~0.12 for high-NO_x). Given an O:C ratio for toluene + OH SOA of ~0.7 (Chhabra et al., 2011), the carbon yields would be 0.94 (low-NO_x) and 0.55 (high-NO_x). (The calculated end of experiment O:C are 0.67 (low-NO_x) and 0.91 (high-NO_x.) This implies that ~6% and ~55% of the product carbon mass remains in the gas-phase for low and high-NO_x conditions, respectively. The oxidation process is a balance between functionalization and fragmentation. In the absence of fragmentation, the carbon yield would asymptote to 100%. The low-NO_x carbon yield in the absence of vapor wall loss is close to 100% and the SOA yield is approximately independent of the total OA mass, which together indicate that fragmentation plays only a minor role. Fragmentation is comparably more important under high-NO_x conditions.

Interestingly, R_{wall} values similar to those determined for the optimal k_{wall}/α pair are obtained when vapor wall-loss is accounted for (i.e. $k_w \neq 0$) but when it is assumed that $\alpha = 1$ (i.e. that gas-particle equilibration is effectively instantaneous) during fitting of each individual experiment (Fig. 2c). This indicates that the magnitude of α is not key to fitting of an individual experiment, but when the experiments are taken together as a combined dataset α is indeed key to matching the observed dependence on seed surface area. Related, α is not key to there being an influence of vapor wall-loss on the overall SOA yield, which is controlled more-so by the magnitude of k_w . The finding that large R_{wall} values are obtained even when $\alpha = 1$ indicates that the general conclusions here regarding vapor wall-loss are robust with respect to knowledge of α . This is important

because other chemical systems might not exhibit as slow mass accommodation but could still be affected by vapor wall loss. Clearly, loss of condensable vapors to the chamber walls can suppress SOA yields relative to those that are relevant for the atmosphere.

4.6 Dependence on experimental conditions

For a given chamber the extent to which vapor wall loss affects SOA yield will depend on the combination of (i) the rate of oxidation and duration of a given experiment, (ii) the precursor VOC concentration, (iii) the particular chemical pathways associated with oxidation of a given species, i.e. the precursor identity, and (iv) the seed SA . This is illustrated for the toluene low- NO_x system by carrying out a series of 18 h simulations where $[\text{OH}]$ is varied from 1-100 $\times 10^6$ molecules cm^{-3} and $[\text{toluene}]_{\text{initial}}$ from 1-300 ppb for a seed $SA = 1000 \text{ m}^{-2} \text{ cm}^{-3}$ using the SOM parameters and optimal k_w/ahe SOM parameters. The calculated R_{wall} varies with oxidant and precursor concentration (actually, VOC loss rate), with smaller R_{wall} when oxidation is faster and at larger precursor VOC concentration (Fig. 3 and Fig. S6). (Note that these calculations do not account for differences that might result from changes in the relative importance of RO_2+HO_2 versus RO_2+RO_2 reactions as $[\text{VOC}]_{\text{initial}}$ and $[\text{OH}]$ are varied.) Such “rate effects” have been observed for SOA produced in aromatic systems (Ng et al., 2007). The seed SA dependence is substantially reduced when the $[\text{VOC}]_{\text{initial}}$ is large, especially at high $[\text{OH}]$. Overall, these dependencies, along with differences in the initial seed SA , may help explain some of the differences (and similarities) in historical aerosol yields measured in different chambers.

4.7 Vapor losses and sensitivity to C_w

The observed time-dependent C_{OA} to which the SOM was fit were corrected to account for physical deposition of the particles to the walls. Loss of vapors, excluding growth of suspended particles, was separately accounted for assuming that the vapors continuously interact with the Teflon chamber walls, with $C_w = 10 \text{ mg m}^{-3}$ (Matsunaga and Ziemann, 2010). Some previous studies (Hildebrandt et al., 2009, Loza et al., 2012) have alternatively assumed that vapors interact only with particles that have deposited to the walls during that experiment, as opposed to with the walls directly, and further that the time-scales associated with partitioning between vapors and suspended or wall-deposited particles are the same (*Supplementary Materials, Particle wall-loss correction*). In this alternative scenario, the effective C_w is time-dependent (and zero at the start of an experiment) and related to the suspended particle concentration and the particle wall-loss rate. Most chamber experiments aim to limit the extent of particle deposition, and thus it is reasonable to assume that, in general, the concentration of wall-deposited particles is less than the suspended particle concentration. Further, most modern experiments limit the observed C_{OA} to $< 0.1 \text{ mg m}^{-3}$, and thus the effective C_w in this alternative case will be substantially smaller than when vapors are assumed to partition into the chamber walls.

It is therefore useful to examine the dependence of the calculated R_{wall} on the assumed C_w , where an assumed $C_w < \sim 0.1 \text{ mg m}^{-3}$ corresponds approximately to the wall-deposited particle alternative scenario. This has been done for the low- NO_x experiments where the SOM was fit to the observations for different assumed C_w , with good fits obtained for all C_w . Above $C_w = 0.2 \text{ mg m}^{-3}$ ($= 200 \text{ } \mu\text{g m}^{-3}$) the calculated R_{wall} is

constant. Below 0.2 mg m^{-3} the calculated R_{wall} falls off, reaching a second plateau at small C_w that is still above unity (Fig. 4). The plateaus at high and low C_w result from the best-fit SOM parameters varying with C_w to compensate for the differing amounts of loss of vapors to the walls while still maintaining the same suspended C_{OA} time-profile (Fig. S7). Since measurements demonstrate that vapors are lost directly to Teflon walls (Matsunaga and Ziemann, 2010), this indicates that when vapor wall-loss is accounted for assuming that the vapors interact only with wall-deposited particles the extent of the vapor loss is underestimated. That R_{wall} is constant above $C_w = 0.2 \text{ mg m}^{-3}$ demonstrates that our conclusions are robust with respect to the assumption regarding the exact value of C_w .

4.8 Consideration of historical experiments

To estimate the potential influence of vapor wall-losses for systems other than toluene, we calculated SOA yield biases for a variety of other VOCs (Ng et al., 2007; Chan et al., 2009; Chhabra et al., 2011, Loza et al., 2012; Cappa et al., 2013) (*Supplementary Materials, Fitting of historical chamber data*). It should be noted that the experimental conditions in the historical experiments are not identical to those for the toluene experiments, especially for high- NO_x conditions (*Supplementary Materials, Historical Experiments*). Although k_w for a given chamber is reasonably independent of the precursor compound, areasonably independent of the precursor. The results for the toluene experiments indicate that smaller α values generally correspond to larger R_{wall} . Therefore, a conservative, likely lower-bound estimate of R_{wall} has been obtained for each precursor assuming that $\alpha = 1$ during fitting and using $k_w = 1 \times 10^{-4} \text{ s}^{-1}$ (instead of 2.5×10^{-4}) to account for potential differences in the chamber used for these historical

experiments (Figs. S8-S10). The use of a smaller k_w will decrease R_{wall} , all other factors being equal. Calculated R_{wall} values range from as small as 1.1 to as large as 4.1 (Table 1 and Fig. S11). The typically smaller values for the high- NO_x vs. low- NO_x experiments reflect the much shorter reaction timescales and higher oxidant and NO_x concentrations in the historical high- NO_x experiments, as compared to the current experiments with toluene. Evidently, the extent to which vapor wall-loss will have influenced historical experiments is variable, yet potentially substantial and deserving of further investigation through new experiments and consideration of other datasets. Importantly, the results here indicate that quantitative analysis of SOA formation in chambers requires use of an explicitly time-dependent model that accounts for the simultaneous and competing condensation of vapors onto particles versus onto the chamber walls, representing a major shift from most historical analyses, which did not take time explicitly into account.

4.9 Implications

Our results show that the effect of vapor wall loss on SOA yields can be substantial. If reported SOA yields are low by factors of ~ 1.1 -4.2, as our results suggest they may be, then SOA concentrations simulated in 3D models will be correspondingly low. While the analysis presented here for the toluene SOA system needs to be comprehensively expanded to other main classes of SOA precursors, beyond the assessment above, it is likely that a lack of proper accounting for vapor wall-losses that suppress chamber-derived SOA yields contribute substantially to the underprediction of ambient SOA concentrations in atmospheric models.

4.10 Acknowledgements

We thank Alma Hodzic, Julia Lee-Taylor, Sasha Madronich (NCAR), Paul Ziemann (CU Boulder), Paul Wennberg (Caltech), Manabu Shiraiwa (MPIC) and Anthony Wexler (UC Davis) for useful discussions. This work was supported by the National Science Foundation grants ATM-1151062 and AGS-1057183, Department of Energy grant DE-SC 0006626, and the California Air Resources Board contract 12-312. Any opinions, findings, and conclusions or recommendations expressed in this material are those of the author(s) and do not necessarily reflect the views of the funding agencies.

4.11 Bibliography

Cappa, C. D. and Wilson, K. R.: Multi-generation gas-phase oxidation, equilibrium partitioning, and the formation and evolution of secondary organic aerosol, *Atmos. Chem. Phys.*, 12, 9505-9528, 2012.

Cappa, C. D., Zhang, X., Loza, C. L., Craven, J. S., Yee, L. D., Seinfeld, J. H.: Application of the Statistical Oxidation Model (SOM) to secondary organic aerosol formation from photooxidation of C12 Alkanes, *Atmos. Chem. Phys.*, 13, 1591-1606, 2013.

Chan, A. W. H., Kautzaman, K. E., Chhabra, P. S., Surratt, J. D., Chan, M. N., Crouse, J. D., Kurten, A., Wennberg, P. O., Flagan, R. C., and Seinfeld, J. H.: Secondary organic aerosol formation from photooxidation of naphthalene and alkylnaphthalenes: implications for oxidation of intermediate volatility organic compounds (IVOCs), *Atmos. Chem. Phys.*, 9, 3049-3060, 2009.

Chhabra, P. S., Flagan, R. C., and Seinfeld, J. H.: Elemental analysis of chamber organic aerosol using an aerodyne high-resolution aerosol mass spectrometer. *Atmos. Chem. Phys.*, 10, 4111-4131, 2010.

Chhabra, P. S., Ng, N. L., Canagaratna, M. R., Corrigan, A. L., Russell, L. M., Worsnop, D. R., Flagan, R. C., and Seinfeld, J. H.: Elemental composition and oxidation of chamber organic aerosol, *Atmos. Chem. Phys.*, 11(17), 8827-8845, 2011.

Crump, J. G. and Seinfeld, J. H.: Turbulent deposition and gravitational sedimentation of an aerosol in a vessel of arbitrary shape, *J. Aerosol Sci.*, 12, 405-415, 1981.

Hildebrandt, L., Donahue, N. M., and Pandis, S. N.: High formation of secondary organic aerosol from the photo-oxidation of toluene, *Atmos. Chem. Phys.*, 9(9), 2973-2986, 2009.

Lee-Taylor, J., Madronich, S., Aumont, B., Baker, A., Camredon, M., Hodzic, A., Tyndall, G. S., Apel, E., Zaveri, R. A.: Explicit modeling of organic chemistry and secondary organic aerosol partitioning for Mexico City and its outflow plume, *Atmos. Chem. Phys.*, 11, 13219-13241, 2011.

Loza, C. L., Chhabra, P. S., Yee, L. D., Craven, J. S., Flagan, R. C., and Seinfeld, J. H.: Chemical aging of m-xylene secondary organic aerosol: laboratory chamber study, *Atmos. Chem. Phys.*, 12(1), 151-167, 2012.

Loza, C. L., Chan, A. W. H., Galloway, M. M., Keutsch, F. N., Flagan, R. C., and Seinfeld, J. H.: Characterization of Vapor Wall Loss in Laboratory Chambers. *Environ. Sci. Technol.*, 44, 5074-5078, 2010.

Loza, C. L., Craven, J. S., Yee, L. D., Coggon, M. M., Schwantes, R. H., Shiraiwa, M., Zhang, X., Schilling, K. A., Ng, N. L., Canagaratna, M. R., Ziemann, P. J., Flagan, R. C.,

and Seinfeld, J. H.: Secondary organic aerosol yields of C₁₂-carbon alkanes, *Atmos. Chem. Phys. Discuss.*, 14, 1423-1439, 2014.

Matsunaga, A. and Ziemann, P. J.: Gas-Wall Partitioning of Organic Compounds in a Teflon Film Chamber and Potential Effects on Reaction Product and Aerosol Yield Measurements. *Aerosol Sci. Technol.*, 44, 881-892, 2010.

McMurry, P. H. and Grosjean, D.: Gas and aerosol wall losses in Teflon film smog chambers, *Environ. Sci. Technol.* 19, 1176-1182, 1985.

Ng, N. L., Kroll, J. H., Chan, A. W. H., Chhabra, P. S., Flagan, R. C., and Seinfeld, J. H.: Secondary organic aerosol formation from m-xylene, toluene, and benzene, *Atmos. Chem. Phys.*, 7(14), 3909-3922, 2007.

Pankow, J. F.: An absorption-model of the gas aerosol partitioning involved in the formation of secondary organic aerosol. *Atmos. Environ.* 28, 189-193, 1994.

Pierce, J. R., Engelhart, G. J., Hildebrandt, L., Weitkamp, E. A., Pathak, R. K., Donahue, N. M., Robinson, A. L., Adams, P. J., and Pandis, S. N.: Constraining Particle Evolution from Wall Losses, Coagulation, and Condensation-Evaporation in Smog-Chamber Experiments: Optimal Estimation Based on Size Distribution Measurements. *Aerosol Sci. and Technol.*, 42, 1001-1015, 2008.

Seinfeld, J. H. and Pandis, S. N.: *Atmospheric chemistry and physics: From air pollution to climate change*, Wiley, New Jersey, 612pp., 2006.

Shiraiwa, M., Yee, L. D., Schilling, K. A., Loza, C. L., Craven, J. S., Zuend, A., Ziemann, P. J., and Seinfeld, J. H.: Size distribution dynamics reveal particle-phase chemistry in organic aerosol formation. *Proc. Nat. Acad. Sci.*, 110(29), 11746-11750, 2013.

Weitkamp, E. A., Sage, A. M., Pierce, J. R., Donahue, N. M., and Robinson, A. L.: Organic aerosol formation from photochemical oxidation of diesel exhaust in a smog chamber. *Environ. Sci. & Technol.*, 41, 6969-6975, 2007.

Table 4.1. Average biases in SOA yields due to vapor wall-losses for various VOCs under low- and high-NO_x conditions.

VOC ^a	Low-NO _x R _{wall} ^b	High-NO _x R _{wall} ^b
toluene (this study)	2.1 – 3.6	2.1 – 4.2
n-dodecane (Loza et al., 2014)	4.1 ± 0.8 ^d	1.16 ± 0.08
2-methylundecane (Loza et al., 2014)	3.7 ± 0.5	1.4 ± 0.2
cyclododecane (Loza et al., 2014)	3.0 ± 0.3	1.10 ± 0.05
hexylcyclohexane (Loza et al., 2014)	2.4 ± 0.3	1.16 ± 0.07
toluene (Ng et al., 2007)	1.9 ± 0.4	1.13 ± 0.06
benzene (Ng et al., 2007)	1.8 ± 0.4	1.25 ± 0.1
m-xylene (Ng et al., 2007)	1.8 ± 0.4	1.2 ± 0.1
m-xylene (Loza et al., 2012)	1.6 ± 0.3	-
naphthalene (Chan et al., 2009)	1.2 ± 0.1	1.2 ± 0.1
α-pinene + OH (Chhabra et al., 2011)	1.6 ± 0.3	1.3 ± 0.1
isoprene + OH (Chhabra et al., 2011)	3.14	2.22

^a For all VOC's except toluene (this study), $k_w = 1 \times 10^{-4} \text{ s}^{-1}$ and $\alpha = 1$. For toluene (this study), $k_w = 2.5 \times 10^{-4} \text{ s}^{-1}$ and $\alpha = 0.002$ (low NO_x) or 0.001 (high-NO_x).

^b Calculated for the period when $C_{\text{SOA}} > 0.5 \text{ } \mu\text{g m}^{-3}$ through the end of a given experiment.

^c For toluene, the reported R_{wall} indicate the range of values determined at different initial seed SA.

^d Uncertainties are 1σ uncertainties are 1 of value.

Figure 4.1. Hourly averaged lower bound SOA yields over the course of a toluene photooxidation experiment as a function of initial AS seed surface area for (A) high- NO_x and (B) low- NO_x conditions. Symbol color indicates the SOA mass concentration and symbol size the time after lights were turned on. The filled circles are from the current experiments and the open diamonds from Ng et al. (2007). The dashed gray line and \times are the end-of-experiment yields from the optimized best-fit SOM simulations.

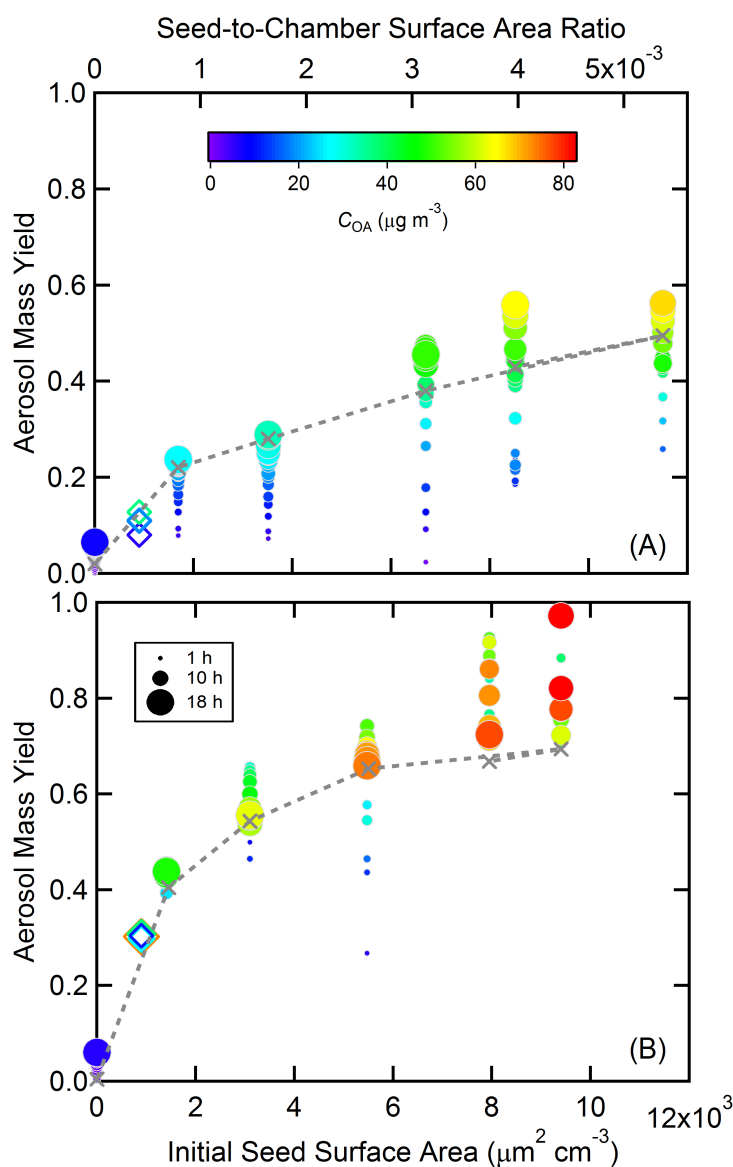


Figure 4.2. Observed (points) and simulated (lines) SOA concentrations for each photochemical oxidation experiment performed for different initial inorganic seed surface area for (A) low- NO_x and (B) high- NO_x conditions. The dashed lines indicate the experiment to which the SOM was explicitly fit, and the solid lines indicate simulation results based on those fits. (C) The wall-loss bias factor, R_{wall} , as a function of seed surface area. Filled symbols use the optimal k_w/α pair and the corresponding best-fit SOM parameters determined from (A) and (B). Open symbols assume $\alpha = 1$ and each experiment was individually fit using the optimal k_w . The error bars indicate the 1σ standard deviation in R_{wall} for each experiment over the period when $C_{\text{OA}} > 0.5 \text{ mg m}^{-3}$.

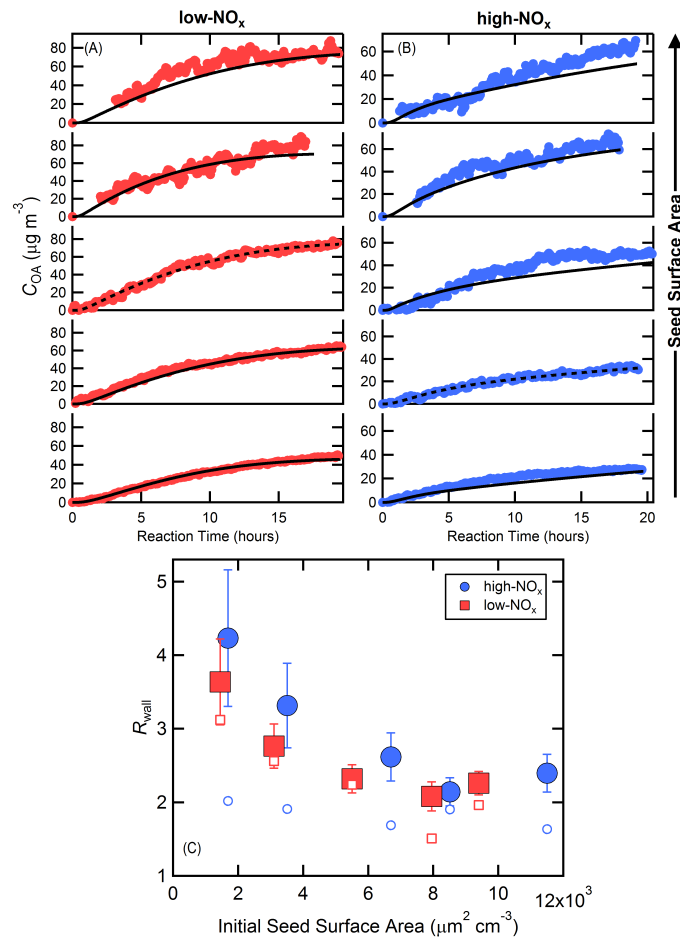


Figure 4.3. Calculated SOA yield bias as a function of initial toluene concentration and OH concentration when $k_w = 2.5 \times 10^{-4} \text{ s}^{-1}$ and $C_w = 10 \text{ mg m}^{-3}$. The R_{wall} values for a given [toluene] and [OH] are indicated by colors and contours and are averaged over the period when $C_{\text{SOA}} > 0.5 \text{ } \mu\text{g m}^{-3}$ to the end of an experiment at 18 h. Results are based on the optimal fit of the SOM to the low- NO_x experiments.

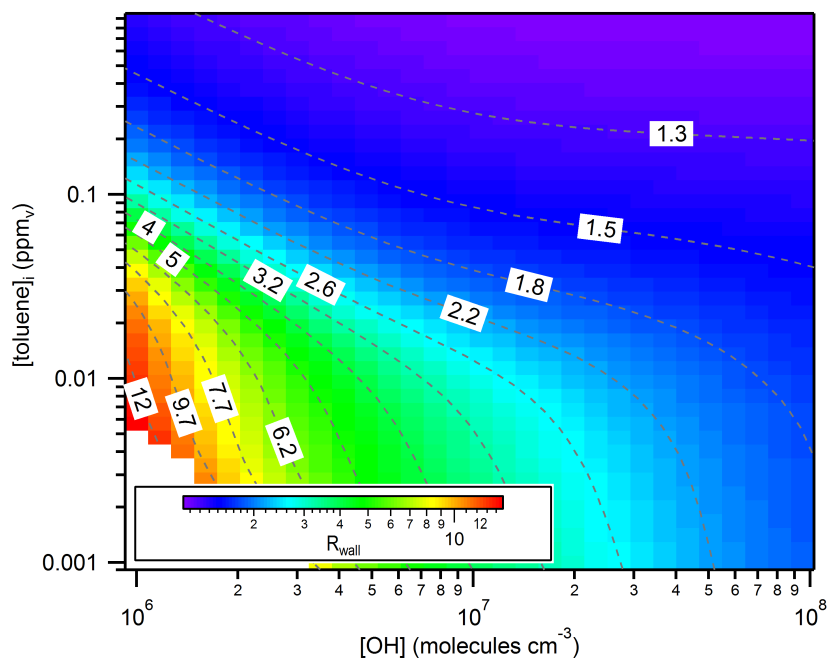
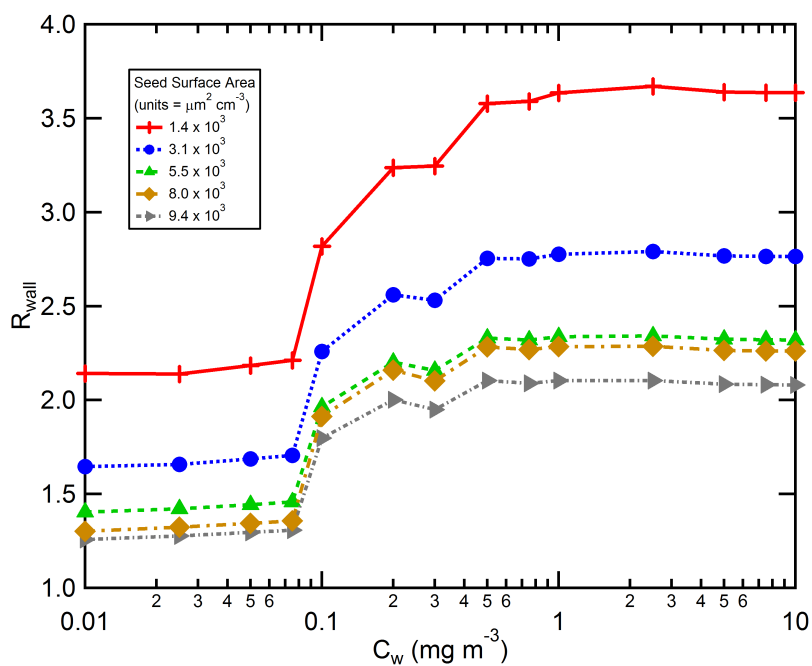


Figure 4.4. Calculated vapor wall-loss bias, R_{wall} , as a function of the effective wall mass concentration, C_w , for the low- NO_x toluene photooxidation experiments at varying initial seed surface area. For each C_w , the SOM was fit to the experiment with seed surface area = $5.5 \times 10^3 \mu\text{m}^2 \text{cm}^{-3}$ using $k_w = 2.5 \times 10^{-4} \text{s}^{-1}$ and $\alpha = 2 \times 10^{-3}$. The determined best-fit SOM parameters were then used to simulate SOA formation for the experiments performed at other seed concentrations but assuming the same C_w .



Supplemental Materials

S4.1 Experiments

S4.1.1 Toluene Photooxidation Experiments

Toluene SOA formation experiments were conducted in the new Caltech dual 24-m³ Environmental Chambers, in which the temperature (T) and relative humidity (RH) are automatically controlled. Prior to each experiment, the Teflon chambers were flushed with clean, dry air for 24 h until the particle number concentration $< 10 \text{ cm}^{-3}$ and volume concentration $< 0.01 \text{ } \mu\text{m}^3 \text{ cm}^{-3}$. Ammonium sulfate (AS) seed aerosol was injected into the chamber by atomizing 0.015 or 0.1 M aqueous $(\text{NH}_4)_2\text{SO}_4$ solution into the chamber for 30 to 120 min. The resulting total AS seed surface area ranged from $\sim 1 \times 10^3 \text{ } \mu\text{m}^2 \text{ cm}^{-3}$ up to $\sim 1 \times 10^4 \text{ } \mu\text{m}^2 \text{ cm}^{-3}$, and the corresponding particle-to-wall surface area ratio ranged from $\sim 1 \times 10^{-3}$ to 7×10^{-3} . Hydrogen peroxide (H_2O_2) was used for the OH source by evaporating 120 μL of 50% *wt* aqueous solution into the chamber with 5 L min^{-1} of purified air for ~ 100 min, resulting in an approximate starting H_2O_2 concentration of 2.0 ppm. 3 μL toluene (Sigma-Aldrich, 99.8% purity) was injected into a glass bulb, which was connected into the Teflon chamber. 5 L min^{-1} of purified air flowed through the glass bulb into the chamber for ~ 15 min, introducing ~ 40 ppb toluene into the chamber. For experiments at elevated NO_x (i.e. high- NO_x conditions) NO and NO_2 were added to the chamber at the start of a given experiment until the concentrations were ~ 17 ppb and 30 ppb, respectively. The initial $[\text{VOC}]/[\text{NO}_x]$ in the high- NO_x experiments ranged from 4.8-6.0 ppbC/ppb. After ~ 90 min mixing, photooxidation was initiated by irradiating the chamber with black lights

with output wavelength ranging from 300 to 400 nm. The irradiation leads to photolysis of H_2O_2 to produce OH radicals with an approximately constant concentration throughout the entire experiment. Temperature and relative humidity of all experiments were ~ 298 K and $\sim 3\%$, respectively. The initial O_3 concentration was below detection limit in all experiments. H_2O_2 exerts an interference on the O_3 detection, increasing the O_3 monitor readout by ~ 2 -3 ppb in the current study. NO was continuously injected into the chamber over the course of each experiment at 80 ppb h^{-1} for the first 2.5 h of reaction, then 50 ppb h^{-1} for the next 4.5 h of reaction, and then 30 ppb h^{-1} for the remainder of the reaction. Experimental conditions (e.g. [VOC], seed surface area, $[\text{NO}_x]$) for each experiment are reported in Table S1.

A suite of instruments was used to monitor toluene SOA formation and evolution. T, RH, NO, NO_x and O_3 were continuously monitored. Toluene concentration was monitored using a gas chromatograph with flame ionization detector (GC/FID, Agilent 6890N), equipped with a HP-5 column (15 m \times 0.53 mm ID \times 1.5 μm thickness, Hewlett-Packard). Particle size distribution and number concentration were measured by a cylindrical differential mobility analyzer (DMA; TSI Model 3081) coupled to a condensation particle counter (TSI Model 3010). The DMA was operated in a closed system with a recirculating sheath and excess flow of 2.67 L min^{-1} and a $5.4 : 1$ ratio of sheath to aerosol flow rate. The column voltage was scanned from 15 to 9850 V over 45 s.

S4.1.2 Historical Experiments

All the other SOA formation experiments used in SOM optimal fitting were carried out in the Caltech dual 28-m^3 Environmental Chambers. Details of experimental

protocols can be found in (Cappa et al., 2013; Chan et al., 2009; Chhabra et al., 2010, 2011; Loza et al., 2012; Ng et al., 2007). Experimental conditions are reported in Tables S2 and S3 and differences in methodology from the above toluene photooxidation experiments are highlighted below. An identical suite of instrumentation was used as in the toluene photooxidation experiments. The historical experiments typically had seed *SA* around $1-2 \times 10^3 \text{ cm}^{-3}$, corresponding to the lowest seeded experiments in the toluene photooxidation experiments. The majority of the historical low- NO_x experiments examined in this study used similar methods and conditions as the new toluene experiments, i.e. used H_2O_2 as the OH source. The experimental procedures associated with the high- NO_x experiments differed from the new toluene experiments. Specifically, for the historical high- NO_x experiments the primary OH source was HONO photolysis, as opposed to H_2O_2 photolysis. This has the practical implication of leading to reaction conditions where (i) the OH concentration is initially $\sim \text{O}(10^7 \text{ molecules cm}^{-3})$ and decays rapidly over a period of $\sim 1-3$ hours and (ii) the initial $[\text{VOC}]/[\text{NO}_x]$ ratio tends to be much smaller compared to the current experiments. Thus, the timescales of SOA formation during the historical high- NO_x experiments were, in general, very different than for the toluene photooxidation experiments: rapid formation over approximately 1-2 hours vs. continuous formation over 18 hours. For high- NO_x experiments, NO_x was added prior to the lights being turned on both from the HONO injection, which introduces some NO_2 , and from addition of NO. Additional NO was produced upon photolysis of HONO. Typical initial NO_x concentrations were on the order of 500 ppb, corresponding to initial $[\text{VOC}]/[\text{NO}_x]$ of $\sim 0.5 \text{ ppbC/ppb}$ (Table S3).

S4.1.3 Particle Wall-Loss Correction

Particle wall losses during an experiment must be accounted for. Two limiting assumptions have been made for the interactions between those particles that have deposited on the wall and suspended vapors in determining the corrected suspended SOA concentrations (Hildebrandt et al., 2009; Loza et al., 2012; Weitkamp et al., 2007). In one case, particles deposited on the wall are assumed to cease interaction with the suspended vapors and no loss of vapors to the walls is accounted for. This case gives the lower bound of the total organic mass concentration, since particles remain the same size as at the moment they deposited on the wall for the remainder of the experiment. SOA concentrations determined from this case are used for the primary analysis in the manuscript, which is appropriate because vapor loss to the walls is treated separately. In the second limiting case, particles deposited on the wall are assumed to continue to interact with the suspended vapors as if they had remained suspended, with the wall-bound particles assumed to grow at the same rate as suspended particles in the chamber. The corrected SOA concentrations in this case are larger than in the first case because of the additional uptake of vapors to wall-bound particles. This case provides an upper-bound on the actual SOA formed under the assumption that the vapors interact with wall-bound particles, but not the Teflon walls (Hildebrandt et al., 2009; Loza et al., 2012; Weitkamp et al., 2007). However, traditional application of this second case does not account for the substantially differing timescales of gas-particle vs. gas-wall transport, nor does it account for loss of vapors to the chamber walls and the substantially larger amount of effective absorbing mass of the walls (C_w) compared to the deposited particles. Compared with

C_w (10 mg m^{-3}), which is assumed as a constant from the onset of the experiment, the total organic mass deposited on the chamber wall over the course of 18 h photooxidation is ~ 3 orders of magnitude lower. As such, this “upper bound” can underestimate the actual SOA formation, as it accounts for only a subset of the overall vapor wall-loss correction. Nonetheless, the “upper bound” corrected results are provided for reference to previous experiments.

For either case, the Aerosol Parameter Estimation (APE) model (Pierce et al., 2008), derived on the basis of the aerosol general dynamic equation (Seinfeld and Pandis, 2006), is employed to calculate these two limits. The suspended particle population evolves as a result of three processes: coagulation, condensation, and wall-loss. The change of suspended particle number-size distribution due to coagulation is well constrained. The size-dependent wall loss rate is determined by experimentally monitoring the decay of dry inert $(\text{NH}_4)_2\text{SO}_4$ particles assuming first-order kinetics. The condensation rate is the only free parameter in the model, which can be obtained by optimal fitting of the APE model predictions to the DMA measured particle size distribution at each time step. Once the condensation rate values are estimated, they can be applied to parameterize the growth of particles on the walls due to condensation of gaseous vapor and deposition of suspended particles. A factor that describes the extent of interactions between deposited particles and suspended vapors is applied when summing aerosol masses in the chamber core and on the walls. A value of 0 for this factor corresponds to no condensation to deposited particles. A value of 1 for this factor corresponds to the case where the condensation rate of gaseous vapors to deposited particles is the same as those suspended. The primary

analysis in this work utilizes the corrected particle mass under the assumption of no condensation to deposited particles because vapor wall loss is treated separately. The evolution of the wall-loss corrected particle size distributions is shown for each experiment in Figure S4.1 for the lower limit case. The time-dependent aerosol growth, from which the aerosol yield can be calculated, is shown for each experiment in Figure S4.2 for both limiting cases.

S4.2 Optimizing k_w and α

The optimal values of k_w and α were determined using the general procedure as outlined below. There were a total of 6 experiments conducted for each NO_x condition, 5 with seed aerosol and 1 without. Only the seeded experiments are considered in the optimization method because of difficulties associated with specification of nucleation. The SOM was fit to one of these 5 seeded experiments for a variety of k_w and α values. For each k_w/α pair a set of best-fit SOM parameters (i.e. DLVP, m_{frag} and the P_{func} array) were determined. Specifically, the experiments with seed $SA = 5.5 \times 10^3 \text{ mm}^2 \text{ cm}^{-3}$ (low- NO_x) and $SA = 3.5 \times 10^3 \text{ mm}^2 \text{ cm}^{-3}$ (high- NO_x) were used for fitting. These best-fit SOM parameters and the associated k_w/α pair were then used to simulate SOA formation for the other 4 seeded experiments. Reduced goodness of fit metric (χ_{red}^2) values were calculated for each experiment as:

$$\chi_{\text{red}}^2 = \frac{1}{n-6-1} \sum \left(\frac{C_{\text{OA,obs}}(t) - C_{\text{OA,model}}(t)}{\sigma_{\text{OA,obs}}(t)} \right)^2 \quad (\text{S4.1})$$

where n is the number of data points per experiment, 6 is the number of model degrees of freedom and $\sigma_{\text{OA,obs}}$ is the uncertainty in the observations. For each

experiment, the minimum c_{red}^2 across all k_w/α pairs was determined, and the set of c_{red}^2 values for each experiment was normalized by the minimum in that set. Normalization ensures that the different experiments carry equal weight in the next step. The composite c_{red}^2 across all seeded experiments was then determined as:

$$\chi_{\text{red,composite}}^2(k_w, \alpha) = \sum_{i=1}^5 \chi_{\text{red, norm, i}}^2(k_w, \alpha) \quad (\text{S4.2})$$

where the sum is over the normalized c_{red}^2 for all seeded experiments. Smaller values of the composite c_{red}^2 indicate overall better agreement across all of the seeded experiments for a given set of best-fit SOM parameters, k_w and α . A contour diagram of the calculated composite c_{red}^2 as a function of k_w and α (Figure S4.3) illustrates that only certain combinations of k_w and α provide for good agreement across all experiments. There is almost no seed effect when $\alpha > 0.1$, and therefore the overall agreement is poor no matter what k_w is used. As α is lowered, a seed effect becomes evident. However, only when α is $O(10^{-3})$ and k_w is $O(10^{-4})$ can overall good agreement with all experiments be obtained. Since the k_w and α values were not determined from a specific fitting algorithm, we refer to the values that provide for best agreement as the “optimal” values rather than “best fit” values. These are: $k_w = 2.5 \times 10^{-4} \text{ s}^{-1}$ and $\alpha = 2 \times 10^{-3}$ for low- NO_x experiments and $k_w = 2.5 \times 10^{-4} \text{ s}^{-1}$ and $\alpha = 1 \times 10^{-3}$ for high- NO_x experiments.

S4.3 The Statistical Oxidation Model

The SOM simulates the oxidation of a given hydrocarbon as a trajectory through a 2-D grid of carbon and oxygen atoms in which “species” are considered particular

carbon/oxygen combinations (e.g. $C_{12}O_4$). Specific rules define the movement through this space, describing the probability that a reaction leads to functionalization or fragmentation, how many oxygen atoms are added per reaction, and the decrease in vapor pressure that occurs upon addition of a single oxygen atom. SOM effectively simulates the multi-generational chemistry that characterizes photooxidation experiments. Full details are provided in Cappa et al. (2012, 2013). The fragmentation probability (P_{frag}) depends on the oxygen content of the reacting species and is parameterized as:

$$P_{\text{frag}} = \left(\frac{N_{\text{O}}}{N_{\text{C}}} \right)^{m_{\text{frag}}} \quad (\text{S4.3})$$

where m_{frag} is an adjustable parameter, and N_{O} and N_{C} are the number of oxygen and carbon atoms comprising an SOM species, respectively. The P_{frag} is always constrained to be ≤ 1 . (Recently, a “bug” in the SOM code was found related to how the fragmentation was being treated. Rather than the probability of fragmentation depending on the oxygen content of the reacting species, it was being determined based on the oxygen content of the product species. This has now been fixed. The SOM was originally written in the IGOR programming language. The SOM has now been independently implemented in Fortran using the framework outlined in Cappa et al. (2013) and the IGOR and Fortran versions produce equivalent results, suggesting that no further “bugs” of this sort exist. The best-fit SOM parameters for the alkanes differ from those reported in Cappa et al. (2013) as a result of this update and because vapor wall-loss has been included.

The functionalization probability (P_{func}) describes the likelihood of adding 1, 2, 3 or 4 oxygen atoms per reaction, and each can be adjusted independently, subject to the constraint that they are positive and must sum to 1. The decrease in vapor pressure (or more specifically, in the log of the saturation concentration, C^* , in mg m^{-3}) per oxygen added is referred to as DLVP, and ranges from ~ 0.7 to 2.5, depending on the type of functional group added. Thus, there are 6 total adjustable (tunable) parameters in the base model: (i) fragmentation, (ii) volatility decrease per oxygen added and (iii-vi) oxygen addition probability. For this study, heterogeneous OH reactions are not simulated.

The reaction rate coefficient matrix associated with reactions of product species with OH radicals has been updated from the original SOM on the basis of comparison with output from the GECKO-A model for simulations of the outflow from Mexico City (Lee-Taylor et al., 2011). The reaction rate coefficient of the parent hydrocarbon with OH, k_{OH} ($\text{cm}^3 \text{ molecules}^{-1} \text{ s}^{-1}$), is specified to be consistent with literature results, e.g. for toluene $k_{\text{OH}} = 5.2 \times 10^{-12} \text{ cm}^3 \text{ molecules}^{-1} \text{ s}^{-1}$. For all other species within the SOM grid, the k_{OH} are determined referenced to the reaction rate coefficient for species with the same number of carbon atoms but zero oxygen atoms as:

$$\log(k_{\text{OH,base}}) = A_1 + A_2 \times N_{\text{C}}^{A_3} \quad (\text{S4.4})$$

and where $A_1 = -15.103$, $A_2 = -3.9481$, and $A_3 = -0.79796$. For a given N_{C} , the k_{OH} is temperature dependent and varies with N_{O} as

$$k_{\text{OH}}(T) = k_{\text{OH,base}} \times T^2 \times \exp\left(-1 \times \frac{E_a}{8.314 \times T}\right) \times \left[1 + \frac{b_1}{\sigma \sqrt{2\pi}} \exp\left(-\frac{1(\ln(N_{\text{O}} + 0.01) - \ln(b_2))^2}{2\sigma^2}\right)\right] \quad (\text{S4.5})$$

and where the variables b_1 , b_2 , and s are functions of N_{C} , with

$$\sigma(N_C \leq 15) = 0.0214 \times N_C + 0.5238; \quad \sigma(N_C > 15) = -0.115 \times N_C + 2.695, \quad (\text{S4.6})$$

$$b_1 = -0.2583 \times N_C + 5.8944, \quad (\text{S4.7})$$

And

$$b_2(N_C \leq 15) = 0.0314 \times N_C + 0.9871; \quad b_2(N_C > 15) = 0.25 \times N_C - 2.183. \quad (\text{S4.8})$$

Within the SOM gas-particle partitioning is treated through the framework of absorptive partitioning theory (Pankow, 1994), in which compounds partition between the gas and particle phases according to their Raoult's Law adjusted vapour pressures. Unlike in previous usages of the SOM, which assumed instantaneous gas-particle equilibrium, the SOM here treats gas-particle mass transfer dynamically. The net flux of molecules to/from the particle is calculated at each time step as:

$$\frac{\partial C_{\text{OA},i}}{\partial t} = 4\pi D_{\text{gas},i} R_p N_p F_{\text{FS}} (C_{\text{gas},i}^{\infty} - \chi_i C_i^*) \quad (\text{S4.9})$$

where $D_{\text{gas},i}$ is the gas-phase diffusivity, R_p is particle radius, N_p is particle number concentration, F_{FS} is the Fuchs-Sutugin correction for noncontinuum mass transfer, $C_{\text{gas},i}^{\infty}$ is the gas-phase concentration, c_i is the mass fraction and C_i^* is the saturation concentration of species i . The entire SOA mass is considered absorbing in the calculation of c_i . It is assumed that $D_{\text{gas},i}$ varies with molecular weight (M_w) and is equal to $D_{\text{CO}_2}(M_{w\text{CO}_2}/M_{w_i})$, with $D_{\text{CO}_2} = 1.38 \times 10^{-5} \text{ m}^2 \text{ s}^{-1}$. The Fuchs-Sutugin correction is equal to:

$$F_{\text{FS}} = \frac{0.75\alpha(1+Kn)}{Kn^2 + Kn + 0.283 \cdot Kn \cdot \alpha + 0.75\alpha} \quad (\text{S4.10})$$

where a is the mass accommodation coefficient onto particles and Kn is the Knudsen number, defined as:

$$Kn = \lambda / R_p \quad (\text{S4.11})$$

and λ is the gas mean free path, which is equal to:

$$\lambda_i = 3 \cdot \frac{D_{\text{gas},i}}{\bar{c}_i} \quad (\text{S4.12})$$

with \bar{c}_i equal to the root mean square speed of the gas, which is equal to:

$$\bar{c}_i = \left(\frac{8N_A kT}{\pi M w_i} \right)^{\frac{1}{2}} \quad (\text{S4.13})$$

with N_A = Avagadro's number, k = the Boltzmann constant and T = temperature. The results obtained with the dynamic partitioning SOM are equivalent to those obtained using the instantaneous equilibrium assumption when $\alpha > 0.1$ and with seed aerosols present. It should be noted that a as used in Eqn. S8 represents the net mass transfer and can include resistances both in the gas-phase and at the particles surface. Full accommodation of vapors into the bulk particle can be limited by diffusion within the particles when particles are highly viscous (Shiraiwa et al., 2013). The dynamic SOM utilized here uses monodisperse particles with a size equal to the number mean diameter and the number concentration adjusted to give the desired initial seed surface area (SA). Although the ideal model would use the actual seed size distribution as input, we have established that for particle diameters larger than ~ 50 nm the model results are sufficiently insensitive to the selected particle diameter for a fixed seed SA . As such, the results here are not limited by the simplification of using monodisperse particles. Nucleation is not explicitly simulated by the SOM. Therefore, dynamic

SOM calculations for the nucleation experiments have been carried out assuming an initial seed size of 5 nm and a seed concentration equal to that observed at the end of the experiment. Given that there is substantial uncertainty associated with this assumption the nucleation experiments have not been quantitatively assessed.

S4.4 Vapor Wall-Loss

Loss of vapors to the chamber walls is simulated as a first-order process, characterized by the first-order wall-loss coefficient k_w (s^{-1}). Vapor wall-losses are assumed to be reversible, characterized by the gas-wall partitioning coefficient, K_w , which is dependent upon compound vapor pressure,

$$K_w = \frac{RT}{M_w \gamma_w P_{\text{sat}}} \quad (\text{S4.14})$$

where R is the ideal gas constant, T is temperature (assumed 298 K), M_w is the effective molecular weight of the wall material, γ_w is the activity coefficient, and P_{sat} is the saturation concentration of the species of interest. It is convenient to use the saturation concentration, C^* (mg m^{-3}), instead of the saturation vapor pressure, where

$$C^* = \frac{I}{K_p} = \frac{M_p \gamma_p P_{\text{sat}}}{RT} \quad (\text{S4.15})$$

with K_p the gas-particle partitioning coefficient, M_p the average molecular weight of the organic species comprising the particles and γ_p is the activity coefficient. The rate coefficient for transfer of gas-phase species onto the walls is given as $k_{w,\text{on}}$ while that for evaporation from the walls is given as $k_{w,\text{off}}$. The $k_{w,\text{on}}$ is specified as a model input

parameter (and is equivalent to the k_w in the main text). The $k_{w,off}$ is obtained from detailed balance as:

$$k_{w,off} = \frac{k_{w,on}}{K_w C_w} = k_{w,on} \left(\frac{C^* M_w \gamma_w}{C_w M_p \gamma_p} \right) \quad (S4.16)$$

and where C_w is the equivalent wall OA concentration ($\mu\text{g m}^{-3}$). If one makes the simple assumption that $M_w = M_p$ and $\gamma_w = \gamma_p$, then C_w can be viewed as an effective concentration that accounts for differences in molecular weight and activity between the particles and walls. The C_w must therefore be estimated from experiments. Matsunaga and Ziemann (2010) report a range of C_w values that are constant within a given class of molecules (e.g. ketones vs. alkanes), with $C_w = 2, 4, 10$ and 24 mg m^{-3} for alkanes, alkenes, alcohols and ketones. For all reported simulations here it has been assumed that $C_w = 10 \text{ mg m}^{-3}$. Results are reasonably insensitive to the choice of C_w over the previously determined range because $C_w \gg C_{OA}$. The sensitivity of our results to the assumed C_w is discussed further below in Section 4.1.4.3. It is assumed that $k_{w,on}$ is not dependent on compound identity. Consequently, the $k_{w,off}$ terms vary with compound identity, specifically with C^* . The value of $k_{w,on}$ can be estimated from consideration of just the gas-phase transport terms within a chamber. McMurry and Grosjean (1985) report an expression for $k_{w,on}$,

$$k_{w,on} = \left(\frac{A}{V} \right) \frac{\left(\frac{\alpha_w \bar{c}}{4} \right)}{1.0 + \left(\frac{\pi}{2} \right) \left[\frac{\alpha_w \bar{c}}{4(k_e D_{\text{gas}})^{0.5}} \right]} \quad (S4.17)$$

where A/V is the surface to volume ratio of the chamber (equal to $6/L$ for a square chamber, and where L is the length of one side), α_w is the mass accommodation

coefficient of vapors onto the chamber walls, \bar{c} is the mean thermal speed of the molecules, k_e is the coefficient of eddy diffusion, and D_{gas} is the molecular diffusivity. It should be noted that α_w is not necessarily equal to α for uptake onto particles. For the type of molecules here, D_{gas} is $\sim 3 \times 10^{-6} \text{ m}^2 \text{ s}^{-1}$ and $\bar{c} \sim 200 \text{ m s}^{-1}$. This leaves k_e and α_w as the two key unknowns. Values of $k_{w,on}$ have been calculated as a function of k_e for α_w ranging from 10^{-7} to 1, where 1 is perfect accommodation. k_e values from 10^{-3} s^{-1} to 1 s^{-1} have been used, which corresponds to mixing timescales of 17 min to 1 s (Figure S4.4). McMurry and Grosjean (1985) reported values for their actively mixed chambers of 0.02 s^{-1} (60 m^3 chamber) and 0.12 s^{-1} (4 m^3 chamber). Since the Caltech chamber is not actively mixed it is expected that the characteristic k_e value is considerably smaller.

The value of k_e for the Caltech chamber is estimated based on observed size-dependent deposition rates of particles in the chamber. The minimum in the k_w for particles as a function of size is dependent upon k_e . This minimum occurs at a diameter of $\sim 350 \text{ nm}$ for the 24 m^3 Caltech chamber and at $\sim 250 \text{ nm}$ for the 28 m^3 chamber (Loza et al., 2012). For particles in a cubic chamber the k_w is related to the eddy diffusion coefficient through the equation (Grump and Seinfeld, 1981):

$$k_w = \frac{1}{L} \left[\frac{8\sqrt{k_e D}}{\pi} + v \coth\left(\frac{x}{2}\right) \right] \quad (\text{S4.18})$$

where v is the particle terminal settling velocity (m s^{-1}) and x is defined as:

$$x = \frac{\pi v}{2\sqrt{k_e D}} \quad (\text{S4.19})$$

From Eqn. S5, k_w has been calculated as a function of particle diameter and the k_e value adjusted until the minimum occurs at 250 nm or 350 nm. The required k_e in the 24 m³ chamber is 0.075 s⁻¹ and in the 28 m³ chamber is 0.015 s⁻¹, similar to the values reported by McMurry and Grosjean for 60 m³ ($k_e = 0.12$ s⁻¹) and 4 m³ ($k_e = 0.02$ s⁻¹) chambers (McMurry and Grosjean, 1985). Therefore, it is expected that the *maximum* $k_w \sim 6.0 \times 10^{-4}$ s⁻¹ for the 24 m³ chamber and $\sim 3 \times 10^{-4}$ for the 28 m³ chamber from consideration of Figure S4.4. Since the accommodation coefficient for the condensing species on the Teflon chamber walls is not known, it is not possible to definitively put a lower bound on the k_w . However, the experimental results of Matsunaga and Ziemann (2010) clearly demonstrate that vapors are taken up to their chamber walls quite rapidly, and they estimate that $\alpha_w \sim 10^{-5}$, which suggests that $k_w \sim 3 \times 10^{-4}$ s⁻¹ (24 m³) or $\sim 2 \times 10^{-4}$ s⁻¹ (28 m³). This theoretical estimate is in very good agreement with the optimal k_w ($= 2 \times 10^{-4}$ s⁻¹) for the 24 m³ chamber.

Loza et al. (2010) report observations of vapor wall-loss rates for two compounds: 2,3-epoxy-1,4-butanediol (BEPOX) and glyoxal. BEPOX is the butadiene derivative of an epoxydiol of isoprene. The uptake of both compounds to the chamber walls was observed to depend strongly on RH and whether a “new” or “old” chamber was used, with the measured values ranging from $\sim 2-7 \times 10^{-5}$ s⁻¹ (Loza et al., 2010). Such new vs. old dependence was not observed by Matsunaga and Ziemann (2010), who investigated wall-losses of alkanes, alkenes, 2-ketones and 2-alcohols. This suggests that the mechanism involved in the uptake of BEPOX and glyoxal was somewhat different than that for the hydrocarbons considered by Matsunaga and Ziemann (2010), or may alternatively indicate complications associated with capturing fast

initial decay during the fill period in the much larger Caltech chamber. Such fill and mixing complications likely also explain the strong differences between the wall-loss rate coefficients for 2-dodecanol determined by Loza et al. (2014) and Matsunaga and Ziemann (2010). Since the vapor uptake to the Teflon chamber walls is reversible, care must be taken in the interpretation of observed wall-loss rates. Only measurements made in the very early stages of uptake will correspond directly to the first-order wall-loss rate coefficient, since as the system approaches equilibrium net vapor uptake will slow. As such, we suggest that the estimates of k_w using the α from Matsunaga and Ziemann (2010) may be more relevant to the current study given the nature of the compounds involved.

S4.4.1 Gas-Particle Partitioning Timescales

The timescale associated with reaching gas-particle equilibrium varies with seed SA , and for a distribution is approximately:

$$\tau_{g-p} \sim (2\pi N_p \overline{D_p} D_{gas} \overline{F}_{FS})^{-1} \quad (S4.20)$$

where N_p is the particle number concentration, $\overline{D_p}$ is the number mean diameter, D_{gas} is the gas-phase diffusivity and \overline{F}_{FS} is the correction to the mass transfer flux due to noncontinuum effects and imperfect accommodation given in Eqn. S8. Values for τ_{g-p} have been calculated for the low- NO_x experiments based on the initial seed number concentration and mean diameter as a function of a , using $D_{gas} = 1 \times 10^{-5} \text{ m}^2 \text{ s}^{-1}$ and $l = 150 \text{ nm}$. The τ_{g-p} vary approximately inversely with a . The optimal α was determined to be $\alpha \sim 0.002$, corresponding to an optimal $k_w = 2 \times 10^{-4} \text{ s}^{-1}$, or a lifetime with respect to wall loss of $t_w = 1/k_w = 83 \text{ min}$. The τ_{g-p} for the experiment with the

smallest seed concentration ($1.4 \times 10^3 \text{ mm}^2 \text{ cm}^{-3}$) when $a = 0.001$ is 230 min, very similar to t_w . As seed SA increases, the τ_{g-p} decrease to ~ 30 min for the highest seed SA . This difference in the relative values of τ_{g-p} vs. t_w explains why the seed effect is seen most strongly when seed SA is less than $\sim 3 \times 10^3 \text{ mm}^2 \text{ cm}^{-3}$, because this is the point at which the two timescales become highly competitive. Similarly, it helps to explain why larger values of a do not lead to a noticeable seed SA dependence; when $a > 0.1$ the $\tau_{g-p} = 2$ min for the experiment with the smallest seed SA .

S4.4.2 Dependence on VOC and OH concentrations

Calculations were performed to determine the magnitude of the wall-loss bias (R_{wall}) as a function of the initial [toluene] and [OH] based on the best-fit of the SOM to the low- NO_x set of experiments. Figure S7 shows the variation in the end of experiment SOA concentration as a function of initial toluene and OH, and corresponds to the results shown in Fig. 3 in the main text.

S4.4.3 Sensitivity to C_w

As discussed in the main text, the sensitivity of our results to the assumed C_w is has been established by performing fits to the observations for varying values of C_w , from 0.01 to 10 mg m^{-3} for the suite of low- NO_x toluene photooxidation experiments (c.f. Fig. 4). Here, it was assumed that $k_w = 2 \times 10^{-4} \text{ s}^{-1}$ and $\alpha = 2 \times 10^{-3}$, consistent with the optimized values determined in the main text. Good fits are obtained over the entire range of C_w . Above $C_w = 0.2 \text{ mg m}^{-3}$ ($= 200 \text{ mg m}^{-3}$) the calculated wall-loss bias, R_{wall} , is constant. Below 0.2 mg m^{-3} the calculated R_{wall} falls off, reaching a second plateau at small C_w that is still above unity. The best-fit SOM parameters vary

systematically with C_w , apparently compensating for the varying levels of vapor wall-loss.

S4.5 Fitting of Historical Chamber Data

Beyond the toluene experiments, which are the focus of the manuscript, best-fit SOM parameters have been determined for a suite of historical photooxidation experiments conducted using a variety of other precursor compounds, both under low- and high- NO_x conditions. The historical experiments were all carried out in the prior 28 m^3 Caltech chamber. Experimental conditions are given in Tables S2 and S3. Fitting of the SOM to the observations is performed for these experiments assuming that $k_w = 1 \times 10^{-4} \text{ s}^{-1}$, $\alpha = 2 \times 10^{-3}$ and $C_w = 10 \text{ mg m}^{-3}$. The results are relatively insensitive to C_w when varied over the range 2-24 mg m^{-3} , as discussed above. The value of k_w for the historical chamber is estimated to be slightly smaller than the optimal value determined for the new 24 m^3 chamber based on consideration of the size-dependent particle wall-loss rates. Best fit SOM parameters for low- NO_x and high- NO_x conditions are given in Table S4. Wall-loss bias values were calculated in the same manner as for the toluene experiments. Experimental data and simulation results are shown in Figures S4.8, S4.9, S4.10, and S4.11.

S4.6 Bibliography

Cappa, C. D. and Wilson, K. R.: Multi-generation gas-phase oxidation, equilibrium partitioning, and the formation and evolution of secondary organic aerosol, *Atmos. Chem. Phys.*, 12, 9505-9528, 2012.

Cappa, C. D., Zhang, X., Loza, C. L., Craven, J. S., Yee, L. D., Seinfeld, J. H.: Application of the Statistical Oxidation Model (SOM) to secondary organic aerosol formation from photooxidation of C₁₂ Alkanes, *Atmos. Chem. Phys.*, 13, 1591-1606, 2013.

Chan, A. W. H., Kautzaman, K. E., Chhabra, P. S., Surratt, J. D., Chan, M. N., Crouse, J. D., Kurten, A., Wennberg, P. O., Flagan, R. C., and Seinfeld, J. H.: Secondary organic aerosol formation from photooxidation of naphthalene and alkylnaphthalenes: implications for oxidation of intermediate volatility organic compounds (IVOCs), *Atmos. Chem. Phys.*, 9, 3049-3060, 2009.

Chhabra, P. S., Flagan, R. C., and Seinfeld, J. H.: Elemental analysis of chamber organic aerosol using an aerodyne high-resolution aerosol mass spectrometer. *Atmos. Chem. Phys.*, 10, 4111-4131, 2010.

Chhabra, P. S., Ng, N. L., Canagaratna, M. R., Corrigan, A. L., Russell, L. M., Worsnop, D. R., Flagan, R. C., and Seinfeld, J. H.: Elemental composition and oxidation of chamber organic aerosol, *Atmos. Chem. Phys.*, 11(17), 8827-8845, 2011.

Crump, J. G. and Seinfeld, J. H.: Turbulent deposition and gravitational sedimentation of an aerosol in a vessel of arbitrary shape, *J. Aerosol Sci.*, 12, 405-415, 1981.

Hildebrandt, L., Donahue, N. M., and Pandis, S. N.: High formation of secondary organic aerosol from the photo-oxidation of toluene, *Atmos. Chem. Phys.*, 9(9), 2973-2986, 2009.

Lee-Taylor, J., Madronich, S., Aumont, B., Baker, A., Camredon, M., Hodzic, A., Tyndall, G. S., Apel, E., Zaveri, R. A.: Explicit modeling of organic chemistry and

secondary organic aerosol partitioning for Mexico City and its outflow plume, *Atmos. Chem. Phys.*, 11, 13219-13241, 2011.

Loza, C. L., Chhabra, P. S., Yee, L. D., Craven, J. S., Flagan, R. C., and Seinfeld, J. H.: Chemical aging of m-xylene secondary organic aerosol: laboratory chamber study, *Atmos. Chem. Phys.*, 12(1), 151-167, 2012.

Loza, C. L., Chan, A. W. H., Galloway, M. M., Keutsch, F. N., Flagan, R. C., and Seinfeld, J. H.: Characterization of Vapor Wall Loss in Laboratory Chambers. *Environ. Sci. Technol.*, 44, 5074-5078, 2010.

Loza, C. L., Craven, J. S., Yee, L. D., Coggon, M. M., Schwantes, R. H., Shiraiwa, M., Zhang, X., Schilling, K. A., Ng, N. L., Canagaratna, M. R., Ziemann, P. J., Flagan, R. C., and Seinfeld, J. H.: Secondary organic aerosol yields of C12-carbon alkanes, *Atmos. Chem. Phys. Discuss.*, 14, 1423-1439, 2014.

Matsunaga, A. and Ziemann, P. J.: Gas-Wall Partitioning of Organic Compounds in a Teflon Film Chamber and Potential Effects on Reaction Product and Aerosol Yield Measurements. *Aerosol Sci. Technol.*, 44, 881-892, 2010.

McMurry, P. H. and Grosjean, D.: Gas and aerosol wall losses in Teflon film smog chambers, *Environ. Sci. Technol.* 19, 1176-1182, 1985.

Ng, N. L., Kroll, J. H., Chan, A. W. H., Chhabra, P. S., Flagan, R. C., and Seinfeld, J. H.: Secondary organic aerosol formation from m-xylene, toluene, and benzene, *Atmos. Chem. Phys.*, 7(14), 3909-3922, 2007.

Pankow, J. F.: An absorption-model of the gas aerosol partitioning involved in the formation of secondary organic aerosol. *Atmos. Environ.* 28, 189-193, 1994.

Pierce, J. R., Engelhart, G. J., Hildebrandt, L., Weitkamp, E. A., Pathak, R. K., Donahue, N. M., Robinson, A. L., Adams, P. J., and Pandis, S. N.: Constraining Particle Evolution from Wall Losses, Coagulation, and Condensation-Evaporation in Smog-Chamber Experiments: Optimal Estimation Based on Size Distribution Measurements. *Aerosol Sci. and Technol.*, 42, 1001-1015, 2008.

Seinfeld, J. H. and Pandis, S. N.: *Atmospheric chemistry and physics: From air pollution to climate change*, Wiley, New Jersey, 612pp., 2006.

Shiraiwa, M., Yee, L. D., Schilling, K. A., Loza, C. L., Craven, J. S., Zuend, A., Ziemann, P. J., and Seinfeld, J. H.: Size distribution dynamics reveal particle-phase chemistry in organic aerosol formation. *Proc. Nat. Acad. Sci.*, 110(29), 11746-11750, 2013.

Weitkamp, E. A., Sage, A. M., Pierce, J. R., Donahue, N. M., and Robinson, A. L.: Organic aerosol formation from photochemical oxidation of diesel exhaust in a smog chamber. *Environ. Sci. & Technol.*, 41, 6969-6975, 2007.

Figure S4.1. Time-dependent volume distributions ($dV/d\log D_p$) of AS seed and organic aerosols after 0 - 18 h of photooxidation of toluene under (top panels) high- NO_x and (bottom panels) low- NO_x conditions. Distributions are colored according to the time after lights were turned on. The lower bound wall-loss correction is used here. For the experiments at higher seed SA , the influence of coagulation on the particle evolution is evident.

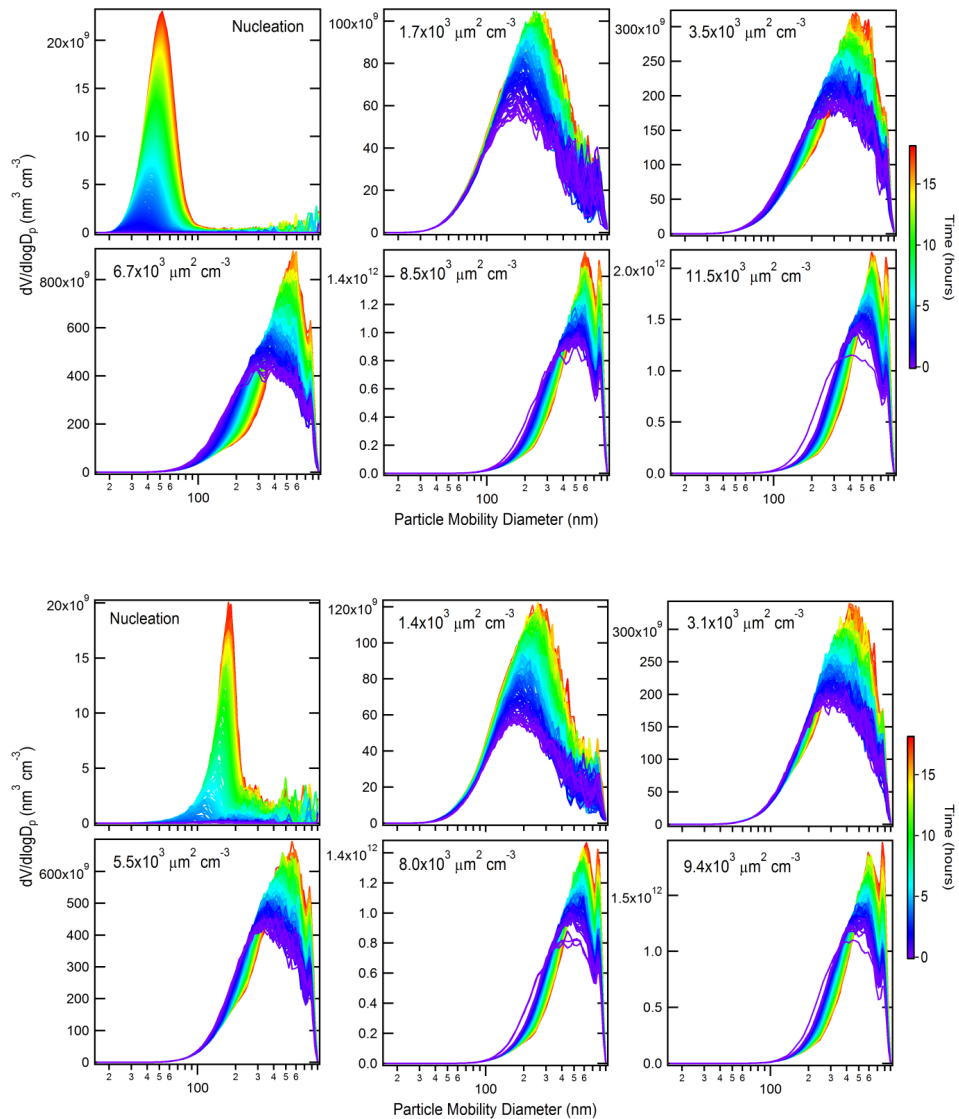


Figure S4.2. Time-dependent SOA growth curves for toluene photooxidation under high- NO_x (HNO_x) and low- NO_x (LNO_x) conditions. Error bars come from the 95% confidence interval associated with determining the size-dependent first-order wall-loss rate for dry inert ammonium sulfate ($(\text{NH}_4)_2\text{SO}_4$) particles.

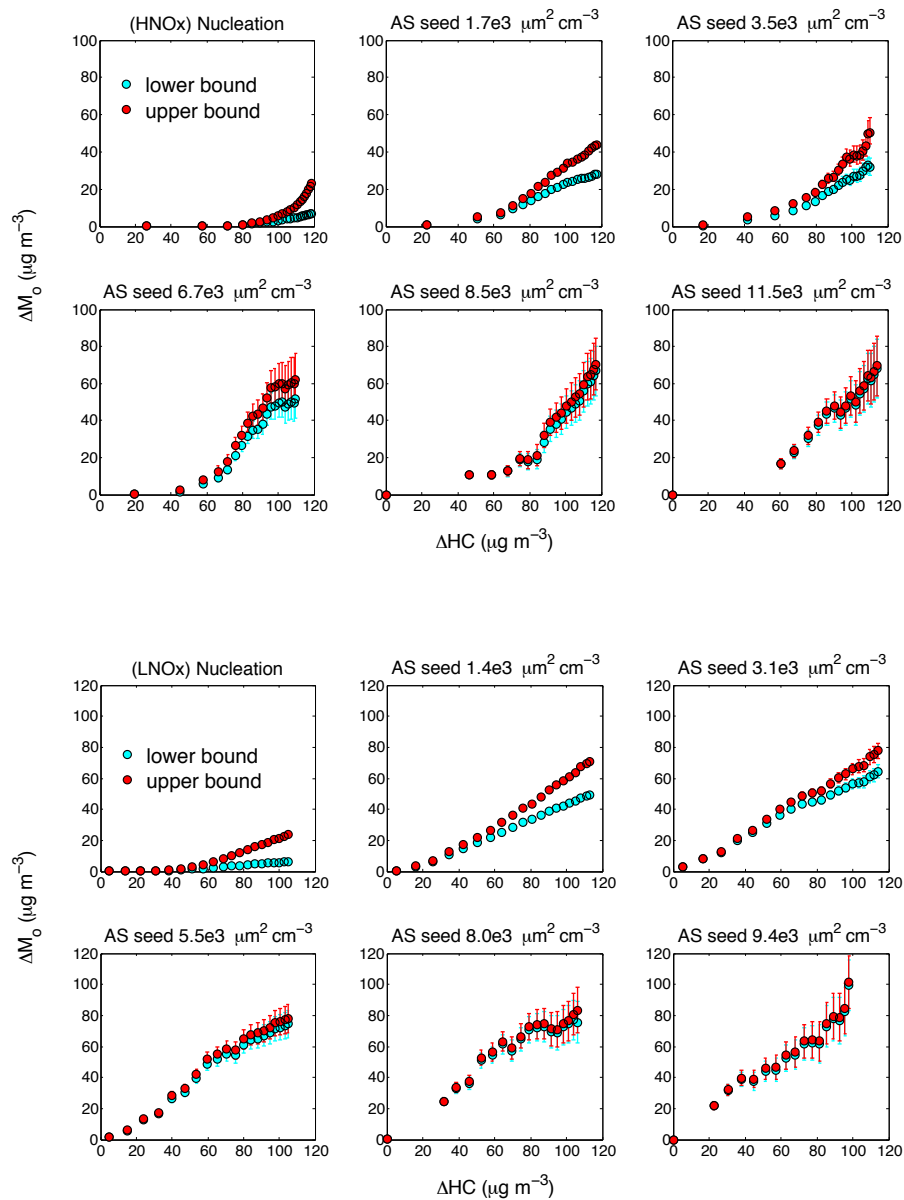


Figure S4.3. Calculated composite reduced chi-square values for (A) high-NO_x and (B) low-NO_x toluene experiments as a function of the mass accommodation coefficient, α , and the first order wall-loss rate coefficient, k_w . The colors indicate the magnitude of the calculated composite reduced goodness of fit metric, with the contours based on the circles. The black x indicates the optimal value: $k_w = 2.5 \times 10^{-4} \text{ s}^{-1}$ and $\alpha = 1 \times 10^{-3}$ (high-NO_x) and $k_w = 2.5 \times 10^{-4} \text{ s}^{-1}$ and $\alpha = 2 \times 10^{-3}$ (low-NO_x).

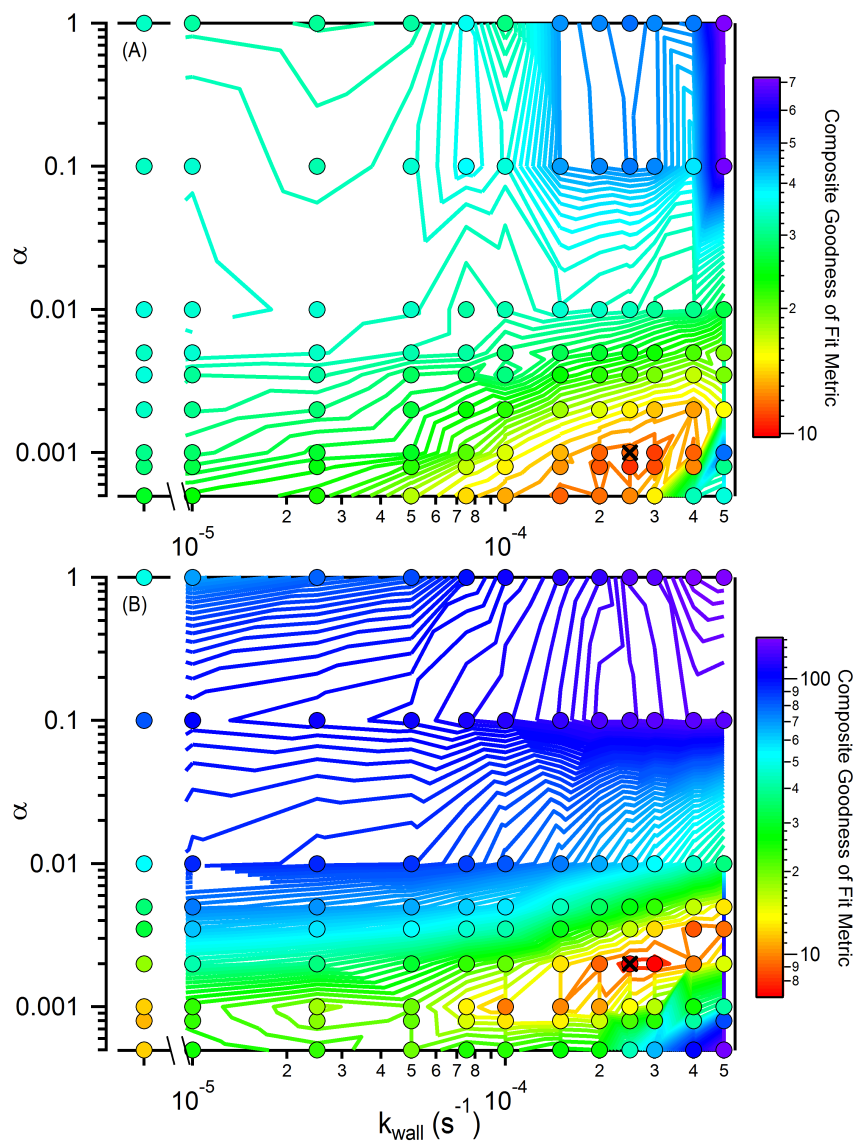


Figure S4.4. Calculated wall-loss coefficients k_w as a function of the coefficient of eddy diffusion, k_e , which characterizes the state of turbulent diffusion in the chamber, for different values of the mass accommodation coefficient onto the walls, α_w . The top axis shows the time-scales corresponding to the eddy diffusion coefficients.

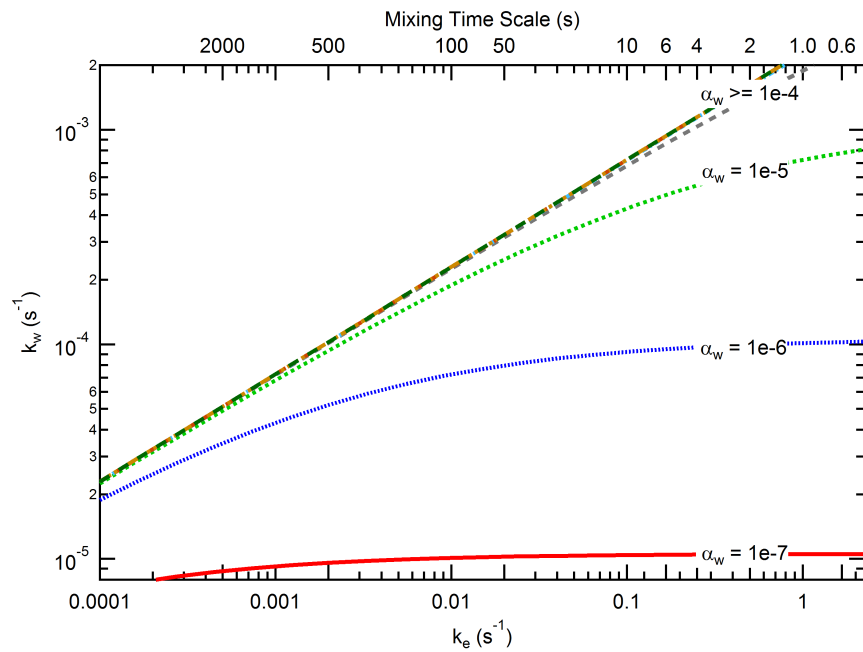


Figure S4.5. Calculated gas-particle equilibration time as a function of the gas-particle mass accommodation coefficient, α , for different seed surface areas corresponding to the low- NO_x experiments. The horizontal gray line indicates the timescale associated with vapour wall-loss for $k_w = 2.5 \times 10^{-4} \text{ s}^{-1}$. The vertical dashed gray lines indicate the optimal values of α determined here for the high- and low- NO_x toluene systems. For the nucleation experiments, it is assumed that the particles are 10 nm diameter.

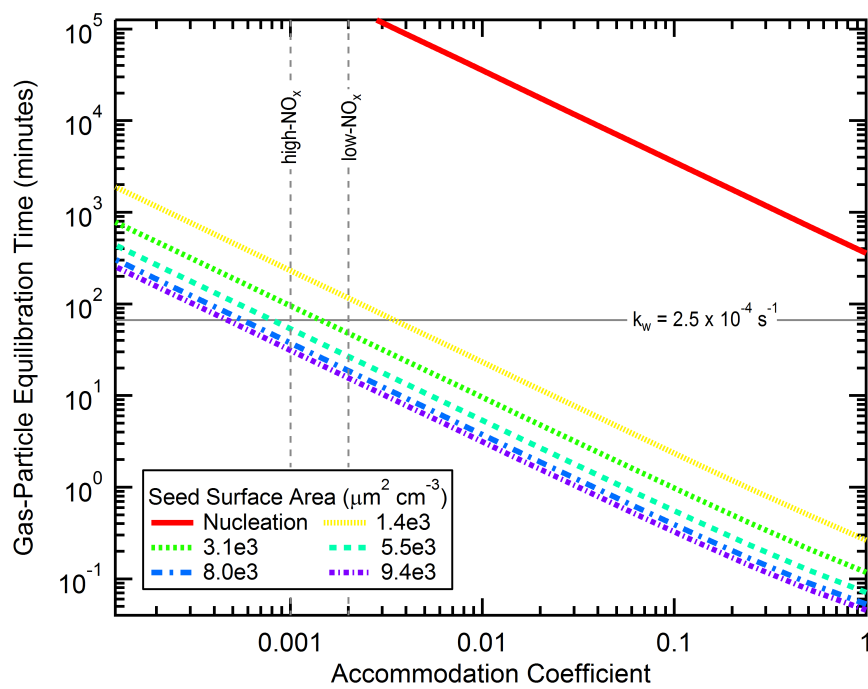


Figure S4.6. Calculated end-of-experiment SOA mass concentrations corresponding to the results shown in Figure 3. The SOA concentration is shown as a function of initial toluene concentration and OH concentration when $k_w = 2.5 \times 10^{-4} \text{ s}^{-1}$ and $C_w = 10 \text{ mg m}^{-3}$. The SOA concentrations for a given [toluene] and [OH] are indicated by colors and contours. Results are based on the optimal fit of the SOM to the low- NO_x experiments.

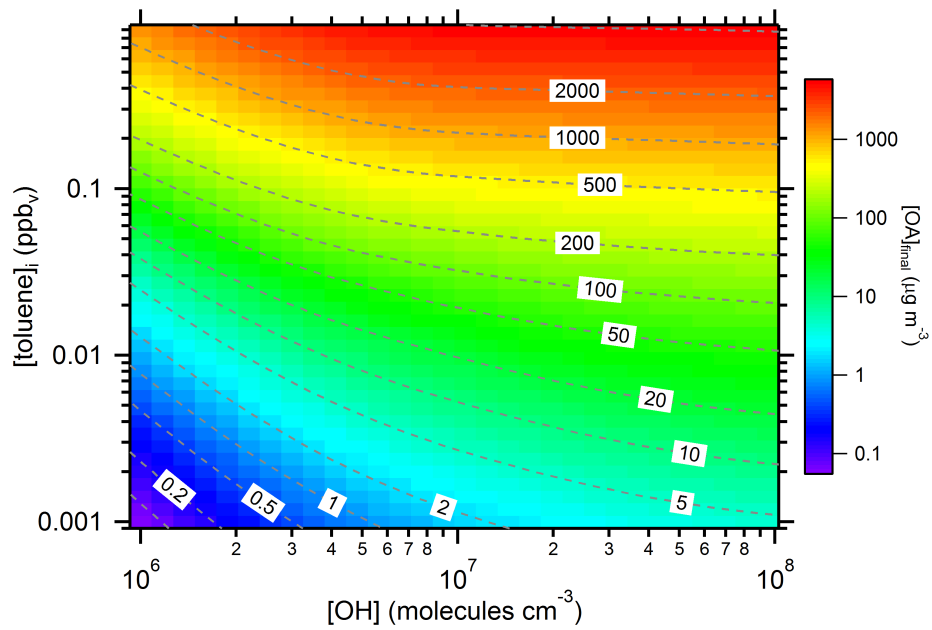


Figure S4.7. The best-fit SOM parameters determined at each C_w corresponding to the results shown in Fig. 4 in the main text. The fragmentation probabilities, P_{frag} , were calculated from the best-fit m_{frag} values and Eqn. S3 using $O:C = 0.5$. DLVP corresponds to the decrease in vapor saturation concentration per oxygen added and P_{func} corresponds to the probability of adding 1, 2, 3 or 4 oxygen atoms per reaction.

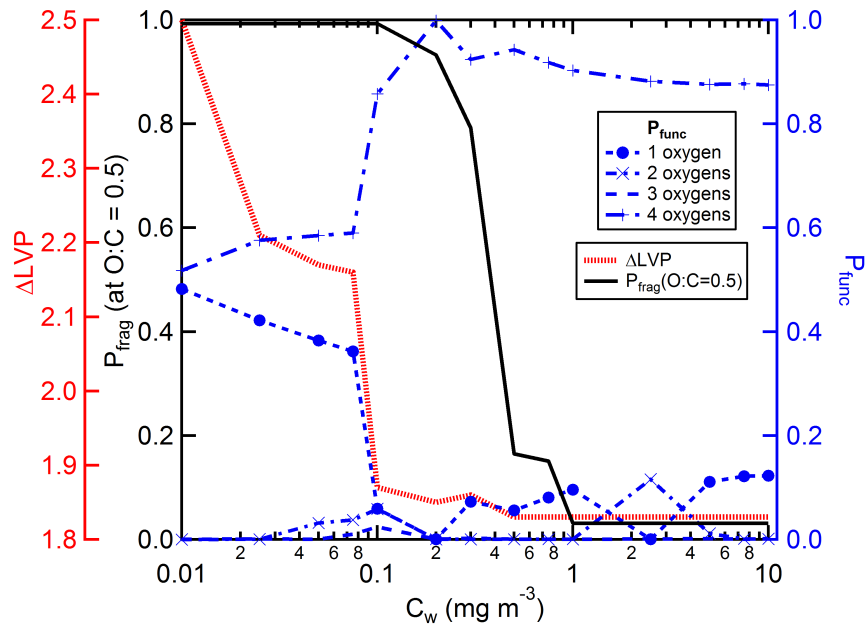


Figure S4.8. Results from historical low (left panels) and high (right panels) NO_x SOA formation experiments for alkane photooxidation (open circles). The solid red lines are best-fit SOM results when wall losses are accounted for assuming that $k_w = 1 \times 10^{-4}$, $\alpha = 1$ and $C_w = 10 \text{ mg m}^{-3}$. The blue dashed lines are the simulated SOA concentrations when wall-loss is turned off, but the SOM parameters determined from the best-fit with wall-loss on are retained.

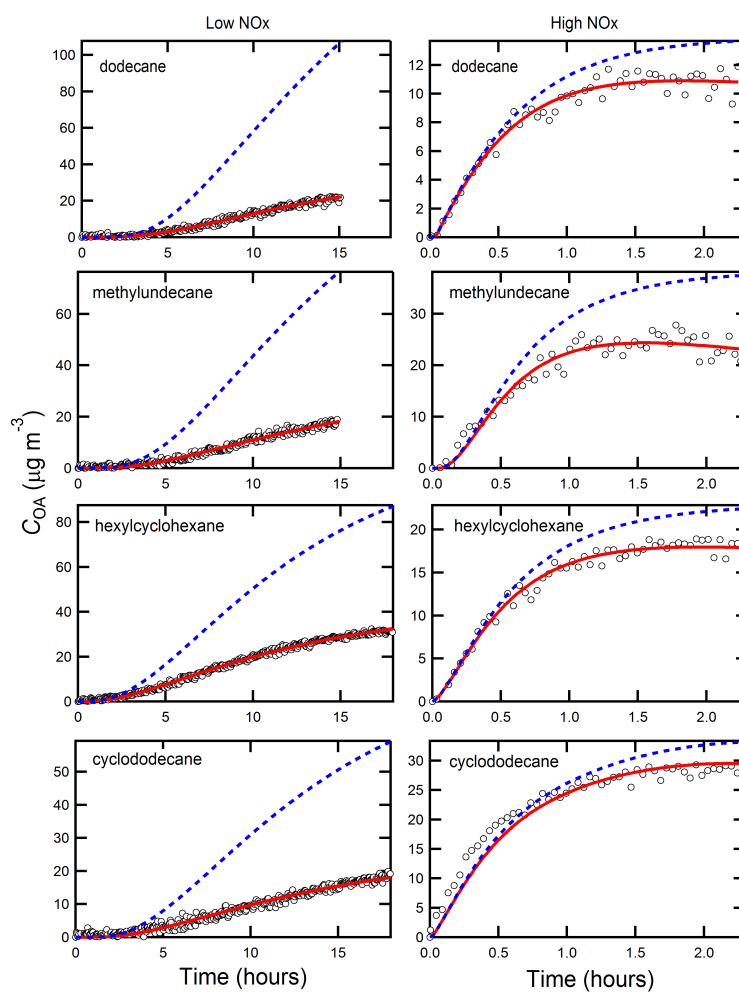


Figure S4.9. Same as Fig. S8, but for aromatics. Importantly, the toluene experimental results are from Ng et al. (2007), not from the current set of experiments. For each experiment, data collected over the full experiment time is shown. However, the SOM fitting has been restricted to the periods shown as colors other than gray (orange or blue). The gray points are data that were collected, but not used in fitting. These data have been excluded to be consistent with the range of data considered in Ng et al. (2007) and Chan et al. (2009), where 2-product fits have been performed. For m-xylene, low- NO_x , fits to data from Ng et al. (2007) and Loza et al. (2012) are shown separately.

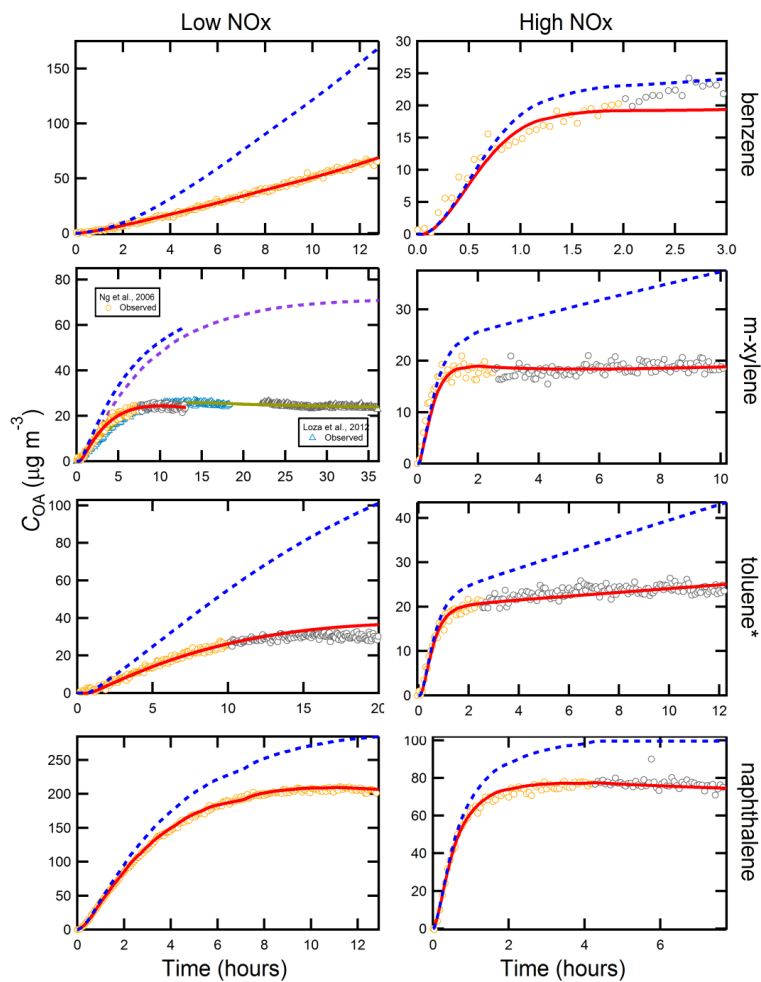


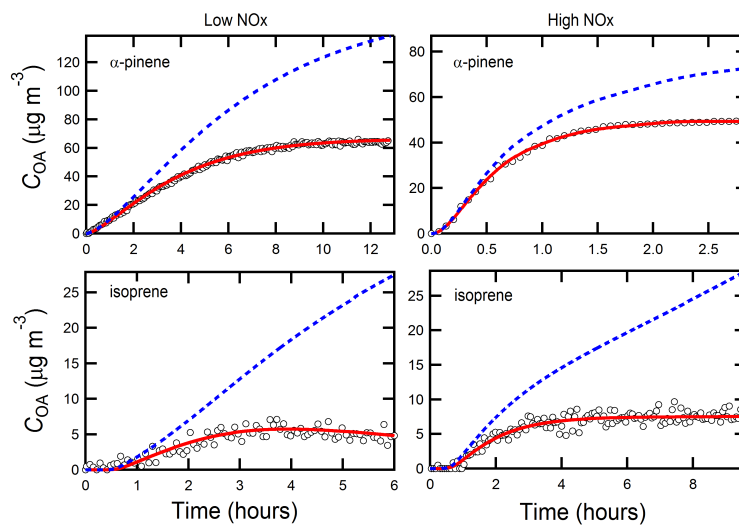
Figure S4.10. Same as Fig. S8, but for α -pinene and isoprene photooxidation.

Figure S4.11. Calculated time-dependent R_{wall} values for historical experiments based on the results shown in Figure S4.10. Results are grouped according to species type and NO_x level. Left panels are low- NO_x and right panels high- NO_x results. Note that the toluene results in the top panels are based on data presented in Ng et al. (2007), not from the current set of experiments. Results are shown for m-xylene, low- NO_x for two separate experimental data sets: Ng et al. (2007) and Loza et al. (2012). The presented results are limited to the period where $C_{\text{OA}} > 0.5 \text{ mg m}^{-3}$.

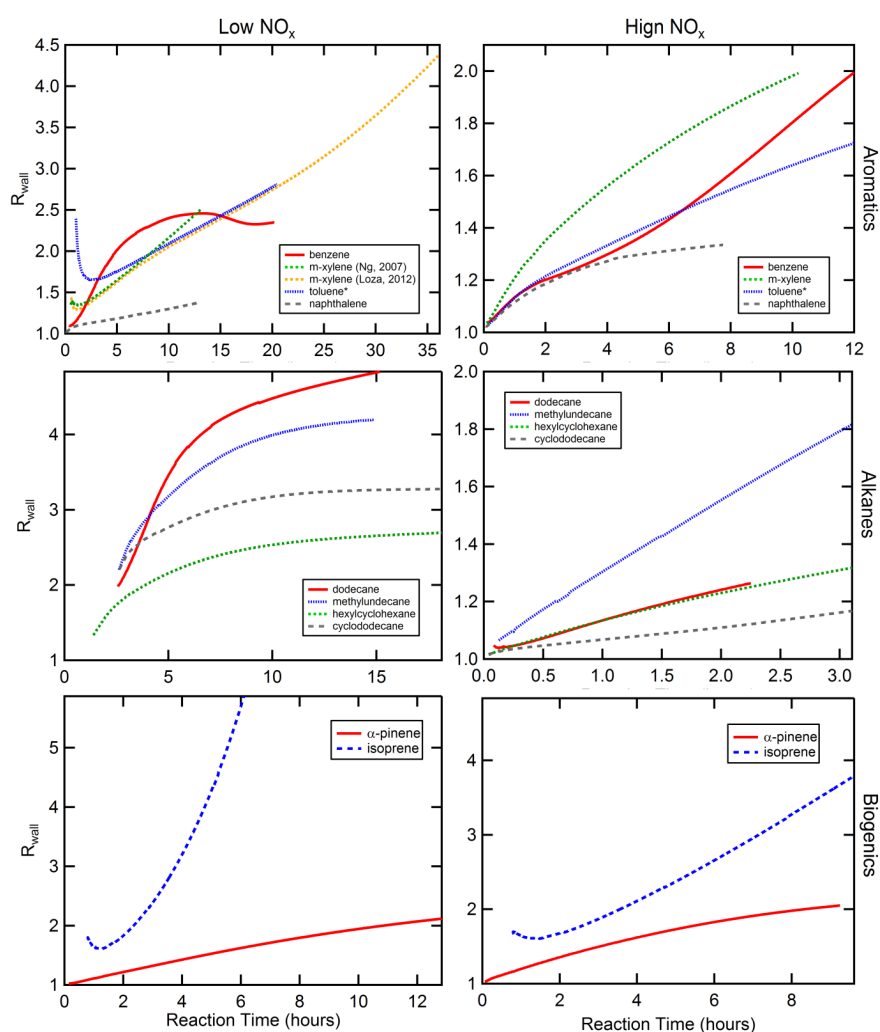


Table S4.1. Experimental conditions for toluene SOA photooxidation experiments in the Caltech dual 24-m³ chambers.

	Exp. (#)	[HC] ₀ (ppb)	[NO] ₀ (ppb)	[NO ₂] ₀ (ppb)	Initial [VOC]/[NO _x] (ppbC/ppb)	Additional NO injection	Initial seed surface area (mm ² cm ⁻³)	Initial surface area ratio (Aerosol/Wall)
	1	~36.8	~ 19.0	~ 34.4	4.8	yes	~ 0	~ 0
	2	~38.7	~ 19.6	~ 32.2	5.2	yes	1.69 × 10 ³	8.57 × 10 ⁻⁴
High NO _x	3	~37.9	~ 15.5	~ 34.9	5.3	yes	3.51 × 10 ³	1.88 × 10 ⁻³
	4	~37.9	~ 17.5	~ 31.7	5.4	yes	6.70 × 10 ³	3.32 × 10 ⁻³
	5	~38.2	~ 13.1	~ 31.5	6.0	yes	8.51 × 10 ³	4.83 × 10 ⁻³
	6	~38.7	~ 16.8	~ 35.3	5.2	yes	1.15 × 10 ⁴	5.72 × 10 ⁻³
	1	~33.9	< DL ^c	< DL	--	--	~ 0	~ 0
	2	~37.6	< DL	< DL	--	--	1.41 × 10 ³	1.03 × 10 ⁻³
Low NO _x	3	~37.3	< DL	< DL	--	--	3.10 × 10 ³	2.13 × 10 ⁻³
	4	~36.8	< DL	< DL	--	--	5.47 × 10 ³	4.07 × 10 ⁻³
	5	~38.7	< DL	< DL	--	--	7.95 × 10 ³	5.17 × 10 ⁻³
	6	~37.9	< DL	< DL	--	--	9.41 × 10 ³	6.70 × 10 ⁻³

^a Detection limits (DL) for O₃, NO, and NO₂ are 0.5 ppb, 0.4 ppb, and 0.4 ppb, respectively.

Table S4.2. Conditions for low-NO_x experiments in the Caltech dual 28-m³ chambers.

VOC	Date [mm/dd/yy]	[VOC] ₀ (ppb)	[NO _x] ₀ (ppb)	[OH] (molecules/cm ³)	% Yield	<i>k</i> _{OH} (cm ³ molecules ⁻¹ s ⁻¹)
n-dodecane	03/16/11	34.0	<2	2.5x10 ⁶	6.1	1.34x10 ⁻¹¹
methylundecane	02/25/11	28.1	<2	2.4x10 ⁶	7.2	1.34x10 ⁻¹¹
cyclododecane	02/23/11	9.8	<2	2.7x10 ⁶	17.2	1.34x10 ⁻¹¹
hexylcyclohexane	03/21/11	15.6	<2	3.0x10 ⁶	15.4	1.34x10 ⁻¹¹
benzene	11/04/06	414	<2	3x10 ⁶	23.8	1.22x10 ⁻¹²
toluene ^c	10/24/06	52.7	<2	3.3x10 ⁶	26.7	5.63x10 ⁻¹²
m-xylene ^d	10/27/06	19.3	<2	3x10 ⁶	28.2	2.31x10 ⁻¹¹
m-xylene ^d	10/11/10	29.2	<2	2.5x10 ⁶	21.4	2.31x10 ⁻¹¹
naphthalene	08/13/08	31.5	2	2x10 ⁶	19.0	2.44x10 ⁻¹¹
a-pinene	06/02/10	66.2	<2	3x10 ⁶	36.8	5.3x10 ⁻¹⁰
isoprene	02/25/09	49	<2	2x10 ⁶	4.3	1x10 ⁻¹⁰

Table S4.3. Conditions for high-NO_x experiments in the Caltech dual 28-m³ chambers.

VOC	Date [mm/dd/yy]	[VOC] ₀ (ppb)	[NO] ₀ & [NO ₂] ₀ (ppb)	[OH] (molecules/cm ³)	% Yield	<i>k</i> _{OH} (cm ³ molecules ⁻¹ s ⁻¹)
n-dodecane	05/12/11	32.2	343/--	4.5x10 ⁷	6.2	1.34x10 ⁻¹¹
methylundecane	03/01/11	72.4	366/--	3.3x10 ⁷	5.1	1.34x10 ⁻¹¹
cyclododecane	05/23/11	13.8	362/--	2.7x10 ⁷	38.3	1.34x10 ⁻¹¹
hexylcyclohexane	03/22/11	22.1	320/--	4.1x10 ⁷	12.3	1.34x10 ⁻¹¹
benzene	01/15/07	336	83/86	3.2x10 ⁷	15.6	1.22x10 ⁻¹²
toluene ^c	10/14/06	138	373/568	3.6x10 ⁷	8.3	5.63x10 ⁻¹²
m-xylene	10/05/06	89.8	469/474	4.2x10 ⁷	3.9	2.31x10 ⁻¹¹
naphthalene	08/14/08	48.6	404/171	2.5x10 ⁷	11.2	2.44x10 ⁻¹¹
a-pinene	06/03/10	44.9	446/398	1.4x10 ⁷	9.5	5.3x10 ⁻¹¹
isoprene	04/04/09	268	535/402	6.6x10 ⁶	1.0	1x10 ⁻¹¹

Table S4.4. Derived SOM parameters for the experiments when vapor wall-loss is accounted for (assuming $C_w = 10 \mu\text{g m}^{-3}$).

VOC ^a	Frag.	DLVP	P1	P2	P3	P4	χ_{red}^2 ^b
<i>Low NO_x</i>							
toluene (this study)	5	1.83	0.123	0.001	0.002	0.875	1.74
n-dodecane	0.671	1.58	0.977	0.016	0.003	0.004	1.47
methylundecane	0.433	1.92	0.997	0.000	0.001	0.002	1.33
cyclododecane	1.56	1.90	0.994	0.000	0.001	0.005	1.73
hexylcyclohexane	0.78	1.84	0.885	0.106	0.001	0.008	0.56
benzene ^c	0.01	2.29	0.284	0.000	0.644	0.072	0.42
toluene ^c	0.01	1.88	0.001	0.001	0.727	0.271	1.36
m-xylene ^c	0.245	1.96	0.000	0.085	0.836	0.079	0.57
m-xylene ^c	0.069	1.88	0.285	0.000	0.613	0.101	0.20
naphthalene	0.072	1.76	0.382	0.027	0.431	0.161	0.04
a-pinene	0.151	1.91	0.262	0.619	0.075	0.044	0.19
isoprene	0.01	2.23	0.000	0.146	0.826	0.028	1.61
<i>High NO_x</i>							
toluene (this study)	1.02	1.42	0.000	0.000	1.000	0.000	1.10
n-dodecane	0.188	1.45	0.963	0.000	0.001	0.036	0.07
methylundecane	0.188	1.12	0.263	0.277	0.455	0.005	0.61
cyclododecane	0.01	1.69	0.664	0.002	0.004	0.33	0.64
hexylcyclohexane	0.153	1.75	0.832	0.086	0.055	0.028	0.14
benzene ^c	0.912	1.47	0.105	0.001	0.893	0.001	1.15
m-xylene ^c	0.18	1.54	0.000	0.000	1.000	0.000	0.64
toluene ^c	0.039	1.46	0.001	0.001	0.906	0.094	1.13
naphthalene ^c	0.64	1.41	0.835	0.001	0.002	0.162	0.17
a-pinen	0.080	1.81	0.193	0.694	0.101	0.012	0.04
isoprene	0.322	2.23	0.679	0.321	0.000	0.000	0.79

^a The toluene experiments from this study were conducted in the 24 m³ Caltech chamber (i.e. “new” experiments) and simulated using $k_w = 2.5 \times 10^{-4} \text{ s}^{-1}$ and the experimentally-determined optimal a ($\sim 2 \times 10^{-3}$). All other experiments, including the toluene experiments from Loza et al. (2014) were conducted in the 28 m³ Caltech chamber (i.e. “historical” experiments”) and simulated using $k_w = 1 \times 10^{-4} \text{ s}^{-1}$ and $a = 1$.

^b The reduced χ^2 associated with the best fit.

^c Fits were performed over the ranges shown in Fig. S8.

Chapter 5

Vapor wall deposition in Teflon chambers

* Reproduced with permission from “Vapor wall depositino in Teflon chambers” by X.Zhang, R. H. Schwantes, R. C. McVay, H. Lignell, M. M. Coggon, R. C. Flagan, and J. H. Seinfeld, *Atmospheric Chemistry and Physics Discussions*, 14, 26765-26802, 2014. Copyright 2014 the authors.

5.1 Abstract

Teflon chambers are ubiquitous in studies of atmospheric chemistry. Secondary organic aerosol (SOA) formation can be underestimated owing to deposition of SOA-forming vapors to the chamber wall. We present here an experimental protocol and a model framework to constrain the vapor-wall interactions in Teflon chambers. We measured the wall deposition rates of 25 oxidized organic compounds generated from the photooxidation of isoprene, toluene, α -pinene, and dodecane in two chambers that had been extensively used and in two new unused chambers. We found that the extent of prior use of the chamber did not significantly affect the sorption behavior of the Teflon films. By optimizing the model output to the observed vapor decay profiles, we identified that the dominant parameter governing the extent of wall deposition of a compound is its wall accommodation coefficient ($\alpha_{w,i}$), which can be correlated through its volatility with the number of carbons and oxygens in the molecule. Among the 25 compounds studied, the maximum wall deposition rate is exhibited by the most highly oxygenated and least volatile compounds. The extent to which vapor wall deposition impacts measured SOA yields depends on the competition between uptake of organic vapors by suspended particles and the chamber wall. The timescale associated with vapor wall deposition can vary from minutes to hours depending on the value of $\alpha_{w,i}$. For volatile and intermediate volatility organic compounds (small $\alpha_{w,i}$), gas-particle partitioning will dominate wall deposition for typical particle number concentrations in chamber experiments. For compounds characterized by relatively large $\alpha_{w,i}$, vapor transport to particles is

suppressed by competition with the chamber wall even with perfect particle accommodation.

5.2 Introduction

Understanding of the mechanism and extent of secondary organic aerosol (SOA) formation from oxidation of volatile organic compounds (VOCs) has been derived largely from experiments in Teflon chambers. Chamber-measured SOA yields (mass of SOA formed per mass of VOC reacted) have been widely parameterized into regional/global atmospheric models, and chemical mechanisms leading to SOA formation and aging have been derived based on the gas/particle-phase identification of intermediate/semi/low-volatility compounds generated in controlled chamber experiments. An unavoidable consequence of the use of an environmental chamber is interaction of vapors and particles with the chamber wall. It has been recently established that SOA formation can be substantially underestimated due to deposition of SOA-forming vapors to the chamber wall rather than growing particles (Zhang et al., 2014a).

Chamber wall-induced decay of organic vapors was reported 30 years ago. Grosjean (1985) and McMurry and Grosjean (1985) measured wall deposition rates of several volatile organic compounds in a chamber constructed from Fluorinated ethylene propylene (FEP) Teflon film. The lifetime of the VOCs with respect to wall deposition was found generally to exceed ~ 15 h. Loza et al. (2010) found that deposition of the isoprene oxidation product surrogate, 2,3-epoxy-1,4-butanediol (BEPOX), and glyoxal to the FEP Teflon chamber wall is reversible on sufficiently long timescales. On the contrary, rapid reversible gas-wall partitioning of *n*-alkanes, 1-alkenes, 2-alcohols, 2-

ketones, monoacids, and 1,2-diols was universally observed by Matsunaga and Ziemann (2010) and Yeh and Ziemann (2014). Following the same experimental protocol, Kokkola et al. (2014) measured that the equilibrium fractions of nopinone and pinanediol on the wall of a 4 m³ FEP Teflon chamber are on average 0.4 and 0.8, respectively.

The extent to which vapors and the chamber wall interact is reflected by properties such as the affinity of the wall for various organic molecules, the degree of reversibility of the vapor-wall partitioning, and the equilibrium solubility of organic vapors in the wall. Organic materials generated in chamber experiments can deposit on the chamber wall to form a coating that can act as the primary absorbing medium, or the Teflon film itself could act as the absorbing medium, in a process akin to the sorption of small molecules by organic polymers. While measurement of vapor wall deposition rates for the thousands of organic molecules that are produced from the oxidation of SOA precursor VOCs is not presently possible, empirical expressions that represent the deposition rates of organic vapors as a function of general molecular properties would be highly useful.

A prime goal of characterizing vapor wall deposition in a chamber is to understand its impact on SOA formation and evolution. We present here an experimental protocol to constrain the nature of organic vapor wall deposition in Teflon chambers. We measured wall-induced dark decay rates of 25 intermediate/semi-volatility organic vapors, which span a range of volatilities and oxidation states, in both unused and previously used chambers constructed with FEP Teflon film. A temperature ramping program (298 – 318 K) was implemented to study the reversibility of vapor-wall partitioning. A model framework is developed to describe interactions between organic vapors and the chamber

wall following the theories for particle wall deposition and gas-particle partitioning. We address the following questions in the present study: 1) What is the physicochemical nature of the chamber wall? 2) What are the key parameters that characterize the vapor-wall interactions and how can these values be determined? and 3) How can one predict the wall deposition rate of a specific compound based on its molecular properties?

5.3 Vapor wall deposition — theory

Figure 1 depicts the steady-state concentration profiles of an organic compound i in the well-mixed core of the chamber ($\bar{C}_{v,i}$), in the boundary layer adjacent to the wall ($C_{v,i}$), at the wall surface ($C_{o,i}$), and in the chamber wall ($\bar{C}_{w,i}$). Vapor molecules in the well-mixed core of a chamber are transported through a boundary layer adjacent to the wall by a combination of molecular and turbulent diffusion. The transport rate depends on both the molecular properties of the individual organic compound, as well as the extent of turbulent mixing in the chamber. As vapor molecules encounter the chamber wall, the fraction of those encounters that lead to uptake is represented by the accommodation coefficient ($\alpha_{w,i}$). The accommodation coefficient depends, in principle, on the nature of the wall surface as well as the compound chemical composition. Molecules deposited on the wall may re-evaporate at a rate that depends on their concentration in the wall. Overall, the net flux across the gas-wall interface is a result of the flux arriving from the gas phase ($J_{v,i}$) and the flux evaporating from the wall ($J_{w,i}$).

A conservation balance on $\bar{C}_{v,i}$, the concentration of vapor i in the well-mixed core of a chamber that is subject only to the deposition process, is given by:

$$\frac{d\bar{C}_{v,i}}{dt} = -k_{w,depo,i}\bar{C}_{v,i} + k_{w,evap,i}\bar{C}_{w,i} \quad (5.1)$$

where $k_{w,depo,i}$ (s^{-1}) is the deposition rate coefficient to the wall, $k_{w,evap,i}$ (s^{-1}) is the evaporation rate coefficient from the wall, and $\bar{C}_{w,i}$ is the concentration of vapor i that has accumulated on the chamber wall. The dynamic behavior of $\bar{C}_{w,i}$ is described by a corresponding balance:

$$\frac{d\bar{C}_{w,i}}{dt} = -k_{w,evap,i}\bar{C}_{w,i} + k_{w,depo,i}\bar{C}_{v,i} \quad (5.2)$$

Note that $\bar{C}_{w,i}$ is assumed to be zero at the onset of vapor i generation, ultimately reaching equilibrium with $\bar{C}_{v,i}$.

5.3.1 Deposition rate coefficient ($k_{w,depo,i}$)

For a chamber that is relatively well mixed, transport to the wall occurs by molecular and turbulent diffusion across a thin boundary layer, of thickness δ , adjacent to the chamber wall. The flux due to molecular diffusion is given by $-\mathcal{D}_i\nabla C_{v,i}$, where $C_{v,i}$ is the local vapor i concentration in the boundary layer and \mathcal{D}_i is its molecular diffusivity. The turbulent diffusion flux is expressed as $-\mathcal{D}_e\nabla C_{v,i}$, where \mathcal{D}_e is the eddy diffusivity. One can invoke the Prandtl mixing length expression near a wall, $\mathcal{D}_e = K_e x^2$, where x is the distance from the wall, and K_e is the coefficient of eddy diffusion (Corner and Pendlebury, 1951; Crump and Seinfeld, 1981). Owing to the small value of δ , a quasi-steady state condition exists in the boundary layer, and the concentration of vapor i within the boundary layer, $0 \leq x \leq \delta$, is governed by:

$$\frac{d}{dx} \left[(K_e x^2 + \mathcal{D}_i) \frac{dC_{v,i}}{dx} \right] = 0 \quad (5.3)$$

Introducing the dimensionless variable z by setting $x = (\mathcal{D}_i/K_e)^{1/2}z$, Eq (3) becomes:

$$(z^2+1) \frac{d^2 C_{v,i}}{dz^2} + 2z \frac{dC_{v,i}}{dz} = 0 \quad (5.4)$$

subject to the boundary conditions,

$$x = 0 \ (z = 0) \rightarrow C_{v,i} = C_{0,i}$$

$$x = \delta \ (z = (K_e/\mathcal{D}_i)^{1/2} \delta) \rightarrow C_{v,i} = \bar{C}_{v,i}$$

where $C_{0,i}$ and $\bar{C}_{v,i}$ are concentrations of vapor i over the wall surface and in the well-mixed core of the chamber, respectively. Note that the accommodation coefficient for vapors on the wall is likely less than unity, and the steady-state concentration is then nonzero at the chamber wall surface. The solution of Eq (4) expressed in the original variables is:

$$\begin{aligned} C_{v,i} &= C_{0,i} + (\bar{C}_{v,i} - C_{0,i}) \frac{\tan^{-1}[(K_e/\mathcal{D}_i)^{1/2}x]}{\tan^{-1}[(K_e/\mathcal{D}_i)^{1/2}\delta]} \\ &\approx C_{0,i} + (\bar{C}_{v,i} - C_{0,i}) \frac{\tan^{-1}[(K_e/\mathcal{D}_i)^{1/2}x]}{\pi/2} \end{aligned} \quad (5.5)$$

Physically, turbulent diffusion dominates molecular diffusion at the outer edge of the boundary layer, so that $(K_e/\mathcal{D}_i)^{1/2}\delta \gg 1$. The vapor flux to the wall surface ($J_{v,i}$) is given by:

$$J_{v,i} = \mathcal{D}_i \left. \frac{dC_{v,i}}{dx} \right|_{x=0} = \frac{\alpha_{w,i} \bar{v}_i C_{0,i}}{4} \quad (5.6)$$

where \bar{v}_i is the species mean thermal speed. Note that the right side of Eq (6) derives from the kinetic theory of gases. Substitution of Eq (6) into the derivative of Eq (5) gives:

$$C_{0,i} = \frac{\bar{C}_{v,i}}{\pi \alpha_{w,i} \bar{v}_i / 8 (\mathcal{D}_i K_e)^{1/2} + 1} \quad (5.7)$$

The deposition coefficient of vapor i per unit volume is therefore:

$$k_{w,depo,i} = \left(\frac{A}{V}\right) \left(\frac{\alpha_{w,i}\bar{v}_i/4}{\pi\alpha_{w,i}\bar{v}_i/8(D_iK_e)^{1/2} + 1}\right) \quad (5.8)$$

where A and V are the surface area and volume of the chamber, respectively.

5.3.2 Evaporation rate coefficient ($k_{w,evap,i}$)

Without loss of generality, vapor wall deposition can be assumed to be reversible. The flux of molecules i that evaporate from the interface back to the gas phase ($J_{w,i}$) depends on the concentration of i in the wall ($\bar{C}_{w,i}$). So we can write $J_{w,i}$ as a function of $\bar{C}_{w,i}$:

$$J_{w,i} \propto \bar{C}_{w,i} \quad \text{or} \quad J_{w,i} = \lambda \bar{C}_{w,i} \quad (5.9)$$

where λ is simply a quantity that reflects the positive correlation between $J_{w,i}$ and $\bar{C}_{w,i}$. If the gas and wall phases are at equilibrium, then

$$J_{v,i,(eq)} = J_{w,i,(eq)} \quad (5.10a)$$

and

$$k_{w,depo,i} \times \bar{C}_{v,i,eq} = k_{w,evap,i} \times \bar{C}_{w,i,eq} \quad (5.10b)$$

Therefore,

$$\lambda = \left(\frac{\alpha_{w,i}\bar{v}_i/4}{\pi\alpha_{w,i}\bar{v}_i/8(D_iK_e)^{1/2} + 1}\right) \frac{\bar{C}_{v,i,eq}}{\bar{C}_{w,i,eq}} = \frac{\alpha_{w,i}\bar{v}_i/4H_i}{\pi\alpha_{w,i}\bar{v}_i/8(D_iK_e)^{1/2} + 1} \quad (5.11a)$$

and

$$\frac{k_{w,evap,i}}{k_{w,depo,i}} = \frac{\bar{C}_{v,i,eq}}{\bar{C}_{w,i,eq}} = \frac{1}{H_i} \quad (5.11b)$$

where H_i is the Henry's law constant of organic species i . Substitution of Equation (11a) into Equation (9) gives:

$$J_{w,i} = \frac{\alpha_{w,i} \bar{v}_i \bar{C}_{w,i} / 4H_i}{\pi \alpha_{w,i} \bar{v}_i / 8(D_i K_e)^{1/2} + 1} \quad (5.12)$$

If applying vapor-particle partitioning theory here, Eq (11b) can be rewritten as:

$$k_{w, \text{evap}, i} = \frac{k_{w, \text{depo}, i}}{K_{w,i} C_w} \quad (5.13)$$

where $K_{w,i}$ is vapor-wall partition coefficient (Matsunaga and Ziemann, 2010):

$$K_{w,i} = \frac{RT}{p_{L,i}^0 \gamma_i \bar{M}_w} \quad (5.14)$$

and where $p_{L,i}^0$ is the vapor pressure of compound i as a liquid.

We calculate $p_{L,i}^0$ by the average of two group contribution methods, ‘SIMPOL.1’ developed by Pankow and Asher (2008) and ‘EVAPORATION’ developed by Compennolle et al. (2011). γ_i , the activity coefficient in the wall layer on a mole fraction basis, is assumed to be unity here, R is the gas constant, T is temperature, and \bar{M}_w is the average molecular weight of the absorbing organic material on the wall, which, following Matsunaga and Ziemann (2010), is assumed to be 250 g mol^{-1} . C_w (g m^{-3}) is an assumed equivalent mass of absorbing organic material on the chamber wall (Matsunaga and Ziemann 2010). It can be regarded as characterizing the equilibrium solubility of individual organic molecules in FEP Teflon polymer and, possibly, in other organic materials deposited on the wall. When $C_w \rightarrow \infty$, the wall presents essentially an absorbing medium of infinite extent, and vapor wall deposition is ultimately an irreversible process. Note, however, that the concept of an ‘equivalent absorbing organic mass’ does not necessarily imply that an actual layer of organic material exists on the chamber wall. C_w might well represent the accumulation of deposited organic material

from previous chamber experiments, or it could reflect the absorption properties of FEP film itself. We will return to the nature of C_w shortly.

Substitution of Eqs (8) and (13) into Eq (1) gives the following conservation equation for the change in the concentration of vapor i in the well-mixed core of the chamber owing to wall deposition:

$$\frac{d\bar{C}_{v,i}}{dt} = \left(\frac{A}{V}\right) \left(\frac{\alpha_{w,i}\bar{v}_i/4}{\pi\alpha_{w,i}\bar{v}_i/8(D_iK_e)^{1/2} + 1}\right) \left(\frac{\bar{C}_{w,i}}{K_{w,i}C_w} - \bar{C}_{v,i}\right) \quad (5.15)$$

5.4 Vapor wall deposition — experiment

Experiments were conducted in the Caltech dual 24-m³ Fluorinated ethylene propylene (FEP) Teflon chambers that are suitable for pristine (low-NO) and polluted (high-NO) conditions (Zhang et al., 2013; Fehner et al., 2014; Loza et al., 2014). Figure 2 shows a schematic of the experimental protocol used to measure deposition of organic vapors to the chamber wall. Oxidized organic vapors were generated via photooxidation of four parent VOCs, isoprene, toluene, α -pinene, and dodecane, in the absence of seed aerosol. Once a sufficient amount of oxidized products is formed with none or limited aerosol formation via nucleation, irradiation is ceased, and the ensuing wall-induced dark decay of the array of oxidation products is monitored by chemical ionization mass spectrometry (CIMS). Following this period, the chambers were heated to investigate the extent to which vapor-wall partitioning is reversible. These experiments were carried out in two chambers that had been used in past SOA studies. Two control experiments were also conducted in two unused 24 m³ Teflon chambers using identical experimental protocols, see Table 1.

Vapor molecules representing SOA products were generated directly via VOC photooxidation, as opposed to the external injection of commercially available chemical standards. In this manner, uncertainty in the initial vapor concentration due to filling and mixing is avoided. In order to generate a spectrum of oxidized compounds characterized by a combination of different carbon numbers and types of functional groups, isoprene, toluene, α -pinene, and dodecane were chosen as the parent VOCs. Prior to each experiment, the Teflon chambers were flushed with purified dry air for 12 h at 45 °C, then “conditioned” by UV irradiation for 24 h in the presence of 2 ppm H₂O₂, followed by purging with purified dry air for ~ 4 days at 25 °C. Experiments were carried out under conditions in which the peroxy radicals formed from the initial OH reaction with the parent hydrocarbon react either primarily with NO (so-called high-NO) or HO₂ and RO₂ (so-called low-NO). For low-NO conditions, hydrogen peroxide (H₂O₂) was used as the OH source by evaporating 120 μ L of 50% wt aqueous solution into the chamber with 5 L min⁻¹ of purified air for ~ 110 min, resulting in an approximate starting H₂O₂ mixing ratio of 2.0 ppm. For high-NO conditions, nitrous acid (HONO) was used as the OH source by dropwise addition of 15 mL of 1 wt% NaNO₂ into 30 mL of 10 wt% H₂SO₄ in a glass bulb and introduced into the chambers with 5 L min⁻¹ of purified air for ~ 40 min. Ozone formation is substantially limited in the presence of a high concentration of HONO, and NO₃ formation is negligible. A measured volume of hydrocarbon (isoprene / toluene / α -pinene / dodecane) was injected via a syringe into a glass bulb, which was connected to the Teflon chamber. Heated 5 L min⁻¹ of purified air flowed through the glass bulb into the chamber for 20 min, introducing 25 - 200 ppb of hydrocarbon into the

chamber. After ~ 60 min mixing, photooxidation was initiated by irradiating the chamber with black lights with output wavelength ranging from 300 to 400 nm. Over the course of the irradiation period, the maximum particle mass concentration formed via nucleation ranged from 0.3 to $2 \mu\text{g m}^{-3}$, corresponding to a particle surface area to chamber wall area ratio of $< 10^{-5}$. Under these conditions, the surface area of particles present in the chamber is sufficiently low that partitioning of organic vapors onto particles is negligible. After $\sim 1 - 7$ h of reaction, UV lights were turned off and the decay of oxidation products due to wall deposition was monitored for $\sim 13 - 16$ h at 25°C . The chamber temperature was then ramped up to 45°C during the remaining $\sim 4 - 6$ h of the experiment with other conditions held constant.

Gas-phase organic compounds were monitored using a custom-modified Varian 1200 triple-quadrupole CIMS (Crouse et al., 2006; Paulot et al., 2009). In negative-mode operation, CF_3O^- was used as the reagent ion to cluster with analytes [R] with strong fluorine affinity such as hydroperoxide, producing $[\text{R}\cdot\text{CF}_3\text{O}]^-$ or $m/z = [\text{M}+85]^-$, where M is the molecular weight of the analyte. For more strongly acidic species [X], the transfer product, $[\text{X}_{[\text{H}]}\cdot\text{HF}]^-$ or $m/z = [\text{M}+19]^-$, is formed during ionization. Carboxylic acids tend to have contributions to both the transfer and cluster products, in which case the trace with higher signal-to-noise ratio is considered. Prior to each experiment, the purified air in the chamber was sampled, and this is subtracted off as the CIMS background signal. Identification of products by CIMS from the photooxidation of isoprene, α -pinene, and dodecane in our laboratory has been previously reported (Paulot et al., 2009; Eddingsaas et al., 2012; Yee et al., 2012; Zhang et al., 2014b).

5.5 Absorbing organic mass on the chamber wall (C_w)

Figure 3 shows the continuous dark decay of the 25 organic vapors generated from the photooxidation of isoprene, toluene, α -pinene, and dodecane under high/low-NO conditions. In contrast to the behavior in Fig. 3, Matsunaga and Ziemann (2010) and Yeh and Ziemann (2014) observed rapid equilibrium established within less than an hour for vapor wall losses of *n*-alkanes, 1-alkenes, 2-alcohols, 2-ketones, monoacids, and 1,2-diols in both 1.7 m³ and 5.9 m³ Teflon chambers. The organic vapor generation period in the present study ranges from 1 h to 7 h, thus precluding the possibility of observing more rapid partitioning that may have occurred. In view of this, we carried out one vapor wall deposition experiment in the α -pinene+OH low-NO system, with the experimental procedures identical to those in Section 3, but with lights on for only 10 min. We also increased the initial mixing ratios of α -pinene and OH radical precursor H₂O₂ to 1 ppm and 4 ppm, respectively, in order to generate sufficient organic vapor CIMS signals during the short irradiation period. Prompt formation of two ions, m/z 269 (-) and m/z 285 (-), was observed on the CIMS after 10 min of photochemistry. These are assigned to be two first-generation products, pinonic acid (C₁₀H₁₆O₃) and pinonic peroxy acid (C₁₀H₁₆O₄), respectively (See Table 2 for the proposed chemical structures). Owing to the short photochemical reaction timescale, the other four possible products in Table 2 were not found in this experiment. Figure 3 (bottom panel) shows the wall induced dark decay of m/z 269 (-) and m/z 285 (-) at 298 K. The best-fit first-order decay rates lie within the same order of magnitude as those reported in Table 2, i.e., $7.61 \times 10^{-6} \text{ s}^{-1}$ vs. $8.95 \times 10^{-6} \text{ s}^{-1}$ for m/z 269 (-) and $1.67 \times 10^{-6} \text{ s}^{-1}$ vs. $2.98 \times 10^{-6} \text{ s}^{-1}$ for m/z 285 (-). No rapid vapor wall

loss was found immediately after lights off, and the deposition rates for both ions were pretty consistent over the course of ~ 15 h dark decay. Note that m/z 285 (-), although having a higher molecular weight, decays more slowly than m/z 269 (-). We will demonstrate later that the wall-induced decay rate depends inversely on the vapor pressure, which is a function of the molecule size and functionalities. The addition of a carboxylic acid group, as in m/z 269 (-), leads to a greater decrease in volatility than that resulting from the addition of a peroxy carboxylic acid group, as in m/z 285 (-). Our observations for these two compounds are consistent with the observed behavior of the other 23 compounds. We tentatively attribute the difference with Matsunaga and Ziemann (2010) and Yeh and Ziemann (2014) to the mixing status of the two chambers, i.e., static chamber (Caltech) vs. actively mixed chamber employed in Matsunaga and Ziemann (2010) and Yeh and Ziemann (2014).

When the chamber temperature was increased from 25 °C to 45 °C, with all the other experimental conditions held constant, the concentrations of most compounds in the chamber increased to a minor degree relative to the initial peak signal, reflecting modest desorption of vapors from the chamber wall. As noted earlier, the chamber wall (in the used chambers) might actually be coated with organic materials from previous experiments, or the FEP Teflon film itself may act as an absorbing medium. In view of the uncertain nature of the wall itself, two control experiments were also conducted in the unused dual 24-m³ FEP Teflon chambers with identical protocols: see Table 1. Organic vapor deposition and evaporation rates between unused and used chambers are compared in Fig. 4. For all the α -pinene photooxidation products studied here, their interaction with the wall in the unused chambers is in general agreement with that in the used chambers,

except for a few oxidation products generated under high-NO conditions. The fact that these particular compounds exhibit slightly higher deposition rates in used chambers might be due to the heterogeneous chemistry on the wall catalyzed by nitric acid, a product from the $\text{NO}_x - \text{O}_3$ photochemical cycle. Overall, we conclude that the extent to which chambers have been previously used is not a significant factor in the sorption behavior of the FEP Teflon films.

The equivalent absorbing organic mass parameter ($C_w / \text{g m}^{-3}$) is estimated using equilibrium partitioning theory. We show in the Supplementary Materials that this theory is suitable for C_w estimation after ~ 18 h of wall-induced vapor decay. The ratio of the concentration of vapor i in the wall phase ($\bar{C}_{w,i}$) to that in the gas phase ($\bar{C}_{v,i}$) is expressed as a function of the corresponding gas-wall partitioning coefficient ($K_{w,i}$) and the total amount of equivalent absorbing organic mass on the chamber wall (C_w). Ideally, C_w can be obtained if the initial total concentration ($\bar{C}_{\text{tot},i}$) and equilibrium gas-phase concentration ($\bar{C}_{v,i}$) of vapor i can be measured by CIMS. However, since the fraction of organic compound i in the chamber wall at the onset of vapor wall deposition is unknown, we estimate C_w via the combination of equilibrium partitioning expressions at two different temperatures, e.g., 298 and 318 K:

$$\frac{\bar{C}_{w,i@298\text{K}}}{\bar{C}_{v,i@298\text{K}}} = \frac{\bar{C}_{\text{tot},i} - \bar{C}_{v,i@298\text{K}}}{\bar{C}_{v,i@298\text{K}}} = K_{w,i@298\text{K}} C_w \quad (5.16)$$

$$\frac{\bar{C}_{w,i@318\text{K}}}{\bar{C}_{v,i@318\text{K}}} = \frac{\bar{C}_{\text{tot},i} - \bar{C}_{v,i@318\text{K}}}{\bar{C}_{v,i@318\text{K}}} = K_{w,i@318\text{K}} C_w \quad (5.17)$$

where $\bar{C}_{\text{tot},i}$ is the total initial concentration of vapor i , $\bar{C}_{v,i@298/318\text{K}}$ is the gas-phase concentration (as indicated by the normalized CIMS signal with unit ‘a.u.’) of vapor i at

298/318 K, and $K_{w,i}@T$ is the corresponding partitioning coefficient at temperature T , see Eq (14). In this manner, both $\bar{C}_{tot,i}$ and C_w can be calculated by solving the equation set (16) and (17). Note that the product $K_{w,i}@TC_w$ is dimensionless, so that the normalized CIMS signal can be directly substituted into Eqs (16) and (17) as the actual gas-phase concentration of organic vapor i . The estimated C_w values vary by approximately five orders of magnitude and exhibit a strong dependence on the volatility of the organics, as shown in Table 2 and Fig. 5a. We will address subsequently why the C_w values span such a wide range.

5.6 Vapor Sorption into FEP Teflon films

It is instructive to consider possible mechanisms of organic vapor interactions with Teflon films. Dual sorption mechanisms in glassy polymers have been identified: ordinary dissolution and microvoid-filling (Meares, 1954; Paul, 1979; Paterson et al., 1999; Tsujita, 2003; Kanehashi and Nagai, 2005). From the point of view of solubility behavior, organic polymers such as FEP Teflon may be idealized as high molecular weight organic liquids (Vieth, et al., 1966). The polymer rubbery state is hypothesized to represent a thermodynamic equilibrium liquid state within which gas solubility obeys Henry's law. The glassy state, on the other hand, is considered to comprise two components: a hypothetical liquid state and a solid state, the latter containing a distribution of microvoids/holes that act to immobilize a portion of the penetrant molecules when the polymer is below its glass transition temperature ($T_g = 339$ K for FEP, Kim and Smith, 1990). The overall solubility of a gas molecule in a glassy polymer

has been expressed by (Barrer et al., 1958; Michaels, et al., 1963; Vieth et al., 1966; Kanehashi and Nagai, 2005):

$$C = C_H + C_L = k_H p + \frac{C'_L b p}{1 + b p} \quad (5.18)$$

where C is the total vapor concentration in the glassy polymer, C_H is the concentration based on Henry's law dissolution, C_L is the concentration based on Langmuir sorption, k_H is the Henry's law constant, p is the partial pressure in the gas phase, C'_L is the hole saturation constant, and b is the hole affinity constant. If $b p \ll 1$, Eq (18) reduces to:

$$C = (k_H + C'_L b) p \quad (5.19)$$

The condition of $b p \ll 1$ holds in the present situation because the partial pressures of organic vapors generated in the chamber are $< 10^{-7}$ atm, and the derived hole affinity constants for small organic molecules are $< 1 \text{ atm}^{-1}$ in glassy polymers (Vieth et al., 1966; Sada et al., 1988; Kanehashi and Nagai, 2005). If Eq (18) holds for the equilibrium sorption behavior of organic vapors by FEP films, then the dimensionless form of the effective Henry's law constant (H_i) can be expressed as a function of the partitioning coefficient of vapor i ($K_{w,i}$) and total absorbing organic mass on the chamber wall (C_w):

$$H_i = \frac{\bar{C}_{w,i}}{\bar{C}_{v,i}} = K_{w,i} C_w \propto (k_H + C'_L b) \quad (5.20)$$

As shown in Fig. 5b, the derived Henry's law constants (H) for the organic oxidation products span approximately two orders of magnitude and depend inversely on saturation concentrations ($C_i^* / \mu\text{g m}^{-3}$). This behavior suggests that organic vapor solubility in FEP films increases with decreasing volatility, i.e., increasing carbon number and functionalization. This behavior provides a qualitative explanation for the wide range of

C_w values calculated for the 25 organic vapors studied here. Although the solubility of low volatility vapors in the FEP Teflon film is relatively high (large H), the total equivalent absorbing organic mass on the wall required for gas-wall partitioning can still be low (small C_w) because low volatility compounds tend to partition preferentially in the wall phase (large $K_{w,i}$). As illustrated in Fig. 5b, the dimensionless Henry's law constant of $m/z = (-) 303$, a product from α -pinene low-NO photochemistry, is ~ 20 times larger than that of $m/z = (-) 185$, a product from isoprene + OH under high-NO conditions. The vapor pressure of $m/z = (-) 303$, however, is \sim six orders of magnitude lower than that of $m/z = (-) 185$. As a result, the C_w value for $m/z = (-) 303$ is \sim five orders of magnitude smaller than that for $m/z = (-) 185$. One infers that the equivalent absorbing organic mass on the chamber wall derived earlier is not constant but specific to individual organic compounds, i.e., a function of volatility and solubility in FEP Teflon polymer. We will show that C_w is not the most dominant parameter, so the assumption of a single value for C_w , does not invalidate the usefulness the theory.

5.7 Accommodation coefficient on the chamber wall ($\alpha_{w,i}$)

One key parameter that emerges from the theory of vapor wall deposition, the total equivalent absorbing organic mass (C_w), can be calculated based on equilibrium gas-wall partitioning at two different temperatures. From this information, we can estimate the other key parameter, the accommodation coefficient ($\alpha_{w,i}$), by optimal fitting of the solution of Eq (15) to CIMS measured organic vapor decay at 298 K:

$$\frac{d\bar{C}_{v,i}}{dt} = \left(\frac{A}{V}\right) \left(\frac{\alpha_{w,i}\bar{v}_i/4}{\pi\alpha_{w,i}\bar{v}_i/8(\mathcal{D}_iK_e)^{1/2} + 1} \right) \left(\frac{\bar{C}_{\text{tot},i} - \bar{C}_{v,i}}{K_{w,i}C_w} - \bar{C}_{v,i} \right) \quad (5.21)$$

Note that Eq (21) is simply Eq (15) in which $\bar{C}_{w,i}$ has been replaced with $(\bar{C}_{\text{tot},i} - \bar{C}_{v,i})$. Thus, Eq (21) constitutes a linear ODE system with the one unknown (estimable) parameter, $\alpha_{w,i}$. The Levenberg-Marquardt method implemented in MATLAB's "System Identification Toolbox" was used for the nonlinear minimization at each time step of its solution. The best-fit $\alpha_{w,i}$ value obtained was then substituted into Eq (21) to give the simulated temporal profile of the organic vapor i . Simulation results (SIM.1) are shown in Fig. 3.

The other limit of wall behavior is that of irreversible gas-wall partitioning ($C_w \rightarrow \infty$). In this case, the accommodation coefficient $\alpha_{w,i}$ is the sole governing parameter and Eq (15) can be simplified as:

$$\frac{d\bar{C}_{v,i}}{dt} = - \left(\frac{A}{V}\right) \left(\frac{\alpha_{w,i}\bar{v}_i/4}{\pi\alpha_{w,i}\bar{v}_i/8(\mathcal{D}_iK_e)^{1/2} + 1} \right) \bar{C}_{v,i} \quad (5.22a)$$

The overall deposition rate of organic vapor i ($k_{w,i}$) is therefore:

$$k_{w,i} = \left(\frac{A}{V}\right) \left(\frac{\alpha_{w,i}\bar{v}_i/4}{\pi\alpha_{w,i}\bar{v}_i/8(\mathcal{D}_iK_e)^{1/2} + 1} \right) \quad (5.22b)$$

Results for irreversible gas-wall partitioning (SIM.2) are shown in Fig. 3.

Simulations using both reversible (SIM.1) and irreversible (SIM.2) vapor wall deposition expressions match the experimental data. Outputs from SIM.1 tend to level off, whereas those from SIM.2 exhibit a continuous decreasing trend at the end of ~ 18 h of vapor decay. The extent of agreement between observations and simulations depends on the nature of vapor wall deposition: most organic vapors in the Caltech Teflon chambers exhibit a continuous decay. The agreement between SIM.1 and SIM.2 indicates that the estimated C_w values are sufficiently large so that the wall-induced vapor

deposition in the Caltech chamber can be treated as an irreversible process ($C_w \rightarrow \infty$) within a relatively long timescale (<18 h).

Overall, results from the two simulations indicate that $\alpha_{w,i}$ is the more influential parameter than C_w in describing the wall-induced deposition of semi-volatile organic vapors. The significance of $\alpha_{w,i}$ is twofold: first, the accommodation coefficient for the desorption of organic molecules from the gas-wall interface equals that for the adsorption/uptake process, which together influence the time needed to establish equilibrium; and second, diffusion in the chamber wall is not considered in the theoretical framework and consequently, the best-fit $\alpha_{w,i}$ will reflect the mass transfer resistance in both the gas-wall interface and the chamber wall layer. We suggest that the vapor wall deposition of individual compounds can be adequately parameterized through the accommodation coefficient $\alpha_{w,i}$ as the single dominant variable. As shown in Table 2 and Fig. 6, for the compounds studied here, estimated values of $\alpha_{w,i}$ span approximately two orders of magnitude ($10^{-8} - 10^{-6}$) and depend inversely on volatility, implying that more highly functionalized compounds dissolve more easily in FEP Teflon film. The correlation of $\alpha_{w,i}$ with the average carbon oxidation state (OS_C), however, is not strong due to the fact that vapor pressures of molecules, although highly oxidized, are not necessarily low.

5.8 Characterizing chamber vapor wall deposition rate

The wall-induced deposition of the 25 organic compounds investigated in the present study can be sufficiently represented by a single parameter, the wall accommodation coefficient ($\alpha_{w,i}$), which is observed to exhibit a strong inverse dependence on C_i^* (Fig.

6). It is possible to formulate an empirical expression for $\alpha_{w,i}$ as a function of C_i^* , a parameter that can be estimated by vapor pressure prediction models.

Linear regression was performed on $\log_{10}\alpha_{w,i}$ vs. $\log_{10}C_i^*$ for the 25 organic vapors studied:

$$\log_{10}\alpha_{w,i} = -0.1919 \times \log_{10}C_i^* - 6.32 \quad (5.23)$$

We employ a group-contribution expression for $\log_{10}C_i^*$ as a function of carbon number (n_C^i) and oxygen number (n_O^i) developed by Donahue et al. (2011):

$$\log_{10}C_i^* = (n_C^0 - n_C^i)b_C - n_O^i b_O - 2 \frac{n_C^i n_O^i}{n_C^i + n_O^i} b_{CO} \quad (5.24)$$

where n_C^0 is the carbon number of 1 $\mu\text{g m}^{-3}$ alkane ($n_C^0 = 28.0483$), b_C is the carbon-carbon interaction term ($b_C = 0.4015$), b_O is the oxygen-oxygen interaction term ($b_O = 2.3335$), and b_{CO} is the carbon-oxygen nonideality term ($b_{CO} = -0.4709$). Best-fit values of n_C^0 , b_C , b_O , and b_{CO} are obtained by optimal fitting Eq (24) to the saturation concentrations of 110 species, including C₅-C₁₄ *n*-alkanes, C₅-C₁₄ carbonyls, C₅-C₁₄ di-carbonyls, C₅-C₁₄ alcohols, C₅-C₁₄ diols, C₅-C₁₄ carboxylic acids, C₅-C₁₄ di-carboxylic acids, C₅-C₁₄ peroxides, C₅-C₁₄ di-peroxides, C₅-C₁₄ nitrates, and C₅-C₁₄ di-nitrates. Vapor pressures of these species are estimated by taking the average of predictions from the two group contribution methods, ‘SIMPOL.1’ and ‘EVAPORATION’.

Combining Eqs (22), (23), and (24), the vapor wall deposition rate of any intermediate/semi/non-volatility compound ($k_{w,i} / \text{s}^{-1}$) can be ultimately related to its carbon and oxygen numbers. This vapor wallloss rate estimation approach, although simplified, proves to be quite useful considering the limited knowledge of the chemical

structures of the thousands of ions detected by mass spectrometry during an experiment. The proper guess of a molecular formula would be able to constrain the wall-induced decay rate of each ion, and thus provide information to better understand its formation and removal dynamics. In this way, one can reasonably constrain the wall-induced organic vapor deposition rate based on only two measurable or predictable properties, volatility and the extent of oxygenation.

As shown in Fig. 7, within a certain volatility range, $k_{w,i}$ increases with decreasing C_i^* , implying that highly functionalized compounds tend to deposit on the chamber wall more efficiently. The maximum value of vapor wall deposition rate is eventually approached for highly oxygenated and extremely low-volatility compounds (which, of course, are precisely those compounds that are most prone to form SOA). Revisiting Eq (22) reveals that the deposition rate of organic vapors is limited either by molecular diffusion or by turbulent mixing. For extremely small $\alpha_{w,i}$ (large C_i^*), $k_{w,i}$ becomes:

$$k_{w,i} = \left(\frac{A}{V}\right) \left(\frac{\alpha_{w,i} \bar{V}_i}{4}\right) \quad (5.25)$$

In this case, the organic vapor wall deposition rate is governed by the molecular identity of individual compounds. On the other hand, if $\alpha_{w,i}$ is sufficiently large (small C_i^*), $k_{w,i}$ is approximately given by:

$$k_{w,i} = \frac{\pi}{2} \left(\frac{A}{V}\right) (\mathcal{D}_i K_e)^{1/2} \quad (5.26)$$

In this case, the vapor wall deposition rate is ultimately controlled by the mixing state in the chamber. Eq (26) provides an expression for the upper limit of vapor wall deposition

rate in a chamber, which is a manifestation of the extent of turbulent mixing in the chamber.

5.9 Impact of vapor wall deposition on SOA yields

The extent to which vapor wall deposition impacts measured SOA yields depends on the competition between uptake of organic vapors by suspended particles and the chamber wall. The timescale ($\tau_{g/p,i}$) associated with establishing equilibrium gas-particle partitioning is governed by three transport processes: diffusion of vapor molecules from the bulk gas phase to the surface of the particle, uptake of vapor molecules by the particle surface, and diffusion of molecules in the bulk particle phase. Depending on a given situation, any of these three transport processes can be the limiting step in determining the overall equilibrium partitioning timescale. Here we represent the diffusional transport processes across the gas-particle interface and in the particle phase itself by a single parameter, the accommodation coefficient of organic vapors on the particle ($\alpha_{p,i}$). In doing so, the mass transfer resistances at the gas-particle interface and in the particle phase are reflected by the single parameter $\alpha_{p,i}$, and the timescale to achieve gas-particle partitioning following a small perturbation of the condensing species in the gas phase is given by (Seinfeld and Pandis, 2006):

$$\tau_{g/p,i} = (2\pi N_p \bar{D}_p \mathcal{D}_i f(Kn, \alpha_{p,i}))^{-1} \quad (5.27)$$

where N_p is the total number concentration of suspended particles, \bar{D}_p is the number mean particle diameter, $Kn (= 2\lambda/D_p)$ is the Knudsen number, and $f(Kn, \alpha_{p,i})$ is the correction factor for noncontinuum diffusion and imperfect accommodation (Seinfeld and Pandis, 2006).

Fig. 8 shows the predicted $\tau_{g/p,i}$ as a function of: 1) the ratio of total particle surface area to chamber wall area (R_a) and 2) $\alpha_{p,i}$. The red solid line represents $\tau_{g/p,i}$ for a typical chamber experiment with seed surface area of $\sim 1000 \mu\text{m}^2 \text{cm}^{-3}$. In this case, equilibrium vapor-particle partitioning is established within a few minutes in the presence of perfect accommodation of organic vapors onto particles ($\alpha_{p,i} = 1$) or when a sufficiently large concentration of suspended particles is present (e.g., $C_{OA} > 10^5 \mu\text{g m}^{-3}$ when $\alpha_{p,i} < 10^{-4}$).

By analogy with the treatment of gas-particle partitioning, the time scale associated with vapor-wall interactions is presumably governed by gas-phase diffusion of vapor molecules to the wall through a boundary layer adjacent to the wall, uptake of vapor molecules at the wall surface, and, potentially, diffusion of molecules in the wall. Again, a single parameter, the accommodation coefficient on the wall ($\alpha_{w,i}$), is employed to represent the latter two processes. Thus, the vapor wall deposition timescale is given by:

$$\tau_{g/w,i} = k_{w,i}^{-1} \quad (5.28)$$

The white solid line in Fig. 8 represents the predicted $\tau_{g/w,i}$, covering a range of several minutes to several hours, as a function of the vapor accommodation coefficient on the chamber wall ($\alpha_{w,i}$). The region to the left of the white solid line is that in which $\tau_{g/w,i}$ and $\tau_{g/p,i}$ are competitive. For low $\alpha_{w,i}$ (e.g., $< 10^{-8}$), $\tau_{g/w,i}$ is comparable to $\tau_{g/p,i}$ only if the vapor has a low accommodation coefficient on the particles ($\alpha_{p,i} < 10^{-4}$) or if a relatively small concentration of particles is present in the chamber ($R_a < 10^{-4}$). For $\alpha_{w,i} > 10^{-4}$, $\tau_{g/w,i}$ is estimated to be of the order of several minutes and, as a result, vapor transport to particles is suppressed by competition with the chamber wall, even with perfect particle accommodation ($\alpha_{p,i} = 1$) or high particle concentrations ($R_a > 10^{-2}$).

Overall, in the region (confined by the white solid and dash lines in Fig. 8) where gas-wall partitioning is competitive with gas-particle partitioning, it is necessary to account for vapor wall deposition when deriving SOA yields from chamber experiments. The theoretical framework developed in this study suggests that the area of this region is ultimately controlled by the accommodation coefficient of organic vapors on particles ($\alpha_{p,i}$) vs. the chamber wall ($\alpha_{w,i}$).

5.10 Conclusions

The wall-induced decay of organic vapors is the result of coupled physical processes involving transport of organic vapors from the well-mixed core of a chamber to its wall by molecular and turbulent diffusion, uptake of organic molecules by the Teflon film, and re-evaporation from the wall. The wall-induced dark decay of 25 intermediate/semi-volatility organic compounds generated from the photochemistry of four parent hydrocarbons was monitored in the Caltech dual 24-m³ FEP Teflon chambers. The extent to which organic vapors and the chamber wall interact was found to be similar in used vs. unused Teflon chambers. Based on this observation, one concludes that the Teflon film itself acts as an effective sorption medium, and organic materials deposited from past chamber experiments, if they indeed exist, do not significantly impact the sorption behavior of organic molecules. Reversibility in gas-wall partitioning was observed: evaporation of all 25 compounds that had deposited on the wall during an 18-h deposition period occurred when the chamber temperature was increased from 25 °C to 45 °C.

Based on a derived model that describes the dynamics of vapor deposition on the chamber wall, a single parameter, the accommodation coefficient ($\alpha_{w,i}$), emerges to

govern the extent of the vapor-wall mass transfer process. Moreover, $\alpha_{w,i}$ exhibits a strong dependence on the molecular properties, such as vapor pressure and oxidation state, of the 25 organics studied. We present an empirical expression for $\alpha_{w,i}$ as a function of the compound vapor pressure, thus affording the possibility to predict the wall deposition rate of intermediate/semi/non-volatility compounds in a Teflon chamber based on their molecular constituency.

Previous studies have observed the chemical transformation of δ -hydroxycarbonyls to substituted dihydrofurans on the chamber wall (Lim and Ziemann, 2005, 2009; Zhang et al., 2014b), suggesting the potential occurrence of heterogeneous reactions on the chamber wall surface. While the extent to which heterogeneous transformations proceed can be potentially represented through the accommodation coefficient, the occurrence of wall-induced chemistry adds another dimension of complexity in predicting vapor wall deposition rates.

Quantifying the impact of vapor wall deposition on the chamber-derived SOA yield is the next step in assessing the effect of vapor wall deposition of SOA formation and evolution. Future studies will be directed at: 1) experiments to determine the accommodation coefficients of organic vapors on particles for a variety of SOA systems, and 2) state-of-art SOA predictive models that describe the dynamics of vapor-wall and vapor-particle interactions to estimate the fraction of organic vapor fluxes transported to the suspended particles vs. the chamber wall.

5.11 Acknowledgements

This study was supported by NOAA Climate Program Office's AC4 program, award # NA13OAR4310058 and State of California Air Resources Board agreement 13-321.

5.12 Appendix

A (m^2): Total surface area of the chamber wall

$\alpha_{p,i}$ (dimensionless): Accommodation coefficient of organic vapor i on particles

$\alpha_{w,i}$ (dimensionless): Accommodation coefficient of organic vapor i on the chamber wall

$C_{\theta,i}$ (g m^{-3}): Concentration of organic vapor i over the gas-wall interface

C_i^* (g m^{-3}): Saturation concentration of organic vapor i

$\bar{C}_{\text{tot},i}$ (g m^{-3}): Total concentration of organic vapor i in the chamber

$\bar{C}_{v,i}$ (g m^{-3}): Concentration of organic vapor i in the well-mixed core of the chamber

$C_{v,i}$ (g m^{-3}): Local concentration of organic vapor i in the boundary layer adjacent to the wall

$\bar{C}_{w,i}$ (g m^{-3}): Concentration of organic vapor i that has accumulated on the chamber wall

C_w (g m^{-3}): Equivalent mass of absorbing organic material on the chamber wall

\bar{D}_p (m): Number mean particle diameter

\mathcal{D}_e ($\text{m}^2 \text{s}^{-1}$): Eddy diffusivity

\mathcal{D}_i ($\text{m}^2 \text{s}^{-1}$): Molecular diffusivity of organic vapor i

δ (m): Thickness of the boundary layer adjacent to the wall

H_i (dimensionless): Henry's law constant of organic compound i

$J_{v,i}$ ($\text{g m}^{-2} \text{s}^{-1}$): Vapor flux arriving at the gas-wall interface

$J_{w,i}$ ($\text{g m}^{-2} \text{s}^{-1}$): Vapor flux evaporating from the wall

K_e (s^{-1}): Eddy diffusion coefficient

$K_{w,i}$ ($\text{m}^3 \text{g}^{-1}$): Gas-wall partitioning coefficient

$k_{w,\text{depo},i}$ (s^{-1}): Deposition rate coefficient to the wall

$k_{w,\text{evap},i}$ (s^{-1}): Evaporation rate coefficient from the wall

\overline{M}_w (g mol^{-1}): Average molecular weight of the absorbing organic material on the wall

N_p (m^{-3}): Total number concentration of suspended particles

$p_{L,i}^0$ (atm): Vapor pressure of organic compound i as a liquid

γ_i (dimensionless): Activity coefficient in the wall layer on a mole fraction basis

\bar{v}_i (m s^{-1}): Mean thermal speed

V (m^3): Total volume of the chamber

5.13 Bibliography

Barrer, R. M., Barrie, J. A., and Slater, J.: Sorption and diffusion in ethyl cellulose. Part III. Comparison between ethyl cellulose and rubber, *J. Polym. Sci.*, 27, 177-197, 1958.

Compernelle, S., Ceulemans, K., and Muller, J. F.: EVAPORATION: a new vapour pressure estimation method for organic molecules including non-additivity and intramolecular interactions, *Atmos. Chem. Phys.*, 11, 9431-9450, doi: 10.5194/acp-11-9431-2011, 2011.

Corner, J. and Pendlebury, E. D.: The coagulation and deposition of a stirred aerosol, *P. Phys. Soc. Lond. B.*, 64, 645-654, 1951.

Crouse, J. D., McKinney, K. A., Kwan, A. J., and Wennberg, P. O.: Measurement of gas-phase hydroperoxides by chemical ionization mass spectrometry, *Anal. Chem.*, 78, 6726-6732, 2006.

- Crump, J. G. and Seinfeld, J. H.: Turbulent deposition and gravitational sedimentation of an aerosol in a vessel of arbitrary shape, *J. Aerosol. Sci.*, 12, 405-415, 1981.
- Donahue, N. M., Epstein, S. A., Pandis, S. N., and Robinson, A. L.: A two-dimensional volatility basis set: 1. Organic-aerosol mixing thermodynamics, *Atmos. Chem. Phys.*, 11, 3303-3318, doi: 10.5194/acp-11-3303-2011, 2011.
- Eddingsaas, N. C., Loza, C. L., Yee, L. D., Seinfeld, J. H., and Wennberg, P. O.: alpha-pinene photooxidation under controlled chemical conditions - Part 1: Gas-phase composition in low- and high-NO_x environments, *Atmos. Chem. Phys.*, 12, 6489-6504, doi: 10.5194/acp-12-6489-2012, 2012.
- Fahnestock, K. A. S., Yee, L. D., Loza, C. L., Coggon, M. M., Schwantes, R., Zhang, X., Dalleska, N. F., and John H Seinfeld: Secondary Organic Aerosol Composition from C₁₂ Alkanes, *J. Phys. Chem. A.*, *in press*, 2014.
- Grosjean, D.: Wall loss of gaseous-pollutants in outdoor Teflon chambers, *Environ. Sci. Technol.*, 19, 1059-1065, 1985.
- Kanehashi, S. and Nagai, K.: Analysis of dual-mode model parameters for gas sorption in glassy polymers, *J. Membrane. Sci.*, 253, 117-138, 2005.
- Kim, C. S. and Smith, T. L.: An improved method for measuring the thermal coefficient of linear expansion of flexible polymer-films, *J. Polym. Sci. Pol. Phys.*, 28, 2119-2126, 1990.
- Kokkola, H., Yli-Pirilä, P., Vesterinen, M., Korhonen, H., Keskinen, H., Romakkaniemi, S., Hao, L., Kortelainen, A., Joutsensaari, J., Worsnop, D. R., Virtanen, A., and Lehtinen, K. E. J.: The role of low volatile organics on secondary organic aerosol formation, *Atmos. Chem. Phys.*, 14, 1689-1700, 2014
- Lim, Y. B. and Ziemann, P. J.: Products and mechanism of secondary organic aerosol formation from reactions of *n*-alkanes with OH radicals in the presence of NO_x, *Environ. Sci. Technol.*, 39, 9229-9236, 2005.

- Lim, Y. B. and Ziemann, P. J.: Effects of molecular structure on aerosol yields from OH radical-initiated reactions of linear, branched, and cyclic alkanes in the presence of NO_x, *Environ. Sci. Technol.*, 43, 2328-2334, 2009.
- Loza, C. L., Chan, A. W. H., Galloway, M. M., Keutsch, F. N., Flagan, R. C., and Seinfeld, J. H.: Characterization of vapor wall loss in laboratory chambers, *Environ. Sci. Technol.*, 44, 5074-5078, 2010.
- Loza, C. L., Craven, J. S., Yee, L. D., Coggon, M. M., Schwantes, R. H., Shiraiwa, M., Zhang, X., Schilling, K. A., Ng, N. L., Canagaratna, M. R., Ziemann, P. J., Flagan, R. C., and Seinfeld, J. H.: Secondary organic aerosol yields of 12-carbon alkanes, *Atmos. Chem. Phys.*, 14, 1423-1439, doi:10.5194/acp-14-1423-2014, 2014.
- Matsunaga, A. and Ziemann, P. J.: Gas-wall partitioning of organic compounds in a Teflon film chamber and potential effects on reaction product and aerosol yield measurements, *Aerosol. Sci. Tech.*, 44, 881-892, 2010.
- Mcmurry, P. H. and Grosjean, D.: Gas and aerosol wall losses in Teflon film smog chambers, *Environ. Sci. Technol.*, 19, 1176-1182, 1985.
- Meares, P.: The diffusion of gases through polyvinyl acetate, *J. Am. Chem. Soc.*, 76, 3415-3422, 1954.
- Michaels, A. S., Barrie, J. A., and Vieth, W. R.: Solution of gases in polyethylene terephthalate, *J. Appl. Phys.*, 34, 1-13, 1963.
- Pankow, J. F. and Asher, W. E.: SIMPOL.1: a simple group contribution method for predicting vapor pressures and enthalpies of vaporization of multifunctional organic compounds, *Atmos. Chem. Phys.*, 8, 2773-2796, doi:10.5194/acp-8-2773-2008, 2008.
- Paterson, R., Yampol'skii, Y., Fogg, P. G. T., Bokarev, A., Bondar, V., Ilinich, O., and Shishatskii, S.: IUPAC-NIST solubility data series 70. Solubility of gases in glassy polymers, *J. Phys. Chem. Ref. Data*, 28, 1255-1450, 1999.
- Paul, D. R.: Gas sorption and transport in glassy-polymers, *Ber. Bunsen. Phys. Chem.*, 83, 294-302, 1979.

Paulot, F., Crouse, J. D., Kjaergaard, H. G., Kroll, J. H., Seinfeld, J. H., and Wennberg, P. O.: Isoprene photooxidation: new insights into the production of acids and organic nitrates, *Atmos. Chem. Phys.*, 9, 1479-1501, doi:10.5194/acp-9-1479-2009, 2009.

Sada, E., Kumazawa, H., Xu, P., and Nishigaki, M.: Mechanism of gas permeation through glassy polymer-films, *J. Membrane Sci.*, 37, 165-179, 1988.

Seinfeld, J. H. and Pandis, S. N.: *Atmospheric chemistry and physics : from air pollution to climate change* (2nd Edn.), John Wiley & Sons, Inc., Hoboken, NJ, 2006.

Tsujita, Y.: Gas sorption and permeation of glassy polymers with microvoids, *Prog. Polym. Sci.*, 28, 1377-1401, 2003.

Vieth, W. R., Tam, P. M., and Michaels, A. S.: Dual sorption mechanisms in glassy polystyrene, *J. Colloid. Interf. Sci.*, 22, 360-370, 1966.

Yee, L. D., Craven, J. S., Loza, C. L., Schilling, K. A., Ng, N. L., Canagaratna, M. R., Ziemann, P. J., Flagan, R. C., and Seinfeld, J. H.: Secondary organic aerosol formation from low-NO_x photooxidation of dodecane: Evolution of multigeneration gas-phase chemistry and aerosol composition, *J. Phys. Chem. A.*, 116, 6211-6230, 2012.

Yeh, G. K. and Ziemann, P. J.: Alkyl nitrate formation from the reactions of C8-C14 n-alkanes with OH radicals in the presence of NO_x: measured yields with essential corrections for gas-wall partitioning, *J. Phys. Chem. A*, 118, 8147-8157, 2014.

Zhang, X., and Seinfeld, J. H.: A functional group oxidation model (FGOM) for SOA formation and aging, *Atmos. Chem. Phys.*, 13, 5907-5926, doi:10.5194/acp-13-5907-2013, 2013.

Zhang, X., Cappa, C. D., Jathar, S. H., McVay, R. C., Ensberg, J. J., Kleeman, M. J., and Seinfeld, J. H.: Influence of vapor wall loss in laboratory chambers on yields of secondary organic aerosol, *P. Natl. Acad. Sci. USA*, 111, 5802-5807, 2014a.

Zhang, X., Schwantes, R. H., Coggon, M. M., Loza, C. L., Schilling, K. A., Flagan, R. C., and Seinfeld, J. H.: Role of ozone in SOA formation from alkane photooxidation, *Atmos. Chem. Phys.*, 14, 1733-1753, doi:10.5194/acp-14-1733-2014, 2014b.

Table 5.1. Experimental conditions for production of oxidized organic vapors.

#	Lights on (h)	Lights off (h)	T program ^a (K [h-h])	OH source	VOC	HC ₀ (ppb)	(NO) ₀ (ppb)	(NO ₂) ₀ (ppb)	Maximum Particle conc. (μg m ⁻³)	FEP Bag condition
~ 1	~ 24.2	~ 24.2	298 [0-17.6] 318 [19.9-25.2]	HONO	α-pinene	~ 30	242	458	~ 0.4	used
~ 1	~ 24.2	~ 24.2	298 [0-17.6] 318 [19.9-25.2]	HONO	α-pinene	~ 30	229	371	~ 0.3	unused
~ 1	~ 23.8	~ 23.8	298 [0-17.3] 318 [20.9-24.8]	HONO	dodecane	~ 50	275	556	~ 2.1	used
~ 2	~ 23	~ 23	298 [0-17.3] 318 [20.8-25]	HONO	isoprene	~ 200	243	460	~ 0.2	used
~ 1	~ 24.2	~ 24.2	298 [0-17.8] 318 [20.3-25.2]	H ₂ O ₂	α-pinene	~ 30	< DL	< DL	~ 1.2	used
~ 1	~ 24.2	~ 24.2	298 [0-17.8] 318 [20.3-25.2]	H ₂ O ₂	α-pinene	~ 30	< DL	< DL	~ 1.1	unused
~ 7	~ 21.6	~ 21.6	298 [0-20.6] 318 [22-28.6]	H ₂ O ₂	dodecane	~ 50	< DL	< DL	~ 0.0	used
~ 5	~ 24.7	~ 24.7	298 [0-21.3] 318 [24.7-29.7]	H ₂ O ₂	toluene	~ 100	< DL	< DL	~ 0.1	used

Table 5.2. Best-fit values of vapor-wall accommodation coefficient ($\alpha_{w,i}$) and calculated equivalent absorbing organic mass (C_w) on chamber walls for vapors with structure proposed based on the CIMS measurement.

Observed m/z	Chemical Formula	Vapor pressure (atm @ 298K) ^a	Vapor wall deposition rate $k_{w,i}$ (s ⁻¹) ^b	$\alpha_{w,i}$ ^c	C_w (g m ⁻³) ^d
269 (-)	C ₁₀ H ₁₆ O ₃	9.64×10 ⁻⁸	(8.95±2.55)×10 ⁻⁶	(9.15±2.63)×10 ⁻⁸	(6.59±3.43)×10 ⁻⁴
285 (-)	C ₁₀ H ₁₆ O ₄	1.05×10 ⁻⁶	(2.98±1.14)×10 ⁻⁶	(3.24±1.20)×10 ⁻⁸	(5.90±3.65)×10 ⁻³
253 (-)	C ₁₀ H ₁₆ O ₂	6.79×10 ⁻⁶	(4.40±0.70)×10 ⁻⁶	(4.31±0.68)×10 ⁻⁸	(4.57±2.45)×10 ⁻³
257 (-)	C ₉ H ₁₆ O ₃	2.65×10 ⁻⁶	(3.19±3.13)×10 ⁻⁶	(3.12±3.07)×10 ⁻⁸	(6.31±4.98)×10 ⁻³
271 (-)	C ₁₀ H ₁₈ O ₃	5.14×10 ⁻⁸	(1.09±0.06)×10 ⁻⁵	(1.15±0.07)×10 ⁻⁷	(5.56±3.86)×10 ⁻⁵
303 (-)	C ₁₀ H ₁₈ O ₅	1.56×10 ⁻¹⁰	(1.32±0.19)×10 ⁻⁵	(1.49±0.22)×10 ⁻⁷	(1.12±1.19)×10 ⁻⁶
227 (-)	C ₇ H ₁₀ O ₃	1.24×10 ⁻⁵	(1.63±0.50)×10 ⁻⁵	(1.52±0.15)×10 ⁻⁷	(1.01±0.91)×10 ⁻²
269 (-)	C ₁₀ H ₁₆ O ₃	3.48×10 ⁻⁹	(1.94±0.30)×10 ⁻⁵	(1.97±0.32)×10 ⁻⁷	(2.80±1.02)×10 ⁻⁵
285 (-)	C ₁₀ H ₁₆ O ₄	6.32×10 ⁻¹¹	(1.51±0.15)×10 ⁻⁵	(1.62±0.16)×10 ⁻⁷	(3.83±3.11)×10 ⁻⁷
300 (-)	C ₁₀ H ₁₇ O ₄ N	1.53×10 ⁻⁷	(1.19±0.13)×10 ⁻⁵	(1.34±0.14)×10 ⁻⁷	(1.79±0.06)×10 ⁻⁴
314 (-)	C ₁₀ H ₁₅ O ₅ N	1.52×10 ⁻⁷	(2.31±0.21)×10 ⁻⁵	(2.94±0.26)×10 ⁻⁷	(1.14±0.10)×10 ⁻³
316 (-)	C ₁₀ H ₁₇ O ₅ N	9.03×10 ⁻¹⁰	(1.85±0.14)×10 ⁻⁵	(2.19±0.17)×10 ⁻⁷	(5.36±9.85)×10 ⁻⁶
215 (-)	C ₇ H ₁₄ O ₂	1.98×10 ⁻⁵	(5.27±1.74)×10 ⁻⁶	(4.50±1.49)×10 ⁻⁸	(3.10±0.55)×10 ⁻²
285(-)	C ₁₂ H ₂₄ O ₂	3.58×10 ⁻⁷	(1.32±0.44)×10 ⁻⁵	(1.42±0.46)×10 ⁻⁷	(3.50±0.81)×10 ⁻³
287 (-)	C ₁₂ H ₂₆ O ₂	1.21×10 ⁻⁶	(8.25±0.67)×10 ⁻⁶	(8.79±0.73)×10 ⁻⁸	(2.81±1.92)×10 ⁻³
301 (-)	C ₁₂ H ₂₄ O ₃	1.30×10 ⁻⁷	(1.19±0.13)×10 ⁻⁵	(1.35±0.15)×10 ⁻⁷	(8.39±7.24)×10 ⁻⁴
315 (-)	C ₁₂ H ₂₂ O ₄	1.56×10 ⁻⁸	(2.68±0.49)×10 ⁻⁵	(3.17±0.61)×10 ⁻⁷	(1.79±2.15)×10 ⁻⁴
332 (-)	C ₁₂ H ₂₅ O ₄ N	2.17×10 ⁻⁸	(1.55±0.07)×10 ⁻⁵	(1.86±0.09)×10 ⁻⁷	(3.93±0.46)×10 ⁻⁴
346 (-)	C ₁₂ H ₂₃ O ₅ N	4.46×10 ⁻⁹	(2.33±0.25)×10 ⁻⁵	(2.91±0.33)×10 ⁻⁷	(1.87±0.21)×10 ⁻⁵
141 (-)	C ₇ H ₆ O ₂	5.30×10 ⁻⁶	(2.04±1.88)×10 ⁻⁶	(1.68±1.35)×10 ⁻⁸	(1.13±0.07)×10 ⁻²
209 (-)	C ₇ H ₈ O ₂	4.89×10 ⁻⁵	(5.78±1.93)×10 ⁻⁶	(4.82±1.62)×10 ⁻⁸	(7.03±1.42)×10 ⁻²
241 (-)	C ₇ H ₈ O ₄	4.00×10 ⁻⁶	(2.04±0.40)×10 ⁻⁵	(1.95±0.39)×10 ⁻⁷	(2.66±0.71)×10 ⁻²
175 (-)	C ₃ H ₆ O ₃	2.21×10 ⁻⁴	(9.68±1.51)×10 ⁻⁶	(6.90±1.08)×10 ⁻⁸	(3.03±1.10)×10 ⁻¹
185 (-)	C ₅ H ₈ O ₂	1.73×10 ⁻⁴	(6.58±0.30)×10 ⁻⁶	(4.93±0.22)×10 ⁻⁸	(7.70±2.01)×10 ⁻²
199 (-)	C ₅ H ₆ O ₃	8.17×10 ⁻⁶	(2.46±0.81)×10 ⁻⁶	(1.96±0.64)×10 ⁻⁸	(1.23±0.31)×10 ⁻²

217 (-)	$C_5H_8O_4$	2.70×10^{-7}	$(1.40 \pm 0.11) \times 10^{-5}$	$(1.22 \pm 0.10) \times 10^{-7}$	$(1.15 \pm 0.60) \times 10^{-4}$
232 (-)	$C_5H_9O_4N$	2.34×10^{-5}	$(5.24 \pm 0.24) \times 10^{-6}$	$(4.76 \pm 0.22) \times 10^{-8}$	$(1.78 \pm 0.42) \times 10^{-3}$
234 (-)	$C_4H_7O_5N$	3.93×10^{-6}	$(3.23 \pm 1.30) \times 10^{-6}$	$(2.97 \pm 0.28) \times 10^{-8}$	$(5.16 \pm 1.36) \times 10^{-4}$
311 (-)	$C_5H_{10}O_8N_2$	1.15×10^{-9}	$(3.10 \pm 0.45) \times 10^{-5}$	$(3.66 \pm 0.54) \times 10^{-7}$	$(8.27 \pm 1.24) \times 10^{-6}$

Figure 5.1. Theoretical framework representing the vapor-wall interactions. Concentrations of organic vapor i in the well-mixed core, in the boundary layer, over the surface of chamber walls, and in the chamber walls are denoted by $\bar{C}_{v,i}$, $C_{v,i}$, $C_{0,i}$, and $\bar{C}_{w,i}$, respectively. Vapor fluxes at the gas-wall interface are denoted by $J_{v,i}$ and $J_{w,i}$.

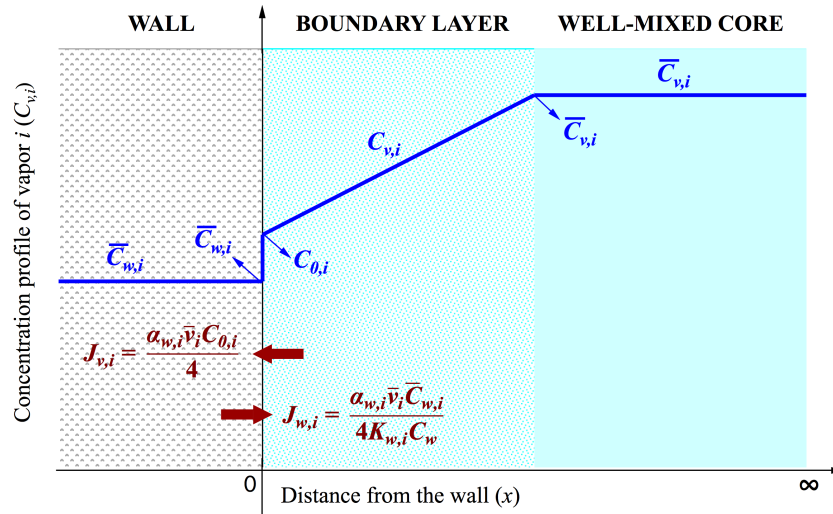


Figure 5.2. Example of the experimental procedure to assess vapor wall deposition using 3-nitrooxy-6-dodecanol ($m/z = (-) 332$): Period (1) organic oxidation product generation; Period (2) vapor wall deposition at 298 K in the dark; Period (3) chamber temperature ramp from 298 K to 318 K; and Period (4) temperature held at 318 K in the dark.

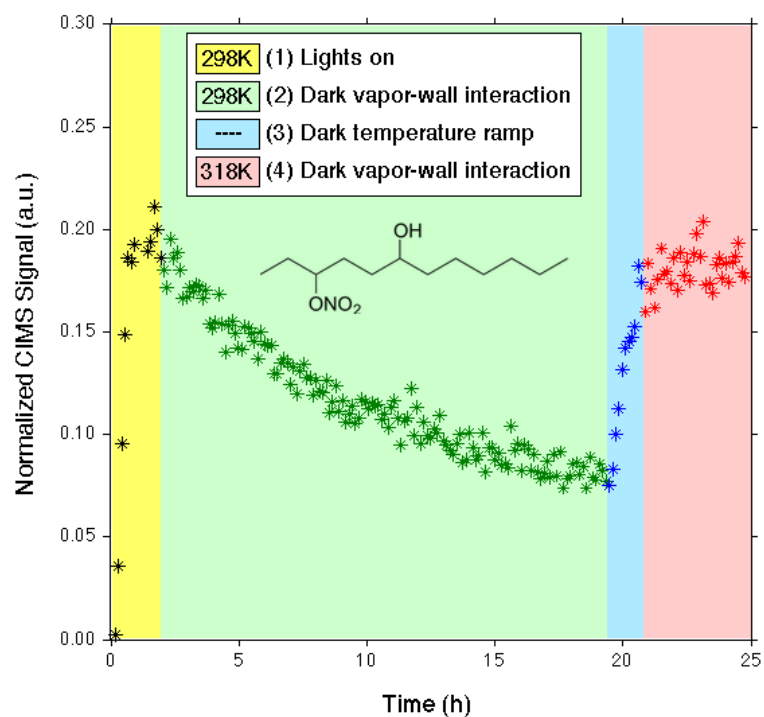
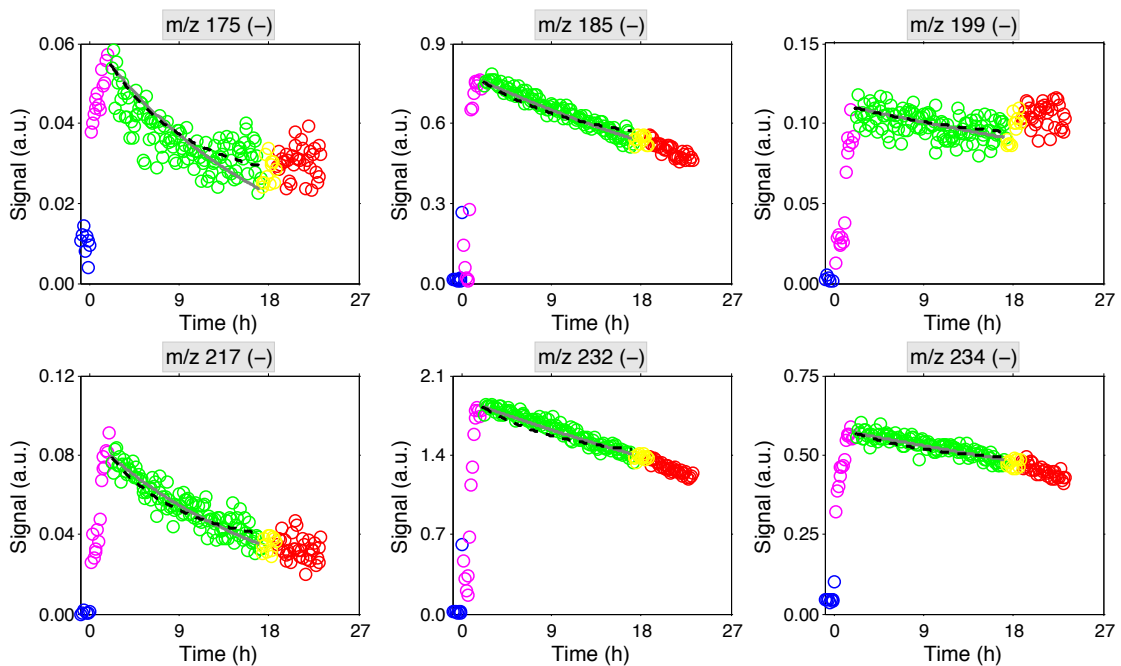
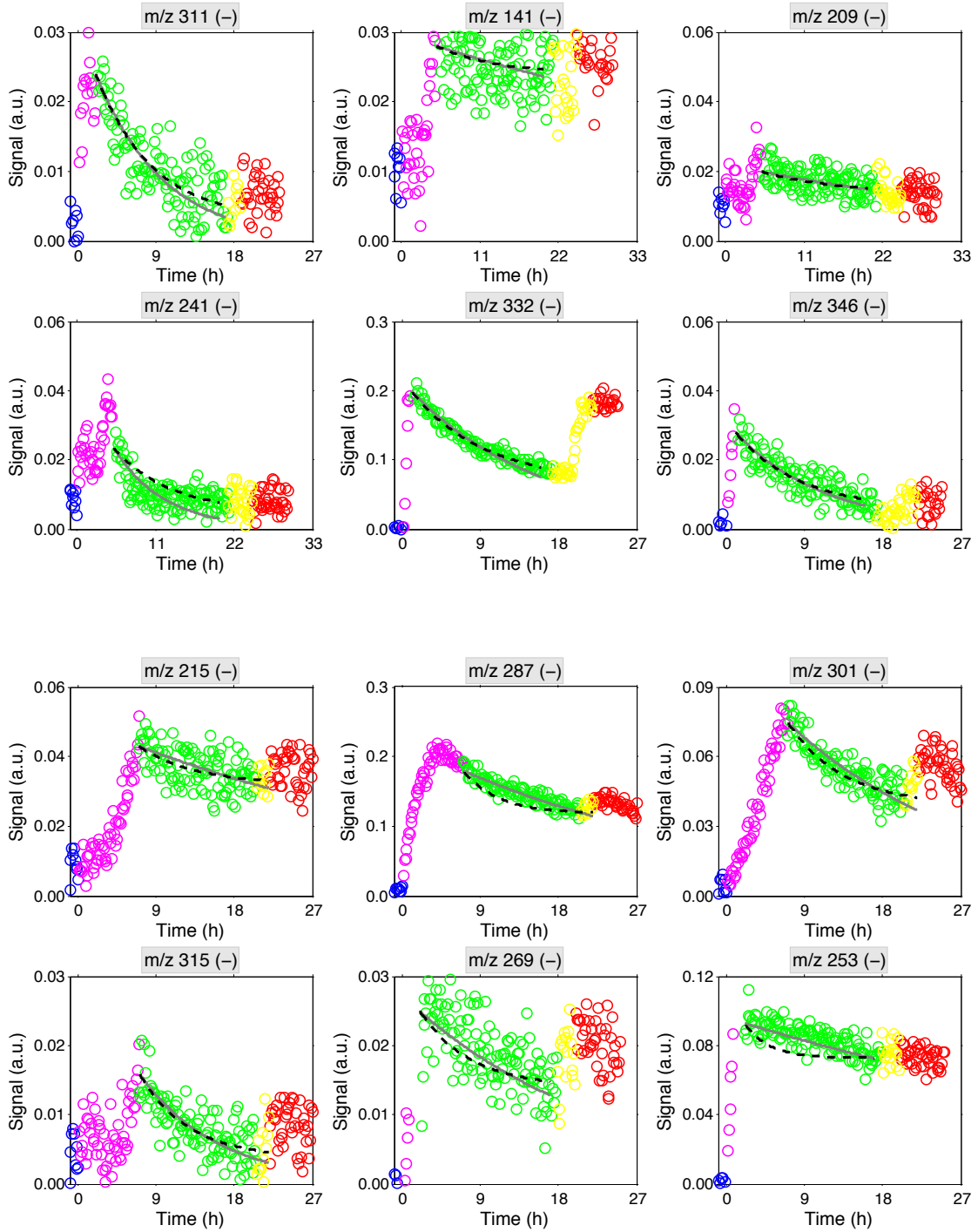


Figure 5.3. CIMS traces of oxidized organic vapors generated from the photooxidation of isoprene, toluene, α -pinene and dodecane under high/low-NO conditions over the four chamber periods in Figure 2. Colored circles represent CIMS measured normalized signals during background (blue), vapor generation (magenta), vapor wall deposition at 298 K (green), temperature ramp (yellow), and vapor re-evaporation at 318 K (red). Black dashed lines and gray solid lines represent the simulated deposition rates generated from SIM.1 and SIM.2, respectively.





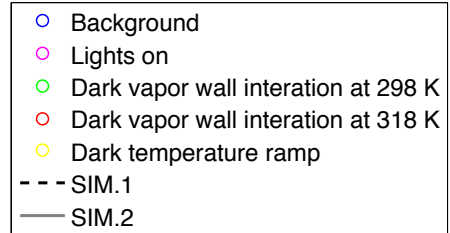
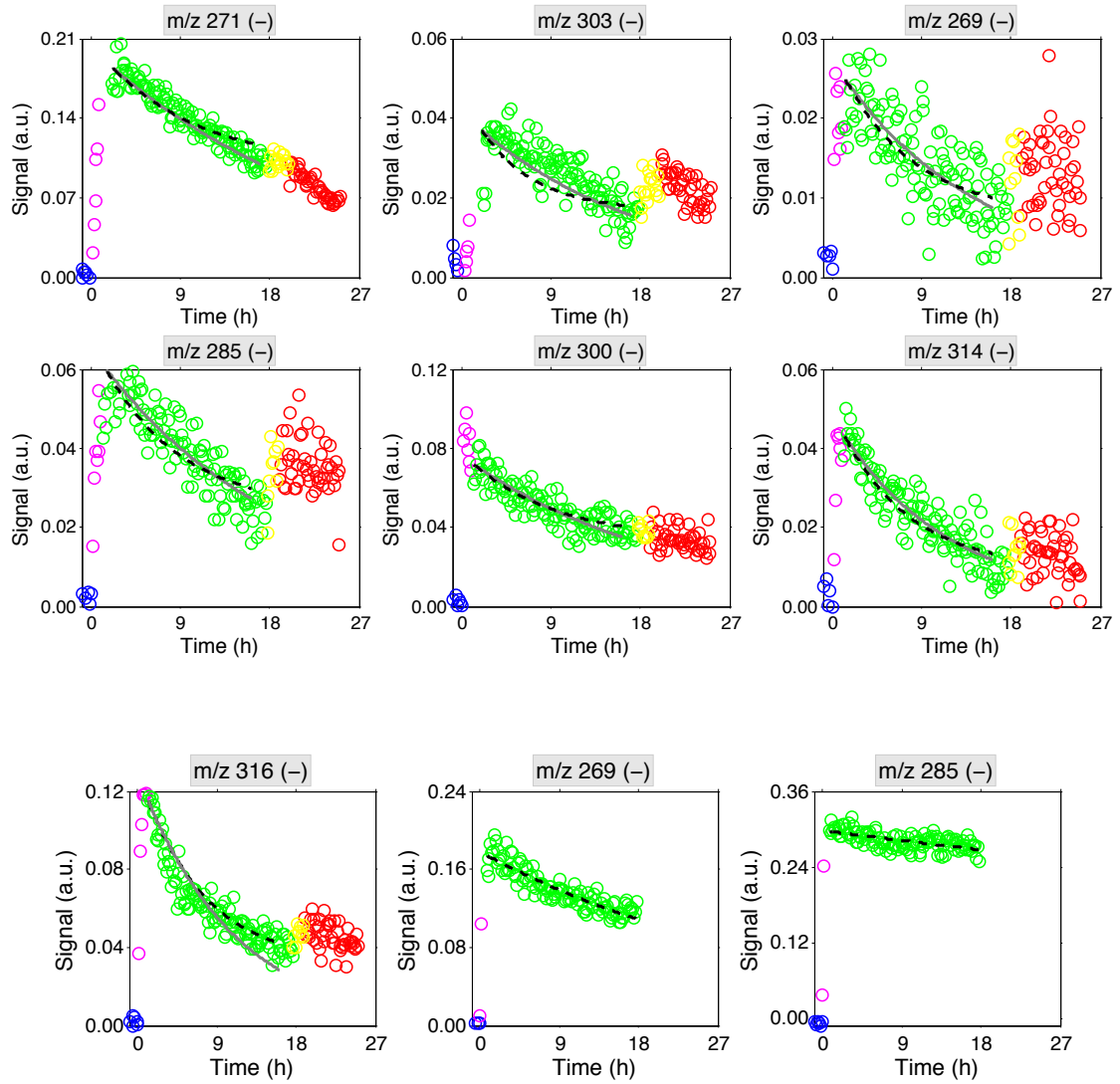


Figure 5.4. Comparison of vapor-wall interactions for α -pinene + OH products under controlled experimental conditions in used (circle) vs. unused (triangle) Teflon chambers. 30-min averaged data are shown here for clarity. Colored bands denote successive experimental periods: vapor generation (magenta), vapor wall deposition at 298 K (green), temperature ramp (yellow), and vapor re-evaporation at 318 K (red).

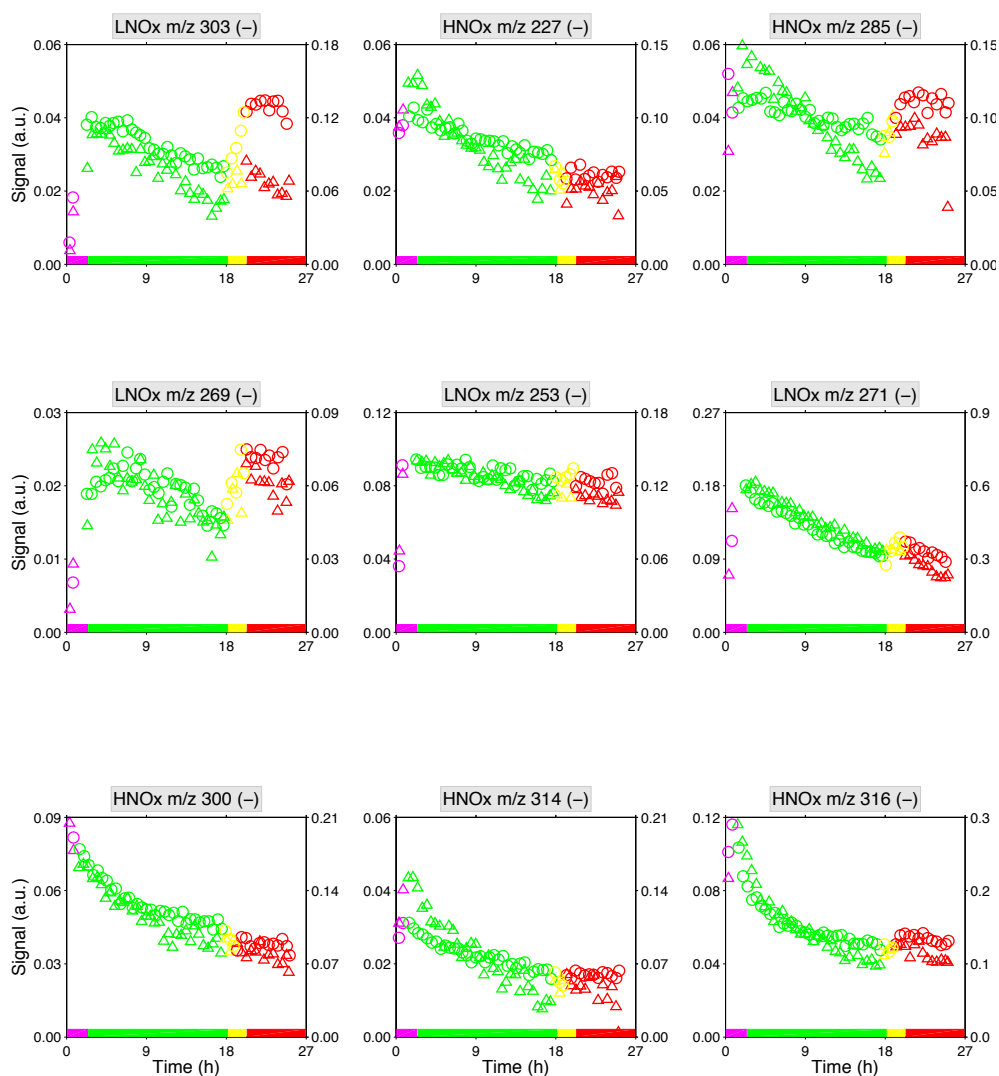


Figure 5.5. Inferred total amount of (a) equivalent absorbing organic mass on chamber walls, C_w (g m^{-3}), and (b) dimensionless Henry's law constants, H_i , as a function of saturation concentration, C_i^* ($\mu\text{g m}^{-3}$). Estimated vapor pressures of organic compounds studied here are obtained from the average of predictions from the two group contribution methods, 'SIMPOL.1' (Pankow and Asher, 2008) and 'EVAPORATION' (Compernelle et al., 2011). The uncertainty bars give the upper and lower limits of C_w values derived from Eq (14), together with (16) and (17), when either 'EVAPORATION' or 'SIMPOL.1' is used to estimate vapor pressures.

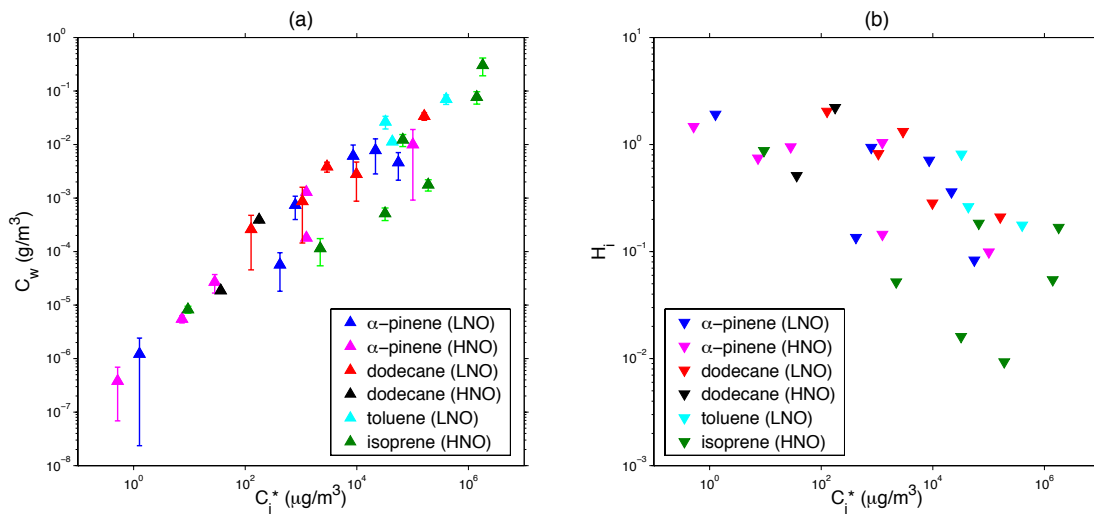


Figure 5.6. Inferred accommodation coefficients of organic oxidation products on chamber walls ($\log_{10}(\alpha_{w,i})$) as a function of saturation concentrations ($\log_{10}(C_i^*)$) and average carbon oxidation state (OS_C). Colored filled circles represent the best-fit α_w assuming irreversible gas-wall partitioning. The black solid line represents the linear regression of $\log_{10}(\alpha_{w,i})$ vs. $\log_{10}(C_i^*)$ for all compounds.

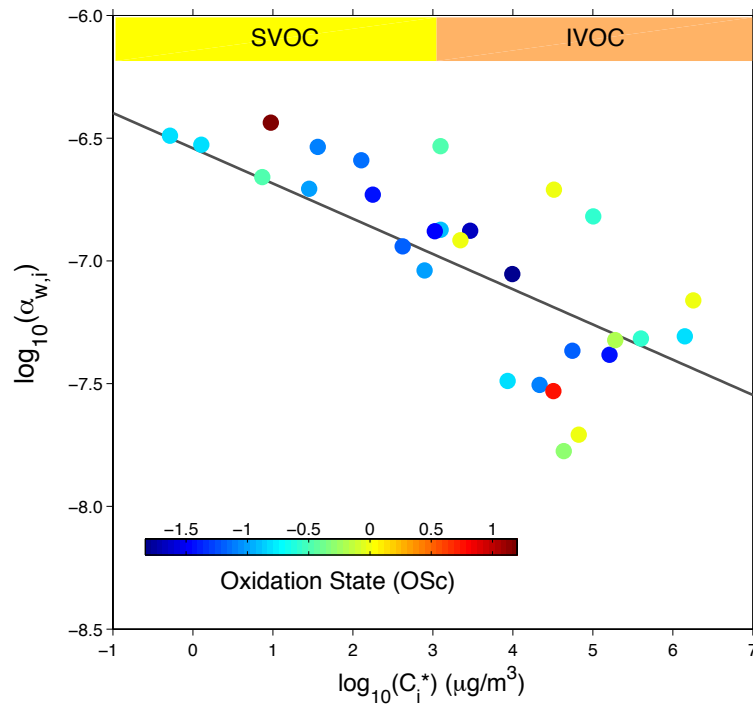


Figure 5.7. Predicted vapor wall deposition rate ($k_{w,i} / \text{s}^{-1}$) of organic compounds in a Teflon chamber as a function of carbon number (n_C) and oxygen number (n_O).

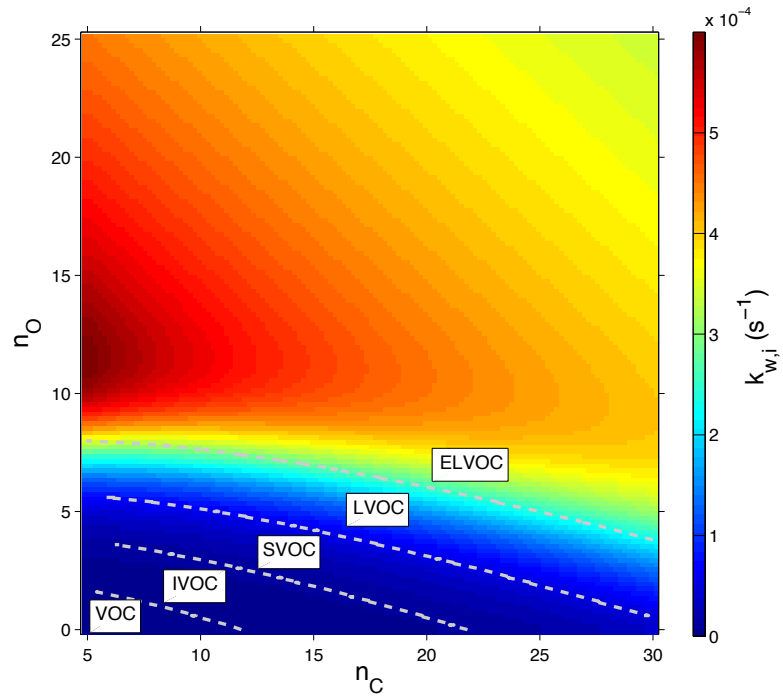
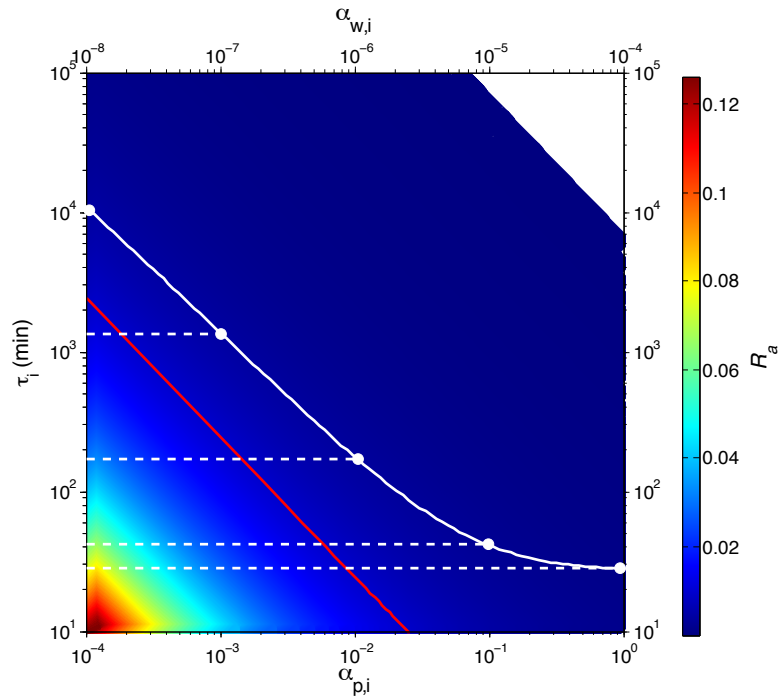


Figure 5.8. Comparison of estimated gas-particle equilibration timescale ($\tau_{g/p,i}$) as a function of the gas-particle mass accommodation coefficient ($\alpha_{p,i}$, lower x-axis) and the ratio of total particle surface area to the chamber wall area (R_a , colour bar), and vapor wall deposition timescale ($\tau_{g/w,i}$) as a function of gas-wall mass accommodation coefficient ($\alpha_{w,i}$, upper x-axis). The red solid line represents the gas-particle equilibration time for a typical chamber experiment with seed surface area of $\sim 1 \times 10^{-3} \mu\text{m}^2 \text{cm}^{-3}$. White solid and dashed lines define the region where $\tau_{g/p,i} \cong \tau_{g/w,i}$. For example, the top dashed white line is a collection data points for which the equality $\tau_{g/p,i} = \tau_{g/w,i} = 1.3 \times 10^3$ min holds. $\tau_{g/w,i}$ is calculated by substituting $\alpha_{w,i} = 10^{-7}$ into Eqs (22), (23), and (24). $\tau_{g/p,i}$ is calculated from Eq (27) by varying $\alpha_{p,i}$ (10^{-4} – 10^{-3}) and R_a (0.01–0.02).



Chapter 6

Conclusions and Future work

Laboratory chambers are very useful to study the SOA formation and evolution from the photochemistry of selected parent hydrocarbons under controlled experimental conditions. This thesis focuses on investigating key processes, particularly gas-particle and gas-wall interactions, that govern SOA formation and aging during chamber experiments.

Vapor wall losses have to be accounted for in chamber experiments to fully understand the source, transformation, and fate of SOA-forming vapors. In Chapter 5, we measured the chamber wall induced decay of a spectrum of SVOCs, which are photooxidation products of isoprene, toluene, α -pinene, and dodecane. It has been recently found that a large amount of extremely low volatility organic compounds (ELVOC) is produced from the ozonolysis of monoterpenes and they condense irreversibly onto the particle phase, accounting for a significant fraction of secondary organic aerosol at the initial particle growth stage. These ELVOCs also have a high affinity on the chamber wall layers, with a measured decay rate as high as 0.011 s^{-1} in a continuously stirred tank reactor. Characterizing the behavior of ELVOCs in chambers, i.e., their interactions with suspended particles vs. chamber walls, is therefore crucial to understand SOA formation from chamber experiments. Commercially available polyols can be used to study the interactions of ELVOCs with the chamber walls. The difficulty of detecting selected polyols lies into the generation of steady vapor flows that can be fed to the reagent ions. Sampling configurations need to be adjusted to improve the detection limits of polyols, such as increasing the overall sampling flow rate and increasing the sampling temperature to minimize the vapor tubing wall loss. Another approach is to study the dynamics of a

population of particles, which could possibly infer the vapor wall loss rate. The primary difference between particles composed of non-volatility compounds and particles consisting of semi/low-volatility compounds is that the evaporation of particle-phase component can be assumed to be negligible for the former. By comparing the evolution of a population of particles composed of non-volatile components vs. low-volatile components, the evaporation rate and subsequent loss rate onto the chamber wall of low-volatile components can be derived.

Quantifying the impact of vapor wall deposition on the chamber-derived SOA yield is the next step in assessing the effect of vapor wall deposition of SOA formation and evolution. Recent evidence suggests that SOA often exists in a semi-solid state. In such a case, the timescale to achieve gas-particle equilibrium increases relative to the timescales for gas-wall partitioning and gas-phase reaction. Retarded gas-particle partitioning resulting from condensed phase diffusion limitations will drive the system toward kinetically-limited SOA growth. The dependence of the SOA yield on seed surface area, as observed in Chapter 4, is important only when SOA growth is kinetically limited. Future studies will be directed at: 1) experiments to determine the accommodation coefficients of organic vapors on particles for a variety of SOA systems, and 2) state-of-art SOA predictive models that describe the dynamics of vapor-wall and vapor-particle interactions to estimate the fraction of organic vapor fluxes transported to the suspended particles vs. the chamber wall.

Appendix 1

**Application of the Statistical Oxidation Model (SOM) to
secondary organic aerosol formation from
photooxidation of C₁₂ alkanes**



Application of the Statistical Oxidation Model (SOM) to Secondary Organic Aerosol formation from photooxidation of C₁₂ alkanes

C. D. Cappa¹, X. Zhang², C. L. Loza³, J. S. Craven³, L. D. Yee², and J. H. Seinfeld^{2,3}

¹Department of Civil and Environmental Engineering, University of California, Davis, CA, 95616, USA

²Division of Engineering and Applied Science, California Institute of Technology, Pasadena, CA, 91125, USA

³Division of Chemistry and Chemical Engineering, California Institute of Technology, Pasadena, CA, 91125, USA

Correspondence to: C. D. Cappa (cdcappa@ucdavis.edu) and J. H. Seinfeld (seinfeld@caltech.edu)

Received: 14 September 2012 – Published in Atmos. Chem. Phys. Discuss.: 15 October 2012

Revised: 23 January 2013 – Accepted: 25 January 2013 – Published: 8 February 2013

Abstract. Laboratory chamber experiments are the main source of data on the mechanism of oxidation and the secondary organic aerosol (SOA) forming potential of volatile organic compounds. Traditional methods of representing the SOA formation potential of an organic do not fully capture the dynamic, multi-generational nature of the SOA formation process. We apply the Statistical Oxidation Model (SOM) of Cappa and Wilson (2012) to model the formation of SOA from the formation of the four C₁₂ alkanes, dodecane, 2-methyl undecane, cyclododecane and hexylcyclohexane, under both high- and low-NO_x conditions, based upon data from the Caltech chambers. In the SOM, the evolution of reaction products is defined by the number of carbon (N_C) and oxygen (N_O) atoms, and the model parameters are (1) the number of oxygen atoms added per reaction, (2) the decrease in volatility upon addition of an oxygen atom and (3) the probability that a given reaction leads to fragmentation of the molecules. Optimal fitting of the model to chamber data is carried out using the measured SOA mass concentration and the aerosol O:C atomic ratio. The use of the kinetic, multi-generational SOM is shown to provide insights into the SOA formation process and to offer promise for application to the extensive library of existing SOA chamber experiments that is available.

formed from condensation of oxidation products of gas-phase reactions of volatile organic compounds, termed secondary organic aerosol (SOA). The extent to which a given parent organic compound forms SOA depends on a variety of factors, including the carbon chain length, structure and reactivity, as well as external factors such as temperature, the abundance of NO_x (=NO+NO₂) and the identity of the oxidant (OH, O₃, NO₃) (Kanakidou et al., 2005). Additionally, the properties of the SOA, e.g. hygroscopicity, volatility and atomic composition, depend on all of the above factors (Jimenez et al., 2009).

Understanding SOA formation via photooxidation (i.e. reactions with OH) presents a unique challenge in that not only is the precursor SOA species (i.e. the parent organic) reactive towards OH, but so are the oxidation products. The extent to which each generation of products contributes directly to SOA formation depends intimately on the details of the atmospheric chemistry for the particular organic. Laboratory chamber experiments are the main source of data on the mechanism of oxidation and the SOA forming potential of a parent organic. Because SOA forms via gas-particle partitioning, the amount of SOA depends on the mass of absorbing material in the aerosol phase, in addition to the unique chemistry. For comparison of SOA formation from different organics, especially in atmospheric models, an SOA model is required. Traditional methods of representing the SOA formation potential, or yield, of an organic do not fully capture the dynamic, multi-generational nature of photooxidation, as they generally treat SOA formation as a one-step process from precursor to products. This includes both the 2-product model (Odum et al., 1996) and static volatility

1 Introduction

Organic aerosol (OA) comprises a major fraction of the atmospheric sub-micron aerosol burden (Zhang et al., 2007; Jimenez et al., 2009), and the dominant portion of OA is

Table 1. Experimental conditions and results from photooxidation experiments.

Alkane	[HC] ₀ (ppbv)	[OH] ^a (molecules cm ⁻³)	C _{OA} ^b (μg m ⁻³)	Yield ^b (%)	Yield ^c (%)	O:C max	O:C min
Low NO _x							
dodecane	34.0	2.5 × 10 ⁶	21.6	10.3	6.1	0.28	0.21
2-methylundecane	28.1	2.4 × 10 ⁶	18.1	10.8	7.2	0.28	0.20
hexylcyclohexane	15.6	2.95 × 10 ⁶	28.9	29.6	15.4	0.32	0.22
cyclododecane	9.8	2.7 × 10 ⁶	15.8	24.4	17.2	0.24	0.15
High NO _x							
dodecane	32.2	4.5 × 10 ⁷ / 1.85	10.6	6.8	6.2	0.33	0.33
2-methylundecane	72.4	3.3 × 10 ⁷ / 1.85	23.5	7.8	5.1	0.26	0.26
hexylcyclohexane	22.1	4.1 × 10 ⁷ / 1.7	17.5	16.4	12.3	0.32	0.32
cyclododecane	13.8	2.7 × 10 ⁷ / 0.92	29.5	41.5	38.3	0.27	0.27

^a For high-NO_x conditions, [OH] is time dependent and has the form [OH]_t = [OH]_{t=0}exp(-kt), where *t* is the time elapsed (in hours) and *k* is the decay constant. The [OH]_{t=0} and *k* values are reported in the table.

^b C_{OA} and yield values are reported after 15 h (low-NO_x) and 3 h (high-NO_x) of reaction, respectively.

^c Yield values are reported for C_{OA} = 10 μg m⁻³.

basis-set (Donahue et al., 2006). Recently, methodologies have been developed that represent photooxidation and subsequent SOA formation within more dynamic frameworks (Aumont et al., 2005; Robinson et al., 2007; Lane et al., 2008; Barsanti et al., 2011; Valorso et al., 2011; Cappa and Wilson, 2012; Donahue et al., 2012). Depending on the specific methodology employed, these models allow for reaction of the first (and later) generation oxidation products, fragmentation and tracking of the detailed composition of the particle and gas-phase.

Here, we apply the Statistical Oxidation Model (SOM) of Cappa and Wilson (2012) to model the formation of SOA from the photooxidation of a series of C₁₂ alkanes of varying structure, two of which are linear (dodecane and 2-methyl undecane) and two of which have ring structures (cyclododecane and hexylcyclohexane). Experiments were conducted under both high- and low-NO_x conditions to explore the important influence of NO_x on the SOA formation. The best-fit model is found to capture the time-evolution of the observed SOA mass concentration and, to a reasonable extent, the O:C atomic ratio under both high- and low-NO_x conditions. Best-fit SOM parameters are reported, and indicate that, per reaction with OH, photooxidation leads to more rapid oxygen addition under high-NO_x conditions than low-NO_x conditions. Despite the more rapid oxygen addition under high-NO_x conditions, the nature of the functional groups added lead to a smaller decrease in volatility (per oxygen added) than under low-NO_x conditions. The success of fitting the SOM to these alkane SOA formation data offers promise to apply the SOM to the extensive library of existing chamber experiments that is available.

2 Experimental methods

Experiments were conducted in the Caltech dual 28-m³ Teflon chambers. Details of the facility have been described previously (Cocker et al., 2001). Prior to each experiment, the chambers were flushed with dried, purified air for >24 h, until the particle concentration was <100 cm⁻³ and the volume concentration was <0.1 μm³ m⁻³.

For all experiments, neutral ammonium sulfate seed aerosol was used to provide surface area for condensation of the semi-volatile oxidation products. Particle size distributions were measured using a differential mobility analyser (DMA, TSI, 3081) coupled with a condensation particle counter (CPC, TSI, CNC-3760).

Photooxidation experiments were run under both high and low-NO_x conditions. Low-NO_x (<1 ppb) experiments were conducted using photolysis of H₂O₂ as the OH radical source. High-NO_x experiments were conducted using photolysis of HONO as the OH radical source. The primary NO_x source is direct photolysis of HONO, although some NO and NO₂ formed as part of the HONO preparation. The gas-phase concentration of the SOA precursor was measured throughout the experiments. Initial concentrations are given in Table 1. Four alkanes are considered here, each with 12 carbon atoms: dodecane (C₁₂H₂₆), 2-methyl undecane (C₁₂H₂₆), hexylcyclohexane (C₁₂H₂₄) and cyclododecane (C₁₂H₂₄).

Photooxidation was initiated by irradiating the chamber with blacklights. Output from the lights is between 300 and 400 nm, with a maximum at 354 nm. Importantly, HONO photolysis is efficient in this wavelength range, and thus the concentration of HONO (and OH) decays towards zero over a period of ~3 h once the lights are turned on. H₂O₂ photolysis is comparably much slower, which facilitates operation at

a nearly constant [OH] throughout the low-NO_x experiments. To access long oxidation times (up to 32 h) in the low-NO_x experiments, the methodology set out by Loza et al. (2012) was followed. As a result, the time series of OA mass concentrations (C_{OA}) under low-NO_x conditions have a “gap” of ~6 h (typically from hours 18–24).

Chemically-resolved aerosol mass concentrations were measured using an Aerodyne high-resolution time-of-flight aerosol mass spectrometer (HR-ToF-AMS, henceforth referred to as AMS). Real-time mass spectra of the particles were collected alternating between “V-mode” and “W-mode”. The “V-mode” provides higher sensitivity while the “W-mode” provides higher resolution. The “W-mode” data were analysed using the software toolboxes PIKA (DeCarlo et al., 2006) and APES (Aiken et al., 2007; Aiken et al., 2008; Chhabra et al., 2010). Through consideration of ions with specific molecular formulas, as determined from the “W-mode” spectra, the elemental composition of the SOA can be determined (in particular, the O:C and H:C atomic ratios). The estimated uncertainty in the O:C is $\pm 30\%$ and in the H:C is 10 %.

A correction for wall loss needs to be applied to determine the SOA mass concentration. Two limiting assumptions can be employed to bound the interactions between particles deposited to the wall and vapors in the chamber. Here we use a lower bound, in which particles deposited on the wall are assumed to cease interaction with suspended vapors after deposition (Loza et al., 2012). The total organic mass deposited to the wall was calculated based on the particle number-weighted size distribution. The wall loss rates for particles of different sizes are obtained from separate characterization experiments. The deposited particle number distribution is added to the suspended particle number distribution to give a wall-loss corrected number distribution, which is then converted to a volume concentration and then mass concentration, assuming spherical particles. For the low-NO_x experiments reported on here, wall loss corrections at long times require extrapolation of the C_{OA} across the “gap”, which decreases the certainty of the correction and, as a result, the accuracy of the wall-loss corrected C_{OA} values after the gap. Thus, only the pre-gap C_{OA} data are used quantitatively here.

3 Statistical Oxidation Model

The statistical oxidation model (SOM) simulates the oxidation of a parent hydrocarbon and its reaction products in time, and is described in detail in Cappa and Wilson (2012). In the SOM, the evolution of the gas and particle phase composition is followed through a space in which all product species are defined solely by their number of carbon (N_{C}) and oxygen (N_{O}) atoms. Equilibrium partitioning between the gas and particle phases is assumed to hold at each time-step of the model (~1–2 min) (Pankow, 1994). It is assumed that the properties of each species (i.e. $N_{\text{C}}/N_{\text{O}}$ pair) can be repre-

sented by some mean values that account for the actual distribution of functional groups within the group of molecules that make up an SOM species. There are a few adjustable parameters within the SOM: (1) the number of oxygen atoms added per reaction, which is represented as an array of probabilities of adding 1, 2, 3 or 4 oxygen atoms, termed P_{func} , (2) the decrease in volatility upon addition of an oxygen atom, termed ΔLVP , which is the difference in the log of the saturation concentration, C_{sat} , per oxygen added, or

$$\Delta\text{LVP} = \log \left[\frac{C_{\text{sat}, N_{\text{O}}}}{C_{\text{sat}, N_{\text{O}}+1}} \right] \quad (1)$$

and (3) the probability that a given reaction leads to fragmentation of the product molecule into two smaller molecules, termed P_{frag} . Note that positive values of ΔLVP correspond to a decrease in vapour pressure upon oxygen addition. These parameters can be adjusted to determine a best fit of the model to the observations. The SOM also includes heterogeneous reactions with OH radicals (Cappa and Wilson, 2012). It is assumed that each heterogeneous OH reaction leads to the addition of one oxygen atom, that the fragmentation probability is assumed equivalent to the gas-phase, and that the reactive uptake coefficient is unity. The model additionally requires as input the initial concentration of the parent hydrocarbon, $[\text{HC}]_0$, and the (potentially time-dependent) oxidant concentration. In this study, for the low-NO_x experiments the [OH] was constant (or nearly constant) throughout, while for the high-NO_x experiments the [OH] decayed rapidly. In either case, the model [OH] was specified so that the observed temporal decay of [HC] was reproduced (see Table 1).

It is not yet clear what the most appropriate functional form is for the fragmentation probability, P_{frag} . Therefore, two parameterizations are considered here: $P_{\text{frag}}(\text{O:C}) = (\text{O:C})^{m_{\text{frag}}}$ and $P_{\text{frag}}(N_{\text{O}} = c_{\text{frag}} N_{\text{C}})$, where m_{frag} and c_{frag} are adjustable parameters, and there is an upper limit of $P_{\text{frag}} = 1$. Smaller values of m_{frag} and larger values of c_{frag} indicate more extensive fragmentation, respectively. It is assumed that the generated fragments are randomly distributed in terms of where the carbon bond scission occurs.

Best-fit values for P_{func} , ΔLVP and P_{frag} are determined by simultaneously fitting the time-dependent model predictions to observations of wall-loss corrected organic aerosol mass concentrations (C_{OA}) and O:C for each system (in this case, C₁₂ compounds reacting with OH radicals under high- or low-NO_x conditions). Alternatively, the SOM was fit only to the C_{OA} observations. The data fitting was performed using the Levenberg-Marquardt algorithm built into the data analysis program Igor. Uncertainties in the measured C_{OA} were assumed to be the larger of $0.5 \mu\text{g m}^{-3}$ or 10 %. Uncertainties in the O:C were $\pm 30\%$. An upper limit of $\Delta\text{LVP} = 2.2$ was applied. The functional group that contributes most to the decrease of vapour pressure per O atom added is the –OH group. The EVAPORATION model (Compernelle et al., 2011) predicts that ΔLVP upon addition of –OH to primary, secondary and tertiary C is 2.23,

1.70 and 1.16, respectively, whereas the SIMPOL.1 model (Pankow and Asher, 2008) predicts 2.76, 2.10 and 1.49, respectively. Here we take the average between the two vapour pressure models as the upper limit to ΔLVP . For low-NO_x experiments, which have a gap in the C_{OA} data from ~18–24 h of reaction, the data are fit only prior to this gap. As noted above, the reason for this is that the uncertainty in the wall-loss correction across the gap leads to larger uncertainty in the C_{OA} after the gap.

Variation in the H:C atomic ratio with oxidation is characterized within the SOM by specifying the average number of hydrogen atoms lost per oxygen atom added, which is equal to the negative slope in a Van Krevelen diagram (a graph of H:C vs. O:C) (Heald et al., 2010). Here, the H-loss-per-O-added is specified a priori based on the observed Van Krevelen slope, although it should be noted that the specification of this relationship has a negligible influence on the evolution of either the C_{OA} or O:C.

Condensed phase reactions (besides heterogeneous OH reactions) are not explicitly accounted for in the SOM. Thus, to the extent that condensed phase reactions (e.g. oligomerization, dehydration, cyclization) alter the observed SOA properties, this will be reflected in the best-fit model parameters.

4 Results

4.1 Low-NO_x conditions

The time-evolution of the observed wall-loss corrected SOA mass concentrations (C_{OA}) and the particle-phase O:C atomic ratios are shown in Fig. 1, along with the tuned model results obtained using both P_{frag} parameterizations and after fitting simultaneously to both C_{OA} and O:C. In general, as oxidation proceeds, the observed C_{OA} increases until the parent [HC] decays to around 10 % of its initial value (which occurs around 15–20 h of oxidation). After this point, the C_{OA} starts to level off, or even decrease slightly, even though there is still OH present in the system. The observed SOA O:C atomic ratio at early times tends to decrease slightly until the parent [HC] decays to around 30 % of its initial value (at 5–10 h of oxidation), after which time it begins to slowly increase. Aerosol mass yields for the two ring-containing compounds are larger than for the non-ring containing compounds (Table 1), consistent with previous results from Lim and Ziemann (2009).

The SOM, after fitting, captures the general time-dependent behaviour of the observed C_{OA}, with the model C_{OA} exhibiting a levelling off or slight decrease at long times for many of the simulations (Fig. 1). The exact time-dependence of the model C_{OA} depends somewhat on the assumed fragmentation parameterization and method. In general, the $P_{\text{frag}}(\text{NO})$ parameterization tends to show a more pronounced turnover in the C_{OA} at long times than the $P_{\text{frag}}(\text{O:C})$ parameterization. The $P_{\text{frag}}(\text{NO})$ results appear

slightly more consistent with the observations, which is an unexpected result given that the more physically intuitive behavior is that the probability of fragmentation for a given molecule should depend on the relative oxygen abundance (i.e. O:C) rather than the absolute oxygen abundance (i.e. NO). However, the uncertainty in the observed C_{OA} after the data gap limits our ability to definitively make this assessment.

The SOM captures the general shape of the observed O:C time-dependence, with the model O:C typically first decreasing before increasing with time, similar to the experimental results (Fig. 1). Despite the satisfactory shape of the model O:C time-dependence, for all of the hydrocarbons considered the absolute value of the model O:C is somewhat greater than the observed O:C, although typically within the experimental uncertainty. Cyclododecane is the notable exception, with a model O:C that is substantially higher than the observed value (although the shape of the calculated and observed time-dependencies are quite similar). The over-prediction is, in part, a consequence of setting an upper limit for $\Delta\text{LVP}=2.2$ during fitting; allowing for larger values of ΔLVP can lead to better model/measurement agreement for most compounds (although not for cyclododecane) and can still allow for a good fit to the observed C_{OA}. The $P_{\text{frag}}(\text{NO})$ parameterization generally yields somewhat lower absolute O:C values compared to $P_{\text{frag}}(\text{O:C})$. An additional reason for the over-prediction of the model O:C relative to the observations could be that the HR-ToF-AMS underestimates the oxygen derived from hydroperoxides, with these species instead detected with the –OOH removed (Craven et al., 2012). This would lead to a measured O:C that is somewhat lower than the actual O:C, with the extent of this disparity potentially dependent upon the hydroperoxide fraction of the oxygenated functional groups.

When the model is fit to both the C_{OA} and O:C, the best-fit ΔLVP is 2.2 for all compounds, i.e. the imposed upper-limit (Fig. 2 and Table 2). This is not surprising given that the model O:C is particularly sensitive to the ΔLVP parameter (Cappa and Wilson, 2012). When the model is fit to only the C_{OA} data, the best-fit values remain high, with $2 < \Delta\text{LVP} < 2.2$. For all compounds considered, the addition of 1 oxygen atom per reaction was most probable, with some smaller fraction of reactions requiring the addition of 2, 3 or 4 oxygen atoms (Fig. 2 and Table 2). The model results indicate that fragmentation is extensive, and the non-ring-containing compounds have larger c_{frag} and smaller m_{frag} values compared to the ring-containing compounds, suggesting more extensive fragmentation of the non-ring containing compounds. For all compounds, the c_{frag} values (for $P_{\text{frag}}(\text{NO})$) were ≥ 0.33 , which indicates that any molecule already containing 3 or more oxygen atoms will exclusively fragment upon reaction. Note that this does not preclude formation of species with >3 oxygen atoms because some reactions add more than 1 oxygen atom and because fragmentation also leads to oxygen addition. It does, however, limit the rate and overall extent

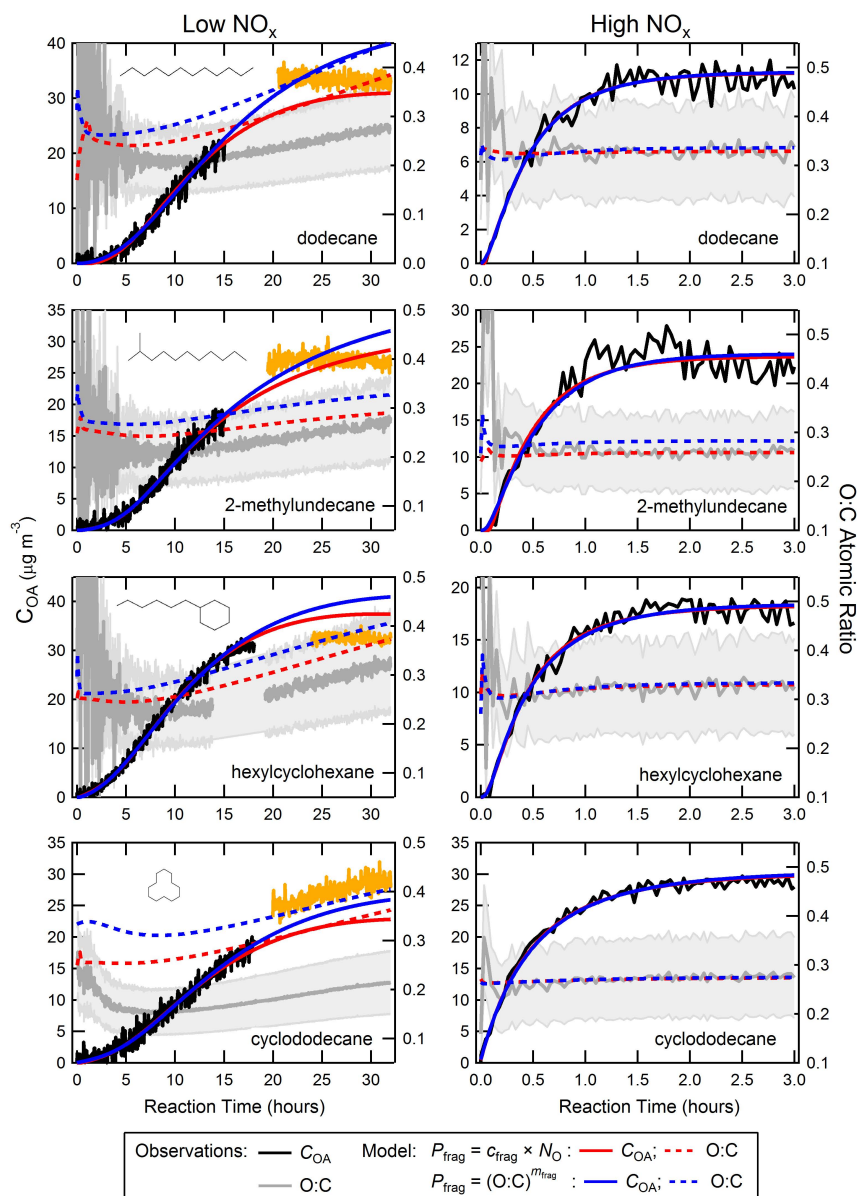


Fig. 1. Evolution of the SOA mass concentration, C_{OA} , (black lines, left axes) and O:C atomic ratio (gray lines, right axes) for low-NO_x (left panels) and high-NO_x (right panels) for dodecane, 2-methylundecane, hexylcyclohexane and cyclododecane (top-to-bottom). The light gray bands on the O:C indicate the estimated uncertainty range ($\pm 30\%$). The model results using $P_{\text{frag}}(N_O)$ and $P_{\text{frag}}(O:C)$ are shown as red and blue lines, respectively. Solid lines are model fits for C_{OA} and dashed lines for O:C. The model has been fit simultaneously to the C_{OA} and O:C data for $t < 15$ h (low-NO_x, black lines) or $t < 3$ h (high-NO_x). For the low-NO_x conditions, the orange lines correspond to data collected after a pause in sampling (indicated by a gap in the C_{OA} time series).

to which such highly oxygenated species can form. Similar conclusions are reached if the $P_{\text{frag}}(O:C)$ parameterization is instead considered, although the exact details are changed somewhat due to the different functional form of the parameterization.

The observed co-variation of H:C with O:C, shown as a Van Krevelen diagram, indicates that the number of H atoms lost per O atom added, or the negative slope on the graph,

ranges from 1.45 to 2.2 (Fig. 3); this parameter is specified within the SOM so as to match the model to the observations. The model aerosol exhibits a continuous evolution of the H:C and O:C throughout the reaction, consistent with the observations, which is indicated by the wide range of values that fall along a line with a constant slope (Fig. 3).

The distribution of molecules in N_C/N_O space at the end of the dodecane + OH reaction is shown for both P_{frag}

Table 2. Statistical oxidation model best-fit parameters when fit to both C_{OA} and O:C.

Alkane	Δ LVP	c_{frag} or m_{frag}	Oxygen Addition Probabilities ^a
Low-NO _x ; $P_{\text{frag}} = c_{\text{frag}} N_{\text{O}}$			
dodecane	2.20 ^b	0.423	[0.57,0.12,0.00,0.31]
2-methylundecane	2.20 ^b	0.455	[0.79,0.00,0.10,0.11]
hexylcyclohexane	2.20 ^b	0.333	[0.80,0.05,0.12,0.03]
cyclododecane	2.20 ^b	0.333	[0.86,0.02,0.12,0.0]
Low-NO _x ; $P_{\text{frag}} = (\text{O:C})^m \text{ frag}$			
dodecane	2.20 ^b	0.077	[0.79,0.17,0.03,0.0]
2-methylundecane	2.20 ^b	0.110	[0.96,0.0,0.04,0.0]
hexylcyclohexane	2.20 ^b	0.214	[0.75,0.17,0.08,0.0]
cyclododecane	2.20 ^b	0.250	[0.88,0.0,0.0,0.11]
High-NO _x ; $P_{\text{frag}} = c_{\text{frag}} N_{\text{O}}$			
dodecane	1.46	0.279	[0.31,0.41,0.07,0.19]
2-methylundecane	1.68	0.397	[0.24,0.50,0.27,0.0]
hexylcyclohexane	1.54	0.233	[0.0,0.50,0.43,0.06]
cyclododecane	2.01	0.279	[0.0,0.0,0.73,0.26]
High-NO _x ; $P_{\text{frag}} = (\text{O:C})^m \text{ frag}$			
dodecane	1.69	0.105	[0.26,0.38,0.31,0.05]
2-methylundecane	1.80	0.113	[0.30,0.57,0.13,0.0]
hexylcyclohexane	1.67	0.191	[0.18,0.23,0.59,0.0]
cyclododecane	2.06	0.251	[0.0,0.0,0.88,0.12]

^a The relative probabilities of adding 1, 2, 3 or 4 oxygen atoms per reaction.

^b Constrained as an upper limit.

parameterizations (Fig. 4a,b). Overall, the OA is dominated by compounds that have $N_{\text{C}} = 12$ (Fig. 4e), although there are interestingly contributions from compounds with as few as 2 carbons at the 0.1 % level. Although the two P_{frag} parameterizations give generally similar results with respect to the temporal variation in the C_{OA} and O:C, the distribution of molecules that make up the OA differ. The $P_{\text{frag}}(\text{O:C})$ parameterization allows for a fragmentation probability that asymptotically approaches 1 (at O:C = 1), and thus it is possible to produce molecules with $N_{\text{C}} = 12$ and with a relatively large number of oxygen atoms, although the contribution of species with $N_{\text{O}} > 3$ to the total OA mass is small. For the $P_{\text{frag}}(N_{\text{O}})$ parameterization the probability of fragmentation linearly varies with N_{O} and, given $c_{\text{frag}} = 0.42$ coupled with a P_{func} array dominated by 1 oxygen per reaction, there is similarly not substantial production of $N_{\text{C}} = 12$ species with $N_{\text{O}} > 3$.

4.2 High-NO_x conditions

The observed variations in wall-loss corrected C_{OA} and O:C with reaction time for high-NO_x conditions for each of the alkanes considered are shown in Fig. 1. It is important to note that the OH concentration during these experiments was time

dependent and decayed rapidly from $> 10^7$ molecules cm⁻³ to zero (by around 3 h). This is in contrast to the low-NO_x experiments, where the OH concentration was constant at around 3×10^6 molecules cm⁻³. The time-dependence of the [OH] was accounted for in the SOM fit to the observations. The observed C_{OA} in each experiment rapidly increased before reaching a plateau by around 2–3 h. Unlike the low-NO_x experiments, this plateau behaviour results primarily from the loss of OH radicals and the cessation of photochemical reactions and not from an evolution in the distribution of gas-phase photooxidation products. The observed SOA O:C were essentially constant with time. Aerosol mass yields were larger for the ring-containing compounds (Table 1).

The SOM reproduces the observed time-dependent behaviour of the C_{OA} and O:C, both in terms of shape and absolute magnitude. Note that the close match between the observed and predicted O:C is different than for the low-NO_x conditions, where O:C was over-predicted. Fitting to either C_{OA} and O:C simultaneously or only to C_{OA} gave generally similar results. The best-fit Δ LVP values ranged from 1.46 to 2.06 (Fig. 2 and Table 2) and are overall substantially lower compared to the low-NO_x systems, with the exception of cyclododecane. Under high-NO_x conditions the optimal fit of the SOM indicates that the majority of reactions

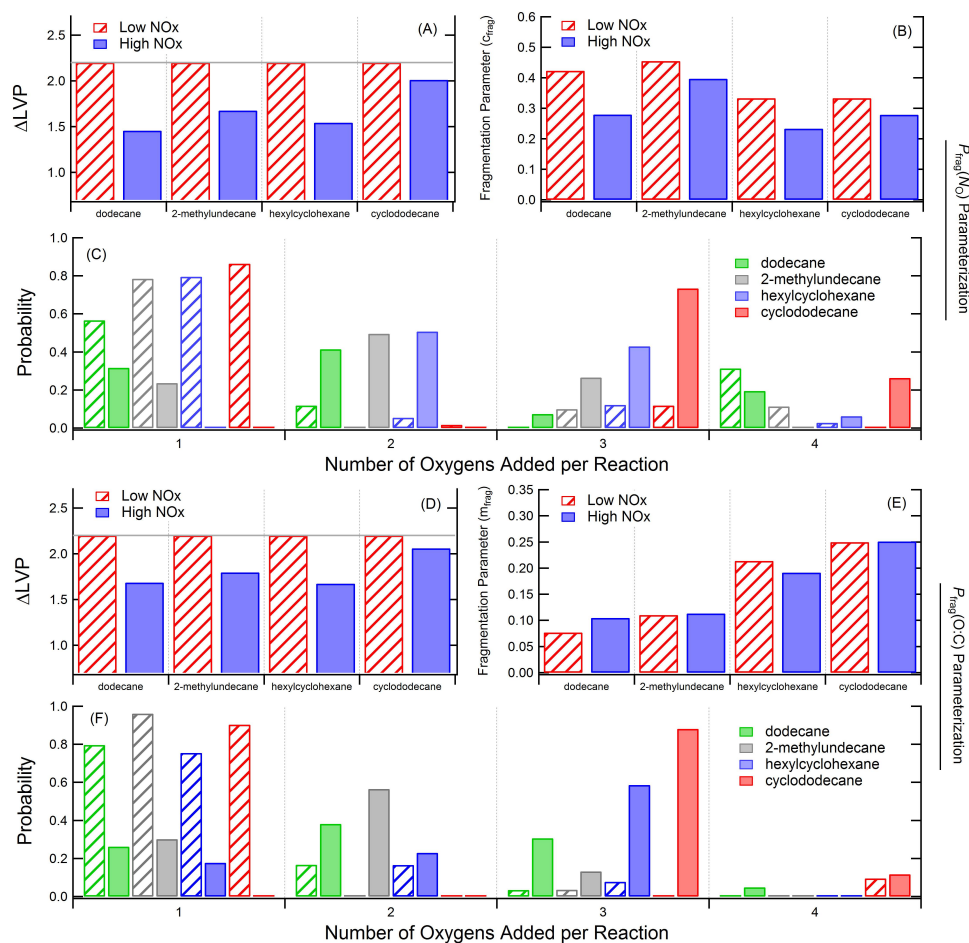


Fig. 2. Best-fit SOM parameters for dodecane, 2-methylundecane, hexylcyclohexane, and cyclododecane under low-NO_x (hashed) and high-NO_x (solid) conditions for different parameterizations for fragmentation: (A–C) used $P_{\text{frag}}(\text{NO})$ while (D–F) used $P_{\text{frag}}(\text{O:C})$. Results are shown for ΔLVP (A and D), the fragmentation parameter (B and E) and the oxygen addition array (C and F). The model was fit simultaneously to the observed C_{OA} and O:C. The two fragmentation parameterizations give generally similar results. Note that for the fragmentation parameter, larger values of c_{frag} correspond to greater fragmentation while smaller values of m_{frag} correspond to greater fragmentation. The grey line in (A) and (D) indicates the upper-limit constraint on ΔLVP .

added 2 to 4 oxygen atoms per reaction, with the exact probability distribution varying for each alkane considered and some probability of adding 1 oxygen per reaction (with the exception of cyclododecane). This is in distinct contrast to the low-NO_x systems, where predominately only 1 oxygen is predicted to be added per reaction. The P_{func} distributions are generally similar between the two fragmentation parameterizations. In general, the non-ring-containing compounds require larger c_{frag} (or smaller m_{frag}) than the ring-containing compounds, indicating more extensive fragmentation. Additionally, the best-fit c_{frag} values are generally larger (and the m_{frag} smaller) under high-NO_x conditions than under low-NO_x conditions for a given compound, although the extent to which the values differ depends on the specific alkane and whether c_{frag} or m_{frag} is considered; in some cases the differences are slight (Fig. 2 and Table 2).

The observed co-variation of H:C with O:C indicates that the number of H atoms lost per O atom added ranges from 1.25 to 1.83, which is slightly less than for low-NO_x conditions (Fig. 3). The SOM captures the observed behaviour (after specifying the H-per-O relationship), namely that the H:C and O:C are both nearly constant throughout the reaction, unlike the low-NO_x systems (Fig. 3).

The distribution of molecules in $N_{\text{C}}/N_{\text{O}}$ space at the end of the reaction is shown for dodecane (Fig. 4c,d). As in the low-NO_x systems, the overall SOA composition is dominated by compounds with $N_{\text{C}} = 12$ (Fig. 4e), although the fractional contribution of compounds with $N_{\text{C}} < 12$ is less than in the low-NO_x experiments. This is likely the result of a greater number of oxygen atoms being added per reaction for the high- vs. low-NO_x case. This predicts that compounds with $N_{\text{C}} = 12$ more rapidly add oxygen, leading to a volatility

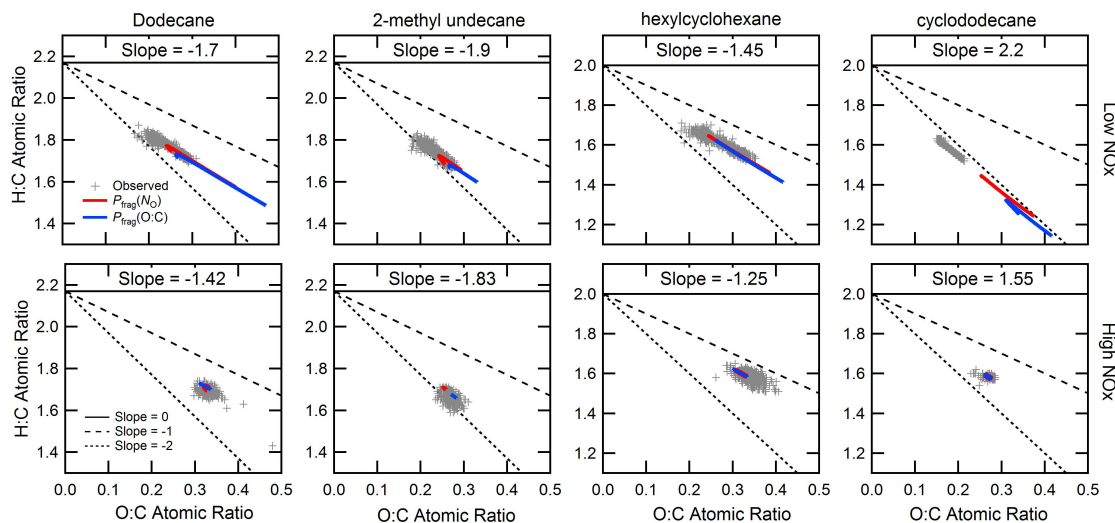


Fig. 3. Van Krevelen diagrams (H:C vs. O:C) for the observed SOA (gray points) and the model SOA using the $P_{\text{frag}}(N_{\text{O}})$ (red lines) and $P_{\text{frag}}(\text{O:C})$ (blue lines) fragmentation parameterizations. The top row shows results for low- NO_x conditions and the bottom row for high- NO_x conditions. The Van Krevelen slopes (defined according to the parent hydrocarbon y-intercept) are given in each panel.

sufficiently low that condensation is efficient even though the ΔLVP tends to be smaller for the high- NO_x mechanisms.

5 Discussion

The observations indicate that aerosol mass yields, defined as $C_{\text{OA}}/\Delta\text{HC}$ (where ΔHC is the amount of precursor reacted), are larger for the ring-containing compounds than for the non-ring-containing compounds for both high- and low- NO_x conditions (Table 1). For equivalent amounts of aerosol formed (specifically, $10\ \mu\text{g m}^{-3}$), the mass yields for each species under high- and low- NO_x conditions are reasonably similar, with the exception of cyclododecane, for which the high- NO_x yield is greater (Table 1). Low- NO_x conditions typically have greater H-loss per O-added (i.e. more negative Van Krevelen slopes) than high- NO_x conditions and also exhibit a more continuous evolution through the Van Krevelen space as the reactions proceed. Considering the model results, the SOM indicates that the decrease in volatility per oxygen added is substantially larger for low- NO_x vs. high- NO_x conditions. The magnitude of the fragmentation parameter, c_{frag} , is generally larger (and m_{frag} smaller) for low- vs. high- NO_x . Under high- NO_x conditions a greater number and broader distribution of oxygen atoms are added, on average, per reaction. Low- NO_x conditions lead to a slightly broader distribution of compounds with $N_{\text{C}} < 12$ in the particle phase compared to high- NO_x conditions.

To facilitate further comparison between the low- NO_x and high- NO_x experiments, which were conducted using different $[\text{OH}]$ temporal profiles and different $[\text{HC}]_0$, time-dependent SOA growth simulations were run under the same reaction conditions using the best-fit parameters determined

above (Fig. 5). Specific reaction conditions and model inputs were: $[\text{OH}] = 2.5 \times 10^6$ molecules cm^{-3} , $[\text{HC}]_0 = 33.5$ ppb, the $P_{\text{frag}}(N_{\text{O}})$ parameterization was used and the model was run for 32 h of oxidation. For all except 2-methylundecane, the C_{OA} formed after a given reaction time is initially somewhat greater for the high- NO_x conditions, but with an eventual cross-over to where the C_{OA} becomes larger for the low- NO_x conditions, often substantially so, at long times. For 2-methylundecane the yield under low- NO_x conditions is always greater than under high- NO_x conditions, with the difference growing with time.

For high- NO_x conditions there tends to be a more pronounced turnover in the C_{OA} with time and with the turnover occurring at shorter times compared to low- NO_x conditions. The overall time-dependent evolution of the gas + particle system reflects the combined influence of all of the parameters (P_{frag} and P_{func} and ΔLVP). Thus, the observed NO_x -dependence on the time-dependent aerosol yields can be understood through the influence of NO_x on both the probabilities of fragmentation vs. functionalization reactions and on the nature of the functional groups formed, specifically the decrease in volatility that occurs upon functional group addition.

There are no clear, systematic differences in the evolution of the O:C with oxidation between the low- and high- NO_x cases, although O:C tends to be slightly higher for high- NO_x . In general, for low- NO_x the O:C first decreases then increases, consistent with the experiments (which were conducted under similar conditions as these simulations). For high- NO_x , both 2-methylundecane and hexylcyclohexane exhibit a noticeable increase in the O:C with oxidation, similar to the low- NO_x cases, whereas dodecane and

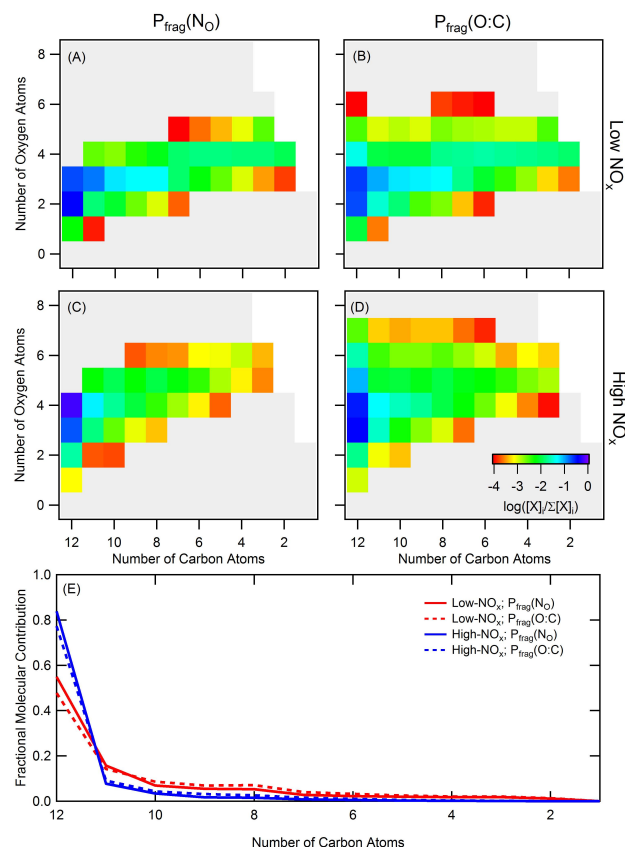


Fig. 4. Distribution of molecules comprising the model dodecane SOA at the end of the experiment for low-NO_x (A, B) and high-NO_x (C, D) for the $P_{\text{frag}}(N_{\text{O}})$ (A, C) and $P_{\text{frag}}(\text{O}:\text{C})$ (B, D) parameterizations. The colors correspond to the log of the fractional molecular abundance, i.e. $\log([X]_j/\Sigma[X]_j)$, with a lower-limit of -4 ($=0.01\%$). (E) The distributions, binned by N_{C} , for low-NO_x (red) and high-NO_x (blue).

cyclododecane exhibit comparably small variations in O:C with oxidation.

5.1 Time-evolution of individual SOA species

The SOM can be used to follow the time-evolution of the individual species (i.e. $N_{\text{C}}/N_{\text{O}}$ pairs) that comprise the model SOA. Tracking of each SOM species can help to understand which species contribute most to the SOA mass at any given time during the experiment, and thus how the composition is evolving. An example of such a time-trace is shown for the low-NO_x dodecane system using the $P_{\text{frag}}(N_{\text{O}})$ parameterization, where the individual species have been normalized to their maximum concentration (Fig. 6). It can be seen that there is some clustering of different species with respect to their specific time-evolution, and species that exhibit similar time-dependent behaviour have been colored similarly. The $N_{\text{C}}=12$ species with 1 and 2 oxygen atoms have unique time-profiles while the $N_{\text{C}}=8$ to 11 species with 1 or 2 oxy-

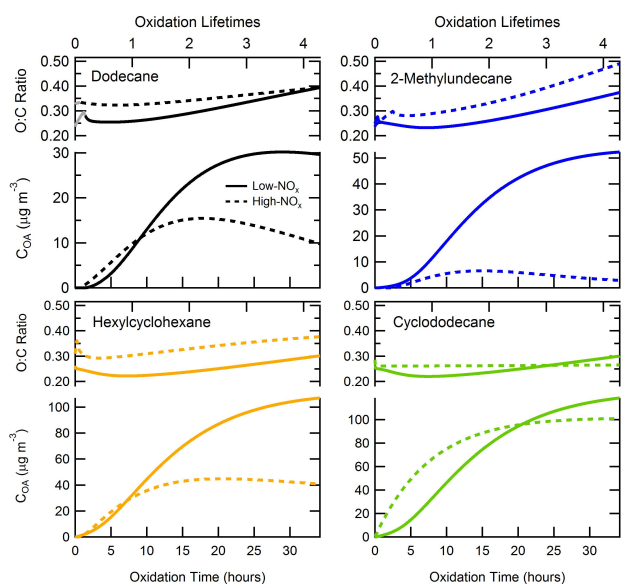


Fig. 5. Simulated time-evolution of C_{OA} and O:C for each of the parent alkanes using the same reaction conditions but with compound-specific best-fit SOM parameters. Results are shown for low-NO_x (solid) and high-NO_x (dashed), assuming $[\text{OH}] = 2.5 \times 10^6$ molecules cm^{-3} and $[\text{HC}]_0 = 33.5$ ppb.

gens cluster together into one predominant mode. Similarly, there is a clustering of species with $N_{\text{C}}=6-7$ and $N_{\text{O}}=2-3$, and of species with $N_{\text{C}}=8-12$ with $N_{\text{O}}=3$. Finally, species with $N_{\text{O}} \geq 4$ cluster together nearly independent of N_{C} . This type of clustering behaviour is consistent with the identification of unique “factors” associated with the formation and ageing of low-NO_x dodecane SOA (Craven et al., 2012). In general, the concentrations of individual particle-phase species with greater numbers of oxygen atoms and smaller carbon atom numbers peak later in time, consistent with their formation occurring only after many generations of oxidation. (Note that the assumption of random fragmentation and the use of a single SOM “grid” preclude direct, quantitative connections between N_{C} , N_{O} and generation number to be made.) The clustering of particular species in terms of their particle-phase concentrations is related to the combined influence of gas-phase formation rates and the volatility of each species.

It is also important to consider the actual time-dependent contributions from each species to the total SOA mass, as the above discussion (which uses normalized traces) might place undue focus on species that contribute negligibly to the SOA mass. Figure 7a shows the actual time-evolution of the particle phase mass concentration for each SOM species, and Fig. 7b–d show snapshots of the concentrations of each species after 5 h, 15 h and 25 h of reaction, normalized to the total particle mass at that time. It is evident that at early times the SOA is dominated by the $N_{\text{C}}=12$, $N_{\text{O}}=2$ species and the cluster of $N_{\text{C}}=8-12$, $N_{\text{O}}=3$ species. As the

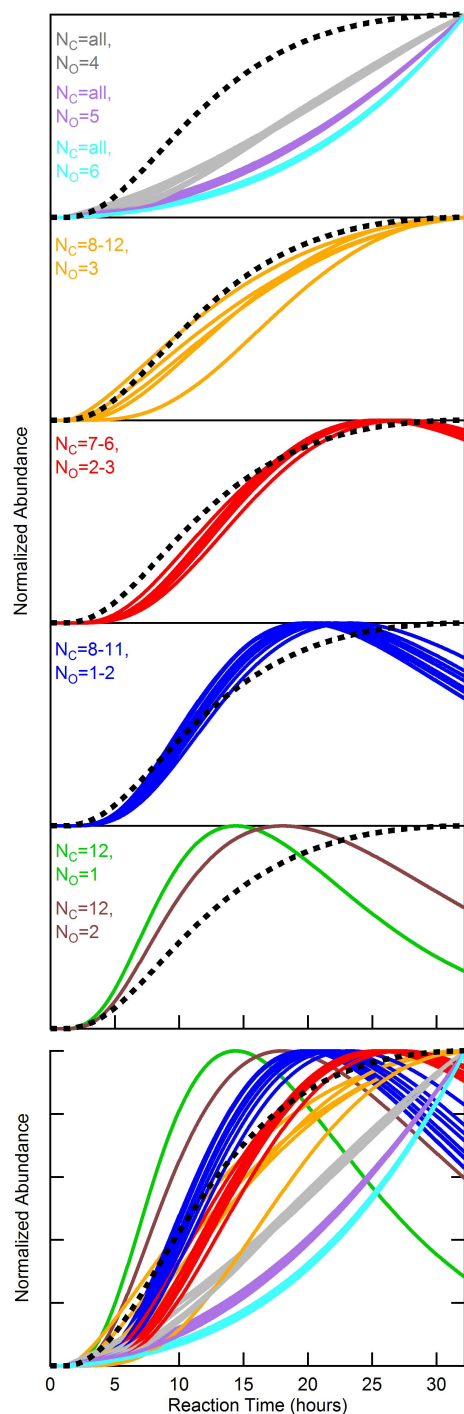


Fig. 6. Simulated time-evolution of each SOM species (i.e. N_C/N_O pair) during the low-NO_x photooxidation of dodecane. Species that exhibit a similar temporal dependence have been grouped into “clusters” and are shown in individual panels with the same color; the N_C and N_O of the species that belong to each “cluster” for each panel are indicated as labels. Each species profile has been normalized to its maximum concentration. For reference, the dashed black trace in each panel shows the time-evolution of the normalized total SOA mass. The bottom panel shows all traces together so that the time-evolution of the various clusters can be compared.

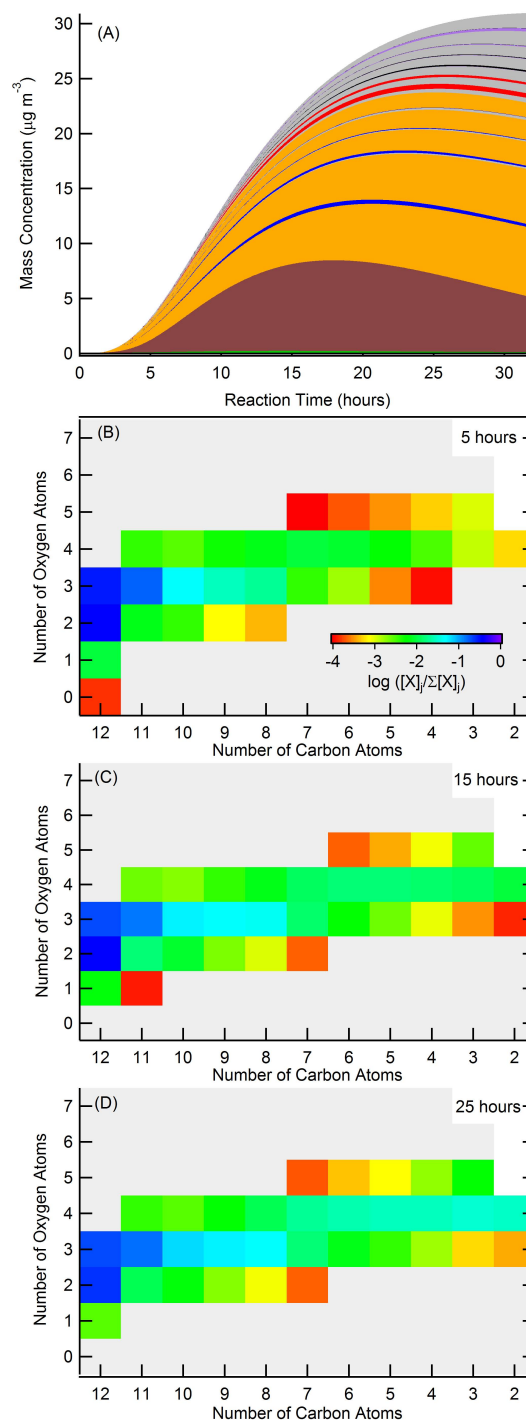


Fig. 7. (A) Simulated mass concentrations of each SOM species, with each species stacked on the previous. The colors correspond to those in Fig. 6 and indicate species of a particular “cluster”. (B), (C) and (D) show snapshots at 5, 15 and 25 hours of reaction, respectively, of the normalized mass concentration of all SOM species on an oxygen/carbon grid, with concentration indicated by the color of each cell in the grid (see legend). For each snapshot, the mass concentration of each species is normalized by the total SOA mass concentration as in Fig. 4; species with a normalized abundance $<10^{-4}$ are shown as gray and species with O:C >2 are shown as white.

reaction progresses, the cluster of $N_{\text{O}}=4$ species begins to contribute significantly while the abundance of the $N_{\text{C}}=12$, $N_{\text{O}}=2$ species decreases as it is converted into more oxidized species. This illustrates the dynamic nature of the SOA composition as it forms and ages.

5.2 Relationship of ΔLVP and oxygen addition

In principle, the addition of different functional groups corresponds to different values for ΔLVP in the SOM. For example, the SIMPOL model of Pankow and Asher (2008) suggests the following: $\Delta\text{LVP}(\text{alcohol}) \sim 2.23$; $\Delta\text{LVP}(\text{ketone}) \sim 0.94$; $\Delta\text{LVP}(\text{aldehyde}) \sim 1.35$; $\Delta\text{LVP}(\text{nitrate}) \sim 0.74$; $\Delta\text{LVP}(\text{hydroperoxide}) \sim 1.24$. (Recall that ΔLVP is defined on a per-oxygen basis.)

Under low- NO_x reaction conditions, likely products from gas-phase pathways are hydroperoxides, carbonyl hydroperoxides, hydroxyl hydroperoxides, carboxylic acids, hydroxylcarboxylic acids, hydroxyperacids and hydroxyl carbonyls (Yee et al., 2012). For the low- NO_x systems the best-fit SOM ΔLVP values are all >2 , which would suggest the addition of predominately hydroxyl ($-\text{OH}$) functional groups. However, addition only of alcohols seems unlikely, both from a mechanistic perspective (Yee et al., 2012) and from consideration of the observed H-loss per O-added (or Van Krevelen slope). Strict alcohol addition would correspond to a Van Krevelen slope of 0, which can be compared with the addition of a ketone or aldehyde (slope = -2) or hydroperoxide (slope = 0). The observed low- NO_x Van Krevelen slopes ranged from -1.45 to -2.2 . Such values are more suggestive of substantial ketone or aldehyde addition, as opposed to addition of alcohols, ketones and hydroperoxides as suggested by Yee et al. (2012). Thus, there appears to be some inconsistency between the model ΔLVP values, the observed Van Krevelen slopes and the expected products.

One potential reconciliation between these differing indications of functional group addition is the presence of condensed phase reactions. The above functional group/ ΔLVP relationships do not account for condensed phase reactions that can alter the nature of the functional groups comprising the SOA (and thus the H:C and O:C relationship) and the apparent volatility of the condensed-phase compounds. Importantly, certain condensed phase reactions involve a change in the Van Krevelen slope while others preserve the slope. Dehydration reactions involve loss of water molecules and lead to a change in the observed H:C vs. O:C slope, moving it towards steeper values. For example, ester formation, typically from the reaction of a carboxylic acid and alcohol, involves loss of a water molecule:



Assuming that this water does not influence the SOA O:C measurement, esterification leads to an overall Van Krevelen slope of -2 relative to the unreacted hydrocarbon and, by forming a longer-chain species (i.e. an oligomer), a de-

crease in vapour pressure despite the loss of functional group (the magnitude of this vapour pressure decrease will depend on the carbon chain length of the molecules involved). Cyclization reactions of hydroxycarbonyl species to form cyclic hemiacetals followed by dehydration to form a dihydrofuran also involve loss of water molecules, again leading to a shift in the Van Krevelen slope towards steeper values. However, such reactions do not lead to oligomerization, and thus the volatility of the dihydrofuran product may be substantially higher than the cyclic hemiacetal. The increased vapour pressure could lead to evaporation of the dihydrofuran, which could undergo further gas-phase processing and, potentially, re-condensation as a more oxidized species. Ultimately, if the dihydrofuran does not remain or end up back in the particle, the Van Krevelen slope of the SOA will be unaffected. It is worth noting that such dehydration reactions will lead to a decrease in the observed SOA O:C, and could provide an explanation for the model over-estimate. Altogether, consideration of the observations and the model results suggest that condensed-phase reactions occur that alter not only the apparent volatility of the SOA species, but also their atomic composition. However, it is possible that a bias against detection of hydroperoxides could also have influenced the observed Van Krevelen slope. Addition of hydroperoxides should yield a slope of 0. Thus, if hydroperoxides are primarily detected following loss of $-\text{OOH}$, the observed slope would be shifted towards more negative values. To the extent that this occurs, the need to invoke condensed phase reactions to explain the differing indications of functional group addition would be lessened.

Under high- NO_x conditions, the model ΔLVP values ranged from 1.46 to 2.06 (or 1.46 to 1.80 if cyclododecane is excluded). Interestingly, these values are significantly larger than that associated with organonitrate addition ($\Delta\text{LVP}=0.74$) even though the best-fit P_{func} array indicates a substantial fraction of reactions add up to 3 or 4 oxygen atoms per reaction, which is consistent with nitrate addition. The mean H-loss-per-O added ranged from 1.25 to 1.83, also significantly larger than expected if nitrate functional group addition dominates (-0.33). Again, these results suggest that condensed phase reactions are altering the observed SOA properties, and thus the interpretation of the SOM best-fit parameters. As with the low- NO_x case, condensed phase reactions that make the Van Krevelen slope more negative (steeper) are suggested to reconcile the observations, expected mechanism and SOM results. In the condensed phase, organonitrates can undergo hydration reactions followed by acid-catalyzed nitrate loss to form alcohols. However, such reactions are unlikely under the very low RH conditions of these experiments, and furthermore would move the slope in the wrong direction (i.e. towards zero). Esterification (dehydration) reactions may also be occurring in the high- NO_x particles, moving the slope towards more negative values and, likely, decreasing the apparent volatility of the condensed species. Taken together, the low and high- NO_x

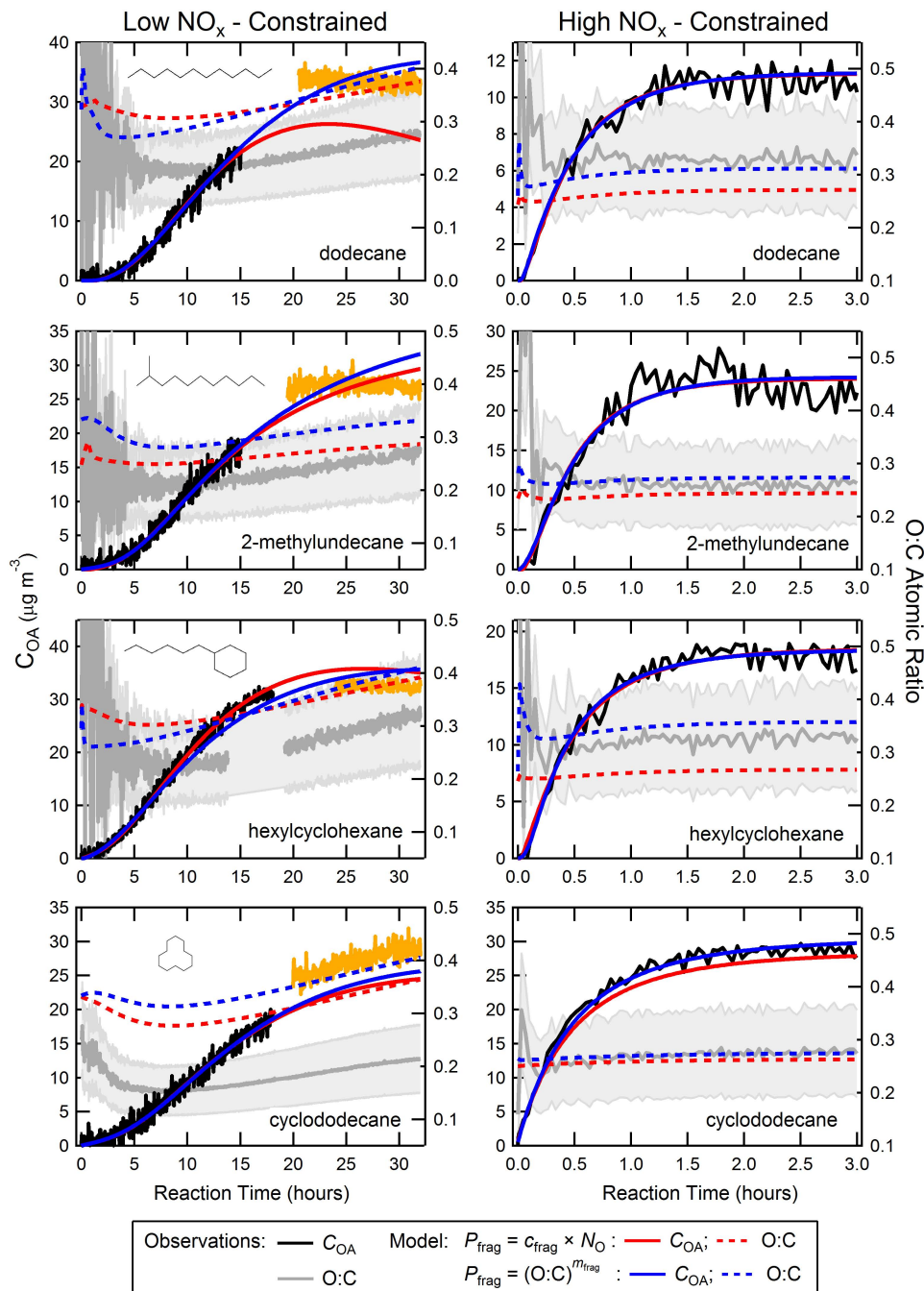


Fig. 8. Same as Fig. 1, but where the high-NO_x and low-NO_x c_{frag} and m_{frag} parameters have been constrained; see text for details.

results illustrate the broader point that interpretation of Van Krevelen diagrams in terms of how the SOA composition relates to the associated gas-phase composition is not necessarily straightforward since the measurements may likely be affected by condensed phase reactions. This conclusion is consistent with the findings of Craven et al. (2012), who determined that movement between the different identified SOA “factors” occurs along multiple Van Krevelen slopes.

When interpreting the best-fit SOM parameters in terms of chemical mechanisms, as above, it is important to consider the robustness of the fit parameters. This is examined here by re-fitting the SOM to observations of C_{OA} only (as opposed to C_{OA} and O:C), but where the P_{frag} parameters (i.e. c_{frag} and m_{frag}) for the high-NO_x reactions are constrained to be equal to the best-fit values from the low-NO_x reactions, and vice versa. The extent to which the constrained c_{frag} and

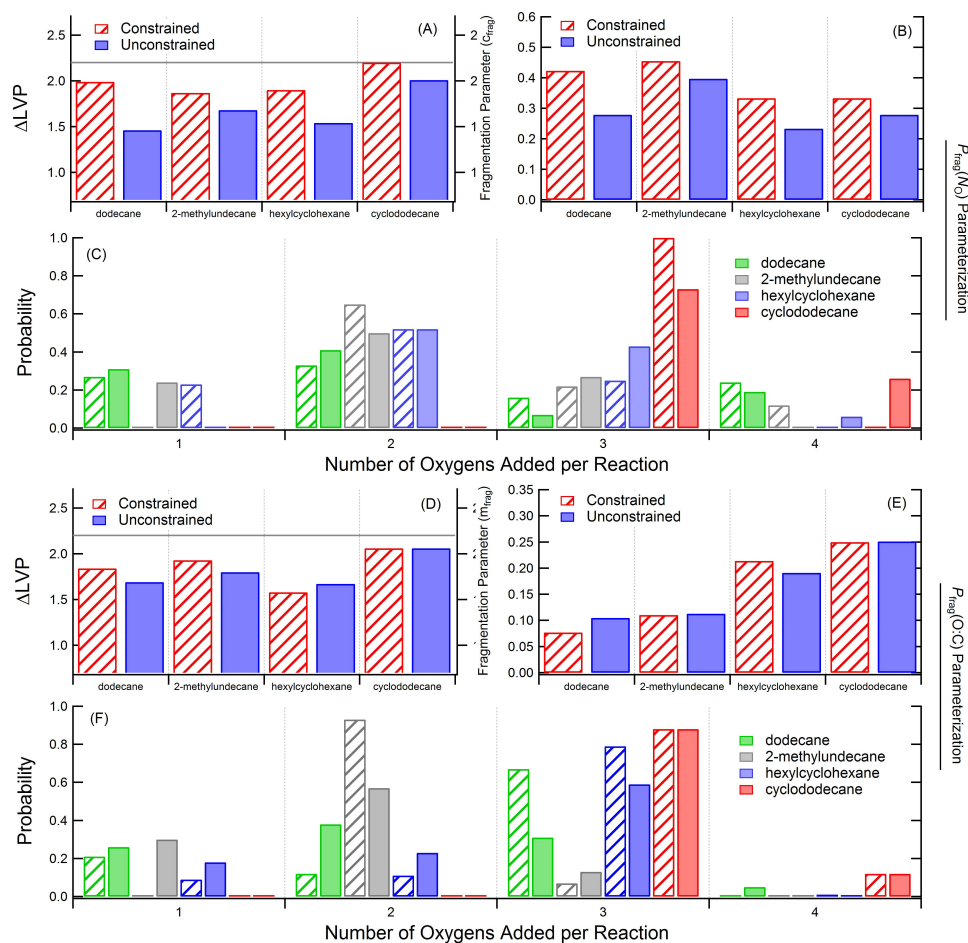


Fig. 9. Best-fit SOM parameters for dodecane, 2-methylundecane, hexylcyclohexane, and cyclododecane under high-NO_x conditions for both the overall best-fit (solid bars, as in Fig. 2) and the best-fit when the c_{frag} and m_{frag} parameters are constrained to be equal to the low-NO_x overall best-fit values (hashed bars). Results are shown for both the $P_{\text{frag}}(\text{N}_\text{O})$ (A–C) and $P_{\text{frag}}(\text{O:C})$ (D–F) parameterizations and include (A and D) ΔLVP , (B and E) the fragmentation parameter, and (C and F) the oxygen addition array. The constrained model was fit only to the observed C_{OA} . The grey line in (A) and (D) indicates the upper-limit constraint on ΔLVP .

m_{frag} values differ from the best-fit values for each alkane, although in general the constrained high-NO_x c_{frag} is larger (and m_{frag} smaller) compared to the overall best-fit, while for low-NO_x reactions the opposite is true (Table 2). In most cases, it is still possible to fit the SOM to the observed C_{OA} growth, although there are a few exceptions where the C_{OA} is under-predicted after fitting (Fig. 8). In general, the extent to which the best-fit ΔLVP and P_{frag} array differ between the constrained and overall fit depends on how different the c_{frag} and m_{frag} parameters are. For the high-NO_x reactions, many of the resulting ΔLVP values for the constrained fits are increased to offset the greater fragmentation, while, importantly, the oxygen distributions are reasonably similar between the constrained and overall best-fit (Fig. 9). The predicted O:C for the constrained fit does not match the observations quite as well as the overall best-fit (although remaining within the $\pm 30\%$ uncertainty for all cases; Fig. 8). For the

low-NO_x reactions, some of the resulting ΔLVP values for the constrained fits are decreased, although for many cases the differences are small, while the oxygen distributions are generally unchanged (Fig. 10). This comparison illustrates that the ΔLVP and P_{frag} parameters can have compensating effects, which indicates that care must be taken in their interpretation. Nonetheless, the results from the constrained and overall best-fits are sufficiently similar that the general conclusions reached above are unchanged.

6 Summary and conclusions

For a comprehensive series of SOA formation experiments from photooxidation of four $N_{\text{C}} = 12$ alkanes, two straight chain and two ring-containing, observations indicate that the SOA yield is larger for these compounds under low- vs. high-NO_x conditions, with the exception of cyclododecane. The

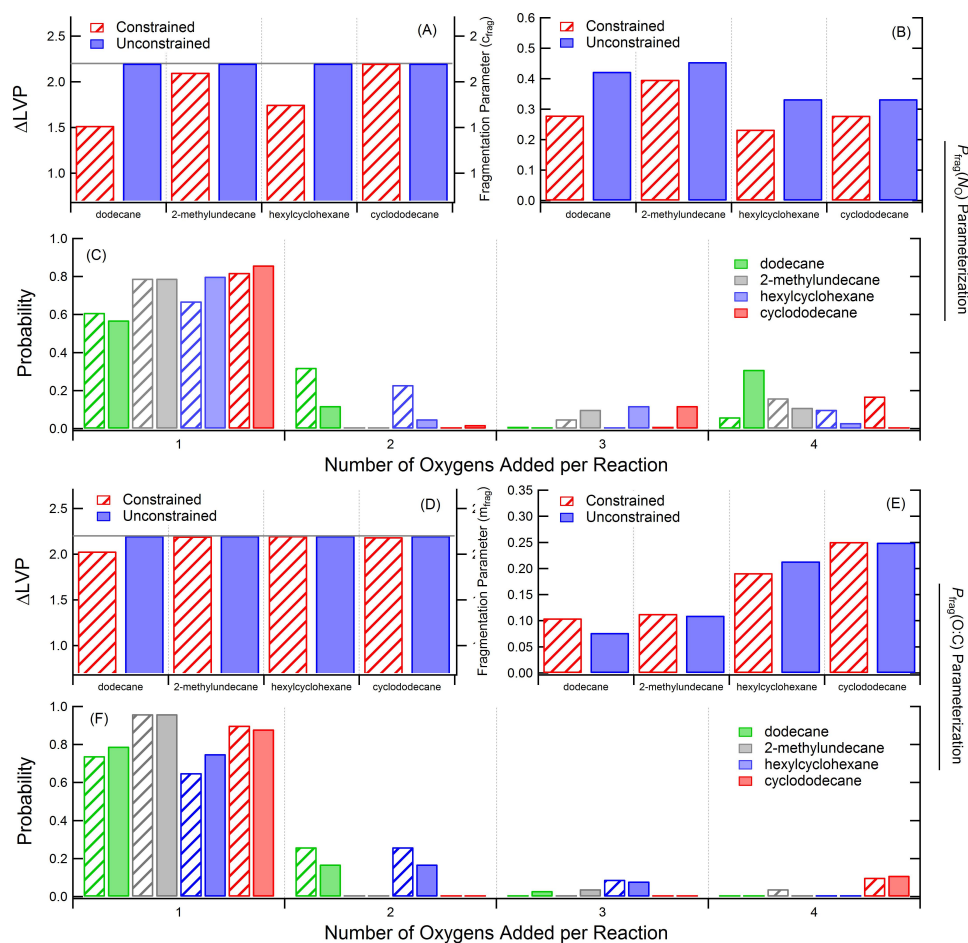


Fig. 10. Best-fit SOM parameters for dodecane, 2-methylundecane, hexylcyclohexane, and cyclododecane under low-NO_x conditions for both the overall best-fit (solid bars, as in Fig. 2) and the best-fit when the c_{frag} and m_{frag} parameters are constrained to be equal to the high-NO_x overall best-fit values (hashed bars). Results are shown for both the $P_{\text{frag}}(\text{N}_\text{O})$ (A–C) and $P_{\text{frag}}(\text{O:C})$ (D–F) parameterizations and include (A and D) ΔLVP , (B and E) the fragmentation parameter, and (C and F) the oxygen addition array. The constrained model was fit only to the observed C_{OA} . The grey line in (A) and (D) indicates the upper-limit constraint on ΔLVP .

O:C atomic ratio is generally similar between high- and low-NO_x, although the low-NO_x experiments exhibit a continuous increase in O:C as oxidation proceeds. This difference results primarily from the differing oxidation conditions: the [OH] during low-NO_x experiments was approximately constant around 2×10^6 molecules cm⁻³, whereas the [OH] during high-NO_x experiments started higher but rapidly decayed due to efficient photolysis of the OH precursor (HONO).

The observed C_{OA} temporal growth curves have been fit to the statistical oxidation model (Cappa and Wilson, 2012) to derive values for the mean decrease in volatility per oxygen added (ΔLVP), the probability of fragmentation and the distribution of oxygens added per reaction. In general, there is excellent model/measurement agreement in terms of the time-evolution of the C_{OA} . This work demonstrates that the use of a kinetic, multi-generation model to represent SOA formation during photooxidation can provide insights into

the SOA formation process and facilitate the interpretation of smog chamber observations.

Acknowledgements. This work was supported by the National Science Foundation (ATM-1151062) and the Department of Energy (DE-SC0006626).

Edited by: F. Keutsch

References

- Aiken, A. C., DeCarlo, P. F., and Jimenez, J. L.: Elemental analysis of organic species with electron ionization high-resolution mass spectrometry, *Anal. Chem.*, 79, 8350–8358, doi:10.1021/ac071150w, 2007.
- Aiken, A. C., Decarlo, P. F., Kroll, J. H., Worsnop, D. R., Huffman, J. A., Docherty, K. S., Ulbrich, I. M., Mohr, C., Kimmel,

- J. R., Sueper, D., Sun, Y., Zhang, Q., Trimborn, A., Northway, M., Ziemann, P. J., Canagaratna, M. R., Onasch, T. B., Alfarra, M. R., Prevot, A. S. H., Dommen, J., Duplissy, J., Metzger, A., Baltensperger, U., and Jimenez, J. L.: O/C and OM/OC ratios of primary, secondary, and ambient organic aerosols with high-resolution time-of-flight aerosol mass spectrometry, *Environ. Sci. Technol.*, 42, 4478–4485, doi:10.1021/es703009q, 2008.
- Aumont, B., Szopa, S., and Madronich, S.: Modelling the evolution of organic carbon during its gas-phase tropospheric oxidation: development of an explicit model based on a self generating approach, *Atmos. Chem. Phys.*, 5, 2497–2517, doi:10.5194/acp-5-2497-2005, 2005.
- Barsanti, K. C., Smith, J. N., and Pankow, J. F.: Application of the np+mP modeling approach for simulating secondary organic particulate matter formation from α -pinene oxidation, *Atmos. Environ.*, 45, 6812–6819, doi:10.1016/j.atmosenv.2011.01.038, 2011.
- Cappa, C. D., and Wilson, K. R.: Multi-generation gas-phase oxidation, equilibrium partitioning, and the formation and evolution of secondary organic aerosol, *Atmos. Chem. Phys.*, 12, 9505–9528, doi:10.5194/acp-12-9505-2012, 2012.
- Chhabra, P. S., Flagan, R. C., and Seinfeld, J. H.: Elemental analysis of chamber organic aerosol using an aerodyne high-resolution aerosol mass spectrometer, *Atmos. Chem. Phys.*, 10, 4111–4131, doi:10.5194/acp-10-4111-2010, 2010.
- Cocker, D. R., Flagan, R. C., and Seinfeld, J. H.: State-of-the-art chamber facility for studying atmospheric aerosol chemistry, *Environ. Sci. Technol.*, 35, 2594–2601, doi:10.1021/es0019169, 2001.
- Comperolle, S., Ceulemans, K., and Müller, J. F.: EVAPORATION: a new vapour pressure estimation method for organic molecules including non-additivity and intramolecular interactions, *Atmos. Chem. Phys.*, 11, 9431–9450, doi:10.5194/acp-11-9431-2011, 2011.
- Craven, J. S., Yee, L. D., Ng, N. L., Canagaratna, M. R., Loza, C. L., Schilling, K. A., Yatavelli, R. L. N., Thornton, J. A., Ziemann, P. J., Flagan, R. C., and Seinfeld, J. H.: Analysis of secondary organic aerosol formation and aging using positive matrix factorization of high-resolution aerosol mass spectra: application to the dodecane low-NO_x system, *Atmos. Chem. Phys.*, 12, 11795–11817, doi:10.5194/acp-12-11795-2012, 2012.
- DeCarlo, P. F., Kimmel, J. R., Trimborn, A., Northway, M. J., Jayne, J. T., Aiken, A. C., Gonin, M., Fuhrer, K., Horvath, T., Docherty, K. S., Worsnop, D. R., and Jimenez, J. L.: Field-deployable, high-resolution, time-of-flight aerosol mass spectrometer, *Anal. Chem.*, 78, 8281–8289, doi:10.1021/ac061249n, 2006.
- Donahue, N. M., Robinson, A. L., Stanier, C. O., and Pandis, S. N.: Coupled partitioning, dilution, and chemical aging of semivolatile organics, *Environ. Sci. Technol.*, 40, 2635–2643, doi:10.1021/es052297c, 2006.
- Donahue, N. M., Kroll, J. H., Pandis, S. N., and Robinson, A. L.: A two-dimensional volatility basis set – Part 2: Diagnostics of organic-aerosol evolution, *Atmos. Chem. Phys.*, 12, 615–634, doi:10.5194/acp-12-615-2012, 2012.
- Heald, C. L., Kroll, J. H., Jimenez, J. L., Docherty, K. S., DeCarlo, P. F., Aiken, A. C., Chen, Q., Martin, S. T., Farmer, D. K., and Artaxo, P.: A simplified description of the evolution of organic aerosol composition in the atmosphere, *Geophys. Res. Lett.*, 37, L08803, doi:10.1029/2010gl042737, 2010.
- Jimenez, J. L., Canagaratna, M. R., Donahue, N. M., Prevot, A. S. H., Zhang, Q., Kroll, J. H., DeCarlo, P. F., Allan, J. D., Coe, H., Ng, N. L., Aiken, A. C., Docherty, K. S., Ulbrich, I. M., Grieshop, A. P., Robinson, A. L., Duplissy, J., Smith, J. D., Wilson, K. R., Lanz, V. A., Hueglin, C., Sun, Y. L., Tian, J., Laaksonen, A., Raatikainen, T., Rautiainen, J., Vaattovaara, P., Ehn, M., Kulmala, M., Tomlinson, J. M., Collins, D. R., Cubison, M. J., Dunlea, E. J., Huffman, J. A., Onasch, T. B., Alfarra, M. R., Williams, P. I., Bower, K., Kondo, Y., Schneider, J., Drewnick, F., Borrmann, S., Weimer, S., Demerjian, K., Salcedo, D., Cottrell, L., Griffin, R., Takami, A., Miyoshi, T., Hatakeyama, S., Shimojo, A., Sun, J. Y., Zhang, Y. M., Dzepina, K., Kimmel, J. R., Sueper, D., Jayne, J. T., Herndon, S. C., Trimborn, A. M., Williams, L. R., Wood, E. C., Middlebrook, A. M., Kolb, C. E., Baltensperger, U., and Worsnop, D. R.: Evolution of organic aerosols in the atmosphere, *Science*, 326, 1525–1529, doi:10.1126/science.1180353, 2009.
- Kanakidou, M., Seinfeld, J. H., Pandis, S. N., Barnes, I., Dentener, F. J., Facchini, M. C., Van Dingenen, R., Ervens, B., Nenes, A., Nielsen, C. J., Swietlicki, E., Putaud, J. P., Balkanski, Y., Fuzzi, S., Horth, J., Moortgat, G. K., Winterhalter, R., Myhre, C. E. L., Tsigaridis, K., Vignati, E., Stephanou, E. G., and Wilson, J.: Organic aerosol and global climate modelling: a review, *Atmos. Chem. Phys.*, 5, 1053–1123, doi:10.5194/acp-5-1053-2005, 2005.
- Lane, T. E., Donahue, N. M., and Pandis, S. N.: Simulating secondary organic aerosol formation using the volatility basis-set approach in a chemical transport model, *Atmos. Environ.*, 42, 7439–7451, doi:10.1016/j.atmosenv.2008.06.026, 2008.
- Lim, Y. B. and Ziemann, P. J.: Effects of Molecular Structure on Aerosol Yields from OH Radical-Initiated Reactions of Linear, Branched, and Cyclic Alkanes in the Presence of NO_x, *Environ. Sci. Technol.*, 43, 2328–2334, doi:10.1021/es803389s, 2009.
- Loza, C. L., Chhabra, P. S., Yee, L. D., Craven, J. S., Flagan, R. C., and Seinfeld, J. H.: Chemical aging of m-xylene secondary organic aerosol: laboratory chamber study, *Atmos. Chem. Phys.*, 12, 151–167, doi:10.5194/acp-12-151-2012, 2012.
- Odum, J. R., Hoffmann, T., Bowman, F., Collins, D., Flagan, R. C., and Seinfeld, J. H.: Gas/particle partitioning and secondary organic aerosol yields, *Environ. Sci. Technol.*, 30, 2580–2585, doi:10.1021/es950943+, 1996.
- Pankow, J. F.: An absorption-model of the gas aerosol partitioning involved in the formation of secondary organic aerosol, *Atmos. Environ.*, 28, 189–193, doi:10.1016/1352-2310(94)90094-9, 1994.
- Pankow, J. F. and Asher, W. E.: SIMPOL.1: a simple group contribution method for predicting vapor pressures and enthalpies of vaporization of multifunctional organic compounds, *Atmos. Chem. Phys.*, 8, 2773–2796, doi:10.5194/acp-8-2773-2008, 2008.
- Robinson, A. L., Donahue, N. M., Shrivastava, M. K., Weitkamp, E. A., Sage, A. M., Grieshop, A. P., Lane, T. E., Pierce, J. R., and Pandis, S. N.: Rethinking organic aerosols: Semivolatile emissions and photochemical aging, *Science*, 315, 1259–1262, doi:10.1126/science.1133061, 2007.
- Valorso, R., Aumont, B., Camredon, M., Raventos-Duran, T., Mouchel-Vallon, C., Ng, N. L., Seinfeld, J. H., Lee-Taylor, J., and Madronich, S.: Explicit modelling of SOA formation from alpha-pinene photooxidation: sensitivity to vapour pressure esti-

- mation, *Atmos. Chem. Phys.*, 11, 6895–6910, doi:10.5194/acp-11-6895-2011, 2011.
- Yee, L. D., Craven, J. S., Loza, C. L., Schilling, K. A., Ng, N. L., Canagaratna, M. R., Ziemann, P. J., Flagan, R. C., and Seinfeld, J. H.: Secondary organic aerosol formation from Low-NO_x Photooxidation of Dodecane: Evolution of Multigeneration Gas-Phase Chemistry and Aerosol Composition, *J. Phys. Chem. A*, 116, 6211–6230, doi:10.1021/jp211531h, 2012.
- Zhang, Q., Jimenez, J. L., Canagaratna, M. R., Allan, J. D., Coe, H., Ulbrich, I., Alfarra, M. R., Takami, A., Middlebrook, A. M., Sun, Y. L., Dzepina, K., Dunlea, E., Docherty, K., DeCarlo, P. F., Salcedo, D., Onasch, T., Jayne, J. T., Miyoshi, T., Shimono, A., Hatakeyama, S., Takegawa, N., Kondo, Y., Schneider, J., Drewnick, F., Borrmann, S., Weimer, S., Demerjian, K., Williams, P., Bower, K., Bahreini, R., Cottrell, L., Griffin, R. J., Rautiainen, J., Sun, J. Y., Zhang, Y. M., and Worsnop, D. R.: Ubiquity and dominance of oxygenated species in organic aerosols in anthropogenically-influenced Northern Hemisphere midlatitudes, *Geophys. Res. Lett.*, 34, L13801, doi:10.1029/2007GL029979, 2007.

Appendix 2

**Organic aerosol formation from the reactive uptake of
isoprene epoxydiols (IEPOX) onto non-acidified
inorganic seeds**



Organic aerosol formation from the reactive uptake of isoprene epoxydiols (IEPOX) onto non-acidified inorganic seeds

T. B. Nguyen¹, M. M. Coggon², K. H. Bates², X. Zhang¹, R. H. Schwantes¹, K. A. Schilling², C. L. Loza^{2,*}, R. C. Flagan^{2,3}, P. O. Wennberg^{1,3}, and J. H. Seinfeld^{2,3}

¹Division of Geological and Planetary Sciences, California Institute of Technology, Pasadena, California, USA

²Division of Chemistry and Chemical Engineering, California Institute of Technology, Pasadena, California, USA

³Division of Engineering and Applied Science, California Institute of Technology, Pasadena, California, USA

*currently at: 3M Environmental Laboratory, 3M Center, Building 0260-05-N-17, St. Paul, Minnesota, USA

Correspondence to: T. Nguyen (tbn@caltech.edu)

Received: 10 October 2013 – Published in Atmos. Chem. Phys. Discuss.: 28 October 2013

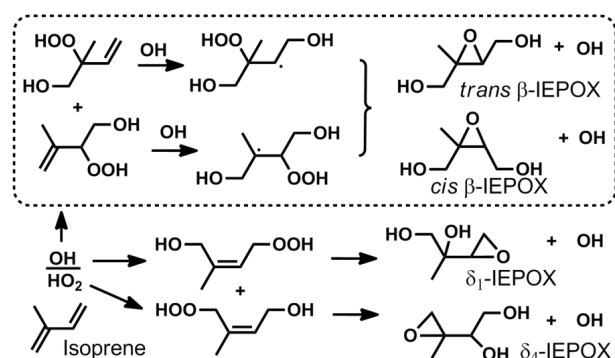
Revised: 8 February 2014 – Accepted: 18 February 2014 – Published: 8 April 2014

Abstract. The reactive partitioning of *cis* and *trans* β -IEPOX was investigated on hydrated inorganic seed particles, without the addition of acids. No organic aerosol (OA) formation was observed on dry ammonium sulfate (AS); however, prompt and efficient OA growth was observed for the *cis* and *trans* β -IEPOX on AS seeds at liquid water contents of 40–75 % of the total particle mass. OA formation from IEPOX is a kinetically limited process, thus the OA growth continues if there is a reservoir of gas-phase IEPOX. There appears to be no differences, within error, in the OA growth or composition attributable to the *cis/trans* isomeric structures. Reactive uptake of IEPOX onto hydrated AS seeds with added base (NaOH) also produced high OA loadings, suggesting the pH dependence for OA formation from IEPOX is weak for AS particles. No OA formation, after particle drying, was observed on seed particles where Na⁺ was substituted for NH₄⁺. The Henry's Law partitioning of IEPOX was measured on NaCl particles (ionic strength ~ 9 M) to be 3×10^7 M atm⁻¹ ($-50/+100$ %). A small quantity of OA was produced when NH₄⁺ was present in the particles, but the chloride (Cl⁻) anion was substituted for sulfate (SO₄²⁻), possibly suggesting differences in nucleophilic strength of the anions. Online time-of-flight aerosol mass spectrometry and offline filter analysis provide evidence of oxygenated hydrocarbons, organosulfates, and amines in the particle organic composition. The results are consistent with weak correlations between IEPOX-derived OA and particle acidity or liquid water observed in field studies, as the chemical system is nucleophile-limited and not limited in water or catalyst activity.

1 Introduction

A significant portion of the organic aerosol (OA) production from isoprene, a non-methane hydrocarbon emitted to the atmosphere in vast amounts, is attributed to the heterogeneous chemistry of isoprene epoxydiols (IEPOX) (Froyd et al., 2010; Chan et al., 2010; McNeill et al., 2012; Surratt et al., 2010; Hatch et al., 2011; Budisulistiorini et al., 2013; Pye et al., 2013). IEPOX, of which there are four isomeric forms (Scheme 1), is a second-generation low nitric oxide (NO) isoprene photooxidation product formed from the OH-oxidation of particular isomers of isoprene hydroxy hydroperoxides (Paulot et al., 2009b). The mechanism for OA production from IEPOX has been proposed as ring-opening of the epoxide group, activated by proton transfer from a strong acid such as sulfuric acid (H₂SO₄), followed by nucleophilic addition of available nucleophiles in the condensed phase, e.g., addition of water to produce tetrols, sulfate to produce organosulfates, and so on (Minerath et al., 2008; Eddingsaas et al., 2010; Surratt et al., 2010). This proposed mechanism has been corroborated by chamber investigations of particle acidity effects on OA formation (Surratt et al., 2007; Lin et al., 2012), wherein dry acidic seeds (MgSO₄ : H₂SO₄, 1 : 1) prompted strong reactive uptake behavior from epoxides (Paulot et al., 2009b), compared to negligible uptake for dry, non-acidified seeds.

Recent field data suggest that the story might be more complex than described above, as weak correlations between particle acidity and the abundance of IEPOX particle-phase tracer products were observed in Southeastern USA sites



Scheme 1 Formation of IEPOX isomers, from relevant isoprene hydroxy hydroperoxide precursors, in the low-NO photooxidation of isoprene. The expected dominant pathway is shown inside the box. The naming convention is based on Paulot et al. (2009b).

(Lin et al., 2013; Budisulistiorini et al., 2013). It should be noted that the indirect definition of “particle acidity,” which relies on charge balance of cations and anions, have several limitations and may not effectively represent the activity of H⁺ in the aqueous phase of particles in some cases (Greigore, 2013). Nevertheless, from the field observations, Lin and coworkers proposed that other factors may possibly modulate OA formation from IEPOX in conjunction with particle [H⁺]. One important distinction between previous chamber investigations, which have all been conducted under dry conditions (relative humidity, RH < 5%), and the Southeastern USA location is the prevalence of particle liquid water on the ammonium sulfate seeds. Water is a ubiquitous and abundant component of the atmosphere, therefore the effect of liquid water on the uptake of OA precursors has important implications for much of the globe. The crystalline ammonium sulfate seeds used in dry chamber experiments may not have adequate liquid water for IEPOX to partition into the aqueous phase, nor sufficient H⁺, NH₄⁺, and SO₄²⁻ activities to promote reactive uptake. Similarly, a particle with a large weight percent of H₂SO₄ may have a sizeable liquid water component, even at RH < 5%, due to the strong hygroscopicity of H₂SO₄ (Xiong et al., 1998), and the difference in reactive uptake of IEPOX may be due either to the differences in particle liquid water or the particle free acidity. In contrast, high concentrations of liquid water may cause dilution of aqueous ions, i.e., changing the acidity or ionic strength, which has been demonstrated to change the effective Henry’s Law partitioning coefficient of glyoxal (Kampf et al., 2013). Despite these important interactions, the effect of liquid water on OA formation from IEPOX has not been systematically explored in the laboratory.

We report here the reactive uptake of two isomers of IEPOX, the *cis* and *trans* β-IEPOX (Paulot et al., 2009b), which together comprise more than 97% of the isomer distribution (Bates et al., 2014). We synthesized authentic stan-

dards and observed the dark OA growth onto non-acidified and hydrated inorganic seeds at several particle liquid water concentrations. In the atmosphere, ammonium ions (NH₄⁺) are one of the most abundant components of aerosols and considerable IEPOX-derived OA are observed, even when a dominant portion of the aerosols are charge-balanced, e.g., [NH₄⁺]: 1/2 × [SO₄²⁻] or [NH₄⁺]: [NO₃⁻] ~ 1 (Lin et al., 2013). The aqueous NH₄⁺ may possibly act as catalyst for OA formation, as has been shown for a number of atmospherically important reactions (Noziere et al., 2009; Sareen et al., 2010; Ervens and Volkamer, 2010; Yu et al., 2011). We study reaction with NH₄⁺ as a potential rate-limiting mechanism for the IEPOX reaction. The role of cation and anion compositions in the seed for OA formation is studied by using ammonium sulfate, ammonium chloride, sodium sulfate, and sodium chloride seeds.

2 Materials and methods

2.1 Experimental procedures

This work utilized a newly constructed 24 m³ FEP Teflon environmental chamber specifically reserved for low-NO_x applications. The walls have not been in contact with strong acids and the chamber was operated in batch mode. Experiments were performed at room temperature (23–24 °C) and in the dark. Prior to the start of experiments, the chamber was thoroughly flushed with dry, purified air until particle concentrations are < 0.01 μg m⁻³. For humid experiments, water vapor was injected until the desired relative humidity (RH) was achieved in the chamber by flowing dry purified air over a Nafion membrane humidifier (FC200, Perma-pure LLC), which is kept moist by recirculating 27 °C ultra-purified (18 MΩ) water (Milli-Q, Millipore Corp). Temperature and RH were measured by a Vaisala HMM211 probe, calibrated with saturated salt solutions in the RH range of 11–95%. For RH < 11%, the water vapor content was quantified by chemical ionization mass spectrometry (Sect. 2.2.1).

Seed particles were injected by atomizing aqueous solutions (0.06 M) of ammonium sulfate ((NH₄)₂SO₄, AS), sodium chloride (NaCl), ammonium chloride (NH₄Cl), or sodium sulfate (Na₂SO₄) at 2100 hPa of air into the chamber through a ²¹⁰Po neutralizer and water trap. All inorganic seeds were injected through a 30 cm custom-built wet-wall denuder kept at 90 °C, such that the seed particles enter the chamber hydrated. Liquid water is expected to evaporate from the seed particles according to the salt’s efflorescence behavior (Lee and Hsu, 2000) at the RH of the chamber, e.g., in a dry chamber it is expected that the hydrated particles will enter the chamber fully dried. Particles were allowed to equilibrate until their volume concentrations are stable prior to organic injections.

Two isomers of isoprene epoxydiols (*cis* and *trans* β-IEPOX) were synthesized via procedures adapted from

Zhang et al. (2012) and purified with normal-phase column chromatography until the estimated purity based on nuclear magnetic resonance (NMR) of the *cis* and *trans* β -IEPOX isomers are 99 % and >92 %, respectively. Details of the synthesis and NMR spectra are reported in Bates et al. (2014). Although the mole fractions of the impurities are low, their high volatility may lead to an over-represented abundance in the gas phase. For the *cis* isomer, we detected experimental interference from the volatile 1,4-dihydroxy-2-methyl-2-butene (a precursor used in the synthesis), comprising ~50 % of the vapor phase measured directly above a bulb of IEPOX droplets by chemical ionization mass spectrometry (CIMS, Sect. 2.2). In order to further purify before experiments were conducted, *cis* β -IEPOX droplets were purged with dry N₂, and combined with 60 °C heating for >8 h until the measured impurity fraction dropped below 2 % (Fig. S1 in the Supplement). After the additional purification, IEPOX was injected into the chamber by flowing a 5–8 L min⁻¹ stream of dry purified air past several droplets in a clean glass bulb heated to 60 °C for 2–4 h. The mixtures of IEPOX and seed aerosols were allowed to equilibrate for >1 h. Most of the experimental conditions were repeated and were found to be reproducible within 15 %. We expect systematic error to dominate over the error of precision in this work.

2.2 Analytical methods

2.2.1 Chemical ionization mass spectrometry (CIMS)

Gas-phase IEPOX was measured with negative-ion chemical ionization mass spectrometry (CIMS) using CF₃O⁻ as the reagent ion, described in more detail previously (Crouse et al., 2006; Paulot et al., 2009a; St. Clair et al., 2010). The mass analyzer is a Varian triple-quadrupole spectrometer with unit mass resolution. Air is brought from the chamber using a 3 mm inner diameter perfluoroalkoxy (PFA) Teflon line with flow rate of 2.5 L min⁻¹. Of the total chamber flow, a 145 mL min⁻¹ analyte flow was sampled orthogonally through a glass critical orifice into the CIMS. The analyte flow was further diluted by a factor of 12 with dry N₂ to minimize the interaction of water vapor from the chamber with the reagent ion in the ion-molecule flow region. The subsequent data analysis corrects for the dilution factor. The operational pressure and temperature were kept at 35.5 hPa and 35 °C, respectively. The CIMS operated in a scanning MS mode (m/z 50–250) and tandem MS mode (MSMS). In MSMS mode, collisionally induced dissociation (CID) with 2.6 hPa of N₂ fragments analyte ions into product ions in the second quadrupole, following the ejection of neutral species. The MS cluster ion C₅H₁₀O₃ · CF₃O⁻ (m/z 203) of IEPOX was used for quantification, due to the higher signal-to-noise (S/N) of this ion compared to MSMS ions. The MSMS product ion C₅H₉O₃ · CF₂O⁻ (m/z 203 → m/z 183), found to be unique to IEPOX in the isoprene OH-oxidation system, was used to differentiate IEPOX from the isobaric isoprene

hydroperoxide (ISOPOOH), which has been documented to yield mainly m/z 63 and a negligible amount of m/z 183 upon CID (Paulot et al., 2009b). ISOPOOH (m/z 203 → m/z 63), was not expected, nor observed, during IEPOX injections.

CIMS calibrations of *cis* and *trans* β -IEPOX were performed by separately atomizing dilute (1–3 mM) solutions of each isomer with equimolar concentrations of hydroxyacetone, used as an internal standard, into the chamber through a 15 cm PFA Teflon transfer line for a few hours. During synthesis, NMR analysis showed that IEPOX was stable in water solution for many hours if no acid was present, so decay of IEPOX in the atomizer solution was not expected over the course of the calibration experiment. Toluene was used as a tracer to obtain the exact volume of the Teflon bag for each calibration experiment. A measured volume of toluene (6 μ L) was injected into a clean glass bulb with a microliter syringe (Hamilton) and quantitatively transferred into the chamber with a 5 L min⁻¹ stream of dry purified air. The gas-phase toluene was monitored by commercial gas chromatograph with flame-ionization detector (GC-FID, Hewlett-Packard 6890N) using a calibrated HP-5 column (15 m, 0.53 mm i.d.). The initial chamber temperature was 35 °C, and the temperature was ramped until 45 °C or until no increase of IEPOX signal was observed in the CIMS. The atomized solution was weighed before and after atomization. Each sensitivity determination was repeated at least twice. The sensitivities of the IEPOX isomers were calculated from the ratio of the normalized ion counts (with respect to the reagent ion signal) to the number of atomized moles. Small amounts of nucleated organic aerosols were observed in the chamber from the atomization, as measured by a scanning mobility particle sizer (Sect. 2.2.3) and that volume concentration was subtracted from the theoretical moles of IEPOX (corrections of <1 %). Based on their calculated dipole moments and average polarizability, the *cis* isomer was expected to have a sensitivity of ~1.6 times greater than the *trans* isomer (Paulot et al., 2009b), and we found the sensitivity of the *cis* isomer to be a factor of 1.8 greater than the *trans* isomer in the MS mode. The difference between the two ratios is within the error of the sensitivity determination.

Additionally, several mixing ratios of water vapor were introduced into the CIMS ion-molecule region to measure the water dependence of the IEPOX detection. Water vapor was quantified by Fourier-transform infrared spectroscopy (FT-IR, Nicolet Magna-IR 560) with a 19 cm pathlength quartz cell. Spectral fitting was performed using the HITRAN spectral database (Rothman et al., 2009) and the nonlinear fitting software NLM4 developed by Griffith (1996). In the low-RH range, outside the calibration limit of the membrane RH probe, the CIMS water ions H₂O · ¹³CF₃O⁻ (m/z 104) and (H₂O)₂ · CF₃O⁻ (m/z 121) were used to quantify water vapor concentration in the chamber after calibration of water vapor with FT-IR. These ions provide excellent sensitivity to water and linearity in the 20–3500 ppm range in the CIMS

ion molecule flow region (corresponding to 1–100 % RH in the chamber at 24 °C, before CIMS dilution). No water dependence in the detection of the IEPOX ions was observed within the range of water vapor observed by CIMS.

In order to quantify the gas-phase concentrations of IEPOX, the CIMS signal was corrected to account for the RH-dependent wall losses of IEPOX. The interactions of IEPOX with chamber walls have not been previously characterized, although those of its C₄ analog have been reported (Loza et al., 2010). IEPOX wall loss experiments were conducted at RH = 3 %, 46 %, and 69 %, as described in Section 2.1, continuously for 5–10 h. Figure S2 shows that the wall losses of IEPOX on non-acidic walls were negligibly small ($\sim 0.4\% \text{ h}^{-1}$ at RH 69 %), within the error of CIMS measurements.

2.2.2 Aerosol mass spectrometry (AMS)

Online particle composition was measured with a high-resolution time-of-flight aerosol mass spectrometer (ToF-AMS, Aerodyne Research Inc.). The ToF-AMS was operated in V mode ($R \sim 2000$ at m/z 200) and W mode ($R \sim 3000$ – 4000 at m/z 200). Prior to experiments, the ToF-AMS ionization efficiency was calibrated using size-selected 350 nm ammonium nitrate particles. The ToF-AMS monitored the content of ammonium (NH_4^+), sulfate (SO_4^{2-}) and other non-refractory ions throughout the course of the experiment. The ammonium to sulfate ratio did not change over the course of the experiment. Gas interferences and elemental ratios were calculated using the fragmentation tables developed by Allan et al. (2004) and Aiken et al. (2008). Data were analyzed in IGOR Pro 6.31 (WaveMetrics, Inc.) using the SQUIRREL v 1.51H and PIKA v 1.10H analysis toolkits. Total concentration of organics ($\mu\text{g m}^{-3}$) was calculated by summing the nitrate-equivalent masses of each high-resolution ion correlated with the organic fraction from the V-mode data.

Particles were sampled through a 130 cm Nafion membrane diffusion drier (MD-110, Permapure LLC) to avoid flow obstructions from wet particles over time, at a flow rate of 0.084 L min^{-1} . It is expected that drying the particles may introduce particle or organic line losses in the drier tube and change the particle bounce characteristics on the AMS vaporizer plate. These perturbations may be corrected by applying a collection-efficiency (CE) factor. It was demonstrated that organic aerosol particles with higher water content have very low bounce probability, which corresponds to a CE of unity (Matthew et al., 2008; Docherty et al., 2013). Comparatively, dry particles have much lower CE (~ 0.25 for pure, dry AS) due to the high bounce rate. The CE of IEPOX-derived organic aerosol-coated particles was calculated by measuring the mass concentrations of organics, sulfate, and ammonium of the wet particles without a drier, wherein CE was assumed to be unity and line losses assumed to be negligible, and comparing with measurements made through a drier. We observe a CE of 0.75 for all conditions in this work,

which is consistent with the collection efficiency of organic aerosols measured previously (Docherty et al., 2013). Further, it is expected that drying particles, relevant to the hydration/evaporation cycles of aerosols in nature, may lead to enhanced interactions between organic and inorganic compounds (De Haan et al., 2011; Nguyen et al., 2012), irreversibly forming OA.

2.2.3 Particle size and number concentration

Particle size and number concentrations were measured with a scanning mobility particle sizer (SMPS), comprised of a custom-built differential mobility analyzer (DMA) coupled to a commercial butanol-based condensation particle counter (CPC, TSI Inc.). The SMPS particle size measurement was calibrated with polystyrene latex (PSL) spheres. The particles entering the chamber have a static polydisperse distribution, with peak dry particle diameter distributions in the range of 50–100 nm. The sample air flow was not dried in humid experiments. Particle mass concentrations were corrected for RH- and size-dependent wall losses. The mass concentration of particles typically ranged from 65 – $90 \mu\text{g m}^{-3}$ for all experiments, using a particle density of 1.2 g cm^{-3} .

For AS-based experiments, the particle liquid water content was calculated based on the size-dependent hygroscopicity of AS (Biskos et al., 2006; Hu et al., 2010). For each particle diameter bin measured by SMPS, a theoretical dry diameter was calculated based on size-dependent literature growth factor data at the RH of the experiment. The difference in the wet (measured) and dry (calculated) integrated area of the mass distribution yielded the liquid water concentration in g m^{-3} . Similarly, the percent of liquid water content is calculated as $\% \text{ LWC} = 100\% \times (V_{\text{wet}} - V_{\text{dry}}) / V_{\text{wet}}$, using the predicted wet and dry diameters.

Particle wall loss characterizations were performed for AS seeds at RH = 3 %, 20 %, 50 %, and 80 % prior to the start of the experimental series to correctly quantify the mass concentrations of particles as a function of time. It was assumed that the loss rates of AS were representative for particles of different composition. Seed aerosols were atomized into the dry or humid chambers in the dark, allowed to stabilize, and particle size and number concentrations were measured for > 12 h. The particle correction method that accounts for wall loss has been discussed in detail previously (Loza et al., 2012).

2.2.4 Filter collection and analysis

Offline OA composition analysis was performed by ultra-high performance liquid chromatography time-of-flight electrospray ionization mass spectrometry (UPLC/ESI-ToFMS). Aerosol samples were collected onto Teflon membrane filters (Millipore, $1 \mu\text{m}$ pore), pulled at a 20 L min^{-1} flow through an activated charcoal denuder to remove the volatile and semivolatile components. Each filter was extracted with

methanol (Fisher, Optima grade, $\geq 99.9\%$) by ultrasonication for 15 min in a 20 mL scintillation vial. The filtered extracts were blown dry under a gentle stream of ultra-high-purity N_2 . The residue was reconstituted with 150 μL of 50 : 50 v/v acetonitrile (Fisher Optima grade, $\geq 99.9\%$) and water (Milli-Q).

Extracts were analyzed by a Waters Xevo G2-S UPLC/ESI-ToF-MS equipped with an Acquity CSH C₁₈ column (1.7 μm , 2.1 \times 100 mm). The solvents used for gradient elution were acetonitrile (Fisher Optima grade, $\geq 99.9\%$) and water with a 0.1 % formic acid spike (solvent “A”). The flow rate was held at 0.5 mL min^{-1} . Accurate mass correction was completed by a lock spray of leucine enkephalin (0.61 $\text{ng } \mu\text{L}^{-1}$ in 50 : 50 v/v acetonitrile/water with 0.1 % formic acid). The ESI source was operated in negative mode, where most analytes are ionized by deprotonation and measured as $[\text{M}-\text{H}]^-$. Ionic molecular formulas were determined from accurate masses (mass resolution of 60 000 at m/z 400) using the elemental composition tool in Mass Lynx. Control filters (no particles) and laboratory controls (seeds only) were analyzed in the same manner.

3 Results and Discussion

3.1 Reactive uptake of *cis* and *trans* β -IEPOX onto ammonium sulfate seeds

3.1.1 Liquid water content of seeds

Figure 1 shows the time profile for the organic aerosol (OA) growth corresponding to reactive uptake of the *trans* β -IEPOX onto ammonium sulfate (AS) seeds at two RH conditions, dry (LWC $\sim 0\%$) and RH 57 % (LWC $\sim 55\%$). The traces shown in Fig. 1 are representative of uptake behavior for both isomers on the experimental timescale. For RH conditions above the ammonium sulfate (AS) efflorescence point tested in this work ($E_{\text{RH}} \sim 35\%$, (Biskos et al., 2006)), prompt and efficient OA growth onto AS seeds was observed for both IEPOX isomers. No OA growth was observed when the AS seeds were dry, in good agreement with other reports (Lin et al., 2012, Surratt et al., 2010).

The OA growth from IEPOX did not halt after the end of the gas-phase injection period (Fig. 1, solid black line), even after periods of > 2 h (Fig. S3, top panel). This behavior is indicative of a non-equilibrium process, as the addition of nucleophiles is not reversible after the rate-limiting step of IEPOX activation (Eddingsaas et al., 2010). The formation of low-volatility compounds should continue as long as a reservoir of gas-phase IEPOX is available. The series of expected reactions leading to the formation of ring-opening products (ROP) is shown below, illustrated using a general proton donor (AH) and nucleophile (Nu).

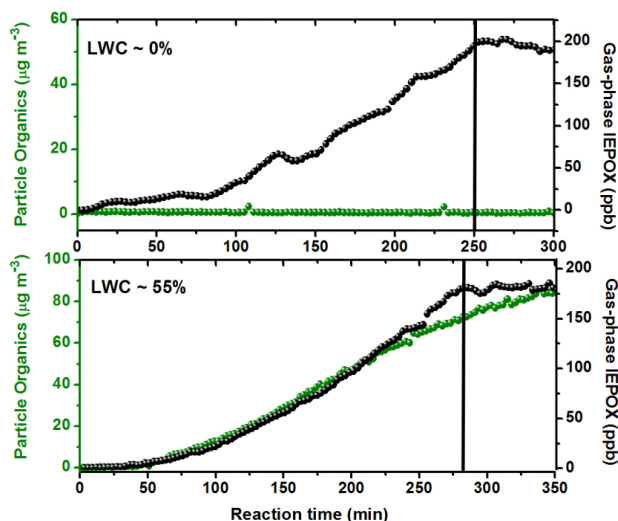
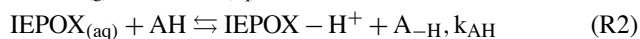
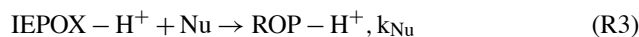


Fig. 1. Typical uptake experiment results as a function of time, shown for *trans* isomer, at dry (top) and humid (bottom) conditions with the corresponding percent of liquid water content (LWC). The solid black line indicates when IEPOX injection stopped and the mixture was allowed to equilibrate. Double y axes correspond to traces of the same color.



For a solution with low AH and Nu activity, the equilibrium accommodation of IEPOX into the aqueous phase, described by the Henry's Law coefficient of IEPOX (K_{H}), can be measured in isolation. Henry's Law may not be an appropriate description of the IEPOX reactive uptake experiments performed on the liquid water of suspended aerosols, as the aerosol water layers represent highly non-ideal solutions and the OA formation is kinetically limited. The OA formation mechanism may include contributions from reactions other than Reactions (1–4). To a first-order approximation, total OA mass formed from gas-phase reactive uptake of IEPOX will be a function of aqueous IEPOX concentration, nucleophile activity, and catalyst activity.

For the sake of comparison between experiments, it is useful to have a metric that includes the ratio of OA formed to gas-phase IEPOX injected and accounts for the variability in the size and number of injected seeds between experiments, which is reflected by the calculated aerosol water at different RH. We define here a reactive partitioning coefficient ($\Phi_{\text{OA/IEPOX}}$), calculated similarly to an effective Henry's Law coefficient, and thus having the same units (Seinfeld and Pandis, 2006):

$$\Phi_{\text{OA/IEPOX}} = (C_{\text{OA}} / C_{\text{IEPOX}}) / [10^{-6} \cdot R \cdot T \cdot P_{\text{LWC}}], \quad (1)$$

where ($C_{\text{OA}} / C_{\text{IEPOX}}$) is the mass concentration ratio of the IEPOX-derived organic aerosol (dried), measured by ToF-AMS, and the gas-phase IEPOX, measured by negative-ion

Table 1. Summary of results from representative reactive uptake experiments onto ammonium sulfate seeds. Mean results from Lin et al. (2012) are shown for comparison.

Exp. index	IEPOX isomer	Seed composition	RH (%)	Particle pH*	Seed ($\mu\text{g m}^{-3}$)	P_{LWC} (g m^{-3})	$C_{\text{OA}}/C_{\text{IEPOX}}$	$\Phi_{\text{OA/IEPOX}}$ (M atm^{-1})
1	cis	(NH ₄) ₂ SO ₄	3	–	70	$< 1 \times 10^{-6}$	5.04×10^{-4}	–
2	cis	(NH ₄) ₂ SO ₄	42	3.67	91	3.74×10^{-5}	0.102	1.15×10^8
3	cis	(NH ₄) ₂ SO ₄	50	3.74	92	4.79×10^{-5}	0.118	1.01×10^8
4	cis	(NH ₄) ₂ SO ₄	86	3.90	81	5.68×10^{-5}	0.179	4.00×10^7
5	trans	(NH ₄) ₂ SO ₄	2	–	65	$< 1 \times 10^{-6}$	4.74×10^{-4}	–
6	trans	(NH ₄) ₂ SO ₄	39	3.65	82	3.44×10^{-5}	0.090	1.06×10^8
7	trans	(NH ₄) ₂ SO ₄	57	3.77	89	4.64×10^{-5}	0.095	8.44×10^7
8	trans	(NH ₄) ₂ SO ₄	81	3.88	88	6.14×10^{-5}	0.115	7.66×10^7
9	trans	(NH ₄) ₂ SO ₄ + NaOH, pH=7	70	~5.5	84	5.33×10^{-5}	0.090	6.89×10^7
Lin et al. (2012)	cis	MgSO ₄ + H ₂ SO ₄ (1 : 1)	< 5	~-10	48	$1.62 \times 10^{-5**}$	0.058	1.47×10^8

* Modeled pH using E-AIM and AIOMFAC models (the value from (Lin et al., 2012) is a_{molality} -based pH), see text (Sect. 3.1.2).

** Based on hygroscopicity of H₂SO₄ at RH 5%, assumed growth factor 1.15, Xiong et al. (1998).

CIMS, P_{LWC} is the liquid water content of the inorganic aerosols prior to IEPOX introduction (g m^{-3}), R is the ideal gas constant ($\text{atm L mol}^{-1} \text{K}^{-1}$), T is the temperature (K), and 10^{-6} is a conversion factor ($\text{m}^3 \text{cm}^{-3}$). $\Phi_{\text{OA/IEPOX}}$ includes the contribution from Henry's Law equilibrium partitioning of IEPOX (Reaction R1), and thus is an upper limit for the effective Henry's Law constant.

We observe that $\Phi_{\text{OA/IEPOX}}$ was not time-dependent when both IEPOX and OA were increasing, as the ratio $C_{\text{OA}}/C_{\text{IEPOX}}$ stabilized when OA grew in response to gas-phase IEPOX (Fig. S3) but increased after IEPOX injection stopped. The stabilized ratio is used for $\Phi_{\text{OA/IEPOX}}$ calculations to compare between experiments. P_{LWC} did not have a significant time dependence due to a stable particle volume distribution before IEPOX gas-phase injections. The uncertainties in the accuracy of the $\Phi_{\text{OA/IEPOX}}$ and K_{H} measurements were estimated to be -50% and $+100\%$, compounded from the uncertainties in the calculated CIMS sensitivities, liquid water fraction, AMS organic mass determinations, and other measurements.

A summary of $\Phi_{\text{OA/IEPOX}}$ and other values is given in Table 1 for all AS-based uptake experiments. Figure 2 shows $\Phi_{\text{OA/IEPOX}}$, as a function of particle liquid water, for the *cis* and *trans* β -IEPOX uptake onto hydrated AS. A trend of decreasing $\Phi_{\text{OA/IEPOX}}$ with increasing LWC was reproducibly observed, despite the uncertainty range in the $\Phi_{\text{OA/IEPOX}}$ determinations. The suppression of $\Phi_{\text{OA/IEPOX}}$ as a function of added water is likely due to dilution. For example, high aerosol sulfate concentrations may cause a “salting-in” effect for IEPOX, or other water-soluble organic compounds (Kampf et al., 2013), which is inversely proportional to water content. Higher water may also reduce the $[\text{H}^+]$, although the dependence of the reaction on catalyst concentrations is not expected to be high. Additionally, higher P_{LWC} dilutes the aqueous IEPOX and nucleophile concentrations in the aerosol liquid water, which reduce the rate of the chemical reaction as these species are direct reagents. The dilution ef-

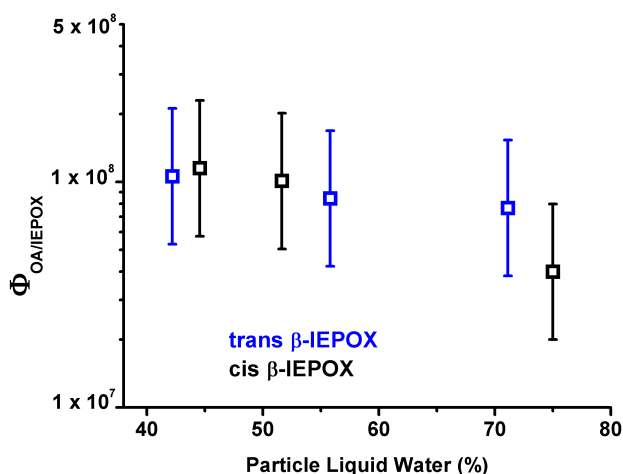


Fig. 2. Reactive partitioning coefficients ($\Phi_{\text{OA/IEPOX}}$) during the gas-phase IEPOX injection phase for the *trans* and *cis* isomers as a function of the particle liquid water concentration. Error bars indicate experimental uncertainty as described in the text.

fect from increasing the pure water fraction at a fixed ion content (moles of NH_4^+ and SO_4^{2-}) is in contrast to a modeled increase in OA mass in areas with high “anthropogenic water”, in other words, mixtures of water-soluble compounds found in urban regions (Carlton and Turpin, 2013). In the atmosphere, the partitioning of anthropogenic gases like NH_3 and SO_2 will simultaneously impact aqueous acidity and inorganic concentration and thus may lead to enhanced OA formation in areas with higher P_{LWC} .

3.1.2 Particle acidity

As the decrease of $\Phi_{\text{OA/IEPOX}}$ with increasing liquid water content may be due to more than one factor, an experiment was carried out to isolate the effect of pH. In experiment 9 (Table 1), the AS solution was neutralized with a strong base

(NaOH) until the atomizer solution reached $\text{pH} = 7$. Solutions of AS without additives had $\text{pH} \sim 5.5$ before atomization because, although no strong acid was present, H^+ is expected to be present in small quantities based on the dissociation equilibria of inorganics, such as the bisulfate/sulfate dissociation, and dissolution of CO_2 . An enhancement in the acidity of the particle may result from a smaller volume of water in the particle and/or through loss of NH_3 upon atomization. In the case of a fully hydrated AS particle, the pH in the particle is predicted to be $\text{pH} \sim 4$ using the E-AIM Model (Clegg et al., 1998), and modeled pH values in the particle for all AS-based experiments are shown in Table 1. As the pH values of the particles in this work are derived using inorganic models, the values obtained may include any uncertainties inherent in the models, including uncertainties in the gas/particle partitioning of NH_3 , hygroscopicity of salts, and/or acid dissociation equilibria. When the RH is below the deliquescence point of AS, the pH was estimated by calculating a concentration factor from the P_{LWC} at the lower RH. It is expected that atomization will also lead to slightly lower pH for the base-neutralized atomizer solution, so the particle may have $\text{pH} < 7$. However, adding NaOH above neutralization to counter this effect may induce side reactions such as base-catalyzed epoxide opening and OH^- nucleophilic addition (Solomons and Fryhle, 2004). NaOH is not explicitly treated in the E-AIM and AIOMFAC (Zuend et al., 2008) inorganic models, therefore, it was assumed that atomization of the AS + NaOH solution may lead to, at most, the same enhancement factor that occurred for the pH of the pure AS solutions.

Figure 3 shows that $\Phi_{\text{OA/IEPOX}}$ for the *trans* β -IEPOX + AS system decreases slightly as pH is increased, reaching a plateau above $\text{pH} \sim 4$. We note that any perceived change is within the error of the measurement, however, it is clear that the trend of $\Phi_{\text{OA/IEPOX}}$ with pH is minor. These results differ from those of Eddingsaas et al. (2010), who observed a linear increase of epoxide reaction rate with H^+ activity. Eddingsaas et al. (2010) used $\text{H}_2\text{SO}_4/\text{Na}_2\text{SO}_4$ solutions, and thus the differences in observations may be entirely due to the high NH_4^+ activity in the AS particles employed in this work. The data suggest that when $[\text{H}^+]$ is small, NH_4^+ may activate reactions leading to OA formation, similarly to its catalytic activity toward glyoxal (Noziere et al., 2009), methylglyoxal (Sareen et al., 2010), and other carbonyls (Nguyen et al., 2013; Bones et al., 2010). Interestingly, $\text{pH} > 4$ is the range where NH_4^+ catalysis is most efficient. This is demonstrated by a stable reactivity of the NH_4^+ -catalyzed reaction to generate brown carbon from limonene SOA at $\text{pH} 4\text{--}9$, but a sharp decline of reactivity below $\text{pH} 4$ (Nguyen et al., 2012). As the H^+ and NH_4^+ ions are reactive toward organics in low-moderate and moderate-high pH ranges, respectively, the resulting pH dependence may appear to be weak in AS-containing seeds. The dual reactivities of H^+ and NH_4^+ to-

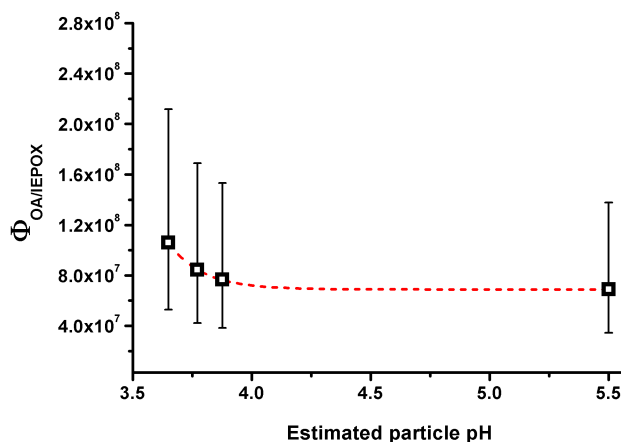


Fig. 3. $\Phi_{\text{OA/IEPOX}}$ for the *trans* β -IEPOX isomer as a function of the modeled particle pH .

ward IEPOX is expected to be important in nature, as NH_4^+ -based seeds are abundant.

In comparison, the $\text{MgSO}_4:\text{H}_2\text{SO}_4$ particles at $\text{RH} < 5\%$ in the work of Lin et al. (2012) are strongly acidic. These particles are predicted to have a non-negligible amount of water due to the large hygroscopicity of H_2SO_4 – and indeed, acidity in particles is not a useful concept if water is not present. At $\text{RH} = 0\text{--}5\%$, pure H_2SO_4 particles have a growth factor of 1.1–1.2 (Xiong et al., 1998). Assuming a growth factor of 1.15, and taking into consideration the inorganic seed mass concentration, we calculated P_{LWC} for the mean results in Lin et al. (2012), shown in Table 1. The AIOMFAC Model (Zuend et al., 2008; Zuend et al., 2011) was used to estimate the pH based on the molal activity of H^+ in the $\text{MgSO}_4:\text{H}_2\text{SO}_4$ (1:1) particle. The calculated pH is ~ -10 and the corresponding mean $\Phi_{\text{OA/IEPOX}}$ is $\sim 1.5 \times 10^8 \text{ M atm}^{-1}$ for *cis* β -IEPOX (the *trans* isomer was not studied). $\Phi_{\text{OA/IEPOX}}$ for the acidic MgSO_4 seeds is slightly higher than, but within the error of, the $\Phi_{\text{OA/IEPOX}}$ values for non-acidified AS seeds when a small amount of water is present ($\text{RH} \sim 40\%$). This comparison is meant to be qualitative and subject to uncertainty because the experiments were not performed under the same conditions. Nevertheless, the comparison shows that a solution of high H^+ activity and a solution of high NH_4^+ activity may both lead to a relatively similar reactive uptake coefficient. As $[\text{NH}_4^+] \gg [\text{H}^+]$ in the particles in this work, a similar $\Phi_{\text{OA/IEPOX}}$ would also suggest that $k_{\text{NH}_4^+} \ll k_{\text{H}^+}$ if the observed rate coefficient for Reaction (2) is defined as $k_{\text{obs}} = k_{\text{AH}} \cdot [\text{AH}]$. Eddingsaas et al. (2010) estimated $k_{\text{H}^+} \sim 5 \times 10^{-2} \text{ M}^{-1} \text{ s}^{-1}$ and Cole-Filipiak et al. (2010) determined $k_{\text{H}^+} = 3.6 \times 10^{-2} \text{ M}^{-1} \text{ s}^{-1}$ for IEPOX.

3.2 Molecular picture of OA formation from IEPOX

3.2.1 Cation and anion substitutions

To further investigate the role of NH_4^+ in IEPOX ring-opening reactions at near-neutral conditions, NH_4^+ was replaced by a cation that cannot act as a proton donor (Na^+). As isomer structure appears to be unimportant for uptake, only the *trans* isomer was used for this portion of the study. Further, many nucleophiles present in the atmosphere are known to add to the protonated epoxide to give the beta-hydroxy ring-opening product, for example: H_2O (Solomons and Fryhle, 2004), SO_4^{2-} ions (Cavdar and Saracoglu, 2009), NH_3 or amines (Clayden et al., 2001), and halide ions (Clayden et al., 2001). Thus, SO_4^{2-} was substituted by Cl^- to study the anion (or nucleophile) effect.

Hydrated particles of AS ($(\text{NH}_4)_2\text{SO}_4$), sodium sulfate (Na_2SO_4), ammonium chloride (NH_4Cl), and sodium chloride (NaCl) were introduced into the chamber in separate experiments, followed by the introduction of *trans* β -IEPOX. The mixtures were allowed to equilibrate for 3.5–6 h. The RH range for these reactions is 60–85 %, chosen at a point well above their respective efflorescence RH (Martin, 2000), so that each seed would contain a considerable fraction of liquid water. The particle size distributions for each seed type were polydisperse and unimodal, with hydrated mobility diameters in the range of 15–600 nm and with 60–120 nm peak diameters. It is expected that the hydrated particles were spherical. The size-dependent hygroscopicities of AS and NaCl are well-studied, however, the calculations of liquid water content for other seed types are subject to error based on the method we described due to limited literature data. Therefore, we opt to present results based only on the $C_{\text{OA}}/C_{\text{IEPOX}}$ for the comparison of inorganic seed compositions.

OA formation after particle drying, as detected by ToF-AMS, is negligible for both sodium salts (NaCl and Na_2SO_4). The OA mass did not grow in response to the addition of IEPOX for the Na^+ -based particles (Fig. S4). Figure 4 shows the average stabilized ratios of OA formed with respect to *trans* β -IEPOX injected for the four inorganic salts used in this work. The atomizer solution pH for Na^+ -based seeds was also ~ 5.5 , a typical pH for a water solution in equilibrium with CO_2 (Reuss, 1977). The large difference in reactivity of IEPOX on Na_2SO_4 vs. $(\text{NH}_4)_2\text{SO}_4$ seeds may be attributed primarily to NH_4^+ activity, although there will be some differences in $[\text{H}^+]$ for the NH_4^+ -based and Na^+ -based seeds due to the slight dissociation of $\text{NH}_4^+ \rightleftharpoons \text{NH}_3$. Additionally, in light of the weak pH dependence for AS solutions, it appears likely that NH_4^+ activity is an important factor in suppressing OA formation on Na_2SO_4 seed particles. The results show that equilibrium partitioning of IEPOX, i.e., any condensed-phase mass formed from unreacted IEPOX, onto salty solutions is not competitive with reactive partitioning for OA formation.

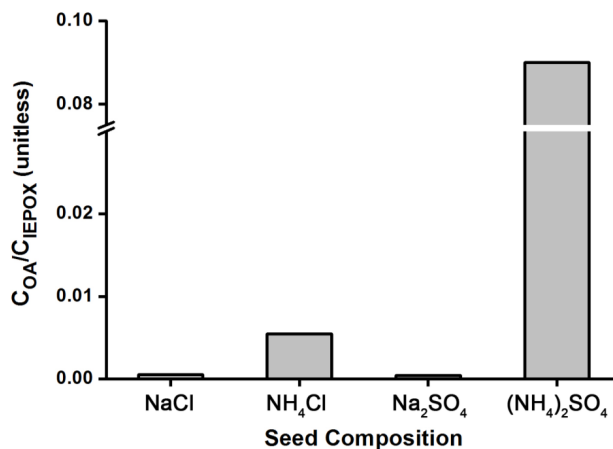


Fig. 4. Ratio of organic aerosol produced to gas-phase *trans* β -IEPOX injected for seeds of various compositions (RH 60–85 %).

For the ammonium salts, NH_4Cl produced an order of magnitude lower mean $C_{\text{OA}}/C_{\text{IEPOX}}$ ratio than $(\text{NH}_4)_2\text{SO}_4$, after an approximate 2h delay (Fig. S4). The modeled pH, using E-AIM, for both ammonium salt systems is similar (pH ~ 4 –4.5), and thus, the difference in reactivity may be attributed to the nucleophilic activity of Cl^- compared to SO_4^{2-} . Interestingly, Minerath et al. (2009) showed that acid-catalyzed ring-opening products of an epoxide with Cl^- may be more efficient than SO_4^{2-} . In that study, sulfuric acid was added to the NaCl + epoxide aqueous solution, which provide sulfate and bisulfate ions to the solution. Therefore, the results may not be directly comparable to this work. If Cl^- can be a good nucleophile in aqueous solutions of IEPOX when coupled with NH_4^+ catalysis, we may expect to observe organochloride products. There was no evidence of organochloride-derived accurate mass fragments in ToF-AMS data for the NH_4Cl reactive uptake organics. Further, gas-phase organochlorides were not observed by the CIMS. It is possible that organochlorides are produced but are easily hydrolyzed in the aerosol liquid water due to the relatively good leaving group ability of Cl^- , i.e., the hydrolysis behavior of organochlorides is more similar to that of tertiary organonitrates than that of organosulfates (Darer et al., 2011). It is also possible that organochlorides are preferentially evaporated in the diffusion drier because they might be more volatile than organosulfates or polyols. In both situations, but more so the latter, the total organic mass from the NH_4Cl experiments would be underestimated by ToF-AMS. Although we did not quantify tetrols and other polyols in this work, it is expected that they are present in substantial quantities because they are the thermodynamically preferred products in the epoxide ring-opening reactions.

3.2.2 Henry's Law constant

Although ToF-AMS did not observe OA formation for experiments using sodium salts (NaCl and Na₂SO₄) after particle drying, the wall-loss-corrected SMPS data (not dried) showed a minor and stable change in particle volume upon injection of IEPOX into the chamber with hydrated NaCl or Na₂SO₄ seeds (Fig. S5a, shown for NaCl). It is likely that the dissolved but unreacted IEPOX was removed from the condensed phase upon particle drying, which would lead to no observed OA mass in the ToF-AMS data throughout the duration of the experiment. The reversibility OA formation on the hydrated seeds indicates equilibrium-partitioning of IEPOX into the aerosol liquid water. The ratio of dissolved OA to injected IEPOX (Fig. S5b) reached a steady-state value at the end of the IEPOX injection period. Because NH₄⁺ is not present, and [H⁺] is not expected to be considerable in the aqueous phase, Reactions (R2) and (R4) are unimportant for this system. Further, in experiments using NaCl seeds, where the nucleophilicity of the solution is weaker, we are able to neglect the contribution of Reaction (R3), thereby isolating the equilibrium partitioning of IEPOX (Reaction R1).

We estimate the Henry's Law coefficient (K_H) for the equilibrium partitioning of IEPOX into a briny liquid (NaCl ~9 M ionic strength) representative of atmospheric aerosol to be 3×10^7 (−50/+100 %) M atm^{−1}. The K_H in a solution of NaCl may be different than the value in pure water, due to complex aqueous interactions of Cl[−] and Na⁺ with water-soluble organics. As an example, the Henry's Law constant for glyoxal was measured to be $K_H = (4.19 \pm 0.87) \times 10^5$ M atm^{−1} in pure water, 1.90×10^6 M atm^{−1} in a 0.05 M NaCl solution, and 8.50×10^5 M atm^{−1} in a 4.0 M NaCl solution at 298 K (Ip et al., 2009). Ip et al. (2009) attributed the increase in K_H for NaCl solutions at low ionic strengths (compared to water) to hydrogen bonding interactions of Cl[−] and OH groups and the decrease at high ionic strength to a “salting-out” effect. The K_H value for IEPOX has not been experimentally determined in the past; however, the range of K_H has been estimated using the HENRYWIN model (EPA, 2008) by several studies. For example, Eddingsaas et al. (2010) estimated $K_H = 2.7 \times 10^6$ M atm^{−1} using a bond contribution method, and $K_H = 2.9 \times 10^{10}$ M atm^{−1} using a group contribution method in version 4.0 of the model. The empirical K_H value reported here is within range of both estimations – closer to the bond contribution method estimate. These results provide a critical constraint in the partitioning coefficient, significantly decreasing the error associated with using K_H in a quantitative manner (from 4 orders of magnitude to a factor of two).

3.2.3 Organic composition

A full analysis of the OA composition is outside the scope of this work. The reader is referred elsewhere for a discussion

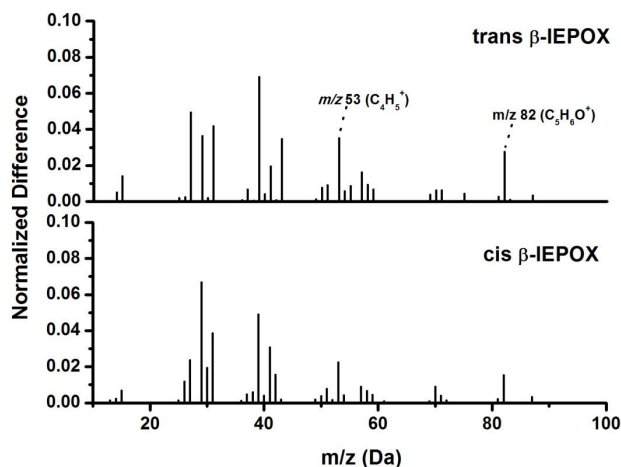


Fig. 5. ToF-AMS normalized difference spectra (composition at peak OA growth minus composition during seed injection), showing the organic composition of the OA produced by reactive uptake of the *trans* and *cis* isomers. Select nominal mass ions previously suggested to be IEPOX-derived OA tracers are labeled.

of the formation of oxygenated hydrocarbons, for example, tetrols and alkenetriols and organosulfates in the aqueous reaction of IEPOX catalyzed by acidic sulfate (Eddingsaas et al., 2010, Surratt et al., 2010). Although strong acid is absent in the systems studied in this work, we observe many similarities in the IEPOX-derived OA composition compared to the existing chamber and field results. For example, organosulfate products are abundant when hydrated AS seeds are used. The dominant ion observed in negative ion mode UPLC/ESI-ToFMS for AS uptake was C₅H₁₁SO₇[−] (Fig. S6), corresponding to the ring-opening trihydroxy organosulfate product of IEPOX. Derivatization was not performed in this work to detect tetrols. Organosulfate fragments were also observed in ToF-AMS (CSO family of fragments, not shown).

IEPOX-derived OA formed under near-neutral conditions in this work have ToF-AMS spectra similar to those of OA observed in the field. The suggested tracers for IEPOX-derived organics, m/z 53 (mostly C₄H₅⁺) and m/z 82 (mostly C₅H₆O⁺) (Lin et al., 2012, Robinson et al., 2011, Budisulistiorini et al., 2013), were observed in uptake experiments using both isomers. These mass fragments were proposed to originate from the electron-impact (EI) ionization of furan-derived molecules that were suggested to be formed from the acid-catalyzed rearrangement of IEPOX (Lin et al., 2013). Although mass fragments produced by EI may have multiple sources, in the pure system used in this study, m/z 82 was found to be a good tracer for IEPOX-derived OA. Figure 5 shows the difference between mass spectra at the end of the experiment and those at the time period prior to organic injection, corresponding to the organic fraction of the OA formed from the uptake of both isomers. The spectral ion distributions are very similar to each other

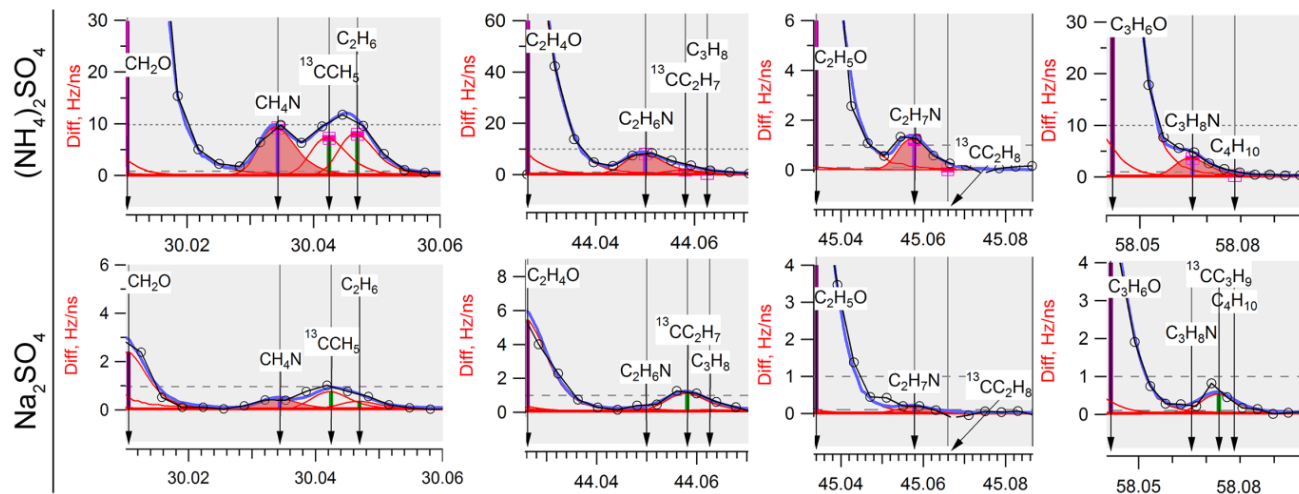


Fig. 6. ToF-AMS difference spectra (open minus closed chopper) showing organic nitrogen (amine) fragments from the reactive uptake of *trans* β -IEPOX onto AS vs. Na_2SO_4 seeds. Similar fragments were observed for *cis* β -IEPOX using NH_4^+ -based seeds and not observed in Na^+ -based seeds.

and m/z 53 and m/z 82 constituted a substantial fraction of the total ion intensity. The ion abundance of tracer fragments increased in accordance with the growth of OA mass (Fig. S7). As m/z 53 (C_4H_5^+) is a reduced fragment, it is also linked to hydrocarbon-like organics in chamber studies and may not be unique to IEPOX-derived OA. m/z 53 was observed in all experiments, including those that used Na^+ -based seeds. However, m/z 82 is abundant only when NH_4^+ -based seeds were used, supporting the suggestion that it can be formed through the EI fragmentation of an IEPOX-derived ring-opening product in ToF-AMS.

A unique aspect of the NH_4^+ -catalyzed ring-opening reaction of IEPOX is the minor possibility of nucleophilic addition by NH_3 , instead of reforming NH_4^+ after neutralizing the addition of another nucleophile. Figure 6 shows ion peaks for organic fragments containing C-N bonds observed in ToF-AMS data from the uptake of *trans* β -IEPOX onto AS vs. Na_2SO_4 seeds. The same C-N fragments were observed in *cis* β -IEPOX experiments using AS. These C-N fragments were not initially present in the AS seeds, and grow linearly following the introduction of IEPOX. Individual C-N fragments correlate well (Fig. S8, linear fit $R^2 = 0.69\text{--}0.88$) with the m/z 82 IEPOX-derived OA tracer fragment ($\text{C}_5\text{H}_6\text{O}^+$), suggesting that the reaction of IEPOX is responsible for the presence of these amines. Comparatively, C-N type fragments were negligible or non-existent in uptake experiments from Na^+ -based seeds. The identification of amines is tentative; however, to the best of our knowledge, this is the first suggestion of amine formation from IEPOX. As organic nitrogen compounds also give rise to non-nitrogenous mass fragments in ToF-AMS, it is not possible to estimate a mass concentration for the amines in this work. However, the C-N family of fragments comprised approximately 10 % of the

$\text{C}_5\text{H}_6\text{O}^+$ signal, an indication that amine formation may not be negligible. The formation of organic nitrogen from the IEPOX + NH_4^+ reaction has important implications in the atmosphere as the ring-opening reaction of epoxides with amines should be more efficient than with NH_3 (Azizi and Saidi, 2005). Further investigations may provide more insight on the source of organic nitrogen from the atmospheric reactions of epoxides.

4 Summary and atmospheric implications

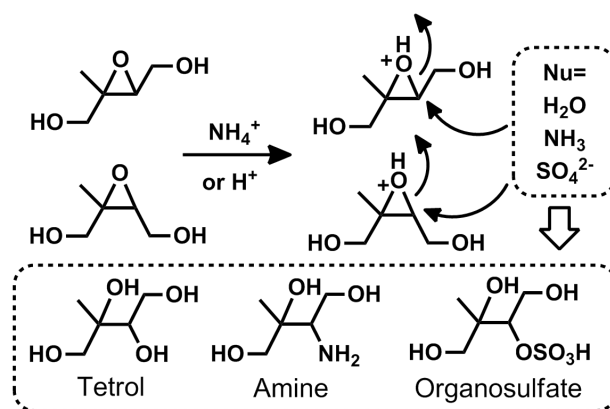
It was demonstrated here that the conversion of IEPOX to organic aerosol (OA) depends on the coupled relationship between the inorganic composition and liquid water content of the particle (P_{LWC}). The inorganic composition governs the catalyst and nucleophile characteristics, and P_{LWC} provides a reaction medium for the partitioning of IEPOX and controls the activities of all the aqueous components. The weak dependence on pH and the strong dependence on nucleophile activity and particle liquid water suggest that the IEPOX reactions in hydrated ammonium salts are nucleophile-limited, rather than catalyst-limited.

We showed that the equilibrium partitioning (Reaction 1) and the rate-limiting step of IEPOX activation (Reaction 2) do not proceed in the absence of liquid water; however, increasing the pure water content does not necessarily increase the reactive partitioning coefficient due to various dilution effects. When the inorganic particle is hydrated, the OA conversion is then determined by the catalyst and nucleophile activities. The rate of OA formation incorporates both Reactions (R2) and (R3), as illustrated by the cation and anion substitution case studies. In the hydrated Na_2SO_4 experiment, there was high activity of a relatively

good nucleophile, but a good catalyst was absent. Therefore, the formation of OA, i.e., the ring-opening product, was not observed because the equilibrium of Reaction (R2) favors IEPOX_(aq). The aqueous IEPOX mass that partitioned from the gas phase (K_H) onto the hydrated Na^+ -based seeds was removed from the condensed phase following the evaporation of water. In the hydrated NH_4Cl experiment, there was high activity of a good catalyst but possibly a poorer nucleophile than sulfate ion. A smaller quantity of OA formed because the rate of Reaction (R3) was slow, which was further supported by the observed 2 h delay in OA formation. Only when P_{LWC} , NH_4^+ activity, and SO_4^{2-} activity are all significant, as in the case of hydrated $(\text{NH}_4)_2\text{SO}_4$ seeds, is the OA formation efficient and prompt. The OA mass formed from IEPOX uptake onto 1:1 $\text{MgSO}_4:\text{H}_2\text{SO}_4$ seeds ($\text{RH} < 5\%$) from previous studies may also be explained in terms of these conditions, as P_{LWC} ($\sim 30\%$), catalyst (H^+) activity and nucleophile (SO_4^{2-}) activity were all sufficiently high in the particle.

In the atmosphere, relationships of water-soluble OA with P_{LWC} may be different and more difficult to interpret compared to laboratory studies because an increase in the P_{LWC} of atmospheric particles is often accompanied by the co-partitioning of water-soluble organic and inorganic compounds. The abundance of water-soluble organic compounds in the Southeast USA has been observed to be proportional to the liquid water contents of particles (Hennigan et al., 2008, 2009, Carlton and Turpin, 2013). In contrast, a weak correlation of modeled P_{LWC} with the abundance of IEPOX-derived OA tracers has also been observed, in the same geographical region (Budisulistiorini et al., 2013). The results of this work may not be directly comparable to field observations, however, they do not necessarily conflict. Particles may experience multiple hydration/evaporation cycles in the atmosphere, and the majority of particles likely contain liquid water at some point during their long lifetimes. The OA produced from IEPOX reactive uptake onto AS is irreversible (not removed from particle drying in this work), and depending on whether it had been sampled in the atmosphere before or after an evaporation cycle, the apparent correlation of IEPOX-derived OA with P_{LWC} would be different. Consequently, systematic studies in the laboratory are important for elucidating observations from the field.

Our results offer an alternate explanation to the abundance of IEPOX-derived OA tracers when the free H^+ acidity in particles is modeled to be low (Lin et al., 2013). It has been suggested that the reason for the weak correlation with acidity is the reaction of an acidic seed particle with IEPOX to form organosulfates, which affects the particle acidity over time (Budisulistiorini et al., 2013). We show here that particle acidity does not appear to be important for the IEPOX + AS system if particle liquid water is present, in that highly acidic seeds and weakly acidic AS seeds both have high potential to form OA from IEPOX reactive partitioning. The apparent correlation between OA mass from IEPOX and P_{LWC} ,



Scheme 2 Addition of weak nucleophiles in the aqueous NH_4^+ – and H^+ -catalyzed ring opening of IEPOX to form low-volatility organic compounds.

ammonium or acidity may be weak whenever water or catalyst concentrations are not limited; thus, in regions with high AS loading and RH, there should be a higher correlation with sulfate. This result would suggest that the OA formation process from IEPOX is insensitive to changes in the degree of neutralization of the particles in many AS-dominated areas, including the Southeast USA. The typical $[\text{NH}_4^+]$ is several orders of magnitude larger than $[\text{H}^+]$ in atmospheric particles, making it very likely to activate the IEPOX ring-opening reaction. Current models consider only H^+ and HSO_4^- activity (McNeill et al., 2012, Pye et al., 2013), likely owing to the lack of experimental data describing the NH_4^+ -initiated reaction with IEPOX, for example, kinetic coefficients like $k_{\text{NH}_4^+}$. Future experimental and modeling studies should consider the NH_4^+ activity of a particle, in addition to the H^+ and HSO_4^- activity, for a more-accurate representation of OA formation from IEPOX.

An updated reaction mechanism appears in Scheme 2, in which NH_4^+ and H^+ are shown to donate a proton to the epoxide oxygen, followed by nucleophilic addition to form oxygenated hydrocarbons, ammonia (or amines), and organosulfates. The ability of NH_4^+ to catalyze a nucleophilic addition reaction is not unprecedented, as NH_4^+ can protonate aldehydes to facilitate nucleophilic addition (Nozriere et al., 2009), and the high ring strain of an epoxide should provide an even greater thermodynamic motivation for the reaction. Indeed, due to the strain of epoxides, ring opening is chemically facile and may be promoted by a wide range of aqueous chemical species and conditions common in atmospheric aerosols, in addition to H^+ and NH_4^+ . For example, Lewis acids such as iron (Fe^{3+}) (Iranpoor and Salehi, 1994) and copper (Cu^{2+}) (Muzart and Riahi, 1992) ions may be even stronger catalysts. Furthermore, the reaction may proceed with no added catalyst, for example, in the presence

of amines (Azizi and Saidi, 2005) or even hot water (60 °C) (Wang et al., 2008). The nucleophiles for these reactions may be water, amines or ammonia, thiols, sulfate ions, nitrate ion, halide ions, carboxylic acids, and alcohols (Iranpoor et al., 1996, Jacobsen et al., 1997, Clayden et al., 2001). Because of the diversity in the composition of atmospheric aerosols and fog/cloud droplets (Graedel and Weschler, 1981), the distribution of IEPOX-derived products in nature may be more complex and varied than currently believed.

Supplementary material related to this article is available online at <http://www.atmos-chem-phys.net/14/3497/2014/acp-14-3497-2014-supplement.pdf>.

Acknowledgements. This research was supported by the National Science Foundation (NSF) grants AGS-1057183 and AGS-1240604. TBN acknowledges funding from the NSF Postdoctoral Research Fellowship program, award AGS-1331360, and from the Foster and Coco Stanback Postdoctoral Fellowship. We are grateful for research support provided by the Brian Stoltz Group at Caltech for the syntheses of the β -IEPOX isomers, with special acknowledgement to Dr. Nathan Bennett. We thank Dr. Nathan Dalleska, director of the Caltech Environmental Analysis Center (EAC), for his assistance with the UPLC/ESI-ToFMS analyses.

Edited by: V. F. McNeill

References

- Aiken, A. C., Decarlo, P. F., Kröll, J. H., Worsnop, D. R., Huffman, J. A., Docherty, K. S., Ulbrich, I. M., Mohr, C., Kimmel, J. R., Sueper, D., Sun, Y., Zhang, Q., Trimborn, A., Northway, M., Ziemann, P. J., Canagaratna, M. R., Onasch, T. B., Alfarra, M. R., Prevot, A. S. H., Dommen, J., Duplissy, J., Metzger, A., Baltensperger, U., and Jimenez, J. L.: O/C and OM/OC ratios of primary, secondary, and ambient organic aerosols with high-resolution time-of-flight aerosol mass spectrometry, *Environ. Sci. Technol.*, 42, 4478–4485, 2008.
- Allan, J. D., Delia, A. E., Coe, H., Bower, K. N., Alfarra, M. R., Jimenez, J. L., Middlebrook, A. M., Drewnick, F., Onasch, T. B., and Canagaratna, M. R.: A generalised method for the extraction of chemically resolved mass spectra from aerodyne aerosol mass spectrometer data, *J. Aerosol. Sci.*, 35, 909–922, 2004.
- Azizi, N. and Saidi, M. R.: Highly chemoselective addition of amines to epoxides in water, *Org. Lett.*, 7, 3649–3651, 2005.
- Bates, K. H., Crouse, J. D., St. Clair, J. M., Bennett, N. B., Nguyen, T. B., Seinfeld, J. H., Stoltz, B. M., and Wennberg, P. O.: Gas phase production and loss of isoprene epoxydiols. *J. Phys. Chem. A*, 118, 1237–1246, doi:10.1021/jp4107958, 2014.
- Biskos, G., Paulsen, D., Russell, L. M., Buseck, P. R., and Martin, S. T.: Prompt deliquescence and efflorescence of aerosol nanoparticles, *Atmos. Chem. Phys.*, 6, 4633–4642, 10, <http://www.atmos-chem-phys.net/6/4633/10/5194/acp-6-4633-2006>, 2006.
- Bones, D. L., Henricksen, D. K., Mang, S. A., Gonsior, M., Bateman, A. P., Nguyen, T. B., Cooper, W. J., and Nizkorodov, S. A.: Appearance of strong absorbers and fluorophores in limonene- O_3 secondary organic aerosol due to NH_4^+ -mediated chemical aging over long time scales, *J. Geophys. Res.*, 115, D05203, doi:10.1029/2009jd012864, 2010.
- Budisulistiorini, S. H., Canagaratna, M. R., Croteau, P. L., Marth, W. J., Baumann, K., Edgerton, E. S., Shaw, S. L., Knipping, E. M., Worsnop, D. R., Jayne, J. T., Gold, A., and Surratt, J. D.: Real-time continuous characterization of secondary organic aerosol derived from isoprene epoxydiols in downtown Atlanta, Georgia, using the Aerodyne aerosol chemical speciation monitor, *Environ. Sci. Technol.*, 47, 5686–5694, 2013.
- Carlton, A. G. and Turpin, B. J.: Particle partitioning potential of organic compounds is highest in the Eastern US and driven by anthropogenic water, *Atmos. Chem. Phys.*, 13, 10203–10214, doi:10.5194/acp-13-10203-2013, 2013.
- Cavdar, H., and Saracoglu, N.: Ring opening of epoxides with $NaHSO_4$: Isolation of β -hydroxy sulfate esters and an effective synthesis for trans-diols, *Tetrahedron*, 65, 985–989, 2009.
- Chan, M. N., Surratt, J. D., Claeys, M., Edgerton, E. S., Tanner, R. L., Shaw, S. L., Zheng, M., Knipping, E. M., Eddingsaas, N. C., Wennberg, P. O., and Seinfeld, J. H.: Characterization and quantification of isoprene-derived epoxydiols in ambient aerosol in the southeastern united states, *Environ. Sci. Technol.*, 44, 4590–4596, 2010.
- Clayden, J., Greeves, N., Warren, S., and Wothers, P.: *Organic chemistry*, Oxford University Press, 386 pp., ISBN 978-380-319-850346-850340, 2001.
- Clegg, S. L., Brimblecombe, P., and Wexler, A. S.: Thermodynamic model of the system $H^+ - NH_4^+ - SO_4^{2-} - NO_3^- - H_2O$ at tropospheric temperatures, *J. Phys. Chem. A*, 102, 2137–2154, 1998.
- Cole-Filipiak, N. C., O'Connor, A. E., and Elrod, M. J.: Kinetics of the hydrolysis of atmospherically relevant isoprene-derived hydroxy epoxides, *Environ. Sci. Technol.*, 44, 6718–6723, 2010.
- Crouse, J. D., McKinney, K. A., Kwan, A. J., and Wennberg, P. O.: Measurement of gas-phase hydroperoxides by chemical ionization mass spectrometry, *Anal. Chem.*, 78, 6726–6732, 2006.
- Darer, A. I., Cole-Filipiak, N. C., O'Connor, A. E., and Elrod, M. J.: Formation and stability of atmospherically relevant isoprene-derived organosulfates and organonitrates, *Environ. Sci. Technol.*, 45, 1895–1902, 2011.
- De Haan, D. O., Hawkins, L. N., Kononenko, J. A., Turley, J. J., Corrigan, A. L., Tolbert, M. A., and Jimenez, J. L.: Formation of nitrogen-containing oligomers by methylglyoxal and amines in simulated evaporating cloud droplets, *Environ. Sci. Technol.*, 45, 984–991, 2011.
- Docherty, K. S., Jaoui, M., Corse, E., Jimenez, J. L., Offenberg, J. H., Lewandowski, M., and Kleindienst, T. E.: Collection efficiency of the aerosol mass spectrometer for chamber-generated secondary organic aerosols, *Aerosol Sci. Technol.*, 47, 294–309, 2013.
- Eddingsaas, N. C., VanderVelde, D. G., and Wennberg, P. O.: Kinetics and products of the acid-catalyzed ring-opening of atmospherically relevant butyl epoxy alcohols, *J. Phys. Chem. A*, 114, 8106–8113, 2010.
- EPA: Estimation programs interface for microsoft windows xp v4.0, US EPA, 2008.
- Ervens, B. and Volkamer, R.: Glyoxal processing by aerosol multiphase chemistry: towards a kinetic modeling framework of sec-

- ondary organic aerosol formation in aqueous particles, *Atmos. Chem. Phys.*, 10, 8219–8244, doi:10.5194/acp-10-8219-2010, 2010.
- Froyd, K. D., Murphy, S. M., Murphy, D. M., de Gouw, J. A., Eddingsaas, N. C., and Wennberg, P. O.: Contribution of isoprene-derived organosulfates to free tropospheric aerosol mass, *Proc. Natl. Acad. Sci.*, 107, 21360–21365, doi:10.1073/pnas.1012561107, 2010.
- Graedel, T. E. and Weschler, C. J.: Chemistry within aqueous atmospheric aerosols and raindrops, *Rev. Geophys.*, 19, 505–539, 1981.
- Gregoire, P.: Implications of ambient ammonia on aerosol acidity and reactive nitrogen measurements, MS, Department of Chemistry, University of Toronto, Toronto, Ontario, Canada, 82 pp., 2013.
- Griffith, D. W. T.: Synthetic calibration and quantitative analysis of gas-phase FT-IR spectra, *Appl. Spectrosc.*, 50, 59–70, 1996.
- Hatch, L. E., Creamean, J. M., Ault, A. P., Surratt, J. D., Chan, M. N., Seinfeld, J. H., Edgerton, E. S., Su, Y., and Prather, K. A.: Measurements of isoprene-derived organosulfates in ambient aerosols by aerosol time-of-flight mass spectrometry – Part 2: Temporal variability and formation mechanisms, *Environ. Sci. Technol.*, 45, 8648–8655, 2011.
- Hennigan, C. J., Bergin, M. H., Dibb, J. E., and Weber, R. J.: Enhanced secondary organic aerosol formation due to water uptake by fine particles, *Geophys. Res. Lett.*, 35, L18801, doi:10.1029/2008GL035046, 2008.
- Hennigan, C. J., Bergin, M. H., Russell, A. G., Nenes, A., and Weber, R. J.: Gas/particle partitioning of water-soluble organic aerosol in Atlanta, *Atmos. Chem. Phys.*, 9, 3613–3628, doi:10.5194/acp-9-3613-2009, 2009.
- Hu, D., Qiao, L., Chen, J., Ye, X., Yang, X., Cheng, T., and Fang, W.: Hygroscopicity of inorganic aerosols: Size and relative humidity effects on the growth factor, *Aerosol. Air. Qual. Res.*, 10, 255–264, 2010.
- Ip, H. S. S., Huang, X. H. H., and Yu, J. Z.: Effective Henry's law constants of glyoxal, glyoxylic acid, and glycolic acid, *Geophys. Res. Lett.*, 36, L01802, doi:10.1029/2008gl036212, 2009.
- Iranpoor, N. and Salehi, P.: Highly efficient, regio- and stereoselective alcoholysis of epoxides catalyzed with iron (iii) chloride, *Synthesis*, 1994, 1152–1154, 1994.
- Iranpoor, N., Tarrarian, T., and Movahedi, Z.: $\text{FeCl}_3 \cdot 6\text{H}_2\text{O}$ supported on SiO_2 catalyzed ring opening of epoxides with alcohols, acetic acid, water, chloride, bromide and nitrate ions, *Synthesis*, 1996, 1473–1476, 1996.
- Jacobsen, E. N., Kakiuchi, F., Konsler, R. G., Larrow, J. F., and Tokunaga, M.: Enantioselective catalytic ring opening of epoxides with carboxylic acids, *Tetrahedron Lett.*, 38, 773–776, 1997.
- Kampf, C. J., Waxman, E. M., Slowik, J. G., Dommen, J., Pfaffenberger, L., Praplan, A. P., Prévôt, A. S. H., Baltensperger, U., Hoffmann, T., and Volkamer, R.: Effective Henry's law partitioning and the salting constant of glyoxal in aerosols containing sulfate, *Environ. Sci. Technol.*, 47, 4236–4244, 2013.
- Lee, C.-T. and Hsu, W.-C.: The measurement of liquid water mass associated with collected hygroscopic particles, *J. Aerosol. Sci.*, 31, 189–197, 2000.
- Lin, Y.-H., Zhang, Z., Docherty, K. S., Zhang, H., Budisulistiorini, S. H., Rubitschun, C. L., Shaw, S. L., Knipping, E. M., Edgerton, E. S., Kleindienst, T. E., Gold, A., and Surratt, J. D.: Isoprene epoxydiols as precursors to secondary organic aerosol formation: Acid-catalyzed reactive uptake studies with authentic compounds, *Environ. Sci. Technol.*, 46, 250–258, 2012.
- Lin, Y.-H., Knipping, E. M., Edgerton, E. S., Shaw, S. L., and Surratt, J. D.: Investigating the influences of SO_2 and NH_3 levels on isoprene-derived secondary organic aerosol formation using conditional sampling approaches, *Atmos. Chem. Phys.*, 13, 8457–8470, doi:10.5194/acp-13-8457-2013, 2013.
- Loza, C. L., Chan, A. W. H., Galloway, M. M., Keutsch, F. N., Flagan, R. C., and Seinfeld, J. H.: Characterization of vapor wall loss in laboratory chambers, *Environ. Sci. Technol.*, 44, 5074–5078, 2010.
- Loza, C. L., Chhabra, P. S., Yee, L. D., Craven, J. S., Flagan, R. C., and Seinfeld, J. H.: Chemical aging of m-xylene secondary organic aerosol: laboratory chamber study, *Atmos. Chem. Phys.*, 12, 151–167, doi:10.5194/acp-12-151-2012, 2012.
- Martin, S. T.: Phase transitions of aqueous atmospheric particles, *Chem. Rev.*, 100, 3403–3453, 2000.
- Matthew, B. M., Middlebrook, A. M., and Onasch, T. B.: Collection efficiencies in an Aerodyne aerosol mass spectrometer as a function of particle phase for laboratory generated aerosols, *Aerosol. Sci. Technol.*, 42, 884–898, 2008.
- McNeill, V. F., Woo, J. L., Kim, D. D., Schwier, A. N., Wannel, N. J., Sumner, A. J., and Barakat, J. M.: Aqueous-phase secondary organic aerosol and organosulfate formation in atmospheric aerosols: A modeling study, *Environ. Sci. Technol.*, 46, 8075–8081, 2012.
- Minerath, E. C., Casale, M. T., and Elrod, M. J.: Kinetics feasibility study of alcohol sulfate esterification reactions in tropospheric aerosols, *Environ. Sci. Technol.*, 42, 4410–4415, 2008.
- Minerath, E. C., Schultz, M. P., and Elrod, M. J.: Kinetics of the reactions of isoprene-derived epoxides in model tropospheric aerosol solutions, *Environ. Sci. Technol.*, 43, 8133–8139, 2009.
- Muzart, J. and Riahi, A.: Palladium- and light-enhanced ring-opening of oxiranes by copper chloride, *J. Organomet. Chem.*, 433, 323–336, 1992.
- Nguyen, T. B., Lee, P. B., Updyke, K. M., Bones, D. L., Laskin, J., Laskin, A., and Nizkorodov, S. A.: Formation of nitrogen- and sulfur-containing light-absorbing compounds accelerated by evaporation of water from secondary organic aerosols, *J. Geophys. Res.*, 117, D01207, doi:10.1029/202011JD016944, 2012.
- Nguyen, T. B., Laskin, A., Laskin, J., Nizkorodov, S. A., Brown carbon formation from ketoaldehydes of biogenic monoterpenes, *Faraday Discuss.*, 165, 473–494, 2013.
- Noziere, B., Dziedzic, P., and Cordova, A.: Products and kinetics of the liquid-phase reaction of glyoxal catalyzed by ammonium ions (NH_4^+), *J. Phys. Chem. A*, 113, 231–237, 2009.
- Paulot, F., Crouse, J. D., Kjaergaard, H. G., Kroll, J. H., Seinfeld, J. H., and Wennberg, P. O.: Isoprene photooxidation: new insights into the production of acids and organic nitrates, *Atmos. Chem. Phys.*, 9, 1479–1501, doi:10.5194/acp-9-1479-2009, 2009a.
- Paulot, F., Crouse, J. D., Kjaergaard, H. G., Kurten, A., St. Clair, J. M., Seinfeld, J. H., and Wennberg, P. O.: Unexpected epoxide formation in the gas-phase photooxidation of isoprene, *Science*, 325, 730–733, 2009b.
- Pye, H. O. T., Pinder, R. W., Piletic, I. R., Xie, Y., Capps, S. L., Lin, Y.-H., Surratt, J. D., Zhang, Z., Gold, A., Luecken, D. J., Hutzell, W. T., Jaoui, M., Offenberg, J. H., Kleindienst, T. E., Lewandowski, M., and Edney, E. O.: Epoxide pathways improve

- model predictions of isoprene markers and reveal key role of acidity in aerosol formation. *Environ. Sci. Technol.*, **47**, 11056–11064, 2013.
- Reuss, J.: Chemical and biological relationships relevant to the effect of acid rainfall on the soil-plant system, *Water Air Soil Pollut.*, **7**, 461–478, 1977.
- Robinson, N. H., Hamilton, J. F., Allan, J. D., Langford, B., Oram, D. E., Chen, Q., Docherty, K., Farmer, D. K., Jimenez, J. L., Ward, M. W., Hewitt, C. N., Barley, M. H., Jenkin, M. E., Rickard, A. R., Martin, S. T., McFiggans, G., and Coe, H.: Evidence for a significant proportion of Secondary Organic Aerosol from isoprene above a maritime tropical forest, *Atmos. Chem. Phys.*, **11**, 1039–1050, doi:10.5194/acp-11-1039-2011, 2011.
- Rothman, L. S., Gordon, I. E., Barbe, A., Benner, D. C., Bernath, P. F., Birk, M., Boudon, V., Brown, L. R., Campargue, A., and Champion, J.-P.: The HITRAN 2008 molecular spectroscopic database, *J. Quant. Spectrosc. Rad. Transf.*, **110**, 533–572, 2009.
- Sareen, N., Schwier, A. N., Shapiro, E. L., Mitroo, D., and McNeill, V. F.: Secondary organic material formed by methylglyoxal in aqueous aerosol mimics, *Atmos. Chem. Phys.*, **10**, 997–1016, doi:10.5194/acp-10-997-2010, 2010.
- Seinfeld, J. H. and Pandis, S. N.: *Atmospheric chemistry and physics: From air pollution to climate change*, Wiley, 2006.
- Solomons, T. W. G. and Fryhle, C. B.: *Organic chemistry*, 8 ed., John Wiley & Sons, Inc., Hoboken, NJ, 1255 pp., 2004.
- St. Clair, J. M., McCabe, D. C., Crouse, J. D., Steiner, U., and Wennberg, P. O.: Chemical ionization tandem mass spectrometer for the in situ measurement of methyl hydrogen peroxide, *Rev. Sci. Instrum.*, **81**, 094102–094106, 2010.
- Surratt, J., Chan, A. W. H., Eddingsaas, N. C., Chan, M., Loza, C. L., Kwan, A. J., Hersey, S. P., Flagan, R. C., Wennberg, P. O., and Seinfeld, J. H.: Reactive intermediates revealed in secondary organic aerosol formation from isoprene, *Proc. Natl. Acad. Sci.*, **107**, 6640–6645, 2010.
- Surratt, J. D., Lewandowski, M., Offenberg, J. H., Jaoui, M., Kleindienst, T. E., Edney, E. O., and Seinfeld, J. H.: Effect of acidity on secondary organic aerosol formation from isoprene, *Environ. Sci. Technol.*, **41**, 5363–5369, 2007.
- Wang, Z., Cui, Y.-T., Xu, Z.-B., and Qu, J.: Hot water-promoted ring-opening of epoxides and aziridines by water and other nucleophiles, *J. Org. Chem.*, **73**, 2270–2274, 2008.
- Xiong, J. Q., Zhong, M., Fang, C., Chen, L. C., and Lippmann, M.: Influence of organic films on the hygroscopicity of ultrafine sulfuric acid aerosol, *Environ. Sci. Technol.*, **32**, 3536–3541, 1998.
- Yu, G., Bayer, A. R., Galloway, M. M., Korshavn, K. J., Fry, C. G., and Keutsch, F. N.: Glyoxal in aqueous ammonium sulfate solutions: Products, kinetics and hydration effects, *Environ. Sci. Technol.*, **45**, 6336–6342, 2011.
- Zhang, Z., Lin, Y. H., Zhang, H., Surratt, J. D., Ball, L. M., and Gold, A.: Technical note: Synthesis of isoprene atmospheric oxidation products: Isomeric epoxydiols and the rearrangement products cis- and trans-3-methyl-3,4-dihydroxytetrahydrofuran, *Atmos. Chem. Phys.*, **12**, 8529–8535, doi:10.5194/acp-12-8529-2012, 2012.
- Zuend, A., Marcolli, C., Luo, B. P., and Peter, T.: A thermodynamic model of mixed organic-inorganic aerosols to predict activity coefficients, *Atmos. Chem. Phys.*, **8**, 4559–4593, doi:10.5194/acp-8-4559-2008, 2008.
- Zuend, A., Marcolli, C., Booth, A. M., Lienhard, D. M., Soonsin, V., Krieger, U. K., Topping, D. O., McFiggans, G., Peter, T., and Seinfeld, J. H.: New and extended parameterization of the thermodynamic model aiomfac: Calculation of activity coefficients for organic-inorganic mixtures containing carboxyl, hydroxyl, carbonyl, ether, ester, alkenyl, alkyl, and aromatic functional groups, *Atmos. Chem. Phys.*, **11**, 9155–9206, doi:10.5194/acp-11-9155-2011, 2011.

Appendix 3

Secondary organic aerosol yields of 12-carbon alkanes



Secondary organic aerosol yields of 12-carbon alkanes

C. L. Loza¹, J. S. Craven¹, L. D. Yee², M. M. Coggon¹, R. H. Schwantes², M. Shiraiwa^{1,3}, X. Zhang², K. A. Schilling¹, N. L. Ng⁴, M. R. Canagaratna⁵, P. J. Ziemann⁶, R. C. Flagan^{1,2}, and J. H. Seinfeld^{1,2}

¹Division of Chemistry and Chemical Engineering, California Institute of Technology, Pasadena, CA, USA

²Division of Engineering and Applied Science, California Institute of Technology, Pasadena, CA, USA

³Multiphase Chemistry Department, Max Planck Institute for Chemistry, Mainz, Germany

⁴School of Chemical and Biomolecular Engineering and School of Earth and Atmospheric Sciences, Georgia Institute of Technology, Atlanta, GA, USA

⁵Aerodyne Research, Inc., Billerica, MA, USA

⁶Air Pollution Research Center, Department of Environmental Sciences, and Environmental Toxicology Graduate Program, University of California, Riverside, CA, USA

Correspondence to: J. H. Seinfeld (seinfeld@caltech.edu)

Received: 29 June 2013 – Published in Atmos. Chem. Phys. Discuss.: 7 August 2013

Revised: 13 December 2013 – Accepted: 23 December 2013 – Published: 7 February 2014

Abstract. Secondary organic aerosol (SOA) yields were measured for cyclododecane, hexylcyclohexane, *n*-dodecane, and 2-methylundecane under high-NO_x conditions, in which alkyl proxy radicals (RO₂) react primarily with NO, and under low-NO_x conditions, in which RO₂ reacts primarily with HO₂. Experiments were run until 95–100 % of the initial alkane had reacted. Particle wall loss was evaluated as two limiting cases using a new approach that requires only suspended particle number-size distribution data and accounts for size-dependent particle wall losses and condensation. SOA yield differed by a factor of 2 between the two limiting cases, but the same trends among alkane precursors were observed for both limiting cases. Vapor-phase wall losses were addressed through a modeling study and increased SOA yield uncertainty by approximately 30 %. SOA yields were highest from cyclododecane under both NO_x conditions. SOA yields ranged from 3.3 % (dodecane, low-NO_x conditions) to 160 % (cyclododecane, high-NO_x conditions). Under high-NO_x conditions, SOA yields increased from 2-methylundecane < dodecane ~ hexylcyclohexane < cyclododecane, consistent with previous studies. Under low-NO_x conditions, SOA yields increased from 2-methylundecane ~ dodecane < hexylcyclohexane < cyclododecane. The presence of cyclization in the parent alkane structure increased SOA yields, whereas the presence of branch points decreased SOA yields due to increased vapor-phase fragmentation.

Vapor-phase fragmentation was found to be more prevalent under high-NO_x conditions than under low-NO_x conditions. For different initial mixing ratios of the same alkane and same NO_x conditions, SOA yield did not correlate with SOA mass throughout SOA growth, suggesting kinetically limited SOA growth for these systems.

1 Introduction

Alkanes are emitted from combustion sources and can comprise up to 90 % of anthropogenic emissions in urban areas (Rogge et al., 1993; Fraser et al., 1997; Schauer et al., 1999, 2002) and 67.5 %, 56.8 %, and 82.8 % of the mass of diesel fuel, liquid gasoline, and non-tailpipe gasoline sources, respectively (Gentner et al., 2012). Upon atmospheric oxidation by OH and NO₃ radicals, alkanes form lower-volatility products that can condense as secondary organic aerosol (SOA). Ambient lifetimes against reaction with OH range, for example, from 0.5 days for *n*-hexadecane to 1.4 days for *n*-octane (Atkinson and Arey, 2003; Seinfeld and Pandis, 2006), allowing for the transport of alkanes from urban to rural areas.

SOA formation under high-NO_x conditions, in which alkyl proxy radicals (RO₂) react primarily with NO, has received much attention. Lim and Ziemann (2005, 2009a, c) developed a mechanism for linear, branched, and cyclic alkane

oxidation that includes the formation of multi-generation oxidation products. SOA yields, defined as mass of SOA formed divided by mass of alkane reacted, have been measured in the laboratory for C₇–C₂₅ alkanes with linear, branched, and cyclic structures (Lim and Ziemann, 2005, 2009b; Presto et al., 2010; Tkacik et al., 2012). In these studies, SOA yields are reported after 50–85 % of the alkane had reacted and may not represent the maximum possible yield. Generally, SOA yield was found to increase with increasing carbon number or the presence of a cyclic structure and decrease with branching of the carbon chain.

SOA formation under low-NO_x conditions, in which RO₂ reacts primarily with HO₂, has received less attention. Yee et al. (2012, 2013) developed an oxidation mechanism for *n*-dodecane and extended it to cyclic and branched compounds. Yee et al. (2012, 2013) also identified multiple generations of alkane oxidation products, and Craven et al. (2012) used positive matrix factorization to demonstrate continuous evolution of the chemical composition of SOA generated during 36 h of low-NO_x dodecane photooxidation. SOA yields for select linear and cyclic structures have been measured, and the same trends for carbon number and presence of a cyclic structure were observed under low-NO_x conditions as under high-NO_x conditions (Lambe et al., 2012).

Here we report SOA yields from 12-carbon alkanes with linear, cyclic, and branched structures under both high- and low-NO_x conditions. In each experiment, 95–100 % of the alkane, a greater percentage than those achieved in previous chamber studies, was oxidized to study the contribution of multi-generation products to SOA yield. Additionally, multiple alkane mixing ratios were used to assess the effect of precursor mixing ratio on gas-particle partitioning.

2 Materials and methods

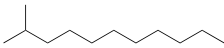
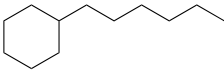
2.1 Experimental setup

Low-NO_x experiments were conducted in the Caltech dual 28 m³ Teflon chambers, details of which are given elsewhere (Cocker et al., 2001; Keywood et al., 2004). High-NO_x experiments were conducted in the Caltech dual 24 m³ Teflon chambers, located in a new facility that replaced the 28 m³ chamber facility. Most components of the old facility, including instrumentation, were moved to the new laboratory, which provides precise temperature control of the chambers (± 1 °C) and flushing at a rate approximately 3 times faster than that in the 28 m³ chamber facility. The difference in chamber volume is not expected to influence the experiment outcomes. Before each experiment, the chambers were flushed with dried, purified air for > 24 h, until the particle number concentration was < 50 cm⁻³ and the volume concentration was < 0.1 $\mu\text{m}^3\text{cm}^{-3}$. First, hydrogen peroxide (H₂O₂, 50 % wt., Sigma Aldrich) was added to the chamber by flowing purified air over a measured volume of H₂O₂

in a glass bulb maintained at 30–35 °C. Volumes of 70 and 280 μL were used for high-NO_x and low-NO_x, experiments, respectively. Next, seed particles were injected by atomizing a 0.015 M aqueous ammonium sulfate solution. *n*-Dodecane (Sigma Aldrich, 99+ % purity), 2-methylundecane (TCI, America, > 98 % purity), or hexylcyclohexane (TCI, America, > 98 % purity) was introduced into the chamber by evaporating a known alkane liquid volume with 5 L min⁻¹ of purified air. Cyclododecane (TCI, America, > 99 % purity) was introduced into the chamber by evaporating a known cyclododecane mass with 5 L min⁻¹ of purified air. During each injection, the glass bulb containing the liquid or solid alkane was heated slightly to facilitate evaporation. For high-NO_x experiments, approximately 100 ppbv NO was then added to the chamber from a 510 ppmv NO in N₂ cylinder (Air Liquide). The chamber contents were allowed to mix for 1 h before beginning irradiation with 350 nm-centered UV broadband lamps (40 W Sylvania 350BL). Different light intensities were used for low- and high-NO_x experiments corresponding to $j_{\text{NO}_2} \sim 4 \times 10^{-3} \text{ s}^{-1}$ and $\sim 6 \times 10^{-3} \text{ s}^{-1}$, respectively. To maintain high-NO_x conditions, 20 sccm of 510 ppmv NO was continuously injected into the chamber during the irradiation period. This additional ~ 21 L of N₂ has a negligible effect on chamber volume. The chamber contents were irradiated for 18 h and 30–36 h for high- and low-NO_x experiments, respectively, to achieve similar OH exposures in all experiments.

A suite of instruments was used to study the evolution of the gas and particle phases. Alkane mixing ratios were measured using a gas chromatograph with flame ionization detector (GC/FID, Agilent 6890N), equipped with a HP-5 column (15 m \times 0.53 mm ID \times 1.5 μm thickness, Agilent). Samples for injection into the GC/FID were taken by drawing 1.3 L of chamber air at a flow rate of 0.13 L min⁻³ through a glass tube packed with Tenax TA resin. The glass tube was subsequently desorbed for 10 min in the inlet of the GC/FID at 260 and 275 °C for low- and high-NO_x experiments, respectively, onto the column, held at 30 °C. After 15 min, the oven temperature was ramped at 10 °C min⁻¹ to 280 °C and held at that temperature for 5 min. The mass response of the detector was calibrated for each alkane using Tenax tubes spiked with standard solutions and analyzed using the same method as the sample tubes. Relative humidity (RH), temperature, NO, NO_x, and O₃ were continuously monitored. Alkane oxidation products were detected using a custom-modified Varian 1200 triple-quadrupole chemical ionization mass spectrometer (CIMS). Details of operation can be found elsewhere (Crounse et al., 2006; Paulot et al., 2009; Yee et al., 2012, 2013). The CIMS was operated in negative mode in which CF₃O⁻ is used as the reagent ion. CF₃O⁻ clusters with the analyte, R, forming ions [R · CF₃O]⁻ at mass-to-charge ratio (m/z) [M+85]⁻, where M is the nominal weight of R. For acidic species, the transfer product forms ions [R · F]⁻ at m/z [M+19]⁻. Some analytes can be seen in both the cluster and

Table 1. SOA precursor and aerosol properties.

Alkane	Structure	$k_{\text{OH}} \times 10^{12\text{a}}$ ($\text{cm}^3 \text{s}^{-1}$)	High- NO_x SOA density ^b (g cm^{-3})	Low- NO_x SOA density ^b (g cm^{-3})
<i>n</i> -Dodecane (Dod)		13.9 ^c	1.28 ± 0.01	1.12 ± 0.03
2-Methylundecane (Mud)		13.1 ± 0.7	1.28 ± 0.01	1.12 ± 0.03
Hexylcyclohexane (Hch)		17.4 ± 0.6	1.29 ± 0.01	1.17 ± 0.03
Cyclododecane (Cdd)		14.7 ± 0.4	1.23 ± 0.02	1.28 ± 0.03

^a Measured from a relative rate experiment at 297 K using dodecane as the reference compound. One standard deviation is given for each rate constant.

^b SOA densities were calculated during nucleation experiments by comparing the diameter of the SOA measured by the DMA to that measured by the AMS. One standard deviation is given for each value.

^c Jordan et al. (2008) for 298 K.

transfer product forms. The signal at each m/z represents the sum of signals from all isomers contributing to that m/z .

Aerosol size distribution and number concentration were measured continuously using a custom-built scanning mobility particle sizer consisting of a differential mobility analyzer (DMA, TSI, 3081) coupled to a condensation particle counter (CPC, TSI, 3010), henceforth referred to as the DMA. The DMA was operated in a closed-loop configuration with a recirculating sheath and excess flow of 2.67 L min^{-1} and a 5.4 : 1 ratio of sheath to aerosol flow rates. The column voltage was scanned either from 10 to 1000 V over 100 s or 15 to 9850 V over 45 s.

Real-time particle mass spectra were collected continuously by an Aerodyne high-resolution time-of-flight aerosol mass spectrometer (AMS, DeCarlo et al., 2006; Canagaratna et al., 2007). The AMS switched between the higher resolution, lower sensitivity “W-mode” and the lower resolution, higher sensitivity “V-mode”. AMS data were processed using the ToF-AMS Unit Resolution Analysis Toolkit, “SQUIRREL” (<http://cires.colorado.edu/jimenez-group/ToFAMSResources/ToFSoftware/index.html>), in Igor Pro Version 6.31 (Wavemetrics, Lake Oswego, OR). “V-mode” data were analyzed using fragmentation table to separate sulfate, ammonium, and organic spectra and to time-trace specific mass-to-charge ratios (Allan et al., 2004). “V-mode” and “W-mode” data were analyzed using the high-resolution spectra toolbox known as PIKA (Peak Integration by Key Analysis) to determine the chemical formulas contributing to distinct m/z ratios (DeCarlo et al., 2006). Organic ions up to m/z 305 were used to calculate elemental ratios. Craven et al. (2012) proposed formulas for organic ions with $m/z > 100$ observed for low- NO_x dodecane photooxidation SOA based on hypothesized fragmentation of products formed in the dodecane photooxidation mechanism (Yee

et al., 2012). Similar analysis was applied to identify organic ions with $m/z > 100$ for SOA from all 4 alkanes investigated here under both low- and high- NO_x conditions. Organic ions CO^+ and C_2H_4^+ were not fit in “V-mode” due to the large interference from the N_2^+ peak, and their signals were estimated from those of particle-phase CO_2^+ and C_2H_3^+ , respectively, using correlations determined from “W-mode” data, which has better resolution of the CO^+ , N_2^+ , and C_2H_4^+ peaks. The ratio of particle-phase CO^+ to CO_2^+ varied by experiment between 0.45 and 3.5, and a specific ratio was used for each experiment (see Table S1). The ratio of C_2H_4^+ to C_2H_3^+ was found to be 0.47 for SOA from dodecane, 2-methylundecane, and hexylcyclohexane and 0.40 for SOA from cyclododecane under both NO_x conditions. Additionally, the intensities of H_2O^+ , OH^+ , and O^+ were calculated from particle-phase CO_2^+ (Aiken et al., 2008). AMS data reported in this work were collected using “V-mode” and averaged over 1 h or 30 min intervals for low- or high- NO_x experiments, respectively.

Experimental OH concentrations were calculated from the measured alkane mixing ratio, the alkane concentration decay rate, estimated from the alkane mixing ratio fit to a differentiable function (typically, a 1- or 2-term exponential function), and the alkane + OH reaction rate constant. A literature OH reaction rate constant was available only for dodecane; rate constants for the other three alkanes were estimated from a relative rate experiment in which 10 ppbv of each alkane was oxidized simultaneously under low- NO_x conditions (Table 1). The measured rate constant for hexylcyclohexane is in good agreement with that calculated from structure–activity relationships (Kwok and Atkinson, 1995), $17.6 \times 10^{-12} \text{ cm}^3 \text{ molec}^{-1} \text{ s}^{-1}$, and the measured rate constants for 2-methylundecane and cyclododecane are lower than those calculated from structure–activity relationships,

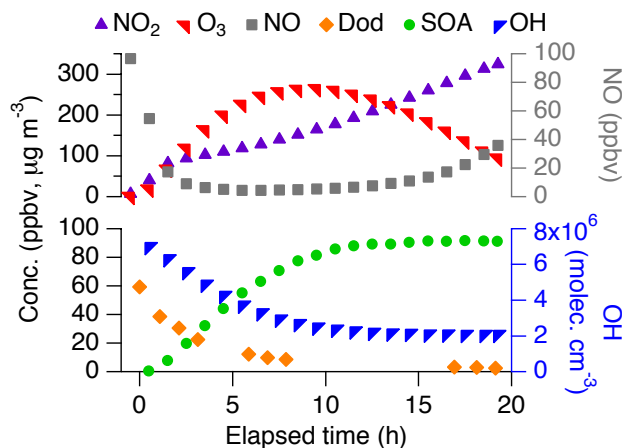


Fig. 1. Temporal trends of gas-phase species and SOA mass concentration during a typical high- NO_x experiment. On the left axis, SOA mass concentration (lower limit) is reported in $\mu\text{g m}^{-3}$, and dodecane, O_3 , and NO_2 mixing ratios are reported in ppbv. NO and OH concentrations are given on the right axis. NO_2 , O_3 , NO , SOA mass, and OH concentrations are hourly averaged. Data are shown for the 57 ppbv dodecane experiment, DH2 (see Table 2). OH concentration was calculated from the dodecane decay.

13.9×10^{-12} and $17.0 \times 10^{-12} \text{ cm}^3 \text{ molec}^{-1} \text{ s}^{-1}$, respectively. To calculate OH exposure, an interpolated OH concentration with a time resolution of 2–3 min is calculated from a fit to experimental data, as described previously, the alkane mixing ratio decay rate, and the alkane + OH reaction rate constant. The interpolated OH concentration is multiplied by the time between data points and summed to each time point to obtain OH exposure.

Photolysis of H_2O_2 under low- NO_x conditions produced a constant OH radical concentration of $(1\text{--}3) \times 10^6 \text{ molec cm}^{-3}$. Under high- NO_x conditions, OH radicals also were produced throughout the entire irradiation period, 18 h, with initial concentrations of $(0.7\text{--}3) \times 10^7 \text{ molec cm}^{-3}$ that decreased steadily to $(1\text{--}5) \times 10^6 \text{ molec cm}^{-3}$ after 18 h. In addition, reaction of HO_2 radicals with NO produced NO_2 , which photolyzed to produce O_3 . O_3 mixing ratios peaked at 200–600 ppbv approximately halfway through the experiment and then decreased as NO was continuously injected into the chamber. The variance in O_3 mixing ratio is not expected to affect SOA formation mechanisms and is discussed below. Typical vapor mixing ratios and SOA growth for a high- NO_x experiment (59 ppbv dodecane) are shown in Fig. 1.

Three oxidants, OH , O_3 , and NO_3 , were produced under high- NO_x conditions. All oxidant concentrations varied during the experiment due to the continuous addition of NO . While O_3 is not expected to react with most alkane photooxidation products, it can react with dihydrofurans, which also react with OH and NO_3 . Variation in O_3 mixing ratios amongst the experiments could influence SOA yields by af-

fecting the fate of dihydrofurans. In the present experiments, the ratios of dihydrofuran sinks were determined by comparing the lifetimes for dihydrofuran against reaction with OH , O_3 , and NO_3 at experimental conditions. Jordan et al. (2008) estimated C_{12} dihydrofuran + OH rate constants as approximately $2.4 \times 10^{-13} \text{ cm}^3 \text{ molec}^{-1} \text{ s}^{-1}$. The rate constants for C_{12} dihydrofuran + O_3 and C_{12} dihydrofuran + NO_3 were taken as 3.49×10^{-15} and $1.68 \times 10^{-10} \text{ cm}^3 \text{ molec}^{-1} \text{ s}^{-1}$, respectively, as measured for 4,5-dihydro-2-methylfuran by Martin et al. (2002). O_3 mixing ratios were measured directly, OH concentrations were calculated from the alkane mixing ratio decay, and NO_3 concentrations were estimated from a photochemical model. The lifetime for dihydrofuran against reaction with O_3 was calculated to be at least an order of magnitude less than that against reaction with OH for all experimental conditions, and the variation in O_3 mixing ratios amongst the experiments had little effect on the fate of dihydrofurans. For the highest estimated NO_3 concentration ($1 \times 10^7 \text{ molec cm}^{-3}$), the lifetime for dihydrofuran against reaction with NO_3 was comparable to that against reaction with O_3 , and at the lowest estimated concentration, the lifetime for dihydrofuran against reaction with NO_3 was an order of magnitude larger than that against reaction with OH . In an urban area such as Mexico City with maximum OH , O_3 , and NO_3 (daytime) concentrations of 4.6×10^6 , $(0.74\text{--}2.0) \times 10^{12}$, and $2.4 \times 10^7 \text{ molec cm}^{-3}$, respectively (Molina et al., 2010; Stephens et al., 2008; Volkamer et al., 2010), the estimated lifetimes for dihydrofuran against reaction with these compounds are 15 min, 2.4–6.4 min, and 4.1 min, respectively. The conditions in the present experiments produce atmospherically relevant ratios of dihydrofuran sinks. Additionally, NO_3 was not a significant sink of either the parent alkane or RO_2 radicals even at the largest estimated NO_3 mixing ratio.

2.2 SOA yield calculations

Particles deposited to the chamber walls are accounted for when calculating the mass concentration of organic aerosol formed. Particle wall-loss corrections were made using the two limiting assumptions of gas-particle partitioning (Weitkamp et al., 2007; Hildebrandt et al., 2009; Loza et al., 2012). In one limit, no suspended vapors are assumed to condense on deposited particles. This limit is termed the lower limit because it represents the smallest possible SOA mass formed during growth. In the other limit, deposited particles are assumed to interact with suspended vapors to the same extent as suspended particles. This limit is termed the upper limit because it represents the largest possible SOA mass formed during growth. A new approach to calculate both upper and lower limit wall loss solely from suspended particle number-size distribution data is described in Appendix A. This approach is an extension of the Aerosol Parameterization Estimation model (Pierce et al., 2008) to calculate both limits to particle wall-loss corrections. Total particle volume

concentration was calculated from the wall-loss corrected number-size distributions. To obtain SOA mass concentration, the seed particle volume concentration was subtracted from the total particle volume concentration, and the resulting organic particle volume concentration was multiplied by the SOA density, calculated from DMA and AMS data from a separate experiment (see Table 1).

SOA yield, Y , was calculated for both upper and lower limit SOA mass concentrations, ΔM_o ($\mu\text{g m}^{-3}$), using

$$Y = \frac{\Delta M_o}{\Delta\text{HC}}, \quad (1)$$

where ΔHC ($\mu\text{g m}^{-3}$) is the mass concentration of alkane reacted.

In addition to particle-phase wall losses, vapor-phase wall losses of 12-carbon alcohols and ketones have been observed in laboratory chambers (Matsunaga and Ziemann, 2010). If vapors condense on chamber walls instead of on particles, then SOA yields will be underestimated. Vapor wall losses were not taken into account for the yields presented here; the effect of vapor wall losses on SOA yields is discussed in Appendix B.

3 Results and discussion

For most SOA precursors, a larger initial hydrocarbon mixing ratio results in a larger source of semivolatile oxidation products, assuming that reactions occur at the same temperature and oxidizing conditions and that the vapor-phase product distributions do not vary over the range of initial hydrocarbon mixing ratios considered. The presence of more condensable products facilitates partitioning of semivolatile product species to the particle phase, leading to increased yields relative to lower mixing ratio experiments. Oxidant exposure also affects SOA yield. SOA yield increases with increasing oxidant exposure as the hydrocarbon reacts forming multiple generations of semivolatile products; however, with ever-increasing oxidation, fragmentation reactions will begin to dominate over functionalization reactions, producing volatile products that do not condense or evaporate from the condensed phase and decreasing SOA yield.

3.1 High- NO_x SOA yield measurements

Conditions for high- NO_x experiments are given in Table 2. The reported ΔM_o and yield correspond to approximately 18 h of irradiation and an OH exposure of $(6\text{--}12) \times 10^7$ molec cm^{-3} h. By this point, at least 95 % of the initial hydrocarbon had reacted. SOA growth occurred continuously as the alkane reacted. Figure 2a shows the SOA yield after approximately 18 h of irradiation as a function of hydrocarbon concentration reacted. The top and bottom of each line correspond to the upper and lower limits to the particle wall-loss correction, respectively. Experiments were

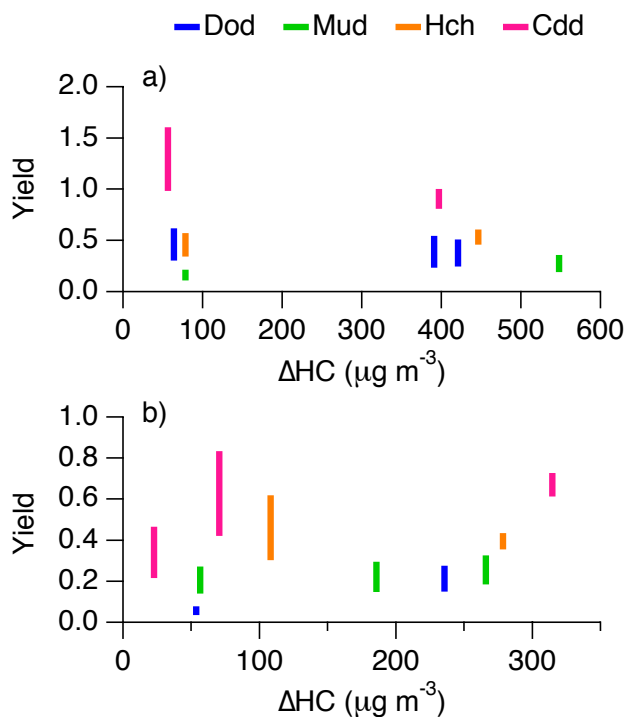


Fig. 2. SOA yield at 95–100 % of initial hydrocarbon reacted under (a) high- and (b) low- NO_x conditions. Each line shows the range between the lower limit (deposited particles do not undergo gas-particle partitioning) and upper limit (gas-particle partitioning to deposited particles is the same as that to suspended particles) SOA yields for an experiment.

run with approximately 10 ppbv ($100 \mu\text{g m}^{-3}$) or 60–80 ppbv ($400\text{--}550 \mu\text{g m}^{-3}$) initial alkane mixing ratio. In both initial alkane concentration regimes, cyclododecane produced the largest yields, while the smallest yields were observed for 2-methylundecane. Dodecane and hexylcyclohexane yields were similar. These results are consistent with the relationship between alkane structure and SOA yield observed by Lim and Ziemann (2009b) and Tkacik et al. (2012). When comparing the yields for each compound between the two initial hydrocarbon concentration regimes, no clear patterns emerge. For 2-methylundecane and hexylcyclohexane, the yield increases as initial alkane concentration increases. For dodecane and cyclododecane, the yield decreases as initial alkane concentration increases. This behavior will be discussed further in Sect. 3.4.

For cyclododecane and hexylcyclohexane, a large difference between upper and lower limit yields is observed in Fig. 2 for experiments with $\Delta\text{HC} < 100 \mu\text{g m}^{-3}$. These experiments had approximately 10 ppbv initial alkane. For experiments shown in Fig. 2 with $\Delta\text{HC} > 100 \mu\text{g m}^{-3}$, those with 60–80 ppbv initial alkane, SOA growth began soon after the onset of irradiation, increasing the suspended particle number-size distribution peak diameter to 250–350 nm.

Table 2. High-NO_x experimental details.

Expt. ^a	Alkane	Seed vol. ($\mu\text{m}^3 \text{cm}^{-3}$)	NO _o ^b (ppbv)	NO _{2,o} ^b (ppbv)	HC _o (ppbv)	ΔHC (ppbv)	ΔM_o^c ($\mu\text{g m}^{-3}$)	Yield ^c (frac.)
MH1	Mud	31.7 ± 9.5	94.1 ± 0.5	6.6 ± 0.2	11.6 ± 0.4	11.6	8.5–17	0.11–0.21
MH2	Mud	41.6 ± 12.5	97.7 ± 0.5	5.8 ± 0.2	79.6 ± 2.5	79.1	100–200	0.19–0.38
DH1	Dod	30.9 ± 9.3	93.8 ± 0.5	6.3 ± 0.2	9.7 ± 0.3	9.2	19–40	0.30–0.62
DH2	Dod	26.1 ± 7.8	96.8 ± 0.5	7.1 ± 0.2	59.2 ± 1.9	56.8	91–210	0.23–0.54
DH3	Dod	30.4 ± 9.1	96.5 ± 0.5	6.1 ± 0.2	63.6 ± 2.0	61.2	100–210	0.22–0.51
HH1	Hch	34.1 ± 10.2	101 ± 0.5	2.6 ± 0.2	11.5 ± 0.4	11.5	27–45	0.34–0.57
HH2	Hch	40.0 ± 12.0	95.4 ± 0.5	2.9 ± 0.2	65.0 ± 2.1	64.9	210–270	0.46–0.61
CH1	Cdd	38.7 ± 11.6	95.6 ± 0.5	6.8 ± 0.2	8.5 ± 0.3	8.5	56–91	0.98–1.6
CH2	Cdd	37.7 ± 11.3	93.4 ± 0.5	7.9 ± 0.2	61.0 ± 2.0	58.6	320–400	0.80–1.0

^a The first letter of each experiment identifier refers to the alkane, and the second letter refers to high- (H) or low- (L) NO_x conditions.

^b One standard deviation is reported, as measured by the instrument manufacturer.

^c The range of values listed correspond to the two limiting assumptions for suspended vapor-deposited particle gas-particle partitioning. The smaller and larger values correspond to the upper and lower partitioning limits, respectively.

During the experiments with ~ 10 ppbv initial alkane, SOA growth did not begin immediately, and the suspended particle number-size distribution peak diameter remained below 200 nm for most of the experiment. The temporal trend of suspended particle number-size distribution peak diameter for the high-NO_x cyclododecane experiments is shown in Fig. S1. In the Caltech chambers, particle wall-loss rate constants are lowest for 200–300 nm particles (Fig. S1, right panel). Typical seed particle number-size distribution peak diameters are 40–60 nm. Because particle growth is slower in ~ 10 ppbv initial alkane experiments and particles remain at a smaller diameter for longer times, more particles are lost to the wall before and during SOA growth in ~ 10 ppbv initial alkane experiments than in those with 60–80 ppbv initial alkane, owing to the size-dependence of particle wall loss. Therefore, a large difference between lower and upper limit yields is observed for the ~ 10 ppbv initial alkane experiments. The difference between upper and lower limit yields for dodecane and 2-methylundecane is similar for all ΔHC . Less overall SOA growth is observed for dodecane and 2-methylundecane; as a result, less difference is observed between the lower and upper limit yields.

SOA yields from cyclododecane were close to or greater than 1 depending on the wall-loss correction method used. SOA yields can be > 1 if most of the functionalized oxidation products generated from a non-functionalized parent hydrocarbon condense to form SOA. SOA yields > 1 have been observed previously from longifolene photooxidation under high-NO_x conditions (Ng et al., 2007a). To determine if the SOA mass produced violated mass conservation, an estimation of maximum potential SOA mass concentration was calculated assuming that all oxidation products formed from the reacted cyclododecane condensed. For the estimation, the average SOA molecular weight was calculated from the oxygen-to-carbon (O : C), hydrogen-to-carbon (H : C), and nitrogen-to-carbon (N : C) ratios measured by the AMS, as-

suming that condensed species retain 12 carbon atoms. Note that ions NO⁺ and NO₂⁺ are included in these calculations and will be discussed further in Sect. 3.4. To calculate the maximum potential SOA mass concentration, the molar concentration of cyclododecane reacted is multiplied by the average SOA molecular weight. This SOA mass concentration is then compared to the observed SOA mass concentration. For experiment CH1 (cyclododecane), the maximum potential SOA formed was $84 \mu\text{g m}^{-3}$, which is greater than the lower wall-loss limit ΔM_o but less than the upper wall-loss limit ΔM_o . For experiment CH2 (cyclododecane), the maximum potential SOA formed was $519 \mu\text{g m}^{-3}$, which is greater than both the lower and upper bound limit ΔM_o . All observed cyclododecane yields except for the upper wall-loss limit yield for CH1 do not violate mass conservation. It is likely that uncertainties in deposited particle growth rates calculated in the upper limit wall-loss correction method (see Appendix A) cause the upper limit yield for CH1 to be overestimated.

Previous studies exist of SOA yields under high-NO_x conditions for dodecane, 2-methylundecane, and cyclododecane. Lim and Ziemann (2009b) measured SOA yields for all three compounds with initial alkane mixing ratios of approximately 1 ppmv, of which 76–83 % was oxidized at the point at which yields were calculated. In the present work, yields were calculated for lower initial alkane mixing ratios with a larger fraction of the initial alkane reacted. Because higher initial alkane mixing ratio and lower extent of alkane reacted have opposite effects on SOA yield that are difficult to decouple, comparison of absolute measurements between Lim and Ziemann (2009b) and the present work are not instructive. Presto et al. (2010) reported SOA yields for dodecane oxidation for 19.1 and 57.8 ppbv initial alkane, and Tkacik et al. (2012) reported SOA yields from 2-methylundecane oxidation for a low alkane mixing ratio (initial alkane mixing ratios were not specified). Both studies parameterized yields using the volatility basis set (VBS)

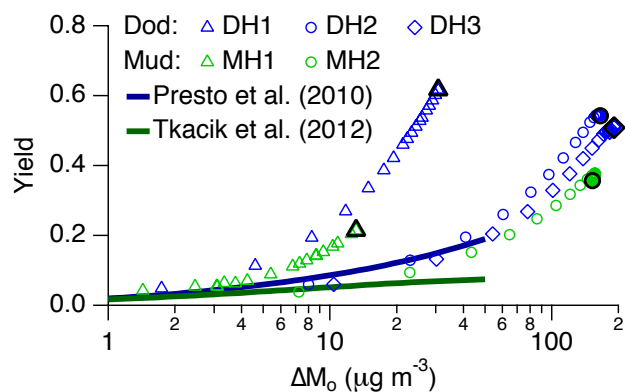


Fig. 3. Comparison of SOA yields as a function of organic aerosol mass concentration, ΔM_0 , observed in the present study with those reported in previous studies. For the present study, final yields (after 95–100 % alkane reacted) are denoted by the black markers.

for $\Delta M_0 < 50 \mu\text{g m}^{-3}$. A comparison of the present work to these studies is shown in Fig. 3. Both Presto et al. (2010) and Tkacik et al. (2012) report the upper limit to particle wall losses. For comparison to these previous studies, the upper limit to particle wall losses and a unit SOA density were used to calculate yields for experiments DH1, DH2, DH3, MH1, and MH2 shown in Fig. 3. The dodecane VBS parameterization presented by Presto et al. (2010) matches the higher final ΔM_0 dodecane experiments, DH2 and DH3, for $\Delta M_0 < 50 \mu\text{g m}^{-3}$; however, it does not match the lower final ΔM_0 dodecane experiment, DH1. This discrepancy can be attributed to different OH exposure. Presto et al. (2010) achieved an OH exposure of approximately $1.2 \times 10^7 \text{ molec cm}^{-3} \text{ h}$ and did not react all of the parent alkane, whereas OH exposure in the present experiments was approximately $7 \times 10^7 \text{ molec cm}^{-3} \text{ h}$ and at $> 95\%$ of the parent alkane reacted. Similar results are observed when comparing 2-methylundecane yields from Tkacik et al. (2012) with those in the present study. The OH exposure achieved in Tkacik et al. (2012), $6 \times 10^6 \text{ molec cm}^{-3} \text{ h}$, was also lower than that achieved in the present work.

3.2 Low- NO_x SOA yield measurements

Conditions for low- NO_x experiments are presented in Table 3. ΔM_0 and SOA yield measurements are reported after 30–36 h irradiation, corresponding to OH exposures of $(6\text{--}12) \times 10^7 \text{ molec cm}^{-3} \text{ h}$, for which at least 95 % of the initial alkane reacted. Figure 2b shows the SOA yield after 30–36 h irradiation, and, as for the high- NO_x data, the top and bottom of each line correspond to the upper and lower limits to the particle wall-loss correction, respectively. The highest yields are observed for cyclododecane, followed by hexylcyclohexane, with the yields for dodecane and 2-methylundecane being similar. The ordering of hexylcyclohexane, dodecane, and 2-methylundecane yields is different

from that observed under high- NO_x conditions and will be discussed further in Sect. 3.4. As with the high- NO_x yields, there are no compound-specific trends for SOA yield with initial alkane concentration.

SOA yields under low- NO_x conditions have not been reported previously for the compounds studied here. SOA yields under low- NO_x conditions have been reported for *n*-decane and *n*-pentadecane in a Potential Aerosol Mass flow reactor (Lambe et al., 2012). Lambe et al. (2012) reported maximum yields of 0.39 and 0.69 at OH exposures of 1.4×10^8 and $9.7 \times 10^7 \text{ molec cm}^{-3} \text{ h}$ and SOA concentrations of 231 and $100 \mu\text{g m}^{-3}$ for decane and pentadecane, respectively. The dodecane SOA yield is expected to lie between those for longer and shorter chain alkanes; however, the dodecane SOA yields measured in the present study (Table 3) are less than that measured for $231 \mu\text{g m}^{-3}$ decane, a much larger initial concentration than those used in the present experiments, by Lambe et al. (2012) at similar OH exposure. Lambe et al. (2012) note that the maximum SOA yield for pentadecane at $16 \mu\text{g m}^{-3}$ is 0.21, which is in much better agreement with the dodecane SOA concentrations and SOA yields in the present study.

3.3 SOA growth parameterization

In Fig. 3, it is interesting to note that different SOA yields are observed from the same alkane and ΔM_0 for different initial alkane mixing ratios (e.g., at $\Delta M_0 = 10 \mu\text{g m}^{-3}$, the yield from 9 ppbv dodecane, DH1, is 0.27, whereas the yield from 57–61 ppbv dodecane, DH2 and DH3, is 0.06). This trend is observed for all four compounds under both high- and low- NO_x conditions and suggests that there may be an alternative to parameterizing yields for these alkanes in terms of ΔM_0 (i.e., assuming quasi-equilibrium growth).

Shiraiwa et al. (2013) predicted that the behavior of the particle size distribution during low- NO_x dodecane photooxidation is consistent with kinetically limited, rather than quasi-equilibrium, growth. Other ambient and laboratory studies also suggest that SOA growth can be kinetically limited (Riipinen et al., 2011; Perraud et al., 2012). For kinetically limited SOA growth, SOA yield should be a function of total particle surface area; however, for the same alkane and NO_x conditions and a given particle surface area, different SOA yields were observed, similar to the results presented in Fig. 3. Instead, SOA yields were parameterized by number of semivolatile organic compound (SVOC)-particle collisions. Total SVOC concentration was simulated for the case of dodecane low- NO_x photooxidation using a kinetic multi-layer model of gas-particle interactions (KM-GAP) (Shiraiwa et al., 2012; Shiraiwa and Seinfeld, 2012; Shiraiwa et al., 2013). KM-GAP explicitly resolves mass transport and chemical reactions in the gas and particle phases. The cumulative number of SVOC-particle collisions per unit chamber volume, C_{sum} , was calculated from the SVOC concentration and total particle surface area. Details of these calculations

Table 3. Low-NO_x experimental details.

Expt. ^a	Alkane	Seed vol. ($\mu\text{m}^3 \text{cm}^{-3}$)	HC _o (ppbv)	ΔHC (ppbv)	ΔM_o^b ($\mu\text{g m}^{-3}$)	Yield ^b (frac.)
ML1	Mud	21.8 ± 6.5	8.5 ± 0.3	8.4	7.9–15	0.14–0.27
ML2 ^c	Mud	16.7 ± 5.0	28.9 ± 0.9	28.1	28–58	0.15–0.31
ML3	Mud	15.9 ± 4.8	40.2 ± 1.3	38.1	49–86	0.19–0.33
DL1	Dod	16.7 ± 5.0	8.2 ± 0.3	7.9	1.8–4.2	0.033–0.078
DL2 ^c	Dod	12.1 ± 3.6	34.0 ± 1.1	33.6	35–65	0.15–0.28
HL1 ^c	Hch	11.2 ± 3.4	15.6 ± 0.5	15.5	33–70	0.30–0.65
HL2	Hch	20.0 ± 6.0	41.3 ± 1.3	40.8	99–120	0.35–0.44
CL1	Cdd	18.9 ± 5.7	3.5 ± 0.1	3.4	4.9–11	0.22–0.46
CL2 ^c	Cdd	15.3 ± 4.6	10.4 ± 0.3	10.3	30–62	0.42–0.86
CL3	Cdd	21.5 ± 6.5	46.6 ± 1.5	45.1	200–230	0.61–0.73

^a The first letter of each experiment identifier refers to the alkane, and the second letter refers to high- (H) or low- (L) NO_x conditions.

^b The range of values listed corresponds to the two limiting assumptions for suspended vapor-deposited particle gas-particle partitioning. The smaller and larger values correspond to the upper and lower partitioning limits, respectively.

^c Due to chamber volume limitations, these experiments were run in two parts. The initial conditions for the two separate experiments are listed Table S2.

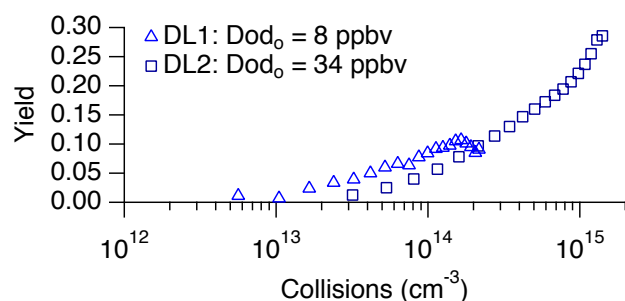


Fig. 4. SOA yield (upper limit) as a function of estimated cumulative SVOC-particle collisions per unit chamber volume for low-NO_x dodecane photooxidation experiments.

are given in Appendix C. Figure 4 shows yield as a function of C_{sum} for the dodecane low-NO_x photooxidation system. Calculations were made with a time resolution of 3 min, but hourly averaged data are displayed. The SOA yields from both experiments trend similarly with C_{sum} . This result indicates that analysis of chamber experiments for any SOA system with kinetic-flux modeling is instructive and provides an alternative to parameterizing SOA yields as a function of ΔM_o .

3.4 Aerosol chemical composition

Organonitrates have been identified previously as products from alkane high-NO_x photooxidation and are expected to be present in the particle phase (Lim and Ziemann, 2005). The AMS can detect organic nitrates as NO⁺ and NO₂⁺, but inorganic nitrates also contribute signal to these ions (Farmer et al., 2010). During the high-NO_x experiments, NO⁺ and NO₂⁺ trend with organic growth measured by the AMS. Dur-

ing this time, nitric acid is also formed from reaction of NO₂ with OH and can partition to particles and interact with the ammonium sulfate seed. The ratio of NO⁺ : NO₂⁺ observed during photooxidation experiments is higher than that from AMS ionization efficiency calibrations, in which ammonium nitrate is atomized into the AMS, indicating that the NO⁺ and NO₂⁺ signals are not likely from inorganic nitrates. Because there is evidence that the signals for NO⁺ and NO₂⁺ likely come from organonitrates in the present experiments, these ions are included when calculating the total organic mass from AMS data. According to a proposed decomposition pathway for organonitrates (Francisco and Krylowksi, 2005; Farmer et al., 2010), the oxygens in NO⁺ and NO₂⁺ are not bound directly to a carbon atom. Therefore, the ion signals at NO⁺ and NO₂⁺ were not included in elemental ratios used to calculate average carbon oxidation state.

Average carbon oxidation state, $\overline{\text{OS}}_C$ (Kroll et al., 2011) was calculated from AMS measurements for comparison of the alkane systems. SOA $\overline{\text{OS}}_C$ from each parent alkane showed similar trends with respect to initial alkane mixing ratio, NO_x conditions, and OH exposure; therefore, data only for cyclododecane are shown in Fig. 5. Under both high- and low-NO_x conditions, SOA formed from a lower initial cyclododecane mixing ratio was characterized by a higher $\overline{\text{OS}}_C$. This trend has been observed in other systems (Shilling et al., 2009) and is expected because a higher initial alkane mixing ratio increases the mixing ratios of semivolatile products, which have lower $\overline{\text{OS}}_C$ than low volatility products, in both the gas and particle phases. Under low-NO_x conditions, SOA $\overline{\text{OS}}_C$ decreases for OH exposures of 0– 2×10^7 molec cm^{-3} h and then gradually increases with increasing OH exposure. Other studies have reported similar trends for O : C formed under low-NO_x conditions (Lambe et al., 2012; Loza et al., 2012). This trend is attributed to

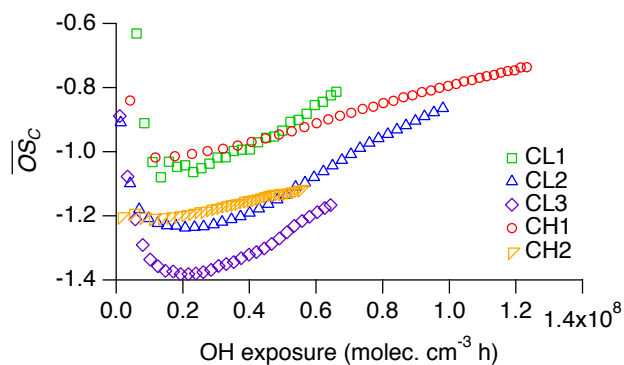


Fig. 5. SOA average carbon oxidation state as a function of OH exposure for high- and low- NO_x cyclododecane photooxidation.

initial condensation of a small amount of low-volatility oxidation products followed by condensation of semivolatile products as the SOA mass increases, and then condensation of more low-volatility products as gas-phase oxidation progresses. Under low- NO_x conditions, over 95 % of the aerosol mass measured by the AMS in the present experiments comes from ions with chemical formulae of C_xH_y^+ , $\text{C}_x\text{H}_y\text{O}^+$, and $\text{C}_x\text{H}_y\text{O}_2^+$. Note that for both NO_x conditions, the ions O^+ , HO^+ and H_2O^+ are included in the mass fraction of $\text{C}_x\text{H}_y\text{O}_2^+$ ions because these concentrations of these ions are calculated from that of CO_2^+ . Initially, the contributions of ions with formula C_xH_y^+ are approximately equal to the sum of those with formulae $\text{C}_x\text{H}_y\text{O}^+$ and $\text{C}_x\text{H}_y\text{O}_2^+$, but as OH exposure increases to 2×10^7 molec cm^{-3} h, the contributions from ions with formula C_xH_y^+ begin to dominate, presumably as more semivolatile species condense. At OH exposures above 2×10^7 molec cm^{-3} h, contributions from ions with formulae $\text{C}_x\text{H}_y\text{O}^+$ and $\text{C}_x\text{H}_y\text{O}_2^+$ increase and those with formula C_xH_y^+ decrease but still comprise a majority of the organic mass. For low- NO_x alkane photooxidation, it has been suggested that peroxyhemiacetal formation triggers initial SOA growth (Yee et al., 2012, 2013; Shiraiwa et al., 2013). The hydroperoxides thought to contribute to initial peroxyhemiacetal formation, such as the carbonyl hydroperoxide, have multiple functional groups, which could explain the initial, higher $\overline{\text{OS}}_C$ values. As the particles grow, other, less functionalized oxidation products can also condense, decreasing $\overline{\text{OS}}_C$. As oxidation continued, multiple generations of gas-phase oxidation products, such as hydroxy carbonyl hydroperoxides and dicarbonyl hydroperoxides, were observed in dodecane photooxidation and proposed for cyclododecane photooxidation and also could partition to particles, increasing $\overline{\text{OS}}_C$. Although the proposed SOA products have multiple oxygen moieties, much of the carbon chain is not functionalized, and C_xH_y^+ fragments are expected to dominate the mass spectrum.

Under high- NO_x conditions, an initial decrease in $\overline{\text{OS}}_C$ was not prominent, and the increase in $\overline{\text{OS}}_C$ as OH expo-

sure increased was less when compared to that under low- NO_x conditions. When comparing high- and low- NO_x experiments with similar initial cyclododecane mixing ratio (CL2 with CH1 or CL3 with CH2), SOA formed under high- NO_x conditions has a higher $\overline{\text{OS}}_C$ during SOA growth but similar $\overline{\text{OS}}_C$ after all cyclododecane reacted. These trends indicate that less OH exposure is required to form low-volatility products under high- NO_x conditions than under low- NO_x conditions. A similar trend was observed by Presto et al. (2009), who used a thermodenuder to measure the volatility of heptadecane SOA formed under high- and low- NO_x conditions. The estimated vapor pressures of many of the condensable species produced under high- and low- NO_x dodecane photooxidation are similar (Jordan et al., 2008; Yee et al., 2012), but the experimental conditions control the rate at which these compounds are formed.

Alkane oxidation by OH generates RO_2 , which can react with NO, HO_2 , or another RO_2 . RO_2 can also react with NO_2 , but the peroxy nitrates formed quickly decompose back to RO_2 and NO_2 ; this pathway will not be considered here. In the present experiments, RO_2 reacted primarily with HO_2 under low- NO_x conditions and with NO under high- NO_x conditions. NO mixing ratio was measured directly and varied from 2–100 ppbv, and HO_2 concentration was estimated from a photochemical model as approximately 1×10^{10} cm^{-3} (Yee et al., 2012). Using RO_2 reaction rate constants from the Master Chemical Mechanism 3.2 (<http://mcm.leeds.ac.uk/MCM>; Jenkin et al., 2003; Saunders et al., 2003), the lifetimes of RO_2 reaction with NO and HO_2 are estimated as 0.04–2 and 4 s, respectively. Shorter RO_2 lifetimes under high- NO_x conditions will allow low-volatility products to form at lower OH exposures.

3.5 Effect of gas-phase fragmentation reactions on SOA yield

For a number of SOA systems, SOA yields are higher under low- NO_x conditions than under high- NO_x conditions (e.g., Song et al., 2005; Ng et al., 2007a; Eddingsaas et al., 2012). A likely explanation is that alkoxy radicals (RO) produced from the reaction of alkyl peroxy radicals (RO_2) and NO undergo fragmentation to form higher volatility species, whereas hydroperoxides produced from the reaction of RO_2 and HO_2 do not. With less fragmentation under low- NO_x conditions, the carbon chain is preserved, resulting in higher yields when compared with those observed for high- NO_x conditions. For linear alkanes with > 6 carbons, isomerization of RO is favored over fragmentation reactions or reaction with O_2 , preserving the carbon chain and producing compounds of lower volatility than fragmentation products (Lim and Ziemann, 2009a). As a result, yields under low- and high- NO_x conditions for these larger alkanes are similar, as shown in Fig. 2.

Additional trends between alkane structure, bulk SOA chemical composition, and SOA yield can be observed from

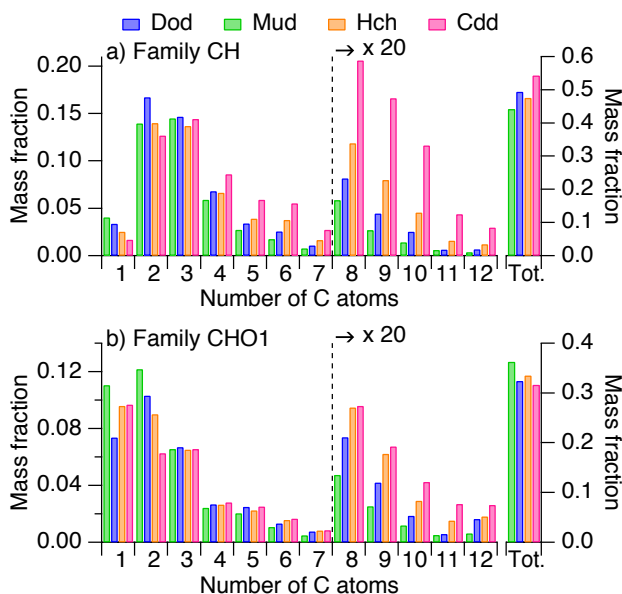


Fig. 6. Contribution of ions detected in the AMS to the bulk organic mass concentration for high- NO_x alkane photooxidation. Ions are grouped into families according to the ion atomic composition and displayed as a function of carbon atoms in the ion. Tot. is the sum over all carbon atom numbers for each family. The data represent a 30 min average of the SOA formed after 95–100 % of the initial alkane had reacted. The data presented are from experiments DH2, MH2, HH2, and CH2.

the AMS mass spectra. Ions can be grouped into “families” according to their elemental composition. The mass spectra are dominated by ions in family CH, ions with formula C_xH_y^+ , and family CHO1, ions with formula $\text{C}_x\text{H}_y\text{O}^+$. Figures 6 and 7 show the contribution of ions in each family as a function of the number of carbon atoms in each ion and the total family contribution for a 30 min averaged sample obtained after 95–100 % of the initial alkane mixing ratio reacted. Only data from experiments with higher alkane mixing ratio (> 50 ppbv and > 25 ppbv for high- and low- NO_x , respectively) are shown; similar trends were observed in experiments with lower initial alkane mixing ratios. In the present study, an increase in yield is characterized by larger mass fractions of ions containing nine or more carbon atoms for both families CH and CHO1. Pearson’s correlation coefficients for each carbon number are given in Tables S4 and S5 for family CH and family CHO1, respectively. Under high- NO_x conditions, the total mass fractions of family CH ions for cyclododecane and dodecane SOA are higher than those for 2-methylundecane and hexylcyclohexane SOA (Fig. 6a), and the trend is reversed for ions in family CHO1 (Fig. 6b). The same trend is not observed under low- NO_x conditions; although, compounds with a larger mass fraction of family CH ions have smaller mass fractions of family CHO1 ions. These trends provide insight into the significance of gas-

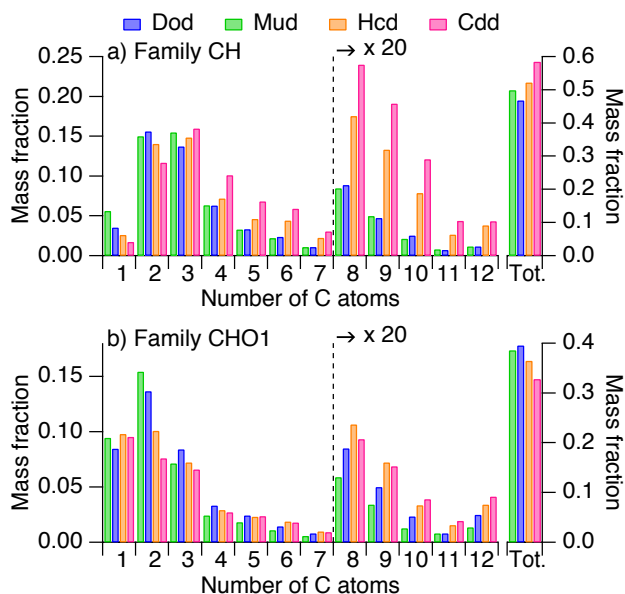


Fig. 7. Contribution of ions detected in the AMS to the bulk organic mass concentration for low- NO_x alkane photooxidation. Ions are grouped into families according to the ion atomic composition and displayed as a function of carbon atoms in the ion. Tot. is the sum over all carbon atom numbers for each family. The data represent a 60 min average of the SOA formed after 95–100 % of the initial alkane had reacted. The data presented are from experiments DL2, ML2, HL2, and CL3.

phase fragmentation reactions under high- and low- NO_x conditions.

During photooxidation, the prevalence of branching in a compound is expected to lead to increased fragmentation, requiring more functionalization to produce condensable species. Greater functionalization increases the oxygen content of product molecules, thus it is reasonable that SOA from branched compounds, 2-methylundecane and hexylcyclohexane, has a higher mass fraction of family CHO1 ions than that from compounds with less branching, cyclododecane and dodecane. These trends are not as apparent under low- NO_x conditions, suggesting that the fragmentation pathway may not be as important under low- NO_x conditions as under high- NO_x conditions. It should be noted that while fragmentation occurs for cyclododecane oxidation products, it results in ring-opening, which preserves the carbon backbone and does not produce a higher-volatility species. Hexylcyclohexane is also a cyclic compound, and an alkoxy radical on the ring α to the branch point may result in ring-opening, which preserves the carbon backbone; thus, fragmentation of hexylcyclohexane will not always result in generation of species with fewer carbon atoms than the parent molecule.

Gas-phase fragmentation products from high- NO_x alkane photooxidation were detected using the CIMS (Table S3). The proposed products have been grouped into “families”

by functionality: carboxylic acid ($C_nH_{2n}O_2$), hydroxy carboxylic acid ($C_nH_{2n}O_3$), carbonyl nitrate ($C_nH_{(2n-1)}NO_4$), or hydroxynitrate ($C_nH_{(2n+1)}NO_4$), where n is the number of carbon atoms in the proposed molecule. For the CIMS ions presented here, the carbon chain is preserved as ionization occurs, whereas heating and ionization in the AMS tends to break the carbon chain, and the ions presented in Figs. 6 and 7 could come from longer chain parent molecules. Figure 8 shows the signal for each product, normalized by ΔHC for a 30 min averaged sample obtained after 95–100 % of the initial alkane mixing ratio reacted. The data are presented assuming that CIMS sensitivity is independent of n for a given family and that sensitivity is the same for all isomers (including cyclic and branched structures) for a given n and family. Mixing ratio calibrations were not performed for all species presented, and trends of ion signal with carbon number are not evaluated. Because the CIMS has unit mass resolution and can detect ions produced as transfer ($m/z = [M+19]^-$) and cluster ($m/z = [M+85]^-$) products, the signals in Fig. 8b could come from an acid or a hydroperoxide. Under high- NO_x conditions, hydroperoxide production is not expected. For almost all products shown in Fig. 8, signals in the cyclododecane experiment are lower than those for the other three alkanes, suggesting that cyclododecane oxidation products undergo little fragmentation, consistent with trends obtained from AMS data. More fragmentation of 2-methylundecane and hexylcyclohexane oxidation products is expected than for those of dodecane; however, the signal from fragmentation products for most families are similar for dodecane, 2-methylundecane, and hexylcyclohexane, suggesting that some fragmentation also occurs during dodecane high- NO_x photooxidation.

Gas-phase fragmentation reactions can also occur under low- NO_x conditions from hydroperoxide photolysis (Yee et al., 2012, 2013). Photolysis of a hydroperoxide forms an alkoxy radical, which can isomerize or decompose depending on the carbon backbone structure. For dodecane, hydroperoxide photolysis is expected to be a minor reaction pathway compared with OH oxidation. The specific case of photolysis of a hydroperoxy group adjacent to a carbonyl produces an aldehyde, which has been shown to react with hydroperoxides to form peroxyhemiacetals. Peroxyhemiacetal formation is proposed to initiate SOA growth in the alkane low- NO_x photooxidation system (Yee et al., 2012, 2013; Shiraiwa et al., 2013). In this case, fragmentation reactions depend more on the relative position of hydroperoxy and carbonyl groups than the structure of the carbon backbone.

When comparing SOA yields between low- and high- NO_x conditions for each compound (Fig. 2), three dominant trends are observed. (1) Under high- NO_x conditions, SOA yields at 95–100 % of the initial hydrocarbon reacted (i.e., the yield at the largest OH exposure for each experiment), for dodecane and cyclododecane are larger for lower initial alkane mixing ratio. (2) For hexylcyclohexane and, more notice-

ably, 2-methylundecane, SOA yields under high- NO_x conditions are higher when the initial alkane mixing ratio is higher. (3) SOA yields for dodecane and cyclododecane are higher under high- NO_x conditions than under low- NO_x conditions. Trends (1) and (2) arise from the role of fragmentation under high- NO_x conditions. At higher initial alkane mixing ratios, semivolatile species can condense preferentially to particles, whereas, for lower initial alkane mixing ratios, semivolatile species remain in the gas phase for further oxidation. For linear or cyclic compounds, further oxidation decreases compound volatility, resulting in additional SOA formation and higher SOA yields. However, for branched compounds, further oxidation results in fragmentation, leading to higher volatility species that do not condense to form additional SOA. At sufficiently high OH exposures, fragmentation will become important for all systems that form SOA (Lambe et al., 2012), but those conditions were not reached in the present experiments. Trend (3) results from differences in the extent of fragmentation under both NO_x conditions. Dodecane and 2-methylundecane have almost identical chemical structures, and one may expect these two compounds to have similar SOA yields. Under low- NO_x conditions, the SOA yields for experiments ML2 and DL2 are 15–31 % (however, the SOA yield observed in ML1 is higher than that observed in DL1), whereas under high- NO_x conditions, higher SOA yields are observed for dodecane than for 2-methylundecane (see Tables 2 and 3). High- NO_x SOA yields are greater than low- NO_x yields for unbranched compounds, but high- and low- NO_x SOA yields are similar for branched compounds as a result of enhanced fragmentation under high- NO_x conditions.

4 Conclusions

In the present study SOA yields have been measured for linear, cyclic, and branched 12-carbon alkanes under high- and low- NO_x conditions in which 95–100 % of the alkane reacted. The highest SOA yields were observed from cyclic alkanes, and the presence of branch points decreased SOA yield, primarily under high- NO_x conditions where vapor-phase fragmentation reactions were more likely to occur. Uncertainties arise in the SOA yield measurements due to particle and vapor wall losses and result in a factor of 2–3 difference between upper and lower limits to SOA yield. Recently, Gentner et al. (2012) assessed SOA formation from diesel and gasoline vehicles and noted that SOA yields for cyclic alkanes with five- and six-membered rings, which comprise 37 % of diesel and 11 % of gasoline, were not well-characterized. This study presents data for one such compound, hexylcyclohexane. Hexylcyclohexane SOA yield was similar to that of dodecane under high- NO_x conditions and greater than dodecane under low- NO_x conditions. Lim and Ziemann (2009b) measured SOA yields for two other branched-cyclic compounds, *n*-butylcyclohexane and

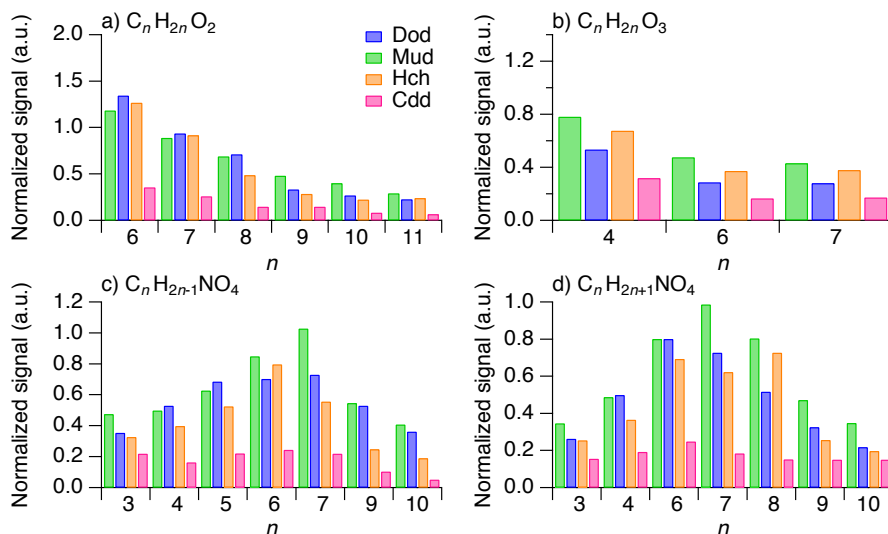


Fig. 8. Comparison of gas-phase fragmentation reaction products from high- NO_x alkane photooxidation measured by the CIMS. The signal is normalized by the mixing ratio of alkane reacted. All molecular formulae are proposed assignments. The data represent a 30 min average of gas-phase species after 95–100 % of the initial alkane had reacted. The ions monitored and their proposed chemical assignments are given in Table S3. The data presented are from experiments DH3, MH2, HH2, and CH2.

n-decylcyclohexane, under high- NO_x conditions but with initial alkane mixing ratios much higher than ambient mixing ratios, approximately 1 ppmv. The authors found that the SOA yield for butylcyclohexane was higher than that for decane, but the yield for decylcyclohexane was less than that for hexadecane. Further characterization of yields from branched-cyclic compounds is necessary to better identify trends and provide more data for models.

Although alkanes are emitted primarily in urban areas under high- NO_x oxidizing conditions, their relatively slow OH reaction rates allow for transport to rural areas with lower NO_x conditions. SOA yields measured in the present study are higher or the same under high- NO_x conditions in comparison to those measured for low- NO_x conditions. Therefore, alkanes exhibit the largest SOA formation potential in urban areas close to their sources.

Appendix A

Particle wall-loss calculations

Pierce et al. (2008) developed the Aerosol Parameter Estimation model to determine the time variance of particle wall-loss rates during an environmental chamber experiment. We have adapted this model to calculate the mass growth rate of suspended particles throughout an experiment. These mass growth rates are then applied to deposited particles to calculate lower and upper limit wall-loss corrections.

The model utilized in the current work is based on the aerosol General Dynamic Equation (Seinfeld and Pandis,

2006):

$$\frac{\partial n_s(D_p, t)}{\partial t} = \left(\frac{\partial n_s(D_p, t)}{\partial t} \right)_{\text{coag}} + \left(\frac{\partial n_s(D_p, t)}{\partial t} \right)_{\text{cond}} + \left(\frac{\partial n_s(D_p, t)}{\partial t} \right)_{\text{wl}}, \quad (\text{A1})$$

where $n_s(D_p, t)$ ($\text{cm}^{-3} \text{cm}^{-1}$) is the suspended particle number-size distribution, D_p (cm) is particle diameter, t (s) is time, and coag, cond, and wl represent the change in suspended particle size-number distribution due to coagulation, condensation, and particle-phase wall loss, respectively.

The change in the suspended particle number-size distribution due to coagulation is described by

$$\left(\frac{\partial n_s(D_p, t)}{\partial t} \right)_{\text{coag}} = \frac{1}{2} \int_0^{D_p} K \left((D_p^3 - q^3)^{\frac{1}{3}}, q \right) n_s \left((D_p^3 - q^3)^{\frac{1}{3}}, t \right) n_s(q, t) dq - n_s(D_p, t) \int_0^\infty K(q, D_p) n_s(q, t) dq, \quad (\text{A2})$$

where $K(D_{p1}, D_{p2})$ ($\text{cm}^3 \text{s}^{-1}$) is the coagulation coefficient for collisions of particles with diameters D_{p1} and D_{p2} (Seinfeld and Pandis, 2006). The DMA measures particle number-size distributions using discrete size bins, and the coagulation coefficient must also be discretized to be applied to these data. The change in suspended particle number-size

distribution due to coagulation becomes

$$\left(\frac{\partial n_s(D_p, t)}{\partial t}\right)_{\text{coag}} = \frac{1}{2} \sum_i \sum_j f_c(D_{pi}, D_{pj}) K(D_{pi}, D_{pj}) N(D_{pi}, t) N(D_{pj}, t) - \sum_i K(D_{pi}, D_{pk}) N(D_{pi}, t) N(D_{pk}, t), \quad (\text{A3})$$

where $f_c(D_{pi}, D_{pj})$ expresses whether the collision of a particle in size bin i with a particle in size bin j produces a particle in size bin k , bounded by diameters D_{pk-} and D_{pk+} :

$$f_c(D_{pi}, D_{pj}) = 1 \quad \text{if} \quad D_{pk-} \leq 2 \left(\left(\frac{D_{pi}}{2} \right)^3 + \left(\frac{D_{pj}}{2} \right)^3 \right)^{\frac{1}{3}} < D_{pk+} \quad (\text{A4})$$

$$f_c(D_{pi}, D_{pj}) = 0 \quad \text{otherwise.} \quad (\text{A5})$$

Particles are not allowed to form outside of the measured size range (Verheggen and Mozurkewich, 2006).

The change in suspended particle number-size distribution due to condensation is described by

$$\left(\frac{\partial n_s(D_p, t)}{\partial t}\right)_{\text{cond}} = -\frac{\partial}{\partial D_p} [I(D_p, t) n(D_p, t)], \quad (\text{A6})$$

where $I(D_p, t)$ (cm s^{-1}) is the rate of change of particle diameter as a result of condensation. Assuming spherical particles with a density ρ_p (g cm^{-3}) that is not a strong function of time,

$$I(D_p, t) = \frac{dD_p}{dt} = \frac{2 \sum J_i}{\pi D_p^2 \rho_p}, \quad (\text{A7})$$

where J_i (g s^{-1}) is the mass flux of species i to the particle. J_i is defined as

$$J_i = \frac{2\pi D_p D_i M_i}{RT} f(Kn, \alpha_i) (p_{\infty, i} - p_{s, i}), \quad (\text{A8})$$

where D_i ($\text{cm}^2 \text{s}^{-1}$) is the diffusion coefficient for species i in air, M_i (g mol^{-1}) is the molecular weight of species i , R ($\text{g cm}^2 \text{s}^{-2} \text{mol}^{-1} \text{K}^{-1}$) is the gas constant, T (K) is temperature, $f(Kn, \alpha_i)$ is a correction factor for non-continuum effects and surface accommodation effects, $p_{\infty, i}$ ($\text{g cm}^{-1} \text{s}^{-2}$) is the vapor pressure of species i in far from the particle, and $p_{s, i}$ ($\text{g cm}^{-1} \text{s}^{-2}$) is the partial pressure of species i at the surface of the particle. Substituting Eqs. (A7) and (A8) into Eq. (A6) yields

$$\left(\frac{\partial n_s(D_p, t)}{\partial t}\right)_{\text{cond}} = \frac{-4}{RT\rho_p} \left[\sum_i D_i M_i f(Kn, \alpha_i) (p_{\infty, i} - p_{s, i}) \right] \frac{\partial}{\partial D_p} \left[\frac{1}{D_p} n_s(D_p, t) \right] \quad (\text{A9})$$

Here we are assuming that ρ_p is constant with respect to D_p at a given time t . If many size bins are used to describe the particle number-size distribution, then ρ_p is likely constant over a small range of D_p , and the magnitude of the error that this assumption produces is reduced. Following Pierce et al. (2008), the unknown parameters in Eq. (A9) can be combined into a single factor, F_c ($\text{cm}^2 \text{s}^{-1}$), defined as

$$F_c = \frac{4}{RT\rho_p} \sum_i D_i M_i f(Kn, \alpha_i) (p_{\infty, i} - p_{s, i}). \quad (\text{A10})$$

Substituting F_c into Eq. (A9) and differentiating gives the final form for the change in suspended number-size distribution due to condensation:

$$\left(\frac{\partial n_s(D_p, t)}{\partial t}\right)_{\text{cond}} = -F_c \left[-\frac{1}{D_p^2} n_s(D_p, t) + \frac{1}{D_p} \frac{\partial n_s(D_p, t)}{\partial D_p} \right] \quad (\text{A11})$$

The model varies F_c to produce a number-size distribution that best fits the observed number distribution.

The change in suspend particle number-size distribution due to particle wall deposition is assumed to follow first-order kinetics with particle size-dependent rate constants, $\beta(D_p)$ (s^{-1}):

$$\left(\frac{\partial n_s(D_p, t)}{\partial t}\right)_{\text{wl}} = -\beta(D_p) n_s(D_p, t). \quad (\text{A12})$$

A theoretical determination of β is described in Crump and Seinfeld (1981) and McMurry and Rader (1985); however, parameters needed to calculate β values are difficult to quantify from theory alone for environmental chambers. Instead, β values can be determined from calibration experiments (Keywood et al., 2004; Ng et al., 2007b; Loza et al., 2012) or can be specified as unknowns in an aerosol general dynamic model (Pierce et al., 2008). The present model employs the former parameterization of β values. β values for AS particles are measured during calibration experiments in which wall deposition is the dominant process affecting the number distribution. Particles containing organics are assumed to behave the same as pure AS particles.

To implement the model, the General Dynamic Equation is solved numerically between each time step for a given experimental data set. First the General Dynamic Equation is discretized into diameter size bins corresponding to those of the measured number-size distribution. Then the model is initialized with a measured number-size distribution at time step t and a guess for the parameter F_c . The model is solved using a Dormand Price pair 4th and 5th order Runge–Kutta method to produce a number-size distribution at time step $t + 1$. The fit of the predicted to the observed number-size distributions at time step $t + 1$ is quantified using various diameter moments. The i th diameter moment is calculated as follows

$$M_i = \int_0^{\infty} D_p^i n_s(D_p) dD_p = \sum_k D_{p,k}^i N_s(D_{p,k}), \quad (\text{A13})$$

where k is the size bin and N_s (cm^{-3}) is the suspended particle number concentration. The best fit of the predicted to the observed number distribution is that which minimizes χ^2 :

$$\chi^2 = \sum_{a=1}^9 \left(\frac{M_{i(a),p} - M_{i(a),o}}{M_{i(a),o}} \right)^2, \quad (\text{A14})$$

where $i(a)$ is the set of diameter moments $[-1, -0.5, 0, 0.5, 1, 1.5, 2, 2.5, 3]$ and moment subscripts p and o are predicted and observed, respectively.

Once values for F_c have been estimated, they can be used in wall-loss corrections to parametrize the growth of particles lost to the chamber walls. The change in the deposited particle number-size distribution also is governed by the the aerosol General Dynamic Equation, but only wall loss and condensation process affect the number-size distribution:

$$\frac{\partial n_w(D_p, t)}{\partial t} = \beta(D_p) n_s(D_p, t) - F_c \omega \left[-\frac{1}{D_p^2} n_w(D_p, t) + \frac{1}{D_p} \frac{\partial n_w(D_p, t)}{\partial D_p} \right], \quad (\text{A15})$$

where $n_w(D_p, t)$ (cm^{-3}) is the deposited particle number-size distribution, and ω is a factor that describes the extent of condensation to deposited particles. ω has a value between 0 (no condensation to deposited particles) and 1 (condensation to deposited particles is the same as that to suspended particles). ω values of 0 and 1 correspond to the lower and upper limits of particle wall-loss corrections, respectively. The aerosol General Dynamic Equations for suspended and deposited particles are solved simultaneously between each time step using the previously determined value for F_c at that time step and a constant value for ω . In the current work, wall-loss corrections were calculated with $\omega = 0$ and $\omega = 1$ to evaluate the limits of condensation behavior to deposited particles.

Appendix B

Effect of vapor wall losses on SOA yields

Condensable species can partition to suspended particles, deposited particles, and the chamber walls. The SOA yields reported here account for the first two processes, but vapor wall losses are not considered. If vapors are lost to the wall instead of forming SOA, then SOA yield will be underestimated. Matsunaga and Ziemann (2010) observed vapor wall losses for alkanes, ketones, and alcohols that are relevant to compounds formed in the present systems. The extent of vapor phase wall losses in both of the Caltech chamber facilities was investigated using experiments in which a known volume of dodecanone, dodecanol, or dodecane was injected into a chamber filled with purified air. The signal for each species was monitored over a period of several

hours. Dodecane wall losses were not significant in either chamber. In the 28 m³ chamber used for low-NO_x experiments, 2-dodecanone wall losses followed first-order kinetics with a rate constant of $k_w = 2.2 \times 10^{-6} \text{ s}^{-1}$ ($\tau = 5.3$ days). In the 24 m³ chamber used for high-NO_x experiments, 2-dodecanol wall losses followed first-order kinetics with a rate constant of $k_w = 1.5 \times 10^{-6} \text{ s}^{-1}$ ($\tau = 7.7$ days). Matsunaga and Ziemann (2010) observed 20 % wall loss of 2-dodecanol in 80 min and 25 % wall loss of 2-dodecanone in 25 min, which equate to first order wall-loss rate constants of $k_w = 3.4 \times 10^{-4} \text{ s}^{-1}$ ($\tau = 49$ min) and $k_w = 9.2 \times 10^{-4} \text{ s}^{-1}$ ($\tau = 18$ min) for 2-dodecanol and 2-dodecanone, respectively; after the initial decrease, the 2-dodecanone mixing ratio remained constant for 400 min, presumably after equilibrium was achieved between the suspended vapors and those sorbed to the walls. Equilibrium was not observed for either compound in the Caltech chambers over a 22 h period, and it was not possible to detect rapid initial losses in the Caltech chambers as a result of the chamber setup and injection procedures. The time required to inject measurable mixing ratios of each compound into the chamber was at least 25 min, and because there is no active mixing in the Caltech chambers, it was necessary to wait an additional 20 min after the end of the injection for the chamber contents to mix. Rapid vapor wall losses occurring during this time period are difficult to distinguish from changes in compound mixing ratio due to injection and mixing. Finally, alkane photooxidation generates a variety of products with multiple functionalization; however, only singly-functionalized compounds were tested for wall loss. Matsunaga and Ziemann (2010) showed that vapor wall loss is a function of compound vapor pressure and structure; therefore, it is difficult to extrapolate wall-loss rates of 2-dodecanol and 2-dodecanone to all compounds formed from alkane photooxidation. In an attempt to quantify vapor wall losses, Shiraiwa et al. (2013) assumed vapor wall losses follow pseudo-first order kinetics and varied vapor wall-loss rate constants of SVOCs generated in KM-GAP simulations of dodecane low-NO_x photooxidation. Using $k_w = 9.6 \times 10^{-6} \text{ s}^{-1}$, the highest value considered, led to a decrease of the SOA mass concentration by approximately 30 %. As a result, SOA yield would increase by 30 %. The combined uncertainties of vapor and particle phase wall-loss result in a factor of 2–3 difference between the upper and lower limits to SOA yields in each system.

Appendix C

SVOC-particle collision calculations

In KM-GAP, the collision flux of SVOC at the particle surface, J_A ($\text{molec cm}^{-3} \text{ s}^{-1}$), is

$$J_A = \frac{1}{4} c_A \bar{c}_A, \quad (\text{C1})$$

where c_A is the SVOC concentration (molec cm^{-3}) and \bar{c}_A is the mean molecular speed of SVOC (cm s^{-1}). J_A can be calculated for discrete time points, i , in an experiment corresponding to particle surface area measurements. The following summation is used to calculate cumulative number of SVOC-particle collisions per unit chamber volume, C_{sum} (cm^{-3}),

$$C_{\text{sum}} = \sum_{i=1}^n J_{A,i} S_i \Delta t_i, \quad (\text{C2})$$

where n is the total number of data points, S_i is the particle surface area ($\text{cm}^2 \text{cm}^{-3}$), and Δt_i is the time between data points i and $i+1$ (s). Here the upper limit wall-loss corrected surface area concentration is used to correspond to the model, which does not simulate particle wall losses.

Supplementary material related to this article is available online at <http://www.atmos-chem-phys.net/14/1423/2014/acp-14-1423-2014-supplement.pdf>.

Acknowledgements. This work was supported by the Office of Science (Biological and Environmental Research), US Department of Energy grant DE-SC 0006626 and National Science Foundation grants AGS-1057183 and ATM-0650061. We thank M. Chan for experimental assistance and A. Matsunaga for information regarding Tenax tube preparation and sampling procedures. C. Loza, L. Yee, and J. Craven were supported by National Science Foundation Graduate Research Fellowships. Manabu Shiraiwa was supported by the Japan Society for the Promotion of Science (JSPS) Postdoctoral Fellowship for Research Abroad.

Edited by: J. B. Burkholder

References

- Aiken, A. C., DeCarlo, P. F., Kroll, J. H., Worsnop, D. R., Huffman, J. A., Docherty, K. S., Ulbrich, I. M., Mohr, C., Kimmel, J. R., Sueper, D., Sun, Y., Zhang, Q., Trimborn, A., Northway, M., Ziemann, P. J., Canagaratna, M. R., Onasch, T. B., Alfarra, M. R., Prévôt, A. S. H., Dommen, J., Duplissy, J., Metzger, A., Baltensperger, U., and Jimenez, J. L.: O/C and OM/OC ratios of primary, secondary, and ambient organic aerosols with high-resolution time-of-flight aerosol mass spectrometry, *Environ. Sci. Technol.*, 42, 4478–4485, doi:10.1021/es703009q, 2008.
- Allan, J. D., Delia, A. E., Coe, H., Bower, K. N., Alfarra, M. R., Jimenez, J. L., Middlebrook, A. M., Drewnick, F., Onasch, T. B., Canagaratna, M. R., Jayne, J. T., and Worsnop, D. R.: A generalised method for the extraction of chemically resolved mass spectra from Aerodyne aerosol mass spectrometer data, *J. Aerosol Sci.*, 35, 909–922, doi:10.1016/j.jaerosci.2004.02.007, 2004.
- Atkinson, R. and Arey, J.: Atmospheric degradation of volatile organic compounds, *Chem. Rev.*, 103, 4605–4638, doi:10.1021/cr0206420, 2003.
- Canagaratna, M., Jayne, J., Jimenez, J., Allan, J., Alfarra, M., Zhang, Q., Onasch, T., Drewnick, F., Coe, H., Middlebrook, A., Delia, A., Williams, L., Trimborn, A., Northway, M., DeCarlo, P., Kolb, C., Davidovits, P., and Worsnop, D.: Chemical and microphysical characterization of ambient aerosols with the Aerodyne aerosol mass spectrometer, *Mass Spectrom. Rev.*, 26, 185–222, doi:10.1002/mas.20115, 2007.
- Cocker, D. R., Flagan, R. C., and Seinfeld, J. H.: State-of-the-art chamber facility for studying atmospheric aerosol chemistry, *Environ. Sci. Technol.*, 35, 2594–2601, doi:10.1021/es0019169, 2001.
- Craven, J. S., Yee, L. D., Ng, N. L., Canagaratna, M. R., Loza, C. L., Schilling, K. A., Yatavelli, R. L. N., Thornton, J. A., Ziemann, P. J., Flagan, R. C., and Seinfeld, J. H.: Analysis of secondary organic aerosol formation and aging using positive matrix factorization of high-resolution aerosol mass spectra: Application to the dodecane low-NO_x system, *Atmos. Chem. Phys.*, 12, 11795–11817, doi:10.5194/acp-12-11795-2012, 2012.
- Crump, J. G. and Seinfeld, J. H.: Turbulent deposition and gravitational sedimentation of an aerosol in a vessel of arbitrary shape, *J. Aerosol Sci.*, 12, 405–415, doi:10.1016/0021-8502(81)90036-7, 1981.
- DeCarlo, P. F., Kimmel, J. R., Trimborn, A., Northway, M. J., Jayne, J. T., Aiken, A. C., Gonin, M., Fuhrer, K., Horvath, T., Docherty, K. S., Worsnop, D. R., and Jimenez, J. L.: Field-deployable, high-resolution, time-of-flight aerosol mass spectrometer, *Anal. Chem.*, 78, 8281–8289, doi:10.1021/ac061249n, 2006.
- Eddingsaas, N. C., Loza, C. L., Yee, L. D., Chan, M., Schilling, K. A., Chhabra, P. S., Seinfeld, J. H., and Wennberg, P. O.: α -pinene photooxidation under controlled chemical conditions-Part 2: SOA yield and composition in low- and high-NO_x environments, *Atmos. Chem. Phys.*, 12, 7413–7427, doi:10.5194/acp-12-7413-2012, 2012.
- Farmer, D. K., Matsunaga, A., Docherty, K. S., Surratt, J. D., Seinfeld, J. H., Ziemann, P. J., and Jimenez, J. L.: Response of an aerosol mass spectrometer to organonitrates and organosulfates and implications for atmospheric chemistry, *P. Natl. Acad. Sci. USA.*, 107, 6670–6675, doi:10.1073/pnas.0912340107, 2010.
- Francisco, M. A. and Krylowksi, J.: Chemistry of organic nitrates: Thermal chemistry of linear and branched organic nitrates, *Ind. Eng. Chem. Res.*, 44, 5439–5446, doi:10.1021/ie049380d, 2005.
- Fraser, M. P., Cass, G. R., Simoneit, B. R. T., and Rasmussen, R. A.: Air quality model evaluation data for organics. 4. C₂-C₃₆ non-aromatic hydrocarbons, *Environ. Sci. Technol.*, 31, 2356–2367, doi:10.1021/es960980g, 1997.
- Gentner, D. R., Isaacman, G., Worton, D. R., Chan, A. W. H., Dallmann, T. R., Davis, L., Liu, S., Day, D. A., Russell, L. M., Wilson, K. R., Weber, R., Guha, A., Harley, R. A., and Goldstein, A. H.: Elucidating secondary organic aerosol from diesel and gasoline vehicles through detailed characterization of organic carbon emissions, *P. Natl. Acad. Sci. USA.*, 109, 18318–18323, doi:10.1073/pnas.1212272109, 2012.
- Hildebrandt, L., Donahue, N. M., and Pandis, S. N.: High formation of secondary organic aerosol from the photo-oxidation of toluene, *Atmos. Chem. Phys.*, 9, 2973–2986, doi:10.5194/acp-9-2973-2009, 2009.
- Jenkin, M. E., Saunders, S. M., Wagner, V., and Pilling, M. J.: Protocol for the development of the Master Chemical Mechanism, MCM v3 (Part B): Tropospheric degradation of aromatic

- volatile organic compounds, *Atmos. Chem. Phys.*, 3, 181–193, doi:10.5194/acp-3-181-2003, 2003.
- Jordan, C. E., Ziemann, P. J., Griffin, R. J., Lim, Y. B., Atkinson, R., and Arey, J.: Modeling SOA formation from OH reactions with C₈–C₁₇ *n*-alkanes, *Atmos. Environ.*, 42, 8015–8026, doi:10.1016/j.atmosenv.2008.06.017, 2008.
- Keywood, M. D., Varutbangkul, V., Bahreini, R., Flagan, R. C., and Seinfeld, J. H.: Secondary organic aerosol formation from the ozonolysis of cycloalkenes and related compounds, *Environ. Sci. Technol.*, 38, 4157–4164, doi:10.1021/es035363o, 2004.
- Kroll, J. H., Donahue, N. M., Jimenez, J. L., Kessler, S. H., Canagaratna, M. R., Wilson, K. R., Altieri, K. E., Mazzoleni, L. R., Wozniak, A. S., Bluhm, H., Mysak, E. R., Smith, J. D., Kolb, C. E., and Worsnop, D. R.: Carbon oxidation state as a metric for describing the chemistry of atmospheric organic aerosol, *Nat. Chem.*, 3, 133–139, doi:10.1038/NCHEM.948, 2011.
- Kwok, E. S. and Atkinson, R.: Estimation of hydroxyl radical reaction rate constants for gas-phase organic compounds using a structure-reactivity relationship: An update, *Atmos. Environ.*, 29, 1685–1695, doi:10.1016/1352-2310(95)00069-B, 1995.
- Lambe, A. T., Onasch, T. B., Croasdale, D. R., Wright, J. P., Martin, A. T., Franklin, J. P., Massoli, P., Kroll, J. H., Canagaratna, M. R., Brune, W. H., Worsnop, D. R., and Davidovits, P.: Transitions from functionalization to fragmentation reactions of laboratory secondary organic aerosol (SOA) generated from the OH oxidation of alkane precursors, *Environ. Sci. Technol.*, 46, 5430–5437, doi:10.1021/es300274t, 2012.
- Lim, Y. B. and Ziemann, P. J.: Products and mechanism of secondary organic aerosol formation from reactions of *n*-alkanes with OH radicals in the presence of NO_x, *Environ. Sci. Technol.*, 39, 9229–9236, doi:10.1021/es051447g, 2005.
- Lim, Y. B. and Ziemann, P. J.: Chemistry of secondary organic aerosol formation from OH radical-initiated reactions of linear, branched, and cyclic alkanes in the presence of NO_x, *Aerosol Sci. Tech.*, 43, 604–619, doi:10.1080/02786820902802567, 2009a.
- Lim, Y. B. and Ziemann, P. J.: Effects of molecular structure on aerosol yields from OH radical-initiated reactions of linear, branched, and cyclic alkanes in the presence of NO_x, *Environ. Sci. Technol.*, 43, 2328–2334, doi:10.1021/es803389s, 2009b.
- Lim, Y. B. and Ziemann, P. J.: Kinetics of the heterogeneous conversion of 1,4-hydroxycarbonyls to cyclic hemiacetals and dihydrofurans on organic aerosol particles, *Phys. Chem. Chem. Phys.*, 11, 8029–8039, doi:10.1039/B904333K, 2009c.
- Loza, C. L., Chhabra, P. S., Yee, L. D., Craven, J. S., Flagan, R. C., and Seinfeld, J. H.: Chemical aging of *m*-xylene secondary organic aerosol: Laboratory chamber study, *Atmos. Chem. Phys.*, 12, 151–167, doi:10.5194/acp-12-151-2012, 2012.
- Martin, P., Tuazon, E. C., Aschmann, S. M., Arey, J., and Atkinson, R.: Formation and atmospheric reactions of 4,5-dihydro-2-methylfuran, *J. Phys. Chem. A*, 106, 11492–11501, doi:10.1021/jp021499h, 2002.
- Matsunaga, A. and Ziemann, P. J.: Gas-wall partitioning of organic compounds in a Teflon film chamber and potential effects on reaction product and aerosol yield measurements, *Aerosol Sci. Tech.*, 44, 881–892, doi:10.1080/02786826.2010.501044, 2010.
- McMurry, P. H. and Rader, D. J.: Aerosol wall losses in electrically charged chambers, *Aerosol Sci. Tech.*, 4, 249–268, doi:10.1080/02786828508959054, 1985.
- Molina, L. T., Madronich, S., Gaffney, J. S., Apel, E., de Foy, B., Fast, J., Ferrare, R., Herndon, S., Jimenez, J. L., Lamb, B., Osornio-Vargas, A. R., Russell, P., Schauer, J. J., Stevens, P. S., Volkamer, R., and Zavala, M.: An overview of the MILAGRO 2006 Campaign: Mexico City emissions and their transport and transformation, *Atmos. Chem. Phys.*, 10, 8697–8760, doi:10.5194/acp-10-8697-2010, 2010.
- Ng, N. L., Chhabra, P. S., Chan, A. W. H., Surratt, J. D., Kroll, J. H., Kwan, A. J., McCabe, D. C., Wennberg, P. O., Sorooshian, A., Murphy, S. M., Dalleska, N. F., Flagan, R. C., and Seinfeld, J. H.: Effect of NO_x level on secondary organic aerosol (SOA) formation from the photooxidation of terpenes, *Atmos. Chem. Phys.*, 7, 5159–5174, doi:10.5194/acp-7-5159-2007, 2007a.
- Ng, N. L., Kroll, J. H., Chan, A. W. H., Chhabra, P. S., Flagan, R. C., and Seinfeld, J. H.: Secondary organic aerosol formation from *m*-xylene, toluene, and benzene, *Atmos. Chem. Phys.*, 7, 3909–3922, doi:10.5194/acp-7-3909-2007, 2007b.
- Perraud, V., Bruns, E. A., Ezell, M. J., Johnson, S. N., Yu, Y., Alexander, M. L., Zelenyuk, A., Imre, D., Chang, W. L., Dabdub, D., Pankow, J. F., and Finlayson-Pitts, B. J.: Nonequilibrium atmospheric secondary organic aerosol formation and growth, *P. Natl. Acad. Sci. USA.*, 109, 2836–2841, doi:10.1073/pnas.1119909109, 2012.
- Pierce, J. R., Engelhart, G. J., Hildebrandt, L., Weitkamp, E. A., Pathak, R. K., Donahue, N. M., Robinson, A. L., Adams, P. J., and Pandis, S. N.: Constraining particle evolution from wall losses, coagulation, and condensation-evaporation in smog-chamber experiments: Optimal estimation based on size distribution measurements, *Aerosol Sci. Tech.*, 42, 1001–1015, doi:10.1080/02786820802389251, 2008.
- Presto, A. A., Miracolo, M. A., Kroll, J. H., Worsnop, D. R., Robinson, A. L., and Donahue, N. M.: Intermediate-volatility organic compounds: A potential source of ambient oxidized organic aerosol, *Environ. Sci. Technol.*, 43, 4744–4749, doi:10.1021/es803219q, 2009.
- Presto, A. A., Miracolo, M. A., Donahue, N. M., and Robinson, A. L.: Secondary organic aerosol formation from high-NO_x photo-oxidation of low volatility precursors: *n*-Alkanes, *Environ. Sci. Technol.*, 44, 2029–2034, doi:10.1021/es903712r, 2010.
- Riipinen, I., Pierce, J. R., Yli-Juuti, T., Nieminen, T., Häkkinen, S., Ehn, M., Junninen, H., Lehtipalo, K., Petäjä, T., Slowik, J., Chang, R., Shantz, N. C., Abbatt, J., Leaitch, W., Kerminen, V. M., Worsnop, D. R., Pandis, S. N., Donahue, N. M., and Kulmala, M.: Organic condensation: A vital link connecting aerosol formation to cloud condensation nuclei (CCN) concentration, *Atmos. Chem. Phys.*, 11, 3865–3878, doi:10.5194/acp-11-3865-2011, 2011.
- Rogge, W. F., Hildemann, L. M., Mazurek, M. A., Cass, G. R., and Simoneit, B. R. T.: Sources of fine organic aerosol. 3. Road dust, tire debris, and organometallic brake lining dust: roads as sources and sinks, *Environ. Sci. Technol.*, 27, 1892–1904, doi:10.1021/es00046a019, 1993.
- Saunders, S. M., Jenkin, M. E., Derwent, R. G., and Pilling, M. J.: Protocol for the development of the Master Chemical Mechanism, MCM v3 (Part A): Tropospheric degradation of non-aromatic volatile organic compounds, *Atmos. Chem. Phys.*, 3, 161–180, doi:10.5194/acp-3-161-2003, 2003.
- Schauer, J. J., Kleeman, M. J., Cass, G. R., and Simoneit, B. R. T.: Measurement of emissions from air pollution

- sources. 2. C₁ through C₃₀ organic compounds from medium duty diesel trucks, *Environ. Sci. Technol.*, 33, 1578–1587, doi:10.1021/es980081n, 1999.
- Schauer, J. J., Kleeman, M. J., Cass, G. R., and Simoneit, B. R. T.: Measurement of emissions from air pollution sources. 5. C₁–C₃₂ organic compounds from gasoline-powered motor vehicles, *Environ. Sci. Technol.*, 36, 1169–1180, doi:10.1021/es0108077, 2002.
- Seinfeld, J. H. and Pandis, S. N.: *Atmospheric Chemistry and Physics*, John Wiley and Sons, Inc., Hoboken, N.J., 2 edn., 2006.
- Shilling, J. E., Chen, Q., King, S. M., Rosenoern, T., Kroll, J. H., Worsnop, D. R., DeCarlo, P. F., Aiken, A. C., Sueper, D., Jimenez, J. L., and Martin, S. T.: Loading-dependent elemental composition of α -pinene SOA particles, *Atmos. Chem. Phys.*, 9, 771–782, doi:10.5194/acp-9-771-2009, 2009.
- Shiraiwa, M. and Seinfeld, J. H.: Equilibration timescale of atmospheric secondary organic aerosol partitioning, *Geophys. Res. Lett.*, 39, L24801, doi:10.1029/2012GL054008, 2012.
- Shiraiwa, M., Pfrang, C., Koop, T., and Pöschl, U.: Kinetic multi-layer model of gas-particle interactions in aerosols and clouds (KM-GAP): Linking condensation, evaporation and chemical reactions of organics, oxidants and water, *Atmos. Chem. Phys.*, 12, 2777–2794, doi:10.5194/acp-12-2777-2012, 2012.
- Shiraiwa, M., Yee, L. D., Schilling, K. A., Loza, C. L., Craven, J. S., Zuend, A., Ziemann, P. J., and Seinfeld, J. H.: Size distribution dynamics reveal particle-phase chemistry in organic aerosol formation, *P. Natl. Acad. Sci. USA*, 110, 11746–11750, doi:10.1073/pnas.1307501110, 2013.
- Song, C., Na, K., and Cocker, D. R.: Impact of the hydrocarbon to NO_x ratio on secondary organic aerosol formation, *Environ. Sci. Technol.*, 39, 3143–3149, doi:10.1021/es0493244, 2005.
- Stephens, S., Madronich, S., Wu, F., Olson, J. B., Ramos, R., Retama, A., and Muñoz, R.: Weekly patterns of México City's surface concentrations of CO, NO_x, PM₁₀ and O₃ during 1986–2007, *Atmos. Chem. Phys.*, 8, 5313–5325, doi:10.5194/acp-8-5313-2008, 2008.
- Tkacik, D. S., Presto, A. A., Donahue, N. M., and Robinson, A. L.: Secondary organic aerosol formation from intermediate-volatility organic compounds: Cyclic, linear, and branched alkanes, *Environ. Sci. Technol.*, 46, 8773–8781, doi:10.1021/es301112c, 2012.
- Verheggen, B. and Mozurkewich, M.: An inverse modeling procedure to determine particle growth and nucleation rates from measured aerosol size distributions, *Atmos. Chem. Phys.*, 6, 2927–2942, doi:10.5194/acp-6-2927-2006, 2006.
- Volkamer, R., Sheehy, P., Molina, L. T., and Molina, M. J.: Oxidative capacity of the Mexico City atmosphere – Part 1: A radical source perspective, *Atmos. Chem. Phys.*, 10, 6969–6991, doi:10.5194/acp-10-6969-2010, 2010.
- Weitkamp, E. A., Sage, A. M., Pierce, J. R., Donahue, N. M., and Robinson, A. L.: Organic aerosol formation from photochemical oxidation of diesel exhaust in a smog chamber, *Environ. Sci. Technol.*, 41, 6969–6975, doi:10.1021/es070193r, 2007.
- Yee, L. D., Craven, J. S., Loza, C. L., Schilling, K. A., Ng, N. L., Canagaratna, M. R., Ziemann, P. J., Flagan, R. C., and Seinfeld, J. H.: Secondary organic aerosol formation from low-NO_x photooxidation of dodecane: Evolution of multigeneration gas-phase chemistry and aerosol composition, *J. Phys. Chem. A*, 116, 6211–6230, doi:10.1021/jp211531h, 2012.
- Yee, L. D., Craven, J. S., Loza, C. L., Schilling, K. A., Ng, N. L., Canagaratna, M. R., Ziemann, P. J., Flagan, R. C., and Seinfeld, J. H.: Effect of chemical structure on secondary organic aerosol formation from C₁₂ alkanes, *Atmos. Chem. Phys.*, 13, 11121–11140, doi:10.5194/acp-13-11121-2013, 2013.